A Search for Anisotropy in the Cosmic Microwave Background on Angular Scales of 1 to 30 Arcminutes

Thesis by

Steven T. Myers

In partial fulfillment of the Requirements
for the Degree of
Doctor of Philosophy

California Institute of Technology
Pasadena, California

1990
(Submitted March 27, 1990)

Acknowledgements

I would like to thank all those who provided support, encouragement, antagonism, and apathy during the completion of this thesis. I would first and foremost like to thank Tony Readhead, my advisor, for his help and guidance, not to mention extreme patience and forbearance in spite of the time dilation accompanying the final stages of the analysis and writing. I would also like to acknowledge the contributions of the staff of the Owens Valley Radio Observatory, especially Mark and Harry, who provided the expertise and support without which the success of this project would not have been possible. The OVRO was my home for a significant fraction of three years and the friendship and humor (and continuous stream of insults from certain persons) made my residence there interesting and bearable despite the behavior of various bits of electronics.

I would also like to thank the members of the faculty, post-docs, and graduate students past and present who have shared my tour of duty over the past 6 years. Arriving in 1984 fresh from the farm, I encountered a strange group of pale beings that inhabited the computer room after midnight. When I discovered that these were the graduate students, I nearly caught the next Greyhound back to Iowa (or something like that). Luckily, I met a fellow rookie named Chuck Steidel and together we mangaged to make it through to the end, along with inmates Blaise (Rapmaster) Canzian, Carl and Debbie (whom I tormented with far too many NASA jokes). Dave Hough introduced me to ”The Contest”, Ralph's Lime Green Yogurt (no natural ingredients), and my first sight of a student in thesis agony. Pawan Kumar managed to get me through QED in one piece. Those who arrived in the following years are to be thanked for putting up with us old-timers, especially Rich, Chris, Alain, Helen, Chris T, Josh (whom Blaise and I lured to Caltech, which I still feel guilty about), and physics types Paolo, John the Greek, and Chris K. I am grateful to the other members of the various volleyball, softball, and soccer teams for humoring my athletic aspirations. I regret not having more time to spend with the youngsters Tom, Jose and Nick, and I hope they keep on being enthusiastic and hard-working—it's kind of cute. There have been various post-docs who have managed to recapture their youth by hanging around us kids, notably Neil Reid and John (DA) Conway, and they have showed us that one can be fun and a Phd. I also would like to thank the faculty members who have been indulgent over these years : Nick Scoville (whom I have caused much grief and I don't regret it), Tony, Wal, Anneila, Tim, and Charles (who says he's the only one who enjoyed Chapter 2). I thank the VLBI group for allowing me to attend their meetings and provide harassment even though I don't do VLBI. I extend my appreciation to Toni Zensus and Fred (Siskel&Ebert) Barnum, who are really Iowans at heart. Finally, I would like to thank the members of "On Beyond Zebra" (Chuck, Gil, Ray, and Doug) for the chance to indulge in the high-powered world of rock music and experience the fame, fortune, and excitement of "Zebra Tour '89" of Madame Wong's.

Abstract

Observations at a frequency of 20 GHz from the Owens Valley Radio Observatory with the 40-meter diameter radiotelescope are used to place limits on the anisotropy of the cosmic microwave background radiation, believed to be a relic from the Big Bang. Two experiments, designated NCP and RING, were performed with the former consisting of deep measurements in 8 fields at the declination $\delta = 89^\circ$ and the latter a survey of 96 fields at declination $\delta = 88^\circ\,10'\,42''$. Bayesian statistical analysis of the 8 NCP field observations place a 95% confidence upper limit of $\delta T/T < 1.9 \times 10^{-5}$ (in fractions of the microwave background temperature 2.735 K) and 4.2×10^{-5} for 99.87% confidence (3σ) on the amplitude of fluctuations with a characteristic correlation length of $2'.6$. The 96 fields of the RING experiment were observed in an interlocked ring-like geometry to enhance the sensitivity of the experiment to larger-scale anisotropies. Because of the larger area of sky covered, this data was more susceptible to contamination by discrete extragalactic radio sources and separate lower frequency observations were used to identify and correct for the contributions of these objects. The statistical analysis of the RING data results in the limits on the anisotropy of $2.5 < \delta T/T < 5.0 \times 10^{-5}$ (95%) and $1.9 < \delta T/T < 6.1 \times 10^{-5}$ (99.87%) for fluctuations with a correlation angle of $2'.6$. *Because of the high probability of residual discrete source contamination, these results are treated as upper limits on intrinsic background fluctuations.* These experiments constrain the amplitude to be less than 3×10^{-4} for correlation angles between $0'.1$ and $30'$ (95%). The implications for cosmology and theories of galaxy formation are discussed, and models without significant non-baryonic matter and/or non-standard recombination are excluded by the observations.

Table of Contents

CHAPTER 1
Introduction

In 1978, two astronomers shared the Nobel Prize for the discovery in 1965 of "excess antenna temperature" in radio antenna measurements at Bell Labs in New Jersey, perhaps the only such award given for the observation of noise. The excess noise of Penzias and Wilson (1965), which was found to have a power level equivalent to that emitted by a $3^\circ.5$ Kelvin blackbody, is of course what came to be called the Cosmic Microwave Background Radiation, or simply the microwave background or cosmic background. In a companion paper Dicke, Peebles, Roll and Wilkinson (1965) explained this radiation, which was found to be isotropic and constant in time, as the relic from an earlier hot phase in the expanding universe. Their work was the culmination of a long chain of theoretical work on the Big Bang cosmological scenario leading back to the work of Gamow (1946) and Alpher and Herman (1949), who predicted a background temperature of 5 K. The isotropy of the microwave background, which by 1967 had been established down to the level of 10^{-3} on degree scales (Conklin and Bracewell 1967), was the best evidence in favor of its cosmological origin. The microwave background has the spectrum of a blackbody at a temperature corresponding to that of the radiation when the Universe passed through the transition from a fully ionized plasma to a mostly neutral medium, with the whole spectrum shifted to lower frequency due to the effect of the Hubble expansion. This era is variously known as the 'epoch of recombination,' as the protons and electrons are able to (re)combine out of the ionized state, or as the time of 'decoupling,' where the photons are decoupled from the matter when the free electrons responsible for the Thomson scattering are removed by formation of neutral atoms. At this point, the universe at recombination acted as a 'surface of last scattering' and thereafter the background photons were allowed to travel relatively freely to our radiotelescopes. The physics for recombination of the expanding universe was worked out by Peebles (1968) and Zel'dovich and Sunyaev (1969). The earliest estimates of the expected fluctuation level from the effect of intervening material (Sachs and Wolfe 1967) and structure at the time of recombination (Silk 1968) were around $\delta T/T \sim 10^{-3}$. This number was arrived at by noting that the density contrast $\delta\rho/\rho$ at present should be near unity at least; assuming that the recombination was abrupt the temperature fluctuations imprinted at the time of recombination are

$$\frac{\delta T}{T} \simeq \frac{1}{3}\frac{\delta\rho_{rec}}{\rho_{rec}} \tag{1.1}$$

and that structure evolved in the linear approximation

$$\frac{\delta\rho_{now}}{\rho_{now}} \sim (1+z_{rec})\frac{\delta\rho_{rec}}{\rho_{rec}} \tag{1.2}$$

with the redshift of recombination given by $z_{rec} \sim 1500$. Later studies showed these assumptions to be too simplistic. Sunyaev and Zel'dovich (1970) in one of several seminal works included the effects of an extended recombination epoch and Thomson scattering opacity within the density fluctuations themselves and found the effect reduced substantially to a level $\delta T/T \sim 10^{-4}$ for angular scales of $5'$–$10'$ corresponding to masses of $10^{15}\ M_\odot$, with the perturbation amplitude increasing with angular and mass scale (see Longair and Sunyaev 1969). By 1970, real calculations of fluctuation amplitude through the decoupling transition were being performed, albeit with *ad hoc* initial perturbations, and anisotropies of order 1.5×10^{-5} were calculated (Peebles and Yu 1970). At the time of the texts by Peebles and Weinberg (Peebles 1972, Weinberg 1972) the theory and observations of cosmic background anisotropy were still in happy agreement.

During the 1970's both experiments and models became increasingly sophisticated. The density fluctuations in the primordial plasma were decomposed into two modes, adiabatic and isothermal (see Sunyaev 1978). The adiabatic perturbations are sound waves in which the matter and radiation components fluctuate in phase and are considered to be the most likely form of fluctuation. Isothermal perturbations are fluctuations of the matter density on a constant background of radiation.

Detailed calculations of the microwave background anisotropies due to these modes became available (*e.g.*, Doroshkevich, Zel'dovich and Sunyaev 1978, Silk and Wilson 1980, and Peebles 1982). The heady enthusiasm displayed by the purveyors of galaxy formation scenarios at I.A.U Symposium 79 on "The Large Scale Structure of the Universe" held in 1977 was typical of this time, with theories of structure formation from primordial density perturbations achieving a state-of-the-art typified by the work of Peebles (Peebles 1980, Peebles 1981, Peebles 1982). Meanwhile, advances in particle physics were pushing quantum field theory to energy scales realized only in the very early universe and such terms as inflation, supersymmetry, cosmic strings, and monopoles were beginning to be heard at astrophysics conferences[1] and in reviews (Rees 1978, Rees 1982). Inflation, as proposed by Guth (1981) and revised by Linde (1982) among others, for the first time suggested a plausible mechanism for solving many of the problems confronting cosmologists at the time, particularly the generation of fluctuations and the isotropy of the microwave background over regions that were never causally connected in the standard Friedmann models. The success of quantum field theory was emboldening physicists to predict many varieties of non-baryonic 'dark matter' particles that could solve missing mass problems in galactic and extragalactic astronomy and possibly dominate over baryonic matter as the principal mass-energy density component of the universe. The strange topological defects known as cosmic strings made their first appearance on the scene as possible seeds for the formation of structure around that time (see Vilenkin 1981). The effect of energy release from protostars and protogalaxies was considered (Ikeuchi 1981, Ostriker and Cowie 1981).

Microwave background observations likewise were beginning to come of age in this period, with a measurement of the dipole anisotropy due to the relative motion of the Earth and our galaxy with respect to the frame of the cosmic background (Boughn, Cheng and Wilkinson 1981) with the claimed detection of a quadrupole signal, and a possible detection of fluctuations at a level of $\Delta T/T = 1.1 \times 10^{-4}$ on the angular scale of 6° (Melchiorri *et al.* 1981). There were also reports coming from the RATAN

---

[1] See *The Very Early Universe*, eds. G.W. Gibbons, S.W. Hawking and S.T. Siklos (Cambridge: Camb. Univ. Press), 1982.

group in the Soviet Union of anisotropy limits below 10^{-4} (Parijskij, Petrov and Cherkov 1977). Most of the theorists working on models of galaxy formation were more concerned with producing the proper galaxy-galaxy correlation function and simulations that matched the observed filamentary structure than with the microwave background anisotropy limits, which were safely consistent with the predicted levels of 5×10^{-5} or higher on angular scales from $1'$ to 6°. The state of the field was such that in 1977, Zel'dovich stated :

> Extrapolating ... to the next symposium somewhere in the early eighties one can be pretty sure that the question of the formation of galaxies and clusters will be solved in the next few years.[2]

This all changed in 1984 with the publication of the results of the Uson and Wilkinson experiment (Uson and Wilkinson 1984a,b,c) who set an upper limit (95% confidence) of $\Delta T/T < 2.1 \times 10^{-5}$ for the *rms* anisotropy on arcminute scales for 12 fields near the North Celestial Pole. The observations were made with the NRAO 140-ft diameter telescope using a cryogenically cooled maser receiver at a frequency of 19.5 GHz in a switching mode of operation to measure the difference in power coming from Gaussian 'beams' of half-power diameter $1'.5$ separated by $4'.5$ on the sky. This limit was far below that predicted by the standard adiabatic density perturbation models with baryonic matter only, and the response from the theoretical community was immediate—non-baryonic dark matter. The particle physics and astrophysics conferences[3] became saturated with a flurry of galaxy formation and fluctuation models with every conceivable candidate for nonbaryonic weakly interacting particles that could begin collapse before and during recombination without disturbing the radiation and generating excessive microwave background anisotropy. This dark matter is classified as hot, warm, or cold based upon how soon after the time at which the mean free path from interaction exceeded the horizon size the particles became nonrelativistic and thus can cluster gravitationally (Bond and Szalay

---

[2] in *The Large Scale Structure of the Universe, I.A.U 97* eds. M.S. Longair and J. Einasto (Dordrecht: Reidel), 1978, p.419.

[3] See *Inner Space/Outer Space*, eds. E.W. Kolb, M.S. Turner, D. Lindley, K. Olive and D. Seckel (Chicago: Univ. Chi. Press), 1984.

1983, Silk 1984). Hot dark matter (HDM) such as neutrinos with masses less than 1 MeV become non-relativistic very late and fluctuations that come within the horizon before this time are erased by the relativistic free-streaming and only the mass scales larger than these will have density variations that will collapse and form structure. Galaxy formation scenarios with HDM (*e.g.*, Doroshkevich 1984) form pancake and filamentary large-scale structure and have a very late time of galaxy formation, the latter of which has brought this scenario into disfavor. Cold dark matter, on the other hand, is nonrelativistic at all times and thus all scales can collapse and form structure, and is efficient at preparing potential wells into which the baryonic matter can fall and form galaxies when recombination allows it to do so. These theories have been the most popular both for galaxy formation simulations and for microwave background anisotropies, as they are computationally tractable, predictive, and produce fluctuations below the observed limits (see Vittorio and Silk 1984, Bond and Efstathiou 1984, Bond 1986). Models with CDM and flat universes $\Omega = 1$ predict fluctuations below the level 10^{-5} on the angular scales probed by the Uson and Wilkinson experiment. Other theories that predict anisotropy levels below the upper limits are those involving baryons with isocurvature fluctuations (nearly equivalent to the isothermal mode perturbations considered earlier), which can give rise to substantial reionization early after recombination to erase fluctuations on the arcminute angular scales (Peebles 1987, Efstathiou and Bond 1987, Efstathiou 1988). Vishniac (1987) demonstrated that in these models some fluctuations remain on small angular scales at a level $\sim 5 \times 10^{-6}$. Explosion models were advanced as alternatives to CDM (Hogan 1984, Ostriker, Thompson and Witten 1987) in which gravity is aided by blast waves in forming structure.

In addition to the Uson and Wilkinson experiment, there were many other new observations providing challenges to those constructing models for galaxy and structure formation. Large maps of the microwave and millimeter wavelength sky were produced by balloon and rocket-borne experiments (Fixsen, Cheng, and Wilkinson 1983, Lubin *et al.* 1985, Halpern *et al.* 1989 and Bernstein *et al.* 1989) as well as the RELIKT satellite experiment (Klypin *et al.* 1987). There was a report of a possible detection of fluctuations on an angular scale of 8° (Davies *et al.* 1987) at a level of

3.7×10^{-5}. Interferometers began to be used for background observations as limits were set on sub-arcminute scale anisotropy using the VLA (Martin and Partridge 1988, Fomalont *et al.* 1988, Hogan and Partridge 1989) near the 10^{-4} level, and on degree scales using a two-horn system (Timbie and Wilkinson 1988) limits of 5×10^{-5} were achieved. Theorists were once again prodded by the reports of a spectral distortion in the microwave background blackbody (Matsumoto *et al.* 1988) until it was swept away by the first results from the COBE satellite (Mather *et al.* 1990). Exploring the local universe, optical galaxy surveys have revealed complex large-scale structures (de Lapparent, Geller and Huchra 1988, Geller and Huchra 1988) and motions (Lynden-Bell *et al.* 1988, Faber and Burstein 1988), complementing the information provided by microwave background anisotropy. Despite the predictions made in the previous decade, a consistent and viable theory for the formation of galaxies has yet to be constructed.

This cursory history of the observations and theory related to the study of the microwave background leads us to the motivation for this work—the search for anisotropy in the background at arcminute scales. A program was begun at the Owens Valley Radio Observatory by the Caltech group in 1984 with the 40-meter diameter radiotelescope using a low-noise maser receiver tuned to a frequency of 20 GHz. These observations eventually culminated in the work reported here, an 8-field high sensitivity experiment published by Readhead *et al.* (1989) included here as Chapter 3, and the 96-field survey that forms the bulk of this thesis. The availability of large amounts of observing time at a dry desert site has enabled us to achieve a sensitivity level significantly better than the best previous limits on any angular scale. As was mentioned, many theories are already ruled out as producing anisotropies above the 2.1×10^{-5} level of Uson and Wilkinson's experiment (although further analysis of their data indicates that the limit should be a factor of two higher—see §2–3 and Kaiser and Silk 1988, Lasenby and Davies 1988) and reducing the limit even 50% strains the credibility of a fair number of models that barely passed the previous test, while limits below 10^{-5} will test nearly all remaining scenarios. It was with this intention that we embarked upon our investigation of the arcminute scale structure of the microwave sky and limits that it can place on the anisotropy of the cosmic background radiation and theories of galaxy formation.

This thesis begins in Chapter 2 with a discussion of the theory of random fields, the statistical inference methods used in the study of the microwave background temperature distribution and the setting of confidence limits on the anisotropy thereof, and the optimization of experimental parameters under these tests. In Chapter 3, we present the results from the Readhead *et al.* (1989) experiment with a discussion of the implications upon theories of galaxy formation. The results from the 96-field RING experiment are given beginning in Chapter 4 with a report on the observations, data reduction techniques, tests of data quality, and the final measurements. Chapter 5 contains the results of a VLA survey of the RING region searching for discrete radio source contamination. Finally, the statistical analysis of the dataset and comparison with published models are presented in Chapter 6 and a summary and concluding remarks is given in Chapter 7.

CHAPTER 2
Statistics of the Microwave Background

2–1 Overview

Because fluctuations in the microwave background (other than the dipole caused by our 'peculiar' motion) have yet to be detected, the importance of statistical analysis in this subject is perhaps greater than in any other field of astronomy. Although nearly all observational and experimental disciplines in science use some form of statistical testing to estimate the true values of a parameter or to characterize the level of agreement or disagreement with predictions of theory, most of the methodology used has been developed under the assumption that the signal is significantly above the noise level. The two major probabilistic ideologies, the frequentist and Bayesian paradigms, provide compatible results in most cases where the distribution of the data values is largely determined by the variables being tested, despite significant differences in formulation. The most straightforward method, that espoused by the frequentists, bases its tests upon the long-term performance under repeated trials. Chi-squared tests for goodness of fit, significance tests for normal distributions, and the Likelihood Ratio class of hypothesis tests all derive from the frequentist statistical theory. On the other hand, the Bayesian method, and its Spartan cousin Likelihood, are predicated upon the use of relative probability of the actual data under the assumptions of the model without recourse to consideration of other possible outcomes or repeated trials. The probabilistic interpretation of the limits obtained under these methods is very different, ranging from the direct statements made by the Bayesian statistician ('the probability that parameter θ is in range X is Y') to the guarded coin-tossing of the frequentists ('if θ is in X then the probability under repeated observation and testing that our test would not reject θ is Y') to the refusal to discuss probabilities by the Likelihood devotee ('if θ is not in X then the observed data is more than Y times less likely than the best value in X'). It falls upon us to find the most appropriate method for the particulars of our experiment, taking into consideration practical implementation as well as philosophical merit, and because our only interface with the world of cosmological theory is through statistical argument, the importance of this endeavor should not be underestimated.

The crucial difference between setting limits in cases where the signal is not readily distinguishable from the noise and instances where the signal is easily detected is in the necessity to condition the results upon the unknown contribution from the noise component. When only upper limits are indicated, the problem is dominated by the noise statistics, which are not available for adjustment by the testing process itself. As we will discover, some of the previous limits on anisotropy turn out to be less than robust to unfavorable realizations of the errors, possibly leading to overestimation of the confidence of said results. Frequentist methods, which average over probable outcomes expected from the noise as well as signal, are most prone to this problem, precisely because they do not condition on the actual observed datum. Bayesian methods, because they assess only the relative probability under the parameter tested, are by construction conditional and are relatively insensitive to unexpectedly large or small error levels. In addition, Bayesian tests are in general easier to perform, especially in cases where the distribution cannot be reduced to a standard form where the percentage points are tabulated.

In the end we hope to find a procedure that provides the best compromise between ease of computation, performance under duress, and clear interpretation of the results. In addition, we can investigate the possibility of aiding our statistical method by optimization of the experimental design, in particular choosing the number and location of the points sampled on the sky. We will first introduce the mathematical background necessary to deal with the analysis of two-dimensional random fields. Then, we will outline the frequentist, Likelihood, and Bayesian methods of statistical inference, pointing out the problems as well as the strengths of each, and then concentrate on the particular Bayesian formulation that will be adopted as our test of choice. Finally, we will discuss the implications of observing strategy as pertains to statistical leverage of upper limits, detection of fluctuations, and removal of unwanted contaminating sources of signal. Most of the material presented here is a further development of topics discussed in (Readhead *et al.* 1989), included here as Chapter 3 and referred to as Paper 1, to which the reader is directed for additional information on issues not discussed in this chapter.

2–2 The Statistics of Random Fields

We desire to gather observational evidence to compare with the predictions of various theories of galaxy formation. These predictions take the form of a prescription for creating a realization of the microwave background. All currently viable scenarios produce structure and thus microwave background anisotropy through the growth of perturbations generated by quantum fluctuations or topological defects at early stages of the evolution of the Universe. The treatment of these perturbations is probabilistic, possibly beginning with the quantum nature of the relevant processes at the time of inflation, progressing with the growth of fluctuations under the influence of gravity, and resulting in the passage through the time of recombination at which point the microwave background radiation is imprinted with the anisotropy that we wish to detect. Our data, therefore, are in the form of samples from a two-dimensional random field, the temperature of the cosmic background on the sky.

A *random variable* x is characterized by its distribution function $P(x)$, where $P(x)dx$ is the probability of the variable assuming a value between x and $x + dx$ in the limit $dx \rightarrow 0$. We can consider a family of distribution functions $P_\Theta(x)$ labeled by the r parameters $\Theta = \{\theta_1, \ldots, \theta_r\}$. A set of n random variables $X = \{x_1, \ldots, x_n\}$ is characterized by the multivariate distribution function $P_\Theta(X)$. A *random field* $F(\mathbf{q})$ on an m-dimensional space for spatial vectors $\mathbf{q} = (q_1, \ldots, q_m)$ can be thought of as a set of functional values $F(\mathbf{q}_i)$, each of which is a random variable with some distribution function $P_\Theta[F(\mathbf{q}_i)]$, and any n of which have the distribution function $P_\Theta[F(\mathbf{q}_1), \ldots, F(\mathbf{q}_n)]$.

Because the angular scale on which we observe is sufficiently small, we can consider our measurements to be a random sample from the whole sky, particularly since the regions were selected in an unbiased manner based on convenient observing geometry. The observations at the Owens Valley Radio Observatory span $\sim 14' \times 2'$

on the sky for a single measurement, covering $< 2 \times 10^{-7}$ of the sky, and the 120 measurements from the two experiments are a random sample from the entire 4π steradians. It is possible that coherent structures on degree scales could mislead us as to the representativeness of our results, but any such effect will be included in the distribution function. Perhaps the most fundamental reason for the random nature of the cosmic background is the question of the uniqueness of our reference frame. It is logical to believe that we occupy no privileged position in the Universe and our view of it can be thought of as merely representative of the possible views afforded other 'observers' from within its whole. We would consider it unnecessary that a viable cosmological theory predict exactly the universe that we see down to the actual positions of galaxies; it would be sufficient if the models resembled reality in a statistical sense. It is the proper measure of statistical agreement that we are searching for, and expect to find, in the mathematical theory of random fields. In the discussion to follow, we generally follow the derivation in the texts by Berger (1985) and Lehmann (1986), but will leave out much of the mathematical and logical rigor in favor of presenting a more transparent discussion of the concepts.

We first consider a real-valued Gaussian random field $F_\Theta(\mathbf{r})$, defined on the infinite two-dimensional space $\mathcal{R}$, with coordinates $\mathbf{r} \in \mathcal{R}$. Our 'observations' consist of n measurements $X = \{x_1, \ldots, x_n\}$, with $x_i = F(\mathbf{r}_i)$ which for convenience we write as a vector $\mathbf{x} = (x_1, \ldots, x_n)$ for purposes of manipulation. The distribution function for the multivariate X is (Kendall and Stuart 1977, Vol. 1)

$$P(X) = (2\pi)^{-n/2}[\det A^{-1}]^{1/2} \, \exp\left[-\frac{1}{2}(\mathbf{x}-\mathbf{u})^T A^{-1}(\mathbf{x}-\mathbf{u})\right] \tag{2.1}$$

with the correlation matrix A

$$A_{ij} = \Big\langle (x_i - \mu_i)(x_j - \mu_j) \Big\rangle \tag{2.2}$$

and mean vector $\mathbf{u} = (\mu_1, \ldots, \mu_n)$. The quantities $\Theta = (\mathbf{u}, A)$ are the free parameters of the model. The angular bracket notation has the usual meaning of expectation value. For a function $G(Y)$ that depends on the values $Y = \{y_1, \ldots, y_m\}$ sampled from F with $y_j = F(\mathbf{r}_j)$ we define

$$\langle G(Y) \rangle = \int_{\mathcal{Y}} d^m Y \, P(Y) \, G(Y) \tag{2.3}$$

over the entire space $\mathcal{Y}$.

Because X is sampled from the Gaussian random field F, assumed to be homogeneous and isotropic, the distribution (2.1) should be independent of the origin and orientation of the coordinate system in which the positions of its sample points are taken, since one region of its space is statistically equivalent to any other. Thus, $(\mathbf{u}, A)$ must be invariant under reordering of the components of $\mathbf{x}$ and translations and rotations of the space $\mathcal{R}$ in which the $x_i = F(\mathbf{r}_i)$ are sampled. Therefore, the $\mu_i = \mu$ are identical and the elements of A are functions only of the relative distance between the locations of the samples x_i and x_j in $\mathcal{R}$

$$\begin{aligned} A_{ij} &= C(\rho_{ij}) \qquad \rho_{ij} = |\mathbf{r}_i - \mathbf{r}_j| && (2.4) \\ &= \left\langle F(\mathbf{q})F(\mathbf{q}')\right\rangle - \mu^2 \qquad \text{all } \mathbf{q}, \mathbf{q}' : |\mathbf{q} - \mathbf{q}'| = \rho_{ij} && (2.5) \end{aligned}$$

where $C(\rho)$ is the *2-point correlation function* for the field F. Thus, our field F can be considered to be derived from a model with parameters $\Theta = \{\mu, C(\rho)\}$. If we consider F to be the anisotropic component about the microwave background mean value, we can take $\mu = 0$ without loss of generality.

Examination of the distribution function (2.1) reveals a common property of all Gaussian random variables—the probability density depends only on the first and second moments of the distribution. The higher order correlation functions are derived from the 2-point function. However, since $C(\rho)$ is actually a function of the distance ρ, in the absence of other information about its form one would need to sample the whole of the space $\mathcal{R}$ to construct an estimator capable of determining the complete form of C. If $C(\rho)$ were also parameterized, perhaps by a fixed functional form $c(\rho)$ and a variable amplitude,

$$C(\rho) = C_o \, c(\rho) \tag{2.6}$$

and/or unknown scale-length

$$C(\rho) = C_o \, c(\rho/\rho_0), \tag{2.7}$$

then it might be possible to reduce the problem to a test involving only a few free variables.

Our microwave background temperature field $F(\mathbf{r})$ is defined on the celestial sphere, with the angular coordinates $\mathbf{r} = (\alpha, \delta)$ known as Right Ascension and Declination. Although it is still correct to define a correlation function $C(\phi)$ where the distance measure ϕ has the range $[0, 2\pi]$ with the continuity requirement

$$C(\phi) = C(2\pi - \phi) \tag{2.8}$$

it is more convenient for consideration of angular scales larger than a few degrees to expand our function in Legendre polynomials

$$C(\phi) = \frac{1}{4\pi} \sum_{\ell} (2\ell + 1)\, C_{\ell}\, P_{\ell}(\cos\phi). \tag{2.9}$$

The use of spherical harmonics and the discrete C_{ℓ} are detailed in various papers describing both observations (*e.g.*, Klypin, Sazhin, Strukov, and Skulachev 1987) and theoretical models (*e.g.*, Bond and Efstathiou 1987) of large-angular scale anisotropies. For small angles $\phi \ll \pi$, however, we choose to retain the standard definition of $C(\phi)$ for angular distance ϕ.

In the development of the theory of random fields for fine-scale anisotropy, we will follow the methodology in Readhead *et al.* (1989) §VIIIb, summarized here for convenience and expanded for completeness where necessary. We first approximate our antenna response pattern or *beam* as some known function $B(\mathbf{q})$, usually taken to be a circularly symmetric Gaussian

$$B(\mathbf{q}) = \exp\left(-\frac{\phi^2}{2\phi_0^2}\right) \qquad \phi^2 = \mathbf{q} \cdot \mathbf{q} \tag{2.10}$$

in angular coordinates $\mathbf{q}$ centered on the beam pattern. The limitations of this approximation are discussed in Chapter 4 (§4–4), Chapter 5 (§5–6) and in Paper 1 (§II, §VIIIc), and it is clear that the deviations from symmetry and Gaussian profile are unimportant for distributed fluctuations on angular scales of importance here. We adopt the value for our beam dispersion $\phi_0 = 0'.764$. Because of the noise filtering requirements presented later in this chapter, we in addition have a switching pattern on the sky $\mathrm{S}(\mathbf{q})$, where in the absence of noise a single sample data point y_i can be represented as

$$y_i = S_i \star F \star B(\mathbf{r_i}) \tag{2.11}$$

with the cross-correlation on the right-hand side as defined in standard texts (c.f., Bracewell 1986)

$$F \star B(\mathbf{r}) = \int d^2\mathbf{q}\; F(\mathbf{q})\; B(\mathbf{q}+\mathbf{r}). \tag{2.12}$$

for real-valued functions F and B. The function S_i consists of δ-functions at the sampled positions multiplied by coefficients :

$$S_i(\mathbf{r}) = \sum_p S_{ip}\; \delta(\mathbf{r} - \mathbf{r}_{ip}). \tag{2.13}$$

We will consider our data to be sampled on the 'smeared' temperature field

$$F_{obs} = F \star B \tag{2.14}$$

with the 'smeared' correlation function obtained through the use of the Fourier relationships for the correlation operation

$$C_{obs} = C \star C_B. \tag{2.15}$$

For our Gaussian beam we will write C_B as

$$C(\phi_0, \phi) = C(\phi) \star \frac{1}{4\pi\phi_0^2}\; \exp\left[-\frac{\phi^2}{4\phi_0^2}\right] \qquad (2.16).$$

In most cases, it is easier to deal with the switching and sampling by relating the measured data points $\mathbf{y} = (y_1, \ldots, y_m)$ to the sampled points of F_{obs}, $\mathbf{x} = (x_1, \ldots, x_n)$. From (2.11–2.14) we get easily

$$y_i = \sum_p S_{ip}\; F_{obs}(\mathbf{r}_{ip}) \tag{2.17}$$

or in our vector notation

$$\mathbf{y} = S\mathbf{x} \tag{2.18}$$

where S is now the $n \times m$ sampling matrix. The two-point correlation matrix A for $\mathbf{y}$ is related to the matrix A' for $\mathbf{x}$ by

$$A = SA'S^T \tag{2.19}$$

or

$$A_{ij} = \sum_p \sum_q S_{ip}\; S_{jq}\; A'_{pq} \tag{2.20}$$

which follows directly from taking expectation values of (2.17) or cleverly relating the exponents of the exponentials in (2.1) for the distribution functions of $\mathbf{x}$ and $\mathbf{y}$.

As an example, we can examine the correlation matrix for the Readhead *et al.* experiment (Paper 1 §VIIIb). Because the separation between data points is much larger than the switching angle $\phi_S = 7'.15$, and any model for which we have significant sensitivity must have a correlation function that falls off measurably at least on the angular scale of ϕ_S (the switching removes the zero and first-order derivatives of the field and the response to fields with long correlation lengths is attenuated correspondingly), it has been assumed that the data points are independent. We find that under this assumption the 2-point matrix is diagonal, and for the 8 fields

$$A_{ii} = \frac{3}{2}C(\phi_0, 0) - 2C(\phi_0, \phi_S) + \frac{1}{2}C(\phi_0, 2\phi_S). \tag{2.21}$$

If we were interested in testing theories with correlation lengths on the order of $30'$ or larger, then it would be advisable to calculate the full correlation matrix (2.20) using A' for the 24 sampled points $\mathbf{x}$. Thus equipped with our weapons for the matrix manipulation, we can return to our distribution function (2.1) with the elements of our matrix A determined by the sampling of the field F_{obs} for assumed Gaussian random fluctuations.

We generally take many measurements for each field observed to help define the noise characteristics as well as to increase the sensitivity. It is theoretically possible to solve for parameters of the noise distribution simultaneously with the parameters of the model, but as we usually have many more integrations per field than the total number of fields observed, even in the weak signal case the confidence region for the variance of the noise is much smaller than that for the signal. We are able to justify both on theoretical grounds (via the Central Limit Theorem) and experimental grounds (Chapter 4–2) the assumption that the statistics of the noise are very nearly Gaussian and independent. We assume that the errors for each field y_i are drawn from a $N(0, \epsilon_i^2)$ normal distribution. Thus, we add an on-diagonal noise term to our correlation matrix for the fields $\mathbf{y}$ given in (2.20) to get

$$A_{ij} = SA'S^T + E \qquad E_{ij} = \epsilon_i^2\,\delta_{ij} \tag{2.22}$$

where δ_{ij} is the Kronecker delta symbol signifying a quantity that is unity when its indices are equal and zero otherwise.

We have thus far succeeded in deriving the form of the 2-point probability distribution function (2.1) for a random field and the associated correlation matrix (2.22). For Gaussian random fields, this is sufficient as all information about the field is extractable from the 2-point function. However, part of the aim of the observations presented in this work is to probe theories that are non-Gaussian in nature, and we must consider the higher order correlation and distribution function for completeness. Unfortunately, the term 'non-Gaussian' only means that the statistics of the random field are not Gaussian, and is descriptive in the same sense that 'anisotropic' signifies the negation of isotropy; when the restrictions on the distribution functions imposed by the term 'Gaussian' are lifted, we are left without any conditions to guide us in the choice of statistic. For these models, we need to specify explicitly the prescription for construction of the random field and the n-point correlation functions. This problem is not just due to the lack of specific non-Gaussian models. For Gaussian distribution functions we have developed a specific formalism, using the 2-point correlation function, with which we can describe and test *any* random field produced by such a theory. It is apparent that there can be many distributions with the same 2-point correlation function, but only one is Gaussian. It is not clear that there are any general classes of non-Gaussian models with similarly simple sets of sufficient parameters. For fields with only mildly non-Gaussian statistics, it may be still useful, though insufficient, to use the 2-point function in the analysis—frequently it is the only tractable alternative. In some models, however, the expectation values (2.6) diverge. This is often the case for random point processes, such as discrete radio sources with power-law number counts, where the second moment is determined by the strength of the brightest source in the region sampled and not limited analytically by the parent model. We therefore leave the further discussion of non-Gaussian statistics until such time that we have specific distributions to test.

We now take the opportunity to discuss general parameterized forms for the correlation function $C(\phi)$. This is also discussed in Paper 1 (§VIIIb). For the correlation function C in two dimensions that is only a function of the single angular distance ϕ, the 2-dimensional Fourier transform is replaced by the Hankel transform (Bracewell 1986) in the standard Fourier theorems for the correlation operation

$$C(\phi) = \frac{1}{2\pi} \int_0^\infty dk\ k\ W(k)\ J_0(k\phi) \tag{2.23}$$

with the Bessel function J_0 multiplying the power spectrum $W(k)$ in the integrand. The equation (2.23) is symmetric in C and W upon inversion. If we take the derivative of (2.23) with respect to ϕ we obtain

$$\frac{d}{d\phi} C(\phi) = -\frac{1}{2\pi} \int_0^\infty dk\ k^2\ W(k)\ J_1(k\phi). \tag{2.24}$$

Because $W(k) \geq 0$ is the power spectrum of the field F, the derivative (2.24) must vanish at the origin and in the limit $\phi \rightarrow \infty$. Thus in general, for non-delta function spectra, C must start at a maximum at the origin and reach zero at infinity. We can characterize the decrease of $C(\phi)$ away from the origin by the *coherence angle*

$$\phi_c = \left[-\frac{C(0)}{C''(0)} \right]. \tag{2.25}$$

If the the functional form of the correlation function was Gaussian

$$C(\phi) = C_0 \exp \left[-\frac{\phi^2}{2\phi_c^2} \right]. \tag{2.26}$$

the angle ϕ_c would be its dispersion. This approximation has been often used to report observational limits in a general form for a variety of scales ϕ_c (Davies *et al.* 1987, Readhead *et al.* 1989). The function (2.26) can then be inserted into the matrix B in (2.22) for constructing the distribution function. Another common approximation is to consider a monochromatic power spectrum

$$W(k) = W_0\ \delta(k - k_0) \tag{2.27}$$

giving from (2.23)

$$C(\phi) = \frac{1}{2\pi}\ k_0\ W_0\ J_0(k_0\phi). \tag{2.28}$$

Calculation of the derivative leads us to the equivalent coherence angle $\phi_c = \sqrt{2}/k_0$. We can also calculate the 'filtering function' for an arbitrary power spectrum for an individual switched measurement y with $\phi_0 = 0'.764$ and $\phi_S = 7'.15$ as in the

Owens Valley experiments. The probability distribution function (2.1) reduces to the standard Gaussian form with dispersion $\sigma^2 = A$ with the scalar A as given in (2.21). If we apply the smearing to (2.23), then we find by multiplying the power spectrum of the fluctuations by the power spectrum of the beam

$$C(\phi_0, \phi) = \frac{1}{2\pi} \int_0^\infty dk\ k\ W(k)\ J_0(k\phi)\ e^{-k^2\phi_0^2}. \tag{2.29}$$

The expected variance of the data is given by

$$\sigma^2 = \int_0^\infty dk\ W(k)\ G(k) \tag{2.30}$$

with the filter function

$$G(k) = \frac{k}{2\pi}\ e^{-k^2\phi_0^2} \left\{ \frac{3}{2} - 2J_0(k\phi_S) + \frac{1}{2} J_0(2k\phi_S) \right\}. \tag{2.31}$$

This filter defines the sensitivity of a single measurement to fluctuations of various wavelengths $2\pi/k$. The function $G(k)$ from (2.31) is shown in Figure 2.1 for the parameters of our experiment. Finally, for future reference, we compute the beam-smeared correlation functions for the two simple approximations given above, for the Gaussian form (see also Paper 1, §VIIIb)

$$C(\phi_0, \phi) = C_0\ \frac{\phi_c^2}{2\phi_0^2 + \phi_c^2}\ \exp\left[-\frac{\phi^2}{2(2\phi_0^2 + \phi_c^2)} \right] \tag{2.32}$$

and for the monochromatic form

$$C(\phi_0, \phi) = \frac{1}{2\pi} k_0\ W_0\ J_0(k_0\phi)\ e^{-k_0^2\phi_0^2}. \tag{2.33}$$

The prescription for the specification of the probability density for data sampled from a random field has now been presented in a reasonably tractable form. The effect of independent Gaussian noise for the measurements has also been incorporated in the formulation. We are now ready to deal with the methodology for the application of statistical tests to the data.

2–3 Methods of Statistical Inference

In this section we will build upon the theory of random fields detailed in the last section, and study the practical problems involved in testing actual experimental data. Although in this work we will use the Bayesian HPD analysis in calculation of limits, previous work both by ourselves (Paper 1) and others has involved the use of a variety of statistical methods. During one particular session at the Aspen Winter Physics Conference on the Microwave Background in January 1990, four different statistical procedures were presented by four different speakers, leaving the audience members in a state of probabilistic shock. Therefore, we will begin with a summary of two of the three most prevalent methods and their strengths and weaknesses. Following this, we will present a detailed explanation of the Bayesian formalism and the modified version that we will adopt in our analysis.

The frequentist perspective is perhaps the most straightforward, and indeed it has been favored by observers in the past. The basis of the method is the frequency distribution of the measurement under repeated trials. Examples of frequentist procedures are standard chi-squared tests, all distribution tests, and the Likelihood Ratio Test. The method of pure Likelihood decides on the relative merit of a set of alternatives by the probability of obtaining the data under them, or likelihood. The range of acceptable models is given by those alternatives where the ratio of probabilites of the data under that value to the best model is larger than a prescribed threshold. Finally, Bayesian methods also utilize the likelihood as well as an algebra of probabilities to set credible sets of alternatives through integration of the probability of the data times a function incorporating prior knowledge. We begin with the frequentist view.

3.1 Frequentist Statistics and Likelihood Ratio Tests

Frequentist methods are characterized by the calculation of the probability distributions of a statistic under the hypotheses being investigated. A detailed discussion of one such test, the Likelihood Ratio Test , is given in Lawrence, Readhead, and Myers (1988). This test has been applied, in slightly different forms, in Boynton and Partridge (1973), Uson and Wilkinson (1984a,b,c), and by ourselves in Paper 1. The mathematical properties of the test are given in Lehmann (1986). The popularity of the method is due to the simplicity of the concepts, which are based on the frequency of outcomes on repeated experiments, such as the flipping of coins, and also to the ease of computation in some cases where standard probability tables are available. Problems with the method are the excessive computation required to establish the frequency distribution in analytically intractable cases, inconsistent results or failure for some classes of models under certain data values, and questions as to the validity and applicability of the fundamental assumptions to actual situations.

The operation of the method is most clear in the case of a hypothesis H and alternative K of which one or the other will be chosen for any given value of the data. The rejection of H (and therefore the acceptance of K) will be indicated if the datum D lies within some subset S of the data space, chosen such that the overall probability of the data under H within this set is equal to some specified value, the *significance*, while the probability under K for data in the region, the *power* of the test, is a maximum. The value of the significance sets the fraction of the time we would expect to reject H if it were true (bad) and the power reflects the probability of rejecting H when K is true (good). The confidence of a test of significance α is $(1-\alpha)$, and is usually taken to be a large value such as 95% or 99%. To maximize the power for a given significance, we look for the region S, which contains the points X where the *likelihood ratio* is minimal

$$\lambda(X) = \frac{P(X|H)}{P(X|K)} \leq k \tag{2.34}$$

where $P(X|\Theta)$ is the probability distribution function of random variate X under model or hypothesis Θ, which we denoted in the previous section as $P_\Theta(X)$. If we find for the data that $\lambda(D) \leq k$ then we reject H and accept K. The value of k is determined by the requirement

$$P(X \in S|H) = \int_S P(X|H)\, dX. \tag{2.35}$$

Because the quantity tested is the likelihood ratio, this is known as the Likelihood Ratio Test (LRT). The fundamental theorem leading to this test is known as the Neyman-Pearson lemma.

It turns out that we can use this prescription to test a real-valued parameter θ, which ranges over some interval of the real line by assigning

$$H : \theta > \theta_0 \qquad K : \theta \leq \theta_0$$

where θ_0 is the $(1 - \alpha)$ upper limit. For it to be possible to perform this test, we must place some requirements on the behavior of the likelihood ratio as a function of the parameter (see Lehmann 1986). If these requirements are met, then the test is equivalent to finding the distribution of a sufficient statistic $T(X, \theta)$ such that

$$\lambda(X) = \lambda(\ T(X, \theta)\ )$$

depends on the data only through T. Furthermore we need to assume that T is monotonic in θ; for simplicity assume that

$$T(X, \theta) \leq T(X, \theta') \qquad \text{for} \quad \theta > \theta'. \tag{2.36}$$

Then, if the distribution of $T(X, \theta) = t$ under θ is given by

$$P(t|\theta) = \int_{X|T(X,\theta)=t} P(X|\theta)\, dX \tag{2.37}$$

we can set $(1 - \alpha)$confidence limits $\theta_0 < \theta < \theta_1$ by finding the locus of the $\alpha/2$ points in the distribution

$$P(t > T(D, \theta_0)|\theta_0) = P(t < T(D, \theta_1)|\theta_1) = \frac{\alpha}{2}. \tag{2.38}$$

Thus, in cases where it is possible to set simple acceptance intervals, the LRT reduces to the standard confidence tests based on frequency distributions (hence the term frequentist), such as detailed in standard statistics texts (c.f. Kendall and Stuart 1979, Vol. 2).

This procedure is well-behaved for models where for every admissible value of the data X, there is a value of the parameter θ for which the probability is maximal

$$P(t = T(X,\theta)|\theta) = \max_t P(t|\theta). \tag{2.39}$$

If this condition is not satisfied, then not only will there be values of the data for which only a one-sided limit is obtainable for certain confidence levels, but there are values of the data for which no θ that satisfy (2.39) can be found. This problem can be removed by increasing the confidence level of the test; as long as the observed value of the data is obtainable with nonzero probability for some model parameter, then the limits (2.39) exist for some confidence $(1-\alpha)$. Another problem, or at least an inconvenience, arises from the necessity to compute the distribution (2.37) and integral probabilities (2.38), particularly in cases where the distribution cannot be reduced to a standard form. Monte-Carlo methods are commonly used in these cases, frequently requiring large amounts of computational time. We are in effect forced by the frequentist formulation to integrate over the (often large) data space.

An example of a distribution that gives these problems is a single Gaussian variable with an added noise ϵ^2 and a free variance θ^2

$$P(X|\theta) = [2\pi(\theta^2+\epsilon^2)]^{-1/2} \exp\left[-\frac{X^2}{2(\theta^2+\epsilon^2)}\right] \tag{2.40}$$

with statistic

$$T(X,\theta) = \frac{X^2}{\theta^2+\epsilon^2} \tag{2.41}$$

and its associated distribution of $t = T(D,\theta)$

$$P(t|\theta) = \sqrt{\frac{t}{D^2}} \exp\left[-\frac{t}{2}\right]. \tag{2.42}$$

Note that the distribution $P(t|\theta)$ is independent of θ; this is an optimal form for the statistic as it simplifies the calculation of the distribution. The $(1-\alpha)$ lower limits (θ_0, θ_1) for the data $X = D$ occur as fixed values of the statistic

$$T(D,\theta_0) = T_0 \qquad T(D,\theta_1) = T_1 \tag{2.43}$$

where (T_0, T_1) depend only on α. If we examine the behavior of the upper limit θ_1 as a function of D, for example, we find that the appropriate solution to (2.43)

$$\theta_1^2 = \frac{D^2}{T_1} - \epsilon^2 \tag{2.44}$$

will have no solution for $\theta \geq 0$ when $T_1 > D^2/\epsilon^2$. Our problem is due to the fact that the observed data may be so unlikely under every value of the model parameter that all θ are excluded at the stated confidence. Note that tests for the mean of a distribution such as (2.41) will not encounter these problems. A discussion of the problem as applied to the microwave background and useful diagnosis of the disease are given in Lawrence, Readhead, and Myers (1988).

Even though the cause is understood, the fact that the test, which began as a method to decide between two alternatives, is indecisive in some cases even when the probabilities of the alternatives are not degenerate is disturbing. In the example above, even though the absolute probability for a small datum D is small for any value of θ, we know from (2.40) that it falls off as θ^{-1} in the limit of large θ and so we would expect that there are some values of the parameter that are relatively more unlikely than others—our test should be able to set intervals based upon this. In frequentist terms, we would not be compromising our results since our test would have an even higher confidence than the one that failed. The probabilistic justification of our frequentist procedure lies in the meaning of $(1-\alpha)$ confidence, that if we were to use our test many times on many different problems, we would find that our confidence interval contained the actual value $100(1-\alpha)\%$ of the time. This may not be particularly reassuring when one has a case where we know that it is likely that we are wrong, regardless of the long-term benefits of the method! As an example, the Uson and Wilkinson dataset (Uson and Wilkinson 1984c) has a standard deviation (from zero) that is 82% of that expected from the noise alone producing a 95% confidence upper limit ($\theta = C_0^{1/2}$) using the LRT

$$\frac{\Delta T}{T} < 2.1 \times 10^{-5}$$

that is 54% of the comparable limit using the Bayesian method

$$\frac{\Delta T}{T} < 3.9 \times 10^{-5}.$$

The power of the test (at the upper limit versus zero amplitude) is 13%, leading us to believe that the limit generated by the LRT is unjustifiably low, since it rejects values of θ for which the likelihood ratio versus zero is as high as $\lambda = 0.44$, an uncomfortably high number. The fixed significance level α of the test forces us to reject parameter values for which the measurement is only 2.3 times less likely than for the 'best' accepted θ because in the long run we wish to reject the 95% limit 5% of the time if it were true. The desire to free our procedure from the consideration of outcomes of the experiment that did not occur leads us to a formulation based upon the relative probability of the observed data, or likelihood, under the various alternative models or values of a parameter. Two such methods will now be discussed.

3.2 Likelihood

The only distribution that we have direct knowledge of is, by the construction of the model, the probability distribution function of the data under the theory considered for the test. Every method for hypothesis testing or statistical inference is based on the idea that a model that is more likely to produce the observed results is to be preferred over a model less likely to produce said measurement. In the frequentist prescription, this was a secondary requirement to be maximized (in the form of the power of the test) after the behavior under repeated trials was fixed (in the form of the significance). However, one could adopt a more pessimistic attitude and state that the *only* information to be gained about the true state of the model parameters is contained in the ratio of the probabilites of the actual measurement between the alternatives. This axiom is known as the *Likelihood principle*, and is discussed in Edwards (1972) and Berger and Wolpert (1984), and forms the basis of the Maximum Likelihood Method (MLM) of estimation and the Likelihood formulation of statistical inference. The veracity of the principle and the admissibility of the proofs offered in its defense are not universally accepted by probability theorists, but as a principle it seems to be both straightforward and common-sense, and no compelling arguments have been offered to prompt its dismissal. On the other hand, if we accept the axiom as the foundation of a theory of statistics, we are led to reject the frequentist prescription that gave us trouble for cases of interest to us. Therefore, we accept the Likelihood principle and forge ahead.

We define as the *likelihood* of a model H based on data D the probability density of the data

$$L(H) = P(H|D). \tag{2.45}$$

The relative likelihood of model H versus alternative K is given by the ratio of the likelihoods (the likelihood ratio of the LRT)

$$\lambda(H,K) = \frac{L(H)}{L(K)} \tag{2.46}$$

and H is to be preferred over K if $\lambda > 1$. We usually consider models having one or more parameters with unknown values and wish to place limits on the range of these variables. For illustration purposes, and because it is the most common case in practice, we will consider a theory with one real-valued free parameter θ. The form of the test is simple : we find the value of $\theta = \hat{\theta}$ for which the likelihood of the data $X = D$ is a maximum

$$\hat{\theta} : L(\hat{\theta}) = \max_{\theta} L(\theta) \tag{2.47}$$

and accept any value of the parameter for which the likelihood versus the maximum likelihood is greater than a given threshold. We define the c_f set $\hat{\mathcal{H}}$ for the parameter as

$$\hat{\mathcal{H}} = \{\theta : \lambda(\theta) > \frac{1}{f}\} \qquad \lambda(\theta) = \frac{L(\theta|D)}{L(\hat{\theta}|D)}. \tag{2.48}$$

Limits where the likelihood ratio has fallen to $1/f$ are sometimes noted as the c_f limits in the literature. The value of f is entirely subjective; a common choice as a standard is the c_{10} limit. If we just want an *estimator* for the most probable or more correctly the most likely value of the true parameter, then we use $\hat{\theta}$ for which the likelihood is maximum. This is the basis of the Maximum Likelihood Method of estimation. We will use the MLM when an approximate 'best value' for a parameter is needed. The use of (2.47) to find the acceptable range of the parameter is the Likelihood method of statistical inference.

It is often clumsy to deal with the likelihood and likelihood ratios that can range over many orders of magnitude. Also, when the data is made up of many individual points, the likelihood function can be complicated. If the datum X is composed of n independent random variates x_i with distribution functions $P_i(x_i|\theta)$, then the distribution of X is given by

$$P(X|\theta) = \prod_{i=1}^{n} P_i(x_i|\theta) \tag{2.49}$$

which implies that the joint likelihood is also a product of the individual likelihoods. It is more convenient to work with the logarithm of the likelihood, called the *support* S (or log-likelihood in some texts)

$$S(\theta) = \ln L(\theta) = \sum_{i=1}^{n} \ln P_i(x_i|\theta). \tag{2.50}$$

This transformation has no effect on the determination of the estimator $\hat{\theta}$, but it is usually much easier to solve

$$\left.\frac{dS}{d\theta}\right|_{\hat{\theta}} = 0 \tag{2.51}$$

than the original product L. Edwards makes a point of the ease of the use of the support, especially the additive property of combined likelihoods, but in fact it is more natural to use the product for the logical *'and'* operation that this implies; we will return to this point later during the next section. The Likelihood formulation when expressed in terms of the support function is called the *Method of Support*, but we will make no distinction between it and formal Likelihood.

Our limits for the range of θ are determined by the support function under the combination of (2.47–2.51)

$$\hat{\mathcal{H}} = \{\theta : |S(\hat{\theta}) - S(\theta)| \geq m\} \tag{2.52}$$

where $m = \ln c$. If θ is a continuous parameter over some open or closed interval of the real line, then the θ that define equality on the right-hand side of (2.52) are known as the *m-unit support limits* on θ. This method of inference and interval determination is extremely simple, involving no integration and a minimum of root finding, but lacks a probabilistic interpretation akin to the frequentist conception of confidence. Edwards advances the opinion that such notions are inappropriate and impossible to codify in a consistent formalism, but his arguments are unsatisfying after all is said. We will use Likelihood and the Method of Support when the simplicity of computation dictates, such as the discussion of optimization in §2–4, and as a base for the development of the next formulation. For the purposes of setting limits on microwave background anisotropy we will proceed to the third and final method to be considered, that of Bayesian inference.

3.3 Bayes's Theorem and Bayesian Inference

The problem that has been vexing us is the interpretation of the results of *a posteriori* statistical inference in terms of common-sense probability. The Likelihood method freed us from the dictates of long-term performance enforced under the frequentist paradigm, but in doing so left us without the means to make probabilistic statements about our acceptance intervals. A proponent of Likelihood would claim that *a posteriori* probabilistic statements about values of properties of the Universe are impossible and that the best one can do is give relative probabilities under the different alternatives. This view has much that is convincing in it, and the arguments of its adherents such as Edwards are persuasive, yet we still hope for something more. The ability to make probabilistic assertions about ranges of parameters based upon the likelihood of the observed data is the capability claimed by the Bayesian method of inference, and it is with this method that we will conclude our survey of statistics.

For now, suppose that we can define the probabilities required for our formulation, and that we would like to use data (D) to infer the probability of a hypothesis (H) for a given observation of D. Then, we are able to construct the joint probability density

$$P(D,H) = P(D)P(H|D) = P(H)P(D|H). \tag{2.53}$$

This equation is known as Bayes's Theorem (c.f. Kendall and Stuart 1979, Vol. 2, and Berger 1985). The conditional probability $P(H|D)$ for H given D is the desired end, the conditional probability for D given H (the likelihood of the data under H) is given, and the absolute probabilities of the data $P(D)$ and hypothesis $P(H)$ are what allow us to calculate what we could not in previous methods— 'inverse probability.' In fact we are no better off in the absolute sense because knowledge of $P(H)$ is denied us in applications of interest to us. In a sense, $P(H)$, the unconditional 'true' distribution of models H, is what we want to know, and if we knew it we would not need statistical inference. If H is the random realization of a random process with frequentist probabilities $P(H)$, then (2.53) will provide us the correct formulation. A Bayesian statistician would claim that $P(H)$ represents *prior* probability of the hypothesis, and should merely represent one's best guess as to the predisposition of H, before data is taken. However, if this is true inductive knowledge about H, then the information should be included as data D and the distribution under H included in $P(D|H)$; if it is pure guesswork, then it is not a probability in the sense we have defined previously, merely a preference. Eventually, the strict veracity of (2.53) will depend on the ability to define an accurate $P(H)$, which is denied us. It may also be argued that for any physically important measurement, the data is but a sample from a realization of a random process H and $P(H)$ is nonzero only at the actual H.

Finally, there is the matter of the curious quantity $P(D)$, the probability of the data. If we integrate (2.53) over the space of the hypotheses H, we obtain

$$P(D) = \int dH P(H) P(D|H). \tag{2.54}$$

This indicates that $P(D)$ is a measure of the probability of the data under the assumed distribution and prior density. Note that if D results from a unique $H = H_0$, then $P(D) = P(D|H_0)$ as expected. Solution of (2.53) with (2.54) then leads us to the Bayesian prescription for inference

$$P(H|D) = \frac{P(H)P(D|H)}{P(D)} \tag{2.55}$$

and intervals in H under this distribution can be constructed by integration of (2.55).

Many clever Bayesians have given up the idea of absolute probabilities and resorted to the relative likelihood approach mentioned in reference to frequentist methods. Suppose that we were to interpret the P's of (2.53–2.55) as relative likelihoods, or *preferences* if you will, and that they are monotonically increasing measures of the confidence we have for the proposition in question. We see that the quantity in question must have the properties and algebra of a positive, additive function, just as for true probabilities, although the requirement of the range $[0, 1]$ is dropped. In this case, the algebra of preferences is but a superset of the algebra of probabilities, and most importantly Bayes's Theorem is tractable. In fact, we see that (2.53) is but a statement of consistency for our definition of preferences. These arguments are described in Kendall and Stuart (1979, Vol. 2) and Skilling (1989) and references therein.

The Likelihood method, as related in the previous section, incorporates the combination of distributions under the logical *'and'* operation as the familiar multiplication operator, as regards the likelihood function. What we really desire when setting limits and intervals is the equivalent of the logical *'or,'* the probability or preference for a set of alternatives. This naturally implies the use of the addition operator, which for a continuous parameter involves integration. We believe that this is a strong argument in favor of the use of Bayes's Theorem; that this is the *only* correct method might possibly be justified by algebraic considerations, but such debates are beyond the limits of our space and practicalities to include here. The primary philosophical advantage of this Bayesian approach is the removal of the need to interpret the terms in the equation as frequentist probabilities and the logical dilemma this entails. The practical advantage is that the integrals involved are over the restricted hypothesis space, not over the large data space as in the frequentist method. From this point forward, we will adopt the viewpoint of preferences in the Bayesian framework, and leave the probabilistic interpretation to the purists. It is this that we will refer to as 'Bayesian' in the remainder of the work.

For a Gaussian random field, the term in (2.53) $P(D|H)$ is equal to the probability distribution function (2.1), which in turn is a function only of the parameter pair (μ, C). If we in turn parameterize the correlation function by its amplitude C_0, fix the form in the model (2.6), and set the mean to zero, then we can deal with a single parameter $\theta = C_0$. The function $P(D|H)$ is just the likelihood function $L(H)$ defined in the previous section. We have for amplitude θ and correlation matrix $A(\theta)$ the Likelihood

$$L(\theta) = P_\theta(Y) = (2\pi)^{-n/2}[\det A^{-1}]^{1/2} \exp\left(-\frac{1}{2}\mathbf{y}^T A^{-1} \mathbf{y}\right). \qquad (2.56)$$

If a form is assumed for the prior preference $P(H)$, usually referred to as the *prior* $\pi(\theta)$, we can compute the *marginal distribution* $m(\mathbf{y}) = P(D)$ of data $\mathbf{y}$ under θ from (2.54)

$$m(\mathbf{y}) = \int d\theta \; \pi(\theta) \; L(\theta). \qquad (2.57)$$

The quantity $m(\mathbf{y})$ is a measure of the likelihood of the data having the observed value under the assumed prior π and correlation function form. If we are able to cast the prior preference in the normalized form required for a probability, then we have a normalized measure for the appropriateness of the assumed prior. Finally, we can compute the *posterior distribution* for θ, or $\pi(\theta|\mathbf{y}) = P(H|D)$, from (2.55) and (2.57)

$$\pi(\theta|\mathbf{y}) = \frac{\pi(\theta) \; L(\theta)}{m(\mathbf{y})}. \qquad (2.58)$$

This is the quantity that expresses our relative preferences for values of the parameter.

If we were to have access to the proper probability distributions in (2.55), then we could compute confidence intervals by integration, as argued above. We would define a $100(1-\alpha)\%$ *credible set* $\mathcal{H}$ to be

$$\mathcal{H} = \{H : \int_{\mathcal{H}} P(H|D)\, dH = 1-\alpha\}. \tag{2.59}$$

The equation (2.59) itself does not suffice to define a unique set $\mathcal{H}$, since there exists a $(1-\alpha)$ credible set that contains any given H. We can characterize a set $\mathcal{H}$ by its *size*, more properly, its Lebesgue measure of the 'volume'

$$s = \int_{\mathcal{H}} dH. \tag{2.60}$$

We can see that there is some interval $\hat{\mathcal{H}}$ for which the size s is minimal; this set contains the H for which $P(H|D)$ is maximum

$$P(H|D) \geq P(H'|D), \qquad H \in \hat{\mathcal{H}} \quad H' \notin \hat{\mathcal{H}}. \tag{2.61}$$

This suggests a definition for setting credible intervals in the case of our single parameter θ with posterior (2.58). We define the $100(1-\alpha)\%$ *Highest Posterior Density* (HPD) credible set consisting of the values of the parameter for which the posterior density is the largest and for which the posterior density integrates to $(1-\alpha)$. Formally,

$$\begin{gathered}\hat{\mathcal{H}}[\alpha] = \{\theta : \int_{\hat{\mathcal{H}}} \pi(\theta|\mathbf{y})\, d\theta = 1-\alpha\} \\ \pi(\theta|\mathbf{y}) \geq \pi(\theta'|\mathbf{y}) \qquad \text{for all} \qquad \theta \in \hat{\mathcal{H}} \quad \text{and} \quad \theta' \notin \hat{\mathcal{H}}.\end{gathered} \tag{2.62}$$

Note that except for the inclusion of a prior, we have a method equivalent to the Likelihood formulation (2.47), since (2.62) leads necessarily to the existence of some posterior c such that

$$\pi(\theta|\mathbf{y}) \geq c \qquad \text{for all} \qquad \theta \in \hat{\mathcal{H}}. \tag{2.63}$$

The Bayesian HPD procedure chooses the value of c according to the probabilities in the theorem (2.53), removing the arbitrary nature of the Likelihood limits.

Much soul-searching and agonizing has occurred in the Bayesian statistical world over the question of the selection of a prior. From the vantage point of preferences, the prior could be used to incorporate any subjective information about the parameter being tested into the procedure. This is the view taken by most Bayesians such as Berger (Berger 1985), and is useful when the prior information is of a type not easily cast into a true probabilistic form. By and large, the most oft-used reasoning for selection of a particular prior is due to *invariance* arguments. The pure Likelihood method, because it chooses the interval limits based upon the relative values of the likelihood $L(\theta)$, is invariant under any transformation of the variable θ and

$$L^*(g) = L^*[\ g(\theta)\ ] = L(\theta) \qquad \theta \rightarrow g(\theta), \quad L \rightarrow L^*. \tag{2.64}$$

However, because of the prior, the construction of confidence intervals in the Bayesian formalism seems not to be of an inherently invariant nature.

The problem of invariance in the definition of the HPD credible set is manifest when we consider the transformation of the prior under $\theta \rightarrow g(\theta)$. The likelihood function is invariant because it is a probability density in the data variable $\mathbf{y}$ which does not change under transformations of the parameter θ. On the other hand, the prior by definition is a density in the variable θ, and therefore must transform with the differential $dg = g'(\theta)\ d\theta$

$$\begin{aligned} \pi^*(g)\ dg &= \pi^*[\ g(\theta)\ ]\ g'(\theta)\ d\theta \\ &= \pi(\theta)\ d\theta. \end{aligned} \tag{2.65}$$

If we regard our prior as a preference instead of probability, then we must regard it as a preference for the parameter to lie in the interval $d\theta$ around θ, for invariance to be maintained. If our transformation is invertible with nonzero derivatives everywhere (except in the limit of endpoints), then

$$\pi^*(g) = \pi[\theta(g)]\ \theta'(g). \tag{2.66}$$

If we try and regard $\pi(\theta)$ as a point preference in the same manner as the likelihood, then we run into trouble. If we only know that a parameter lies within some (possibly large) interval $[a, b]$ we might use the 'uninformative' prior

$$\pi(\theta) = \frac{1}{b-a} \quad \theta \in [a, b], \qquad \pi(\theta) = 0 \quad \theta \notin [a, b] \tag{2.67}$$

which expresses our ignorance other than to the general range containing the true value. We logically expect that ignorance of θ implies similar ignorance about any function of θ,

$$\pi^*(g) = \frac{1}{|g(a) - g(b)|} \quad g \in [g(a), g(b)], \qquad \pi^*(g) = 0 \quad g \notin [g(a), g(b)] \tag{2.68}$$

however our rule of transformation (2.66) requires that in fact

$$\pi^*(g) = \frac{\theta'(g)}{b-a} \quad g \in [g(a), g(b)], \qquad \pi^*(g) = 0 \quad g \notin [g(a), g(b)]. \tag{2.69}$$

This is deemed as unseemly behavior and uninformative priors are chosen such that under specific transformations g, $\pi(\theta)$ and $\pi^*(g)$ have the same functional form. That there is no prior truly uninformative under all generally admissible transformations should be no surprise; the whole purpose of a prior was claimed to be to provide extra information about a parameter, and it is not obvious that the fact that there is no information is information itself in the sense that we can assign a prior distribution to it. Choosing a specific function $\pi(\theta)$ mathematically states that we know the probability distribution at every point in the range, and the probability that θ lies in any subinterval of the range. The proponents of Likelihood have advanced strong arguments against 'uninformative priors' (Edwards 1972), and based on our investigations above we are inclined to believe them.

From the arguments above, it would seem that because of our inability to choose a truly universal prior, uninformative for all transformations of the parameter, we are prevented from our goal of an acceptable and consistent Bayesian inference method. To help us out of our dilemma, we take notice of the fact that at some point we will have to do some numerical integration, and we obviously cannot integrate over an infinite parameter space. The posterior distribution (2.58) has two contributions, one from the prior, and one from the likelihood. It is thus apparent that information from the prior where the likelihood L is low will not contribute much to the posterior, just as the converse is true. Unless we have strong reasons for using a prior that has substantial weight where L indicates low likelihood, then there is no point in worrying about what $\pi(\theta)$ does in these regions. We assume that if we had strong preference for a prior, we would not be debating the problem. The effect of a mismatched prior and Likelihood is to reduce the amplitude of the marginal distribution $m(\mathbf{y})$ which for a normalized prior is a measure of the likelihood of the data under the prior and Likelihood. We have been considering Gaussian distribution functions for which $L(\theta)$ will tend exponentially to zero in the limit $\theta \to \infty$, and in this case and a whole general class of random fields with nondivergent second moments there is no gain in carrying the integration out to infinity. We will therefore use the uniform intervallic prior of (2.67) with the minor reservations expressed above.

Under prior (2.67), our marginal distribution becomes

$$m(\mathbf{y}) = \frac{1}{b-a} \int_a^b L(\theta)\, d\theta \tag{2.70}$$

and in calculation of the HPD interval all integrations are finite. It is interesting that for our class of uniform priors $[a, b]$, the marginal distribution increases as our interval collapses around the maximum likelihood estimator $\hat{\theta}$ for which $L(\theta)$ is a maximum. In general we have the disturbing result that the prior $\hat{\pi}(\theta)$ that globally maximizes $m(\mathbf{y})$ is the prior with all its weight at the maximum likelihood

$$\hat{\pi}(\theta) = \delta(\theta - \hat{\theta}), \qquad \hat{\theta} : L(\hat{\theta}) = \max_{\theta} L(\theta). \tag{2.71}$$

Thus, the selection of a prior based upon maximizing the marginal distribution is misleading. If the prior is not truly based on information not contained in the Likelihood, then the 'maximum marginal method' merely says that the best prior is the most likely value predicted solely by consideration of the Likelihood function! This would tend to lead one to adopt the Likelihood Principle mentioned earlier, which states that all information about some parameter from data alone is contained in the Likelihood function for the actual measurement.

We have finally arrived at an acceptable prescription for setting distribution parameters from data. We will use the Bayesian HPD credible set (2.62) under the restricted uniform prior (2.67). By definition, this interval will contain the value of the parameter for which the Likelihood is a maximum. If we are interested in a single estimator for the parameter, then the value that provides the maximum likelihood of obtaining the observed data is the only logical and consistent choice. Despite our misgivings about the ability to use a prior, we are content with this formulation. The algebra of preferences is a powerful tool that prompts us to integrate the likelihood and prior to obtain our 'preferred' interval. The ratio of the HPD integral to that outside the interval is our likelihood of the chosen range containing the true value of the parameter

$$\frac{L(\theta \in \hat{\mathcal{H}})}{L(\theta \notin \hat{\mathcal{H}})} = \frac{1-\alpha}{\alpha} \tag{2.72}$$

and we can make the statement that

$$P(\theta \in \hat{\mathcal{H}}) = 1 - \alpha$$

with at least the same weight of conviction that bettors assign odds to the outcomes of sporting events. Because there is a defined lower limit to the relative likelihood of the values of the parameter contained within the HPD interval, we have at least the same confidence about our claims as proponents of strict Likelihood have about theirs, regardless of the probabilistic interpretation. We have already stated that the long-run performance of the test in the frequentist sense is not compelling, although in the limit that the chosen prior reflects the long term frequency of true models, Bayes's theorem is the correct formulation in this sense also. Finally, if we consider inappropriate models or parameterizations, inappropriate results will be obtained regardless of the statistical method.

In our discussion of the LRT, we pointed out that in some cases where the data is unusually unlikely under all values of the parameter, spuriously low upper limits can be set. This was evidenced as an increase in the relative likelihood of the θ values rejected by the test. As demonstrated in Paper 1 (§VIIIa), the Bayesian upper limit increases with the enlarged errors because the likelihood curve broadens out (this can be seen by examination of the simplified expression 2.74 in the next section). Both the Likelihood method and the Bayesian analysis thus give *larger* upper limits for overestimated errors, in contrast to the behavior of the LRT. As explained in the Paper 1 comparison of tests, the Bayesian method is also more robust versus changes in the data values than the Likelihood Ratio Test. From these considerations, we believe that the adoption of the Bayesian HPD procedure will protect us from possible problems of the type described above, which have been encountered in past and present microwave background experiments. It must be stressed that no statistical test is completely immune to misuse or unfortunate luck; such a test would be unable to reject any hypothesis!

It has been traditional to quote the 95% 'confidence' limits in the reporting of statistical comparisons of microwave background observations with theoretical models or in the analysis of the noise characteristics of the data for signal. In this work we will likewise present results for $\alpha = 0.05$, if only to allow comparison of our limits with those obtained by other experiments. It is not particularly reassuring to be using as our measure of rejection for theoretical parameter values a level commensurate with only a $1.96\,\sigma$ deviation from a normal distribution, or in other terms a 1-in-20 chance of error. In problems relating to the detection of signal in the presence of noise it is common to use 3σ as the fiducial criterion for acceptance, which corresponds to $(1-\alpha) = 0.9987$ for a two-sided limit. In the analysis of the RING (Chapters 4 and 6) as well as the NCP results (Paper 1), we prefer the 99.87% Bayesian HPD limits, and we will compute the limits for both $\alpha = 0.05$ and $\alpha = 0.0013$. It should be noted that many of the problems noted previously when dealing with data for which the observed value of the statistic is unlikely are alleviated by increasing the confidence level of the test, and in practice the use of 99.87% limits is sufficiently conservative that only in the most singular cases will difficulties due to abnormally low scatter cause noticeable bias in the results.

In this section, we have made an attempt to cover the topics most important to the fundamental assumptions and applications of the statistical tests, but make no claim that all points were pursued in the detail that they deserve. There are many points dealing with the use and performance of Bayesian methods that we have not had the space nor the inclination to present in this work. The text by Berger is highly recommended for its clarity and completeness, although much space is devoted to decision theory and the strange formalism that it entails. For the frequentist perspective, the work by Lehmann is serviceable, if a bit dense with somewhat difficult notation. For Likelihood, the book by Edwards is extremely good, especially as a view from outside the borders of frequentist and Bayesian statistics, and includes detailed examples of the use of the Method of Support for multivariate distributions and problems with unwanted parameters. Finally, a good discussion of all three methods as well as others in addition to all one needs to know about the theory of probability and statistics is contained within the 3 volume set by Kendall and Stuart (the topic of statistical inference is in Volume 2). It is likely that any scientist that needs to infer parameters of random distributions from data will encounter one or more of the problems discussed here. Perhaps the content of the preceding sections will provide illumination in the often foggy world of the Statistician.

2–4 Optimal Observing Strategies

In both the planning and analysis phases of an observational program is it necessary to have a proper grasp of sensitivity of the experiment to signals and interference, whatever they may be. Since microwave background anisotropy programs such as ours are primarily detection experiments, where the probable target signal is at or below the level of our noise and statistical methods are necessarily relied upon to set the limits, it is especially important to know the response of the analysis method to both the signal under investigation and any confusing signal. In the case of the experiments detailed here, we are interested in determining the properties of random fields on the sky, with both Gaussian and non-Gaussian statistics, using the Bayesian statistical inference method detailed in the previous section. Here, we will assume we are to test models that produce fluctuations characterized by a zero-mean Gaussian random field and that the free parameter is C_0, the amplitude of the correlation function.

For a given amount of observing time, we would like to determine the best allocation of that time among a number of measurements. If we observe a small number of fields, then the noise level on any given field will be correspondingly small, allowing detection of faint signals. On the other hand, if a large number of fields are observed, then the uncertainty on each field will be large, but the increased number of degrees of freedom will provide an increased sensitivity to the tail of the distribution. If our aim is to set upper limits on the amplitude of fluctuations in the microwave background, then for a given statistical test and model parameterization there is likely to be an optimal strategy based on the tradeoff between signal-to-noise and statistical leverage. If we are interested in unambiguous detection of said fluctuations, it is generally advantageous to observe few fields deeply rather than distribute the integration time among the many separate samples. We will discuss this problem in context of statistical inference of random fields.

Another complication in our observing strategy arises when the cosmological signal of interest is contaminated with another confusing signal. If the source of the interference is celestial and more or less nonvariable, then supplementary observations at other frequencies or other telescopes may allow removal of the contamination. If the interfering signal is time-variable, or associated with terrestrial sources, then switching and filtering schemes can be used to attenuate the effect of the confusion. The ideal experiment, in terms of maximum sensitivity and flexibility, would be single beam measurements without any differencing, as all spatial information other than that lost by convolution with the primary beam is retained in the data. However, in the real world of receiver instability and atmospheric noise we are forced to adopt some form of switching to allow calibration and compensation for such effects. If we were faced only with gain variations, then periodic injection of a known calibration signal or switching against an internal load would provide relief without reduction in sensitivity to the fluctuation spectrum. However, the water vapor and oxygen in the lower atmosphere introduce a large noise component that is both time-variable and spatially correlated. A gain-compensated but unswitched receiver system would find a very large fluctuating signal due to the movement of structures in the atmosphere across the telescope field of view. Fortunately, because the offending sources are confined to the troposphere within a few kilometers of the ground, experiments aimed at angular scales of less than about one-half of a degree are able to remove a large fraction of the atmospheric noise through spatial switching. The contribution from planar structures can be eliminated through single switching (between two points on the sky) while gradients can be removed through a second differencing (three points). If the angular separation of the switched positions is sufficiently small, then the beams pass through nearly identical patches of the atmosphere and cancellation is complete to high accuracy. Because there is a significant first derivative to the water vapor component, double switching has been the normal mode of operation in microwave background anisotropy experiments, especially at high frequencies (c.f. Uson and Wilkinson 1984a and 1984b, Davies *et al.* 1987). However, constant and gradient terms in the microwave background are also removed by this switching, causing a degradation in the sensitivity for fluctuation distributions that are correlated on the angular scales of the switching, and this effect is seen in the off-diagonal terms in the correlation matrix (2.20). The double switching strategy as applied to the Readhead *et al.* (1989) experiment is discussed in Paper 1 (§III.).

For models with significant correlation on scales larger than the switching, we can recover some sensitivity by careful placement of the fields on the sky. In particular, we can devise an interlocking scheme such that sources in the negative beams of one pointing appear in the positive lobe of another. Examination of the correlation matrix formulation (2.17–2.20) reveals that we are allowed some freedom in choosing the locations of the points $\mathbf{x}$ and if they are chosen such that the off-diagonal terms are large, then redundancy in the measurements enhances the sensitivity to fluctuations on these angular scales. We have chosen for our experiment to overlap the reference beams with the main beams from adjacent fields, a compromise between close sampling with pointing center separations less than the switching angle ϕ_S and well separated observations where the maximum area of sky is covered and the matrix A is nearly diagonal allowing easier analysis. A benefit of this scheme is that strong point sources near the center of the beam will produce a recognizable signature in the data as it will appear in several fields with opposite sign. We will discuss the ramifications of the geometry in Chapter 4 when the data is presented and in Chapter 5 when radio source contamination is discussed. We accept the necessity of double switching and have specified the desired geometry. It then remains to choose the number of fields to be observed.

The sensitivity of an experiment can be characterised naively by the HPD upper limit that would be set by the experiment in the absence of a signal. Suppose that we have available a fixed amount of integration time such that if we observed a single field then we would have a noise level of σ_{tot} and if we observed n independent fields each would have a 1σ error bar of $n^{1/2}\sigma_{tot}$. We wish to calculate the expected upper limit for zero fluctuation amplitude and the smallest detectable amplitude. First, to simplify our computations, we will use the Likelihood formulation instead of the Bayesian HPD method, removing the need for numerical integrations. Because the fields are independent, the correlation maxtrix A is diagonal and we can multiply the likelihood functions for the single measurements as in (2.49) treating $A = C_0$ as a scalar (see 2.21 as an example). For our set of n observations $\{x_i\}$, we have the likelihood function (for zero mean) of the *rms* amplitude $\theta = C_0^{1/2}$

$$L_n(\theta) = \left[2\pi(n\sigma_{tot}^2 + \theta^2)\right]^{-n/2} \exp\left[-\frac{1}{2}\sum_{i=1}^{n}\frac{x_i^2}{n\sigma_{tot}^2+\theta^2}\right]. \tag{2.73}$$

Let us deal with Gaussian fluctuations and take the expectation value of the summation term for the likelihood (the tilde denotes the fact that we are replacing the sample variance by an expected variance),

$$\tilde{L}_n(\theta) = \left[2\pi(n\sigma_{tot}^2 + \theta^2)\right]^{-n/2} \exp\left[-\frac{n}{2}\frac{\left\langle x_i^2\right\rangle}{n\sigma_{tot}^2+\theta^2}\right] \tag{2.74}$$

The support function is given by the logarithm of (2.74)

$$\tilde{S}_n(\theta) = -\frac{n}{2}\ln 2\pi - \frac{n}{2}\ln(n\sigma_{tot}^2+\theta^2) - \frac{n}{2}\frac{\left\langle x_i^2\right\rangle}{n\sigma_{tot}^2+\theta^2}. \tag{2.75}$$

Differentiation of (2.75) with respect to θ^2 and equating to zero finds the maximum likelihood value

$$\hat{\theta}^2 = \left\langle x_i^2\right\rangle - n\sigma_{tot}^2. \tag{2.76}$$

If the true value of the correlation amplitude is C_0, then

$$\left\langle x_i^2\right\rangle = n\sigma_{tot}^2 + C_0 \tag{2.77}$$

and the maximum occurs at $\hat{\theta} = C_0^{1/2}$, demonstrating that $\hat{\theta}$ is the MLM estimator for $C_0^{1/2}$. The likelihood ratio versus the maximum likelihood $L(\hat{\theta})$ is, after some manipulation

$$\lambda_n(\theta) = \left[\frac{C_0 + n\sigma_{tot}^2}{\theta^2 + n\sigma_{tot}^2}\right]^{\frac{n}{2}} \exp\left[\frac{n}{2}\frac{\theta^2 - C_0}{\theta^2+n\sigma_{tot}^2}\right]. \tag{2.78}$$

To further simplify matters, we can define the auxiliary function

$$z(\theta|C_0,n) = \frac{C_0 + n\sigma_{tot}^2}{\theta^2 + n\sigma_{tot}^2} \tag{2.79}$$

such that our likelihood ratio becomes

$$\lambda(z) = \left[z\, e^{1-z}\right]^{n/2}. \tag{2.80}$$

The Likelihood method solves the above equation (2.80) for a fixed $\lambda = e^{-m}$

$$z\, e^{1-z} = e^{-2m/n} \tag{2.81}$$

to produce the m-unit support limits. For $m > 0$ there are two solutions to this equation, the branch $0 < z < 1$ corresponding to upper limits ($\theta > C_0$) and the branch $z > 1$ corresponding to lower limits ($\theta < C_0$).

We determine the lowest upper limit that would be set in the case of null model by setting $C_0 = 0$ in (2.79) after solution of (2.81). The resulting θ will be the m-unit upper limit on $C_0^{1/2}$ expected when C_0 is truly zero. This is the $(0,1)$ branch of the equation with z ranging from 1 to 0 as θ is increased from zero to infinity with λ falling monotonically with z. Equation (2.81) can be solved by iteration on

$$z = \exp\left[z - 1 - \frac{2m}{n}\right] \tag{2.82}$$

for

$$\theta^2 = n\sigma_{tot}^2\, \frac{1-z}{z}. \tag{2.83}$$

The results θ/σ_{tot} versus n are shown in Figure 2–2 for $m = 2$ and $m = 4$. We find that there is an optimum strategy for observing that depends upon the desired level of significance. For a 2-unit support, then there is a maximum sensitivity for 9 fields; for 4-unit support the appropriate number is 17. We can explore the asymptotic behavior with increasing n by the substitution

$$t = \frac{\theta^2}{n\sigma_{tot}^2} \qquad z = \frac{1}{1+t} \tag{2.84}$$

transforming (2.82) into

$$\frac{1}{1+t} + \ln(1+t) = \frac{2m}{n} + 1. \tag{2.85}$$

After series expansion ($t < 1$) of the left-hand side of (2.85), we obtain

$$\frac{1}{2}t^2 - \frac{2}{3}t^3 + \frac{3}{4}t^4 - \ldots = \frac{2m}{n} \tag{2.86}$$

and in the limit $n \gg 1$, $t \ll 1$ we preserve only the first term in the expansion and find after substitution for t

$$\theta^2 = \sigma_{tot}^2\, (4mn)^{1/2}. \tag{2.87}$$

If we denote the upper limit on the amplitude $\tilde{C}_0^{1/2} = \theta$, we then find the limiting behavior on the *rms* of the random field

$$\tilde{C}_0^{1/2} \propto n^{1/4}. \tag{2.88}$$

The relatively slow rate of increase of the upper limit with number of fields allows some tradeoff of sky coverage against individual field noise levels without severe loss of sensitivity. A similar analysis of the LRT reveals similar behavior.

The calculation of the behavior of the Bayesian HPD test is significantly more complicated. The general outline is given in the Appendix to Paper 1, along with a plot of θ versus n. If we wish to integrate versus the *rms* θ, as is typically done, and we change variables to t as in (2.84), we find the value $t = \tau$ such that

$$\int_0^\tau t^{-1/2}\, \lambda_n(t)\, dt = (1-\alpha) \int_0^\infty t^{-1/2}\, \lambda_n(t)\, dt \tag{2.89}$$

where the likelihood is given by

$$\lambda_n(t) = \left[\frac{1}{1+t} \exp\!\left(1 - \frac{1}{1+t}\right)\right]^{n/2}. \tag{2.90}$$

After determining τ, we can find our limit on θ by inversion of (2.84) with $t = \tau$. Numerical evaluation of the integrals in (2.89) and subsequent root-finding results in the solid curves shown in Figure 2–3 calculated for $\alpha = 0.05$ (lower curve, 95% credible set) and $\alpha = 0.0013$ (upper curve, 99.87%). The asymptotic behavior appears to be slightly flatter than $n^{1/4}$, as the likelihood $\lambda_n(\tau)$ increases roughly logarithmically with n

$$\lambda_n(\tau) \approx \lambda_0 + \beta\, \ln n \qquad \lambda_0 \sim 0.246, \quad \beta \sim 0.0054 \tag{2.91}$$

over the range $400 \leq n \leq 10000$, although it appears that the θ curve is approaching $n^{1/4}$ as n increases. Thus, the Bayesian method approached a fixed likelihood test as a limit, but because it is flatter, the equivalent likelihood of the HPD is increasing with the number of fields (for the 95% HPD limit at $n = 96$ we find $\lambda = 0.252$ compared to $\lambda = .173$ at $n = 14$). In Figure 2–3 the results for a $\lambda = 0.3$ Likelihood limit are shown as a dashed curve; this test is equivalent the the HPD test for $n = 2000$. As in the Likelihood test, there is an optimum number of fields that increases as α is decreased. We find that the minimum upper limit occurs at $n = 14$ for $(1-\alpha) = 0.95$ and $n = 25$ at $(1-\alpha) = 0.9987$ (also see Appendix, Paper 1).

For Gaussian fluctuations at a level much below the instrumental noise level, the above considerations indicate that for a given HPD $(1-\alpha)$ test there is an optimum number of fields n. Splitting the observing time between a larger number of fields than that specified then increases the expected upper limit roughly as the fourth-root of the number of fields. For 95% limits and 96 independent fields, the limit is increased by 1.26 over the best value at $n = 14$, an acceptable loss in sensitivity if the increased area of sky covered brings compensating benefits. More serious than the slight increase in the expected upper limit is the inability to detect the individual fluctuations. Our parameter t is the ratio of the fluctuation level to the noise level in each field and decreases as the number of fields is increased approaching

$$t \propto n^{-1/2}$$

in the limit of large n. The increased statistical leverage that large values of n provides in the likelihood function nearly makes up for the increased field noise levels, but the increase in the sample size cannot make up for the loss in signal-to-noise ratio as the individual error bars grow. For example, a fluctuation amplitude at the 95% HPD credible limit for 96 fields yields a 0.2% probability of finding one or more out of 96 that contains a signal three or more times the noise level, compared to 3.0% for 14 field limit. In addition, the increase in n will increase the number of noise deflections above the same 3σ level, confusing the real signal and necessitating a more stringent cutoff in signal-to-noise ratio for reliable discrimination. For Gaussian fluctuations, a sample size larger than around 25 provides a marginal increase in the upper limit but a severe loss in the probability of obtaining a significant detection— only the existence of a non-Gaussian tail to the fluctuation distribution will justify such a choice in experiment on the basis of statistical procedure.

Even though there is a scarcity of well characterized non-Gaussian distributions for microwave background anisotropies produced under cosmological models, we do have a source of non-Gaussian contamination to our observations — the discrete radio source population (see Chapter 5). The differential number counts of these objects is reasonably represented by a power law with source strength. The number of sources with a flux density within the range S to $S + dS$ to be found within a solid angle Ω is given by

$$N(S) \propto S^{-\gamma}\,\Omega \tag{2.92}$$

which upon integration gives the counts for sources above flux density S,

$$N(> S) \propto S^{1-\gamma}\,\Omega. \qquad \gamma > 1 \tag{2.93}$$

Therefore, if we wish to know the number expected above a level q times the noise level $\sigma = n^{1/2}\sigma_{tot}$ in n fields of area $\Delta\Omega$ each, then we find

$$N(> q\sigma) \propto q^{1-\gamma}\,n^{(3-\gamma)/2}\,\Delta\Omega \tag{2.94}$$

which is an increasing function of n for power law indices $\gamma < 3$. It turns out, unfortunately, that for the flux density ranges of interest the known discrete source population has a sufficiently flat index ($1 < \gamma < 3$) and radio source confusion is indeed a problem for observations such as ours. On the other hand, cosmologically interesting fluctuations with similar behavior would be more easily detected in a large experiment. It is with the intention of extending the applicability of our limits to a wider range of theoretical models that we have engaged in the undertaking of the 96 field RING survey, despite the drawbacks outlined above. The lack of firm theoretical justification should not dissuade us as it is theory that must derive validity from the observational evidence, not the converse. Later, after the results have been presented, we will return to this question and try and point the direction for future models.

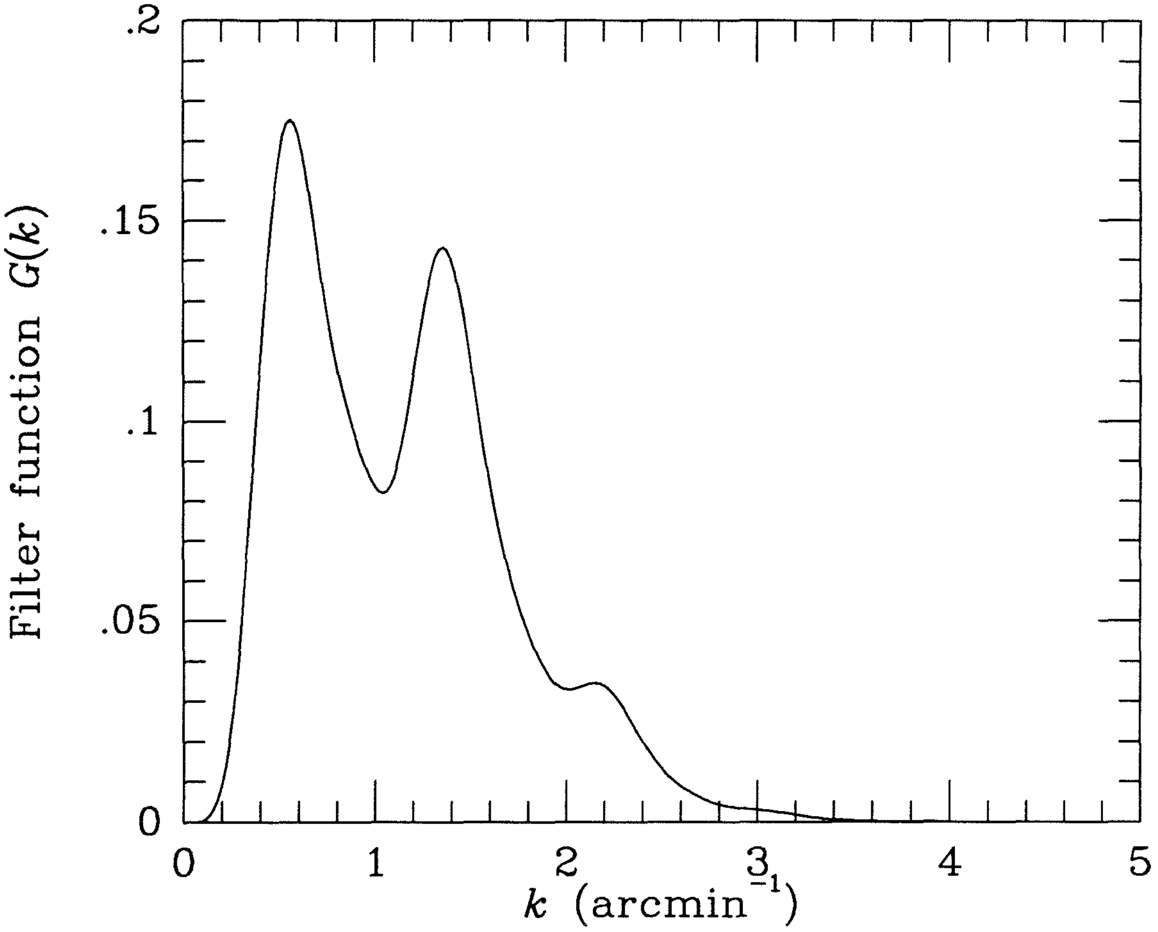

FIGURE 2–1. The filter function $G(k)$ for a set of independent OVRO switched measurements ($\phi_0 = 0'.764$, $\phi_S = 7'.15$).

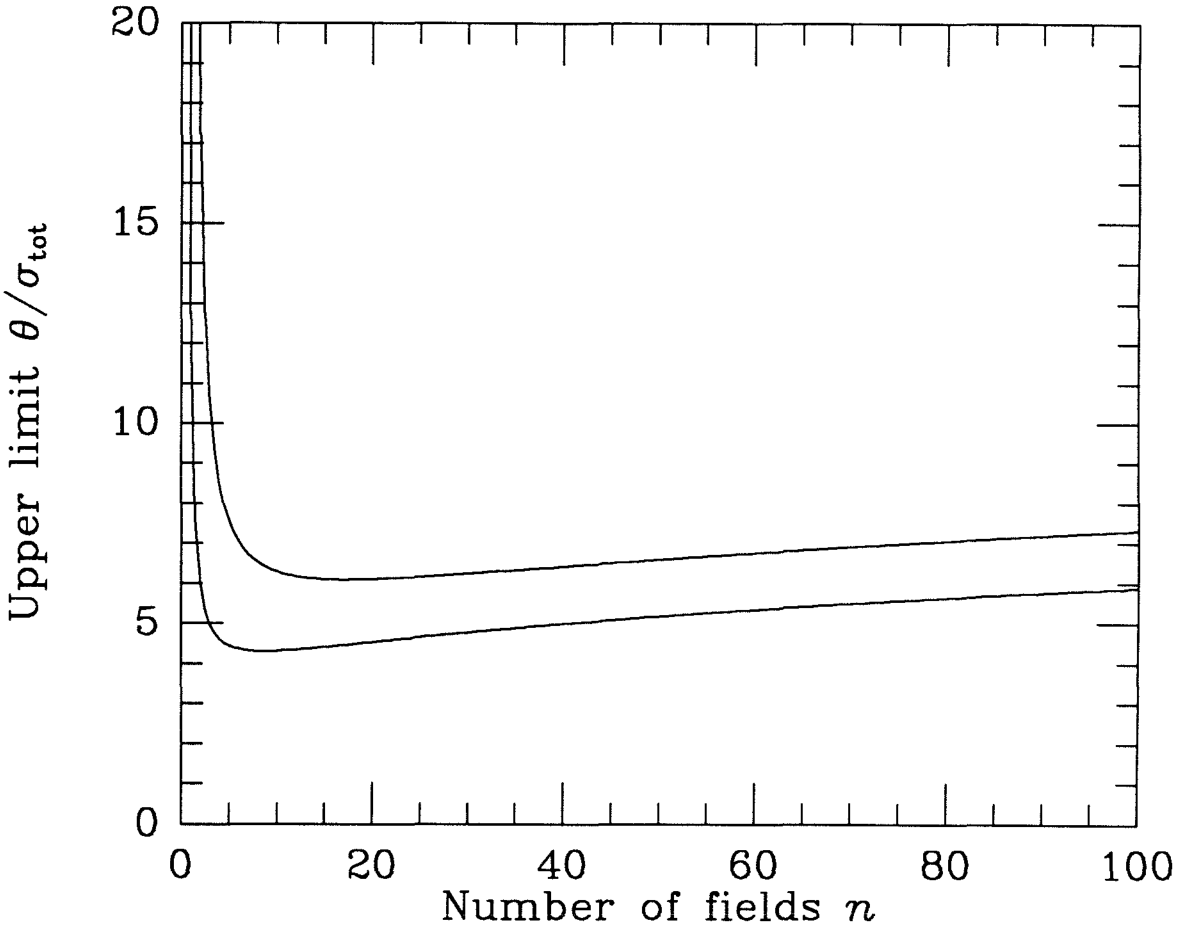

FIGURE 2–2. Expected upper limit for the results of a Likelihood analysis as a function of the number fields observed given a fixed total integration time. Units on the ordinate axis are in terms of the 1σ error in the mean if only a single field were observed. The upper curve is the $m = 4$ support limit and the lower curve the $m = 2$ limit.

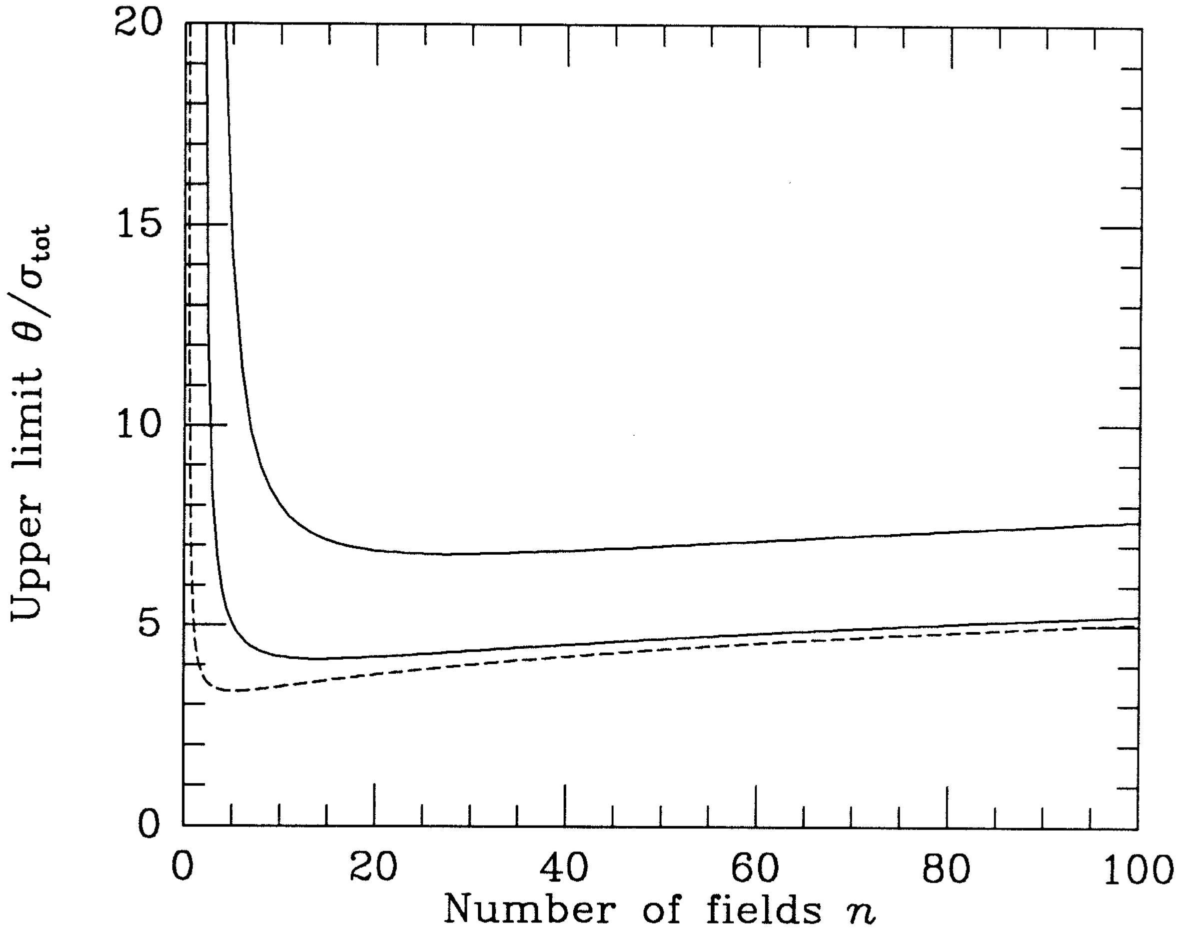

FIGURE 2–3. Expected upper limit for the results of a Bayesian HPD analysis as a function of the number fields observed given a fixed total integration time (solid curves). Units on the ordinate axis are in terms of the 1σ error in the mean if only a single field were observed. The upper curve is the 99.87% limit and the lower curve the 95% limit. Also shown is the $\lambda = 0.3$ Likelihood limit corresponding to the Bayesian 95% limit at $n = 10^4$ (dashed curve).

CHAPTER 3

A Limit on the Anisotropy of the Microwave Background Radiation on Arcminute Scales

Reprinted from *The Astrophysical Journal*, **346**, 566, 1989.

THE ASTROPHYSICAL JOURNAL, 346: 566–587, 1989 November 15

A LIMIT ON THE ANISOTROPY OF THE MICROWAVE BACKGROUND RADIATION ON ARC MINUTE SCALES

A. C. S. READHEAD, C. R. LAWRENCE, S. T. MYERS, W. L. W. SARGENT,
H. E. HARDEBECK, AND A. T. MOFFET
Owens Valley Radio Observatory, California Institute of Technology
Received 1988 October 3; accepted 1989 May 15

ABSTRACT

Observations at the Owens Valley Radio Observatory at a frequency of 20 GHz give an upper limit on the anisotropy of the microwave background radiation of $\delta T/T < 1.7 \times 10^{-5}$ (95% confidence) for uncorrelated patches of sky that are uniform on a 2′ scale. This limit is more than a factor of 2 lower than previous limits on comparable angular scales. For the more realistic case of fluctuations with a Gaussian autocorrelation function with coherence angle ϕ_c, the corresponding upper limits are 9.4×10^{-5} ($\phi_c = 12''$), 1.9×10^{-5} ($\phi_c = 2'.6$), and 3.0×10^{-4} ($\phi_c = 25'$). These results place useful constraints on models of galaxy formation based on adiabatic or isocurvature fluctuations in baryonic matter, provided that any reionization of the intergalactic medium occurred at $z < 40$. Adiabatic models are ruled out with greater than 95% confidence, and isocurvature models with $\Omega < 0.8$ are inconsistent with our limits. Theories of galaxy formation that invoke nonbaryonic matter, biased galaxy formation, or a significant fraction of ionized hydrogen at $z > 40$ predict levels of anisotropy a factor of 2 or 3 (and in extreme cases a factor of 10) below the present limit. In the case of nonstandard recombination our limits may provide useful constraints on possible reionization processes. The predictions of most popular contending theories of galaxy formation are within reach of the techniques used in this study.

Subject headings: cosmic background radiation — cosmology — galaxies: formation

I. INTRODUCTION

The origin and nature of the density fluctuations that produced the observed large-scale structure of the universe have been recognized as a fundamental problem since the early days of theoretical cosmology. The pioneering papers by Lemaître (1927) on the "primaeval atom" and of Gamow (1935) on what is now called the "hot big bang" both devoted attention to this problem. The theory of the growth of density fluctuations in an expanding universe was first worked out by Lifshitz (1946). More recently, theoretical activity has been spurred by observations of the isotropy of the microwave background radiation (Partridge 1980*a*, *b*; Uson and Wilkinson 1984*a*, *b*, *c*; Davies *et al.* 1987), the discovery of superclusters and voids (Kirschner *et al.* 1981; Bahcall and Soneira 1982), and indications of large-scale streaming motions (Rubin *et al.* 1976; Aaronson *et al.* 1982, 1986; Bahcall 1987; Dressler *et al.* 1987).

Although several plausible scenarios for galaxy formation have been proposed over the years, ranging from strong perturbation scenarios invoking explosions or shock waves (Doroshkevich, Zel'dovich, and Novikov 1967; Rees 1972; Ostriker and Cowie 1981), to linear, weak perturbation scenarios (Zel'dovich 1967; Harrison 1970; Peebles and Yu 1970), there is no compelling theoretical reason to prefer one over another. As Zel'dovich has pointed out (1972), "No *a priori* preference can be given to small or big perturbation theories—the analysis of observations is the unique approach to the problem."

Observations of the microwave background radiation are important for a number of other reasons, as well:

1. The isotropy of the microwave background radiation, which demonstrates the large-scale homogeneity of the observable universe, is the principle justification for the acceptance of the Robertson-Walker metric and Friedmannian world models.

2. Any structure in the microwave background radiation on a scale larger than ~3° must reflect inhomogeneities at decoupling ($z \approx 1500$) and is therefore a probe of the universe at much earlier times than are accessible through direct observations of galaxies and quasars. This may also be true of the structure on smaller scales if there is no early reionization.

3. Fluctuations at decoupling must have derived from physical processes, possibly quantum fluctuations, that occurred in the very early universe. Thus the microwave background radiation is a direct link between the physical processes that gave rise to the fluctuations and the large-scale structure observed today. Indeed, limits on microwave background fluctuations have already proved to be a powerful discriminant between various inflationary scenarios (Hawking 1982; Starobinsky 1982; Guth and Pi 1982; Bardeen, Steinhardt, and Turner 1983).

4. If the intergalactic medium was reionized before $z \approx 40$, the ionized medium will have imposed its own structure on the microwave background radiation on angular scales less than 3°. Background fluctuations on small scales are then a useful fossil record of this important epoch.

Proposed theories of galaxy formation range from those based on adiabatic or entropy fluctuations both with and without nonbaryonic dark matter (Zel'dovich 1967; Peebles and Yu 1970; Wilson and Silk 1981; Vittorio and Silk 1984; Bond and Efstathiou 1987), through those that include early reionization (Hogan 1980; Efstathiou and Bond 1987; Peebles 1987*a*; Vishniac 1987) and biased theories of galaxy formation (Kaiser 1984*a*, *b*; Kaiser 1986), to theories based on explosive galaxy formation (Ikeuchi 1981; Ostriker and Cowie 1981; Ikeuchi, Tomisaka, and Ostriker 1983; Hogan 1984; Vishniac and Ostriker 1985). Cosmic strings have also been invoked as the primary agents of galaxy formation (Zel'dovich 1980; Brandenberger, Albrecht, and Turok 1986; Ostriker, Thomson, and Witten 1986; Bertschinger and Watts 1988). Expected rms fluctuations in the background temperature range from 3 to 3000 μK. As yet there are no detailed predictions of the angular spectrum of fluctuations produced by strings, although recently some progress has been made on this problem (Ostriker and Thomson 1987; Scherrer 1987; Stebbins 1987; Bouchet, Bennett, and Stebbins 1988).

If intrinsic fluctuations are less than 3 μK, they will be exceedingly difficult to measure in the presence of nonthermal radiation from extragalactic radio sources and the Galaxy (below 30 GHz; Danese, De Zotti, and Mandolesi 1983; Franceschini *et al.* 1988), and thermal radiation from interstellar clouds (above 30 GHz). However, the most popular theories predict rms fluctuations between 15 and 100 μK on angular scales from 1′ to a few degrees, and it is therefore likely that significant progress can be made through observations of the angular spectrum of anisotropies in the microwave background radiation.

In 1982 we installed a sensitive *K*-band maser receiver, built by the Microwave Electronics Group of the Jet Propulsion Laboratory, on the 40 m telescope of the Owens Valley Radio Observatory (OVRO). The broad bandwidth (400 MHz), low noise temperature (26 K), and symmetric feed configuration (separation 7′.15) of this receiver make it suitable for both intrinsic anisotropy observations and for observations of the Sunyaev-Zel'dovich effect in clusters of galaxies. Although atmospheric water vapor fluctuations are a major source of systematic error at centimeter and millimeter wavelengths, the precipitable water above the OVRO is less than 3 mm ~20% of the time from November through March. This cold, arid winter climate makes the OVRO a good site for microwave background observations, and during cold dry periods observations are often limited primarily by the thermal noise of the receiver.

In this paper we report the results of our first five observing epochs. The sensitivity achieved, near 1 part in 10^5, enables us to constrain important cosmological parameters in the context of specific models. We show that a factor of 3 improvement in sensitivity should be possible with this approach in the future, placing almost all theories of galaxy formation within reach.

II. ANTENNA AND RECEIVER

The observations were made on the OVRO 40 m altazimuth telescope. Great care was taken to ensure that the sensitivity of the system was limited only by thermal receiver noise or the atmosphere. This section and the next describe, respectively, how the receiver and the observing strategy were tailored to reduce both systematic and random sources of extraneous noise. Table 1 in § III*a* summarizes the steps that were taken and lists some instrumental problems not mentioned elsewhere that were solved along the way.

Telescope pointing was adjusted at least once every 2 hr by observing a nearby unresolved source. From the size of the required adjustments we estimate the rms pointing error to be 12″. Telescope focus was adjusted automatically as a function of zenith angle, but was checked periodically by the observer.

The maser receiver used in the these observations was based on a design by Moore and Clauss (1979, see also Moore 1980), and has an instantaneous bandwidth of 400 MHz at a center frequency of 20.0 GHz. Figure 1 shows the essential components of the receiver: corrugated scalar feeds (A and B) 3.8 cm apart and symmetric about the telescope axis, which look at areas 7′.15 apart on the sky (1 and 2); a Dicke switch at 10.2 K operating at 10 Hz; the maser itself, with gain *G* and equivalent noise temperature $T_{\rm maser}$; a second 10 Hz switch, synchronous with the first; two amplifiers with adjustable gains g_A and g_B; and a square law detector that is sampled and digitized at 2 Hz. Dicke-switch transients, which persist for up to 4 ms, are blanked out.

The beam pattern was measured by scanning across 3C 84 in zenith angle and azimuth, over a range of zenith angles from 14° to 69°. The scans were divided into several groups according to zenith angle, and a beam map was produced for each group. While these maps were not identical, the differences were of the same order of magnitude as the level of systematic error in the measurements, judged by the strength of features that were clearly artifacts of the scanning procedure. Accordingly, we added all scans together to achieve the best possible signal-to-noise ratio. The resulting average beam, which should accurately represent the true beam at the pole for all but the lowest contour levels, is shown in Figure 2. As we show in § VIII*c*, the results of this work are quite insensitive to the detailed beam shape at low levels.

A two-dimensional Gaussian fit to the average of the two beams has FWHM of 108″ ± 1″. The symmetry of the beams ensures cancellation of many possible sources of systematic error such as ground spillover or solar radiation in distant sidelobes. The main beam solid angle measured from this map is $3.2 \pm 0.1 \times 10^{-7}$ sr. The beam and aperture efficiencies, determined from observations of six nonvarying, unresolved objects and the planet Mars, are 0.47 ± 0.02 and 0.27 ± 0.01, respectively.

An important feature in the calibration of the observations is that the same noise diode was used in both the determination

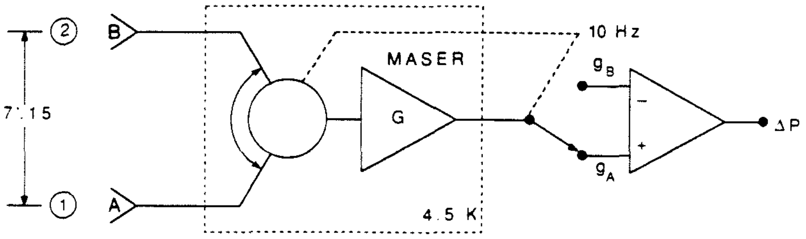

FIG. 1.—Block diagram of the OVRO *K*-band maser receiver. Two feeds, A and B, symmetrical about the radio axis, look at sky areas 1 and 2 separated by 7′.15. The input to the maser (with gain *G*) is switched between the two feeds at 10 Hz by a cooled switch. The maser output is switched synchronously to amplifiers with adjustable gains g_A and g_B. The output of the radiometer is the power difference between the two sides, and is sampled every 0.5 s. A noise tube is used to calibrate the measurements.

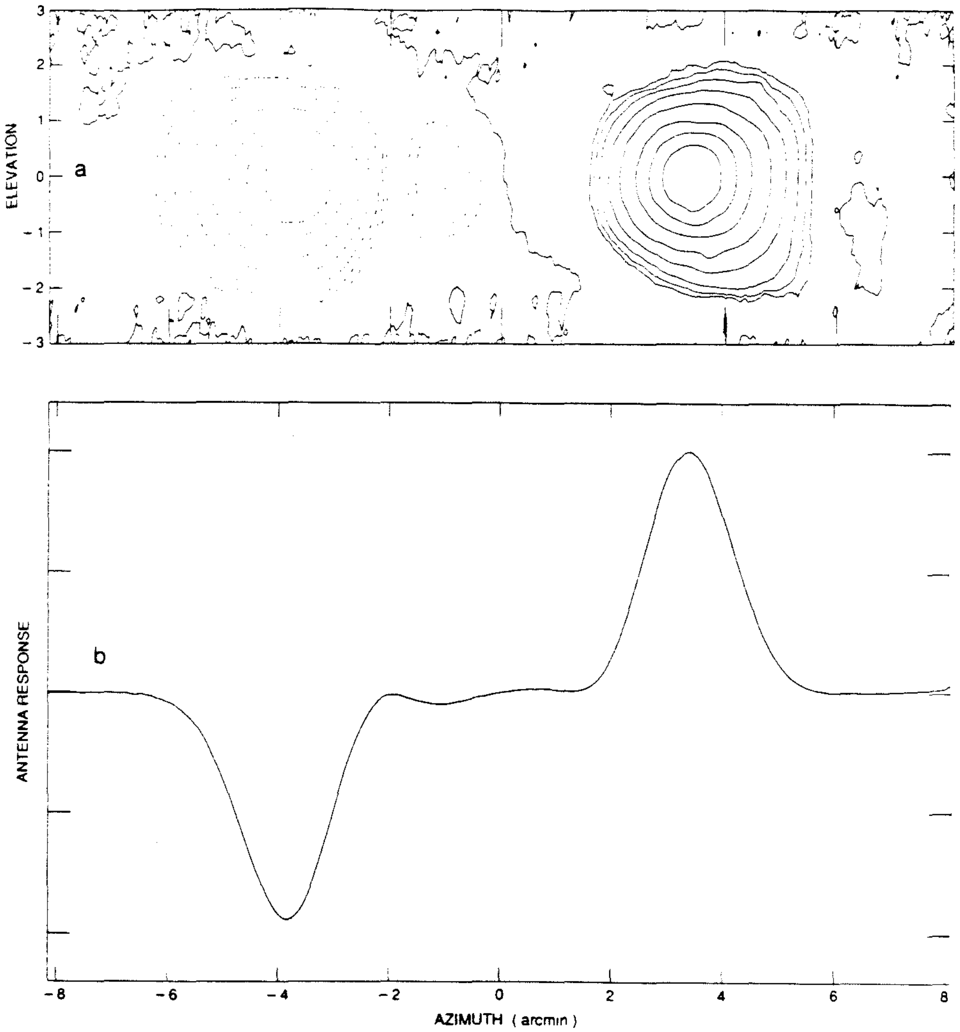

FIG. 2.—(*a*) Contour map of the antenna beam pattern, made from observations of 3C 84 at a zenith angle near 50°. Contour levels are 0, ±2, ±3, ±5, ±10, ±20, ±40, ±60, and ±80% of peak. (*b*) Cross section through the beam map. A two-dimensional Gaussian fit to the average of the two beams has FWHM of 108'' + 1''.

of the beam efficiency and in the calibration of the temperature scale. Any error in the estimated temperature of the noise diode cancels out when the measured temperature differences are divided by the beam efficiency to yield a sky temperature. Thus the only systematic errors in the calibration of our temperature scale arise from the measurement of the beam solid angle and from any variations in the noise diode which last for a significant fraction of the observing epoch.

The total noise temperature of the system at the zenith is typically 40–45 K in good weather, of which 26 K is from the receiver itself, 2.8 K from the microwave background, 4–11 K from the atmosphere, and the rest (presumably) from ground pickup. This gives a thermal noise limit on the sky, corrected for beam efficiency, of 9 mKs$^{1/2}$ for a bandwidth of 400 MHz. The above temperatures were determined from measurements with ambient and 77 K absorbers filling the beams. The noise source used to calibrate the observations was changed several times during the course of the observations reported in this paper. Its temperature was determined initially and then checked regularly either by observations of unresolved sources (using the flux density scale of Baars *et al.* 1977) or as part of the absolute calibration just described.

Unwanted emission from the ground and the atmosphere, with equivalent noise temperatures $T_{\rm gnd}$ and $T_{\rm atm}$, enters the feeds along with the interesting radiation $T_{\rm sky}$. The feeds, wavelengths, and Dicke switch are imperfect, and have losses $l_{\rm A}$ and $l_{\rm B}$ in the two arms distributed over components at physical temperatures $\Theta_{\rm A}$ and $\Theta_{\rm B}$ ranging from 4 K to 300 K. The excess noise contributed by these losses can be found by integrating along the two arms: $\int \Theta_{\rm A}\, dl_{\rm A}$ and $\int \Theta_{\rm B}\, dl_{\rm B}$. The radiometer measures the power difference

$$\begin{aligned}\Delta P = {} & G[g_{\rm A}(1 - l_{\rm A})T_{\rm sky\,1} - g_{\rm B}(1 - l_{\rm B})T_{\rm sky\,2}] \\ & + G[g_{\rm A}(1 - l_{\rm A})(T_{\rm atm\,1} + T_{\rm gndA}) - g_{\rm B}(1 - l_{\rm B})(T_{\rm atm\,2} + T_{\rm gndB})] \\ & + G\left[g_{\rm A}\int \Theta_{\rm A}\, dl_{\rm A} - g_{\rm B}\int \Theta_{\rm B}\, dl_{\rm B} + g_{\rm A}(1 - l_{\rm A})T_{\rm inject}\right] \\ & + G[(g_{\rm A} - g_{\rm B})T_{\rm maser}]\,, \end{aligned} \tag{1}$$

where G is the maser gain, $T_{\rm maser}$ is the equivalent noise temperature of the maser, and $T_{\rm inject}$ will be described shortly. Only the first term is astronomically interesting. In an ideal receiver, all other noise sources would be balanced in the two channels, and would cancel out one for one. Specifically, we would like to have (1) $T_{\rm atm\,1} = T_{\rm atm\,2}$; (2) $T_{\rm gndA} = T_{\rm gndB}$; (3) $\int \Theta_{\rm A}\, dl_{\rm A} = \int \Theta_{\rm B}\, dl_{\rm B}$; (4) $l_{\rm A} = l_{\rm B}$; and (5) $g_{\rm A} = g_{\rm B}$. We will discuss these in turn.

The instantaneous structure of the atmosphere is complicated, and for short integration times the atmospheric terms in equation (1) dominate. However, averaged over a sufficiently long time, $T_{\rm atm}$ will be function of zenith angle only. Accordingly, for observations at constant zenith angle, $\langle T_{\rm atm\,1}\rangle \approx \langle T_{\rm atm\,2}\rangle$, where the brackets denote time averages. (The residual effects of atmospheric fluctuations on the data will be discussed in § V.)

Ground pickup and atmospheric effects vary much less with azimuth than with zenith angle, and variations in $T_{\rm atm}$ and $T_{\rm gnd}$ are minimized by moving the telescope as little as possible, particularly in zenith angle. The only part of the sky that can be observed for a long time at almost constant zenith angle is the area near the celestial pole. With an altazimuth mounting, the pole can be observed continuously with only small motions in azimuth as well. Thus by observing near the pole we come as close as possible to satisfying conditions (1) and (2) above.

The construction of the receiver makes significant differences between $\Theta_{\rm A}$ and $\Theta_{\rm B}$ unlikely. Unfortunately, we have no control over the distribution of losses along the two arms, so $\Theta_{\rm A} = \Theta_{\rm B}$ does not imply (3) above. In fact, the power measured in the two feeds differs by ~4 K, independent of the absolute power level (e.g., changes in sky temperature). Gain differences in the two horns, for example, would not produce such an effect. This is direct evidence that (3) above does not hold. Therefore, no settings of $g_{\rm A}$ and $g_{\rm B}$ can make the last three terms in equation (1) vanish for all values of $T_{\rm sky}$, $T_{\rm atm}$, $T_{\rm gnd}$, Θ, and $T_{\rm maser}$.

Although we cannot adjust the losses in the two arms, we can inject excess noise (~4 K) in one arm to balance the *noise* contributions of the losses. In practice, we set $g_{\rm A} = g_{\rm B}$, and then adjust $T_{\rm inject}$ for $\Delta P = 0$. The uncompensated difference in *attenuation* due to $l_{\rm A} \neq l_{\rm B}$ results in incomplete cancellation of atmospheric and ground noise, but the third and fourth terms in equation (1) are eliminated.

We have found that the value of $T_{\rm inject}$ that gives $\Delta P = 0$ varies diurnally by 0.1–0.4 K. For observations taken as described in § III, this may in the worst case introduce systematic errors of ~10 μK. While it is clear that in the long run this source of noise must be eliminated, it is too small to affect the observations reported here.

Observing near the NCP, setting the gains equal, and balancing the noise in the premaser components considerably reduce the extent to which instrumental or environmental fluctuations mimic actual temperature differences on the sky. In addition, the 10 Hz switch is faster than most atmospheric fluctuations. Nevertheless, it is not hard to imagine ways in which ΔP could be shifted systematically away from zero for long periods. This problem and its solution are discussed in § III*a*.

III. OBSERVATIONS

a) Strategy

The goal of microwave background isotropy measurements is to detect temperature differences several million times smaller than the equivalent noise temperatures of the equipment used. Even in ideal (thermal noise-limited) conditions, a system with a bandwidth of 400 MHz would require days of integration to reach this level. It is conceivable that for short periods the last three terms of equation (1) could be reduced to the required level using the techniques of § II, but it is inconceivable that this could be done for periods as long as a few days.

The standard solution to this problem is to observe the field being measured for an equal time through both feeds, as shown in Figure 3. We measure

$$\begin{aligned}\mathscr{P} = {} & \frac{1}{\tau}\int_0^{\tau} \Delta P\, dt - \frac{1}{\tau}\int_{\tau+s_1}^{2\tau+s_1} \Delta P'\, dt \\ & - \frac{1}{\tau}\int_{2\tau+s_1}^{3\tau+s_1} \Delta P'\, dt + \frac{1}{\tau}\int_{3\tau+s_1+s_2}^{4\tau+s_1+s_2} \Delta P\, dt\,. \end{aligned} \tag{2}$$

With this switching scheme, all instrumental terms that are constant or vary linearly with time, and all "sky" terms that are constant or vary linearly with position, cancel out if the telescope move times are equal ($s_1 = s_2$).

Instrumental terms quadratic in time survive, but are minimized by choosing τ small; however, since move times s_1 and s_2 are fixed, observing efficiency favors large τ. Most data reported in this paper were taken with $\tau = 20$ s, which provides over 70% observing efficiency and no noticeable increase in noise over $\tau = 10$ s. The telescope control program does not guarantee that $s_1 = s_2$, but move times measured under operating conditions were equal within measurement errors of ~5%.

The combination of Dicke switching between the feeds and antenna switching between sky areas is often called "double switching," and has been used successfully for many observations (e.g., Lake and Partridge 1980; Birkinshaw, Gull, and Hardebeck 1984; Uson and Wilkinson 1984*a*, *b*). Except for atmospheric fluctuations, the largest nonlinear effects that we have thought of would cause errors less than 10^{-5} K even if they persisted for hours.

The temporal and spatial behavior of the atmosphere does have higher order terms that are not removed by double switching. As will be seen in § VI, in the best weather the atmosphere introduces no systematic error, but the total noise

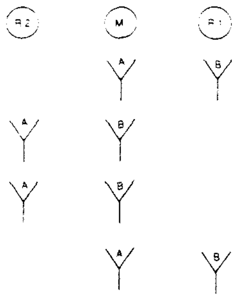

FIG. 3.—Observing cycle. M, R1, and R2 are areas on the sky at the same zenith angle, separated by 7:15. We integrate for time τ, with feeds A and B pointed at M and R1, respectively, then move the antenna in azimuth only (move time = s_1) so that A and B look at R2 and M, respectively. After integration time 2τ, the antenna moves back to the original position (move time = s_2) for rime τ. The cycle then repeats. For each cycle, we measure (see eq. [1])

$$\frac{1}{\tau}\int_0^{\tau} \Delta P\, dt - \frac{1}{\tau}\int_{\tau+s_1}^{2\tau+s_1} \Delta P'\, dt - \frac{1}{\tau}\int_{2\tau+s_1}^{3\tau+s_1} \Delta P'\, dt + \frac{1}{\tau}\int_{3\tau+s_1+s_2}^{4\tau+s_1+s_2} \Delta P\, dt\ ,$$

where primed measurements are made with the feeds looking at R2 and M. For one cycle, the temperature difference measured is $\Delta T_i = T_M - \frac{1}{2}(T_{R1} + T_{R2})$.

increases to 30% above the thermal limit. Nevertheless, $\langle T_{atm} \rangle$ is a nonlinear function of zenith angle, and the steady change of zenith angle required to track a source away from the meridian could introduce a sizable systematic error. To minimize this effect, observations must be made not only near the pole, but also at upper or lower culmination. Table 1 summarizes the observing strategy and instrumental adjustments required to control systematic errors.

b) Observed Fields and the Effective Beam Pattern

For a fixed total integration time the optimum number of fields to observe for maximum sensitivity depends on the spectrum of microwave background fluctuations. We show in the Appendix that for Gaussian fluctuations, and including the likely effects of systematic errors in the observations, 10–15 fields is best. We chose 12 fields at $\alpha = 1^h, 3^h, \ldots, 23^h$, $\delta = 89°$ (epoch 1985.0), hereafter referred to as NCP 1 through NCP 23. As a check of systematic errors, we initially observed four fields at both upper and lower culmination, and four fields at upper culmination only. Each field was observed for 2 hr centered on transit. The 24 hr sequence consisted of fields NCP 1–NCP 15 at upper culmination, then NCP 5–NCP 11 at lower culmination. Only results for these eight fields are given in this paper, since the number of observations on the remaining four fields is small.

Reference fields R1 and R2 are always at the same zenith angle as M. When a field M is tracked, the sky positions of R1 and R2 change continuously. After 2 hr, the reference fields have become 30° arcs, as shown in Figure 4. These reference arcs are labeled "A1" and "A2" to distinguish them from the simple reference fields R1 and R2 for short observations. Table 2 gives the coordinates of all fields.

The observing cycle shown in Figure 3 usually consists of four 20 s integrations (some early data used 40 s integrations). Since the radiometer sampling time is 0.5 s, each cycle consists of 160 samples. The mean and standard deviation of the samples are recorded. Measurements of the calibrated noise tube every 10 cycles, along with the known beam efficiencies, provide the conversion from power (eq. [1]) to temperature on the sky. Following this conversion, we have for the *i*th cycle a temperature difference $\Delta T_i \pm \sigma_i$, where

$$\Delta T_i = T_M - \tfrac{1}{2}(T_{R1} + T_{R2})\ . \tag{3}$$

In the analysis to follow error estimates are based on the scatter in the measurements. This will be discussed fully in § IV.

c) Dates of Observations

We have undertaken five major series of observations, as shown in Table 3.

TABLE 1

ELIMINATION OF SYSTEMATIC ERRORS

Noise Source	Size	Strategy
Atmosphere: different T_{atm} in two beams	0.1–5 K	Minimize length of track by observing near NCP at upper and lower culmination Double switch Discard data for which there were clouds within 2 hr Discard data for which $\langle T_{atm} \rangle > 11$ K air mass^{-1}, and $(T_{atm})_{rms} > 0.4$ K air mass^{-1} Discard data for which $\Delta T_i > 2 \times$ thermal limit
Differential ground spillover	~0.1 K	Minimize length of track by observing near NCP at upper and lower culmination Double switch
Receiver:		
Changes in maser gain and noise	0.1–1 K	Dicke switch at 10 Hz Set $g_A = g_B$ to better than 0.05% Inject noise to balance two channels
Fluctuations in JT return pressure	~0.5 mK	Install large ballast tank in JT return line
Cycling of compressor fans	~20 mK	Stop cycling
Interference (RF pickup on IF cables between telescope and control building)	~0.2 mK	Convert to digital output at telescope
Other	<50 μK	

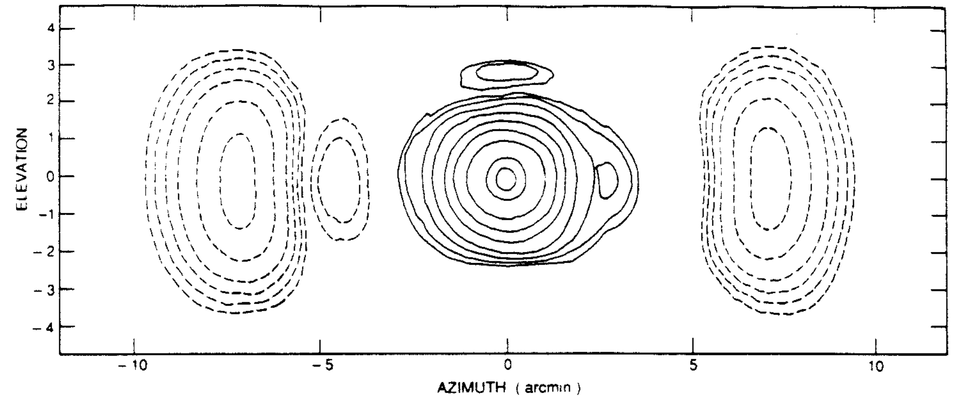

FIG. 4.—Effective beam pattern for 2 hr observations. Contour levels are ±0.5, ±1, ±2, ±4, ±8, ±20, 40, 60, and 80% of peak.

IV. DATA EDITING AND REDUCTION

Bad weather and certain kinds of equipment malfunction produce corrupted data for which there is no statistical remedy. Other instrumental problems produce occasional glitches that can be handled by automatic procedures. In this section we describe how bad data of both types are removed, and how good data are combined.

In general, neither major equipment failures nor bad weather is hard to recognize, but the atmospheric requirements for microwave background anisotropy work at 20 GHz are unusually stringent. It is often not possible to tell by looking at the sky whether conditions are good or bad. Before we turn to the criteria used to reject data, we describe an instrument available for some of the observations that provided an objective measure of atmospheric conditions.

TABLE 2

COORDINATES OF FIELD CENTERS[a]

	EPOCH 1985.0		EPOCH 1950.0	
FIELD	R.A.	Decl.	R.A.	Decl.
NCP 1_{A1}	$00^{h}32^{m}49^{s}0$	$88^{\circ}59'34''$	$00^{h}25^{m}51^{s}6$	$88^{\circ}47'58''$
NCP 1	01 00 00.0	89 00 00	00 48 37.8	88 48 38
NCP 1_{A2}	01 27 11.0	88 59 34	01 11 35.6	88 48 34
NCP 3_{A1}	02 32 49.0	88 59 34	02 07 26.2	88 49 59
NCP 3	03 00 00.0	89 00 00	02 30 42.7	88 51 12
NCP 3_{A2}	03 27 11.0	88 59 34	02 54 34.6	88 51 41
NCP 5_{A1}	04 32 49.0	88 59 34	03 53 03.5	88 54 17
NCP 5	05 00 00.0	89 00 00	04 17 39.0	88 55 56
NCP 5_{A2}	05 27 11.0	88 59 34	04 43 13.8	88 56 47
NCP 7_{A1}	06 32 49.0	88 59 34	05 46 28.9	89 00 04
NCP 7	07 00 00.0	89 00 00	06 13 21.4	89 01 52
NCP 7_{A2}	07 27 11.0	88 59 34	06 41 33.1	89 02 49
NCP 9_{A1}	08 32 49.0	88 59 34	07 51 44.9	89 05 58
NCP 9	09 00 00.0	89 00 00	08 21 46.8	89 07 34
NCP 9_{A2}	09 27 11.0	88 59 34	08 53 07.9	89 08 13
NCP 11_{A1}	10 32 49.0	88 59 34	10 10 49.4	89 10 13
NCP 11	11 00 00.0	89 00 00	10 43 47.2	89 11 11
NCP 11_{A2}	11 27 11.0	88 59 34	11 17 21.5	89 11 06
NCP 13_{A1}	12 32 49.0	88 59 34	12 38 38.0	89 11 07
NCP 13	13 00 00.0	89 00 00	13 12 13.2	89 11 13
NCP 13_{A2}	13 27 11.0	88 59 34	13 45 12.9	89 10 15
NCP 15_{A1}	14 32 49.0	88 59 34	15 03 00.2	89 08 17
NCP 15	15 00 00.0	89 00 00	15 34 24.0	89 07 39
NCP 15_{A2}	15 27 11.0	88 59 34	16 04 28.8	89 06 03

[a] Positions for A1 and A2 give reference beam centers (see Fig. 3).

TABLE 3

SUMMARY OF OBSERVATIONS

Session	Dates	Usable Time[a]
Jan85	1984 Nov 4–17 1984 Dec 17–1985 Feb 2	2.28
Nov85	1985 Nov 2–1985 Dec 2	4.14
Dec85	1985 Dec 12–1985 Dec 27	6.05
Dec86	1986 Dec 1–7	1.93
Jan87	1987 Jan 7–20	2.15

[a] Integration time in days on all fields used to produce the results of Table 4 in § VI. The total for all sessions is 16.6 days, corresponding to ~24 days of perfect observations with a typical observing efficiency of 70%.

a) The Water Vapor Radiometer

During the Jan85, Nov85, and Dec85 sessions a water vapor radiometer at the observatory measured atmospheric emission from sky dips through the north celestial pole about once every 15 minutes. Figure 5 shows the strong correlation between sky temperature at 20.7 GHz and data quality. The transition from good to bad data was not sharp, and typically occurred somewhere between 8 and 14 K per air mass. Although the correlation between sky temperature and fractional cloud cover was also strong, there were many clear periods during which the sky temperature was high and the data were poor. More surprising to us was the fact that good data were sometimes obtained even when the sky temperature was high. It turned out that when this occurred, the scatter in successive sky temperature measurements was always low, indicating that the atmosphere was uniformly stratified. It is clear that the water vapor radiometer provides an objective, independent check of the data quality, and increases the efficiency of the observations.

b) Preliminary Editing

Two hour (i.e., single-field) blocks of data were rejected according to four criteria, none of which can bias the results. Specifically, data were rejected if:

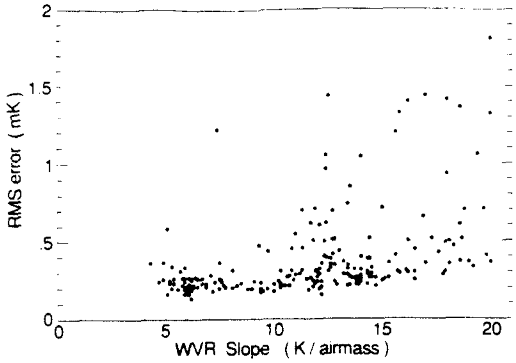

FIG. 5.—rms scatter in 1 hr blocks of data vs. atmospheric temperature per air mass measured by the water vapor radiometer at 20.7 GHz. Above 11 K per air mass the likelihood of large scatter increases significantly; however, if the error in the sky temperature measurement (not shown) was less than 0.4 K per air mass (indicating a smooth, stable atmosphere), the scatter in the data remained low. Data taken when the sky temperature and error were above 11 and 0.4 K per air mass, respectively, were not used.

1. There was an equipment failure, or any receiver adjustments were set to nonstandard values.

2. The weather was bad. If water vapor radiometer measurements were available, data were rejected if the sky temperature exceeded 11 K per air mass and the scatter in successive measurements exceeded 0.4 K per air mass. If WVR measurements were not available, data were rejected if there were clouds anywhere except low in the west over the Sierra Nevada within 2 hr of the observations. On dark nights thin clouds cannot be seen, so all data taken at night were rejected if clouds were visible at subset or sunrise.

3. The rms scatter in a 2 hr block of data indicated a noise level greater than 16 mK s$^{1/2}$. This is twice the thermal noise level under the absolute best conditions when $T_{sys} = 40$ K at the pole, and ~1.8 times the thermal noise level under typical very good conditions. Two hour blocks contained up to 66 successive observations of a single field. Since the rms value can be perturbed seriously by widely discrepant measurements, any measurement more than 3 times the rms distance from the mean was excluded, and the mean and scatter recalculated, to convergence. (If the scatter with rejection was below twice the thermal value, however, *all* data in the block were kept for analysis by the procedure of § IVc.) There was rarely an obvious cause of bad data rejected by this criterion. Nevertheless, such a noise level is a sure sign of trouble. We emphasize that this criterion applies to the *scatter* of the measurements in a 2 hr block of data, not to the deviation of the 2 hr mean from the mean of all data for a given field. By this criterion, therefore, we do not excise outlying points in the overall distribution for a given field, rather we eliminate *all* data taken when the scatter is large. If the excess noise is random, the only effect of this rejection will be to reduce the total integration time. If, as is much more likely, the excess noise is not random (e.g., noise from persistent structures in the atmosphere), this rejection protects the final data set against the introduction of measurements with systematic errors large compared to the final estimated error in the mean for a given field (~30 μK), but small compared to the width of the distribution of all measurements (9 mK s$^{1/2}$ × [160 s]$^{-1/2}$ ≈ 700 μK). In the best weather almost no data were rejected by this criterion; however, when the water vapor radiometer was not working this criterion was our only protection against the condition described above of clear skies but large atmospheric fluctuations.

4. The number of data points in 2 hr was less than one-third the expected number, and no cause harmless to data quality could be determined.

One 40 minute period of data was rejected because the mean value was more than 3 σ away from the average of all the data for this field.

c) Final Editing and Data Reduction

The editing method just described easily removes data ruined by causes that persist for more than 30 minutes or so, but would be tedious to use for the removal of isolated bad points. In the best weather when the receiver appears to be working perfectly, the measured values of ΔT_i have a Gaussian distribution with width near the thermal noise limit, and the values of σ_i are all about the same. In merely good weather the distribution remains Gaussian, but the width increases consistent with the increase in the values of σ_i. The automatic procedure described below rejects individual values of ΔT_i or σ_i that are inconsistent with the underlying Gaussian distribution.

Let ΔT_i and σ_i, $i = 1, \ldots, N$ be the calibrated mean values and their standard deviations for a given field. Suppose that these N measurements were made in j 2 hr blocks. (During a complete observing day there would be two blocks each for fields 5–11, and one each for fields 1, 3, 13, and 15.) Let n_j be the number of measurements in the jth block (note that $n_j \leq 66$). Then $N = \sum_j n_j$. We calculate the weighted mean of the jth 2 hr block of data

$$B_j = \frac{\sum_{i \in J} \sigma_i^{-2} \Delta T_i}{\sum_{i \in J} \sigma_i^{-2}} ,$$

and a measure of the scatter about the mean

$$\sigma_j^2 = \frac{\sum_{i \in J} \sigma_i^{-2} (\Delta T_i - B_j)^2}{\sum_{i \in J} \sigma_i^{-2}} ,$$

where J is the set of all i in the jth block. Note that if all the σ_i are the same, and are accurate measures of the errors in the ΔT_i, then σ_j will be equal to σ_i. Systematic errors in the ΔT_i not reflected in σ_i will give $\sigma_j > \sigma_i$.

We assign a weight to each ΔT_i given by

$$w_i = (\sigma_i^2 + \sigma_j^2)^{-1} .$$

Since σ_i is a measure of the scatter in 0.5 s integrations, and σ_j is a measure of the scatter in 80 s integrations, both short- and medium-term fluctuations are represented in the weight. We calculate the weighted mean temperature

$$\overline{\Delta T} = \frac{\sum_{i=1}^{N} w_i \Delta T_i}{\sum_{i=1}^{N} w_i} , \tag{4a}$$

the estimated variance of the mean

$$\sigma^2 = \frac{1}{N-1} \frac{\sum_{i=1}^{N} w_i (\Delta T_i - \overline{\Delta T})^2}{\sum_{i=1}^{N} w_i} , \tag{4b}$$

the rms average of all σ_i

$$\sigma^* = \left(\frac{1}{N} \sum_{i=1}^{N} \sigma_i^2 \right)^{1/2} ,$$

and the rms average of the σ_i for each 2 hr block

$$\sigma_j^* = \left(\frac{1}{n_j}\sum_{i \in J}\sigma_i^2\right)^{1/2} .$$

The ith measurement is rejected if $|\Delta T_i - \overline{\Delta T}| \geq q\sigma_i$ or $\sigma_i \geq 2\sigma^*$, where q is a constant whose initial value is arbitrarily chosen to be 4.0. The first criterion eliminates measurements whose deviations from the mean are too large to be statistically plausible based on the scatter in the 160 constituent 0.5 s samples. The second eliminates measurements with extremely large scatter in the 160 samples. The factor of 2 in this criterion is justified by the distribution of σ_i/σ^* in Figure 6, which shows that any value near 2 would distinguish normal from discrepant values.

Similarly, the jth block of data is rejected if $|B_j - \overline{\Delta T}| \geq q\sigma_j(n_j - 1)^{-1/2}$ or $\sigma_j \geq 2\sigma_j^*$. Once again, the first criterion eliminates blocks of data with a mean implausibly far from the overall mean, based on the scatter in the n_j 80 s values. The second eliminates blocks of data whose 80 s values have large scatter in their constituent samples.

The above procedure is repeated to convergence, with deleted measurements or blocks added back in as necessary, for $q = 4.0, 3.9, \ldots, 2.7$. About 5% of the measurements are rejected when $q = 4.0$, and ~10% when $q = 3.0$. A common cause of individual measurements rejected by this procedure is loss of LO phase lock. *All results reported in this paper are for* $q = 3$. This choice is based on the following consideration. There are on average 2000 measurements per field in our final data set. If the σ_i were the true errors, we would expect about five measurements per field to be rejected erroneously with $q = 3$. In fact, the σ_i typically underestimate the true errors by ~30% (see § V), so we expect ~40 measurements per field to be rejected erroneously. This will cause a slight reduction in the variance of the final data set, but it cannot introduce a bias. The other 160 or so measurements per field that are rejected with $q = 3$, however, cannot be drawn from the underlying Gaussian distribution of the good data, and could easily introduce a bias.

The catalog of causes of bad data is, without elaboration: bad weather; refrigerator failure; compressor failure; compressor fan cycling; pressure variations in the refrigerator JT return line; temperature oscillations of the 4 K stage; loss of LO phase lock; and high voltage relay glitches. We believe that bad data produced by any of these have been recognized and deleted. The important question of whether there are unidentified sources of systematic error will be addressed next.

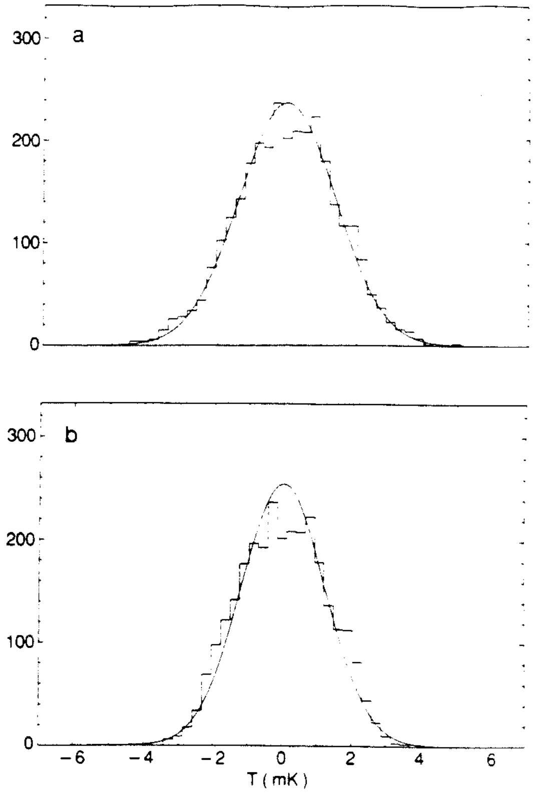

FIG. 7.—Distribution of ΔT_i from NCP 9 accepted by the procedure of § IV*c* with (*a*) $q = 4.0$; (*b*) $q = 3.0$. The width of the distribution, given by $\sigma_{\rm dist}^2 \equiv \Sigma w_i(\Delta T_i - \overline{\Delta T})^2/\Sigma w_i$ (eq. [4]), is 1.38 mK for $q = 4.0$ and 1.22 mK for $q = 3.0$. The curves superposed on the distributions are Gaussians with dispersion $\sigma_{\rm dist}$.

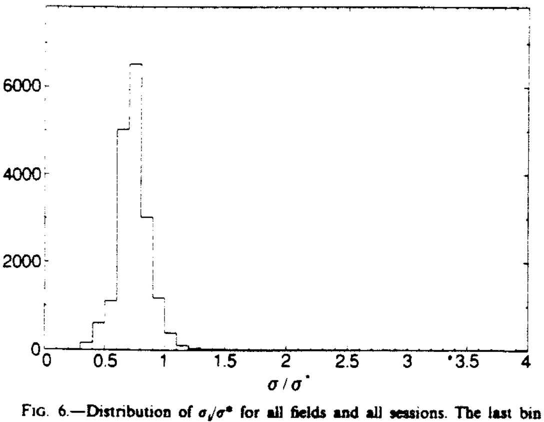

FIG. 6.—Distribution of σ_i/σ^* for all fields and all sessions. The last bin includes all values greater than 3.9. Data with $\sigma_i/\sigma^* > 2$ are deleted.

V. TESTS OF DATA QUALITY

The greatest danger in measurements such as these is persistent systematic effects with a nonzero mean. Such effects may be difficult to detect, since deviations from zero of even $T_{\rm sys} \times 10^{-6}$ are intolerable, yet only the data can reveal them. In this section we discuss the answers to four questions: (1) Are the ΔT_i normally distributed? (2) What are the time scales for systematic errors? (3) Is there a diurnal component in ΔT_i? (4) Is the mean value of all measurements for all fields zero?

As will be discussed in § VI, the observations of NCP 7 are corrupted by a weak radio source in the wings of the beam, and must be excluded from some of the tests of this section.

Figure 7 shows the distribution of accepted measurements (~2 days total integration time) for one of the fields for two values of q, the rejection parameter from § IVc. The plotted curves are Gaussians with the same variance as the measurements. Specifically, $\sigma_{\rm dist}^2 \equiv \Sigma w_i(\Delta T_i - \overline{\Delta T})^2/\Sigma w_i$ is 1.38 mK for $q = 4.0$, and 1.22 mK for $q = 3.0$. A measurement $\Delta T_i \pm \sigma_i$ is rejected if $|\Delta T_i - \overline{\Delta T}| \geq q\sigma_i$. (Blocks of data far from the mean compared to their internal scatter are similarly rejected.) However, this truncation does not lead to sharp edges in the distribution in Figure 7*b* because of the width of the distribution of σ_i shown in Figure 6. We find that $\sigma_{\rm dist}$ can be up to 10% larger than the dispersion for 2 hr blocks of data, and up to 50% (typically 30%) larger than the dispersion for 80 s of data. From this it is clear that fluctuations on time scales longer than 80 s have a significant effect on the width of the distribution, and therefore that σ_i underestimates the true errors. The fair agreement between $\sigma_{\rm dist}$ and the dispersion for 2 hr blocks of data shows that there are no dominating fluctuations on time scales longer than 2 hr, a conclusion supported also by Figure 8. The distributions are sufficiently Gaussian that the procedure of § IV*c* is reasonable. The question of systematic biases from long-term fluctuations must be answered by other tests given blow.

Figure 8 shows the relationship between integration time t and variance σ^2. The value of $t\sigma^2$ rises from the typical thermal limit on time scales less than a few minutes to $(1.2)^2$ times this limit on a time scale of tens of minutes, and then remains at this level for integration times up to 17 days. This shows that there are systematic errors, which we attribute to the atmosphere, with characteristic time scales of minutes to hours, but that no longer term systematic effects are seen in our data.

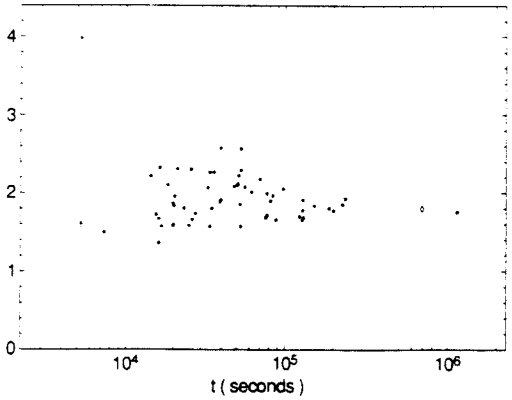

FIG. 8.—Test for correlated errors. For independent data points with uncorrelated errors, we expect $\sigma^2 \propto t^{-1}$, where σ^2 is the variance of the mean of a series of observations extending over a total integration time t. We have plotted $t\sigma^2$ for (1) each field for each observing session (●); (2) the concatenation of all sessions for each field (•); (3) the concatenation of all sessions except Dec85 for each field (○); and (4) the concatenation of all fields for all sessions (★), and for all sessions except Dec85 (◇). Also shown is $t\sigma^2$ for one 2 hr block of data in very good weather (↑). The plot is normalized to the thermal noise level for the best $T_{\rm sys}$ ever achieved during the observations (i.e., 40 K at the pole), and the horizontal line shows the thermal noise level for more typical performance of $T_{\rm sys} = 45$ K at the pole. Although the measurements in the concatenated data sets are the same as for individual fields and sessions, there could have been systematic differences in mean values for different sessions and fields, giving larger values of σ for the concatenated data sets. That is not the case. Two hour blocks of data with variances exceeding four times the 40 K thermal level (↓) are edited out (see § IV*b*). Correlated atmospheric fluctuations on time scales of minutes to 2 hr increase the noise to ~20% above the typical thermal limit. There is no sign of correlated errors for times longer than 2 hr.

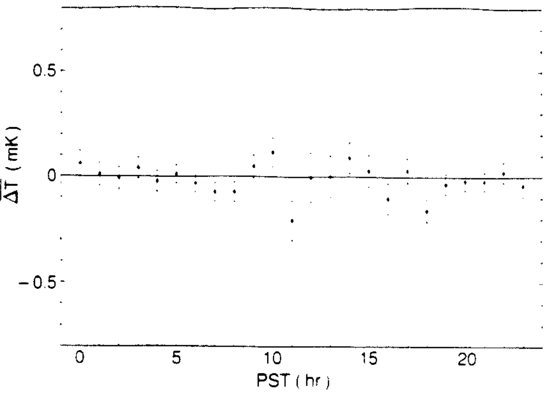

FIG. 9.—$\overline{\Delta T} \pm \sigma$ as a function of time of day. Data accepted by the procedures of § IV (with $q = 3.0$) for all fields except NCP 7 have been combined, then divided into 1 hr blocks according to the PST of the observations (0^h–1^h, etc.). The weighted mean and error for each block were found using the procedure of § IV*c*. The size of the error bars varies with the number of measurements in the block. There are fewer daytime measurements, because the daytime atmosphere is noisier, and because instrumental adjustments are scheduled during the day. For example, bins 4–6 contain 2491 measurements, while bins 11–13 contain only 587. For 24 degrees of freedom $\chi_\nu^2 = 0.83$, and there is little evidence for diurnal systematic errors.

Figure 9 shows the mean temperature and error as a function of time of day. This is the best way to detect systematic errors caused by the Sun. No systematic deviations from zero are seen, although the scatter in the measurements is larger during the day than at night, and, as a result, more measurements have been rejected by our editing procedures.

Figure 10 shows the mean temperature and error as a function of observing session. This is the best way to detect low-level systematic errors that persist for weeks. The expected

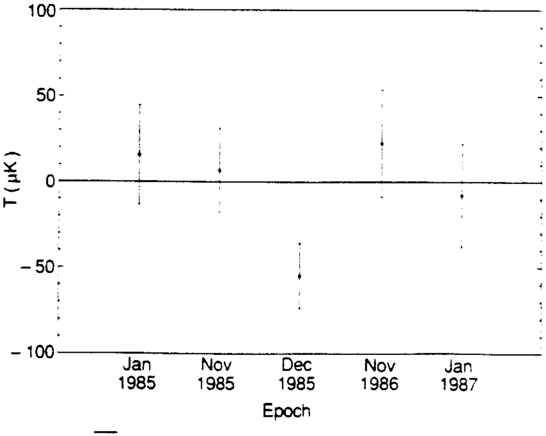

FIG. 10.—$\overline{\Delta T} \pm \sigma$ for the five observing sessions. For each session, data accepted by the procedures of § IV (with $q = 3.0$) for all fields except NCP 7 have been combined, and the weighted mean and error found using the procedure of § IVc. The reduced χ^2 value is 1.85 for 5 degrees of freedom, and the probability of a value for χ^2 greater than this is 10% for a Gaussian distribution.

mean for many fields in differential measurements is zero. Primarily because of the low mean for Dec85, the probability of such a set of five values from Gaussian distributions is 10%. Despite a concerted effort to uncover sources of systematic error that could produce offsets of tens of microkelvins, none has been found. The Dec85 mean value is not so low as to be manifestly due to bad data, yet it remains the most serious strain in our claim that no significant systematic errors bias the data. The results from several more observing sessions should clarify this situation. When run on the combined data from all fields except NCP 7, the procedure of § IV*c* gives $\overline{\Delta T} = -11 \pm 10$ μK, not inconsistent with zero. It should be noted that an instrumental bias is unlikely to cancel a real temperature difference in the microwave background radiation, so that the upper limits derived below are likely to overestimate the limit on the true sky noise.

VI. RESULTS

Table 4 and Figure 11 give the results of the OVRO measurements. These are thermodynamic temperature differences on the sky, including a 4% correction for atmospheric absorption and a 1% correction for the difference between $\partial I_{\text{Rayleigh-Jeans}}/\partial T$ and $\partial I_{\text{Planck}}/\partial T$ at $T = 2.78$ K. The most obvious feature is the 8 σ mean in field NCP 7. No measurement of any other field in any session has such a significant nonzero value. We believe that the only reasonable interpretation is that there is a real temperature difference on the sky near this field.

TABLE 4

OVRO MEASUREMENTS

Field	$\overline{\Delta T} \pm \sigma$ (μK)
NCP 1	-64 ± 35
NCP 3	20 ± 34
NCP 5	-29 ± 27
NCP 7	217 ± 28
NCP 9	34 ± 26
NCP 11	-23 ± 26
NCP 13	-20 ± 32
NCP 15	-36 ± 39

VII. EXTRANEOUS SOURCES OF ANISOTROPY

We have discussed at some length the procedures used to control systematic errors arising from receiver or atmospheric noise and believe that no such errors remain in the edited data at a level of a few tens of microkelvins. Discrete radio sources, the Sunyaev-Zel'dovich decrement due to hot gas in galaxy clusters, galactic synchrotron emission, and interstellar dust are possible sources of anisotropy contributing to the measurements in Table 4. For even a modest number of fields, discrete sources or clusters are unlikely to cancel fluctuations in the microwave background. Thus anisotropy estimates based on data uncorrected for such sources are likely to overestimate the anisotropy of the microwave background itself.

The total anisotropy produced by clusters through the Sunyaev-Zel'dovich effect depends on the redshift at which

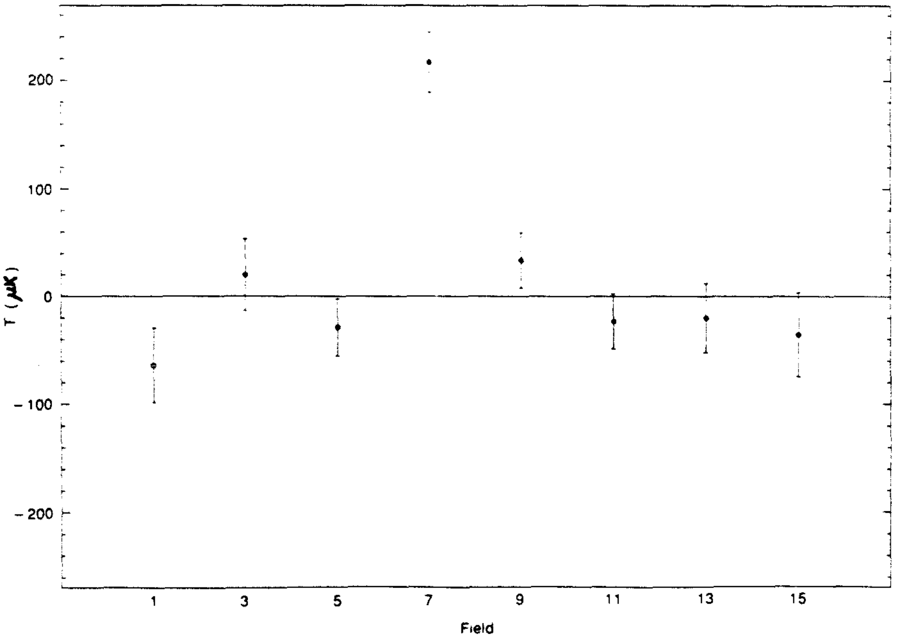

FIG. 11.—Results of the OVRO measurements for fields NCP 1–NCP 15 after data editing as described in § IV. The result for NCP 7 deviates significantly from zero, because of a confusing source (PT 58, see § VII). The remaining seven fields are consistent with zero.

clusters formed. Since this is not known, no *a priori* estimates can be made. Instead, limits on the anisotropy of the microwave background provide useful constraints on the redshift at which clusters formed (Sunyaev 1977, 1978; Rephaeli 1981).

The effects of discrete sources could be subtracted, using the beam map in Figure 4*a*, if their flux densities *during the microwave background observations* were known; however, for weak sources accurate flux densities require long integrations. Given that at 20 GHz we expect many sources to be variable, such long integrations would have to be repeated at every observing epoch, and flux density observations could easily dominate the observing program. Moreover, at flux levels where the density of sources on the sky is greater than about one source per 10 beam areas, a different telescope with higher resolution must be used. Based on source-count estimates of Danese, De Zotti, and Mandolesi (1983) and Franceschini *et al.* (1989) the sensitivity limit for the 40 m telescope set by discrete sources will be in the range 15–45 μK. It remains to be seen whether the limit set by clusters is even higher.

The $8\,\sigma$ detection in NCP 7 is far from the confusion limit and is well above previous upper limits on microwave background anisotropy. It is due to source 58 in the 4.85 GHz Pauliny-Toth *et al.* (1978) survey of the north celestial pole. Table 5 gives all sources in this survey within 10′ of any field in Table 2, along with 20 GHz flux densities measured at OVRO. In the beam map in Figure 4*a* PT 58 appears at the 3% level for upper culmination observations and the 6% level for lower culmination observations. Thus for the range of measured flux densities in Table 5, PT 58 should produce temperatures in NCP 7 of 130–380 μK—just what has been found. Indeed, it became clear early in the course of these observations that there was a variable source in field NCP 7; however, since a significant positive result provided reassurance that the system was working correctly, we continued to observe the field. Therefore NCP 7, the only field that was suspect on the basis of these observations alone, has been excluded from the analysis that follows.

The only other source in the Pauliny-Toth sample that affects our data is PT 82, 1′.4 from the center of NCP 9_{A2}. From the 20 GHz flux densities in Table 5 and the beam map we would expect a -28 to -49 μK shift in NCP 9. The results on this field show no such effect. However, when the data for NCP 9 are divided according to parallactic angle, we measure -53 ± 36 μK at parallactic angles for which the reference beam covers PT 82, and 78 ± 30 μK at angles for which PT 82 does not affect the measurements. From this we deduced that a source too weak to appear in the Pauliny-Toth catalog lay near the main field of NCP 9. A map of this region at 5 GHz, made for us by P. Crane with the VLA, does indeed show a small-separation double $\sim 75''$ from NCP 9. A source at this level with a spectral index of -0.75 ± 0.15 (see, e.g., Donnelly, Partridge, and Windhorst 1987) would raise the temperature of NCP 9 by 90 ± 20 μK. Our direct 20 GHz measurements of PT 82 show that it is variable, so we cannot correct the NCP 9 data for it. If we take the 78 ± 30 μK value for parallactic angles at which PT 82 does not affect the data, and apply a 90 ± 20 μK correction for the double (which is unlikely to be a variable source), we obtain -12 ± 36 μK for NCP 9.

While the Pauliny-Toth *et al.* survey has helped to focus our attention on the problems of discrete sources, correcting for such sources requires observations down to 1 mJy, much below the Pauliny-Toth *et al.* cutoff at 14 mJy. At present such correction, based on the VLA image, is possible only for NCP 9. Using -12 ± 36 μK in place of the value in Table 4 gives a limit $\sim 6\%$ lower than that derived in § VIII. If NCP 9 were excluded entirely from our analysis, our derived upper limit on sky fluctuations would increase by 10%, because of the decrease from seven to six fields. Thus the choice between making no corrections to NCP 9, correcting NCP 9, or excluding NCP 9 entirely has no important consequence. We have chosen the first course, since in doing this we reject only the one field (NCP 7) for which there is clear evidence *in our own observations* of a variable discrete source, and since we prefer to delay the correction of NCP 9 until we can treat all fields equally using VLA maps of comparable sensitivity. Accordingly, in the analysis below we use the seven values in Table 4 excluding NCP 7.

The successful prediction and subsequent detection of a source in the main beam of NCP 9 gives us confidence that our data can be trusted at the 50 μK level. In the future it will be possible to subtract the effect of sources like the double near NCP 9, which are unlikely to vary; however, variable sources like PT 58 and PT 82 must be avoided.

VIII. ANALYSIS

Table 4, along with Figures 2 and 4 and equation (4), provides a complete summary of our results. The question that we now turn to is: what is the largest anisotropy of the microwave background radiation consistent (in some sense to be specified) with the seven measurements in Table 4 (excluding NCP 7). This is a statistical question, and its answer, and the most appropriate method for deriving it, depends on the unknown distribution of sky fluctuations. We will assume Gaussian fluctuations because this provides a common starting point for comparison of our results with those of other observers and with model predictions, which, with few exception (e.g., cosmic

TABLE 5

SOURCES FROM THE PAULINY-TOTH[a] 4.85 GHz SURVEY WITHIN 10′ OF NCP FIELDS

	EPOCH 1985.0		EPOCH 1950.0		FLUX DENSITY (mJy)		
SOURCE	A.	Decl.	R.A.	Decl.	4.85 GHz[a]	20.0 GHz[b]	RELATIVE POSITION
PT 42.....	$05^{\rm h}38^{\rm m}14^{\rm s}.8$	89°04′51″	$04^{\rm h}49^{\rm m}46^{\rm s}.0$	89°02′30″	28.8	9–15	6′.0 from NCP 5_{A2}
PT 58.....	06 56 42.8	88 58 14	06 11 21.0	88 59 58	26.0	18–25	2′.0 from NCP 7
PT 82.....	09 28 26.3	88 58 06	08 55 28.0	89 06 48	18.2	1.4–2.4	1′.4 from NCP 9_{A2}
PT 87.....	10 51 21.1	89 03 31	10 31 56.0	89 14 32	71.5	12–15	4′.1 from NCP 11
PT 90.....	14 19 54.6	88 52 22	14 44 19.0	89 01 35	18.8	6	8′.1 from NCP 15_{A1}
PT 91.....	15 01 11.5	89 08 32	15 42 46.0	89 16 00	28.4	5	8′.5 from NCP 15

[a] Pauliny-Toth *et al.* 1978. The flux density limit was 14 mJy; position errors were typically 15″.

[b] From OVRO, 1987 Jun, 1988 Jan, and 1988 Feb. Typical errors are ±0.4 mJy.

strings) assume Gaussian fluctuations. Moreover, as we show in the Appendix observations of seven fields are well-suited to the detection of Gaussian fluctuations, but any power-law tail in the fluctuation spectrum with an index greater than -2 would be detected with greater probability in an experiment with more fields.

We first derive a limit on $\theta_{\rm sky}^2$, the variance of the distribution of sky fluctuations from the mean background temperature *for the triple beam* of Figure 4. We then calculate corresponding limits on the autocorrelation function of the microwave background fluctuations, under simple assumptions.

a) Limits on $\theta_{\rm sky}^2$

Arguments about the "best" statistical procedure to use in deriving limits on $\theta_{\rm sky}^2$ can be misleading, because statistical procedures that are optimal according to some criterion may be inappropriate if the assumptions on which they are based are not justified. We use two different procedures to derive limits on $\theta_{\rm sky}^2$. One (the likelihood ratio test) has been used widely in past microwave background work, the other (likelihood) has not. The limits given by the two procedures are about the same. However, as we discuss at the end of this section, the relative insensitivity of the likelihood procedure to certain problems that may afflict real data sets makes it the preferred procedure for microwave background work.

i) Likelihood

The variance of the (assumed Gaussian) distribution of sky fluctuations for the triple beam in Figure 4 is $\theta_{\rm sky}^2$. The mean of the distribution of fluctuations is zero, since the triple beam samples only deviations from mean sky temperature. Thus the probability density for a measurement $\Delta T \pm \sigma$ is

$$p(\Delta T, \sigma) = [2\pi(\sigma^2 + \theta_{\rm sky}^2)]^{-1/2} \exp\,[-\Delta T^2/2(\sigma^2 + \theta_{\rm sky}^2)]\ .$$

The joint density for the seven fields (excluding NCP 7) is

$$\begin{aligned} L(\{\Delta T_i\} \mid \theta_{\rm sky}) &\equiv \prod_{i=1}^{7} p(\Delta T_i, \sigma_i) \\ &= \prod_{i=1}^{7} [2\pi(\sigma_i^2 + \theta_{\rm sky}^2)]^{-1/2} \exp\left[\frac{-\Delta T_i^2}{2(\sigma_i^2 + \theta_{\rm sky}^2)}\right]. \end{aligned}$$

$L(\{\Delta T_i\} \mid \theta_{\rm sky})$, called the *likelihood function*, can be thought of as the relative probability of the set of seven measurements as a function of the assumed sky variance. This function, normalized to its maximum value, is given in Figure 12 for the measurements in Table 4.

The value of $\theta_{\rm sky}$ for which our results have the maximum likelihood is 14 μK; however, $L(\theta_{\rm sky} = 0)$ is almost as large, so that this cannot be claimed as a detection. Upper limits can be determined in two ways. The first is to find the value of $\theta_{\rm sky}$ at which the relative likelihood has fallen to some specified value, say e^{-2}, 0.05, or 0.01. From Figure 12, these relative likelihood values occur at 57, 72, and 98 μK, respectively.

Alternatively, we can use Bayes's formula, which gives the probability density of $\theta_{\rm sky}$ given the set of observations $\{\Delta T_i\}$ as

$$p(\theta_{\rm sky} \mid \{\Delta T_i\}) \propto L(\{\Delta T_i\} \mid \theta_{\rm sky}) p(\theta_{\rm sky})\ ,$$

where $p(\theta_{\rm sky})$ and $p(\theta_{\rm sky} \mid \Delta T_i)$ are known, respectively, as the *prior* and *posterior* densities (see Berger 1985 and Berger and Wolpert 1984 for general discussions of Bayesian methods; and Edwards 1984 for an alternative interpretation of the likelihood function). Our (possibly nonexistent) knowledge of $\theta_{\rm sky}$ before the observations is represented by $p(\theta_{\rm sky})$. The simplest prior density consistent with the one fact we know (i.e., $\theta_{\rm sky}^2 \geq 0$), is $p(\theta_{\rm sky}) = c$ for $\theta_{\rm sky} \geq 0$, and $p(\theta_{\rm sky}) = 0$ for $\theta_{\rm sky} < 0$. Then the posterior density, i.e., the density of $\theta_{\rm sky}$ determined from what we knew before the observations plus the observations themselves, will look just like Figure 12 except for normalization. In this case, the area under the curve from 0 to θ^* gives the probability that $0 \leq \theta_{\rm sky} \leq \theta^*$. Specifically, $P(\theta_{\rm sky} < 58$ μK$) = 0.95$, and $P(\theta_{\rm sky} < 127$ μK$) = 0.9987$. Thus 58 μK can be taken as a 95% upper limit to $\theta_{\rm sky}$, and 127 μK can be taken as an equivalent 3 σ upper limit.

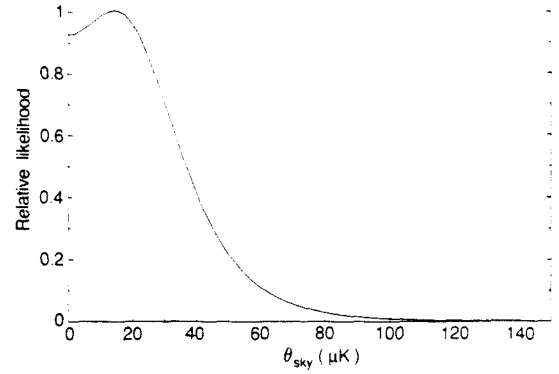

FIG. 12.—Likelihood function for the measurements in Table 4 excluding NCP 7, normalized to the maximum value. The maximum occurs at $\theta_{\rm sky} = 14$ μK, but $L(0)$ is so large that no detection of fluctuations can be claimed.

Invariance arguments suggest that when no other information is available the prior density of a parameter that is a *scale factor* (as is $\theta_{\rm sky}$ in the absence of measurement errors, see Berger 1985) should be uniform in θ^{-1} rather than θ. With such a prior density, a cutoff must be imposed at small values of $\theta_{\rm sky}$ to make the posterior density normalizable, and the derived upper limit to $\theta_{\rm sky}$ depends somewhat on the value chosen. This is unappealing, but it is not a serious problem if observations of galaxies and clusters do provide a physical basis for such a cutoff. We find 95% limits in the range 30 μK to 36 μK for cutoffs between 0.1 μK and 1.0 μK. However, the measurement errors fix a level below which the actual value of $\theta_{\rm sky}$ makes little difference, and what we measure for each field is determined almost entirely by the errors. Yet a $1/\theta$ prior distribution gives much more weight to values of $\theta_{\rm sky}$ below this level than it does to large values where our measurements have real discriminating power, leading to quite low limits on $\theta_{\rm sky}$. We therefore prefer a conservative prior density uniform in $\theta_{\rm sky}$, and will adopt the corresponding limit of 58 μK.

Figure 12 shows $L(\{\Delta T_i\} \mid \theta_{\rm sky})$ only for $\theta_{\rm sky}^2 \geq 0$. Whether we think of this as a restriction of the prior density or the likelihood function itself to positive sky variances makes little difference. The ease with which this physical constraint can be imposed makes the likelihood function estimate relatively insensitive to a problem that can seriously affect the method described in the next section.

ii) Likelihood Ratio Tests

Likelihood ratio tests have been used for analysis of microwave background data by many authors, e.g., Boynton and

Partridge (1973), Lasenby and Davies (1983), and Uson and Wilkinson (1984*a*, *b*, *c*). For a general discussion of likelihood ratio tests and definitions of the statistical terms used here, see Lehmann (1986).

The problem is to choose between an hypothesis H and an alternative hypothesis K. Specifically, given a set of measurements whose distribution is known in terms of a parameter θ, we must find θ. We assume that if θ is known, it is known whether H is true. A "test" is a set of criteria used to accept or reject H. The *level of significance* or *size* α of the test is the probability of rejecting H if H is true, i.e., a type I error. The *power* β of the test is the probability of rejecting H if K is true, so that $1 - \beta$ is the probability of a type II error (i.e., of accepting H when K is true). Traditionally it has been assumed that type I errors are worse than type II errors, and tests have been devised that maximize β for a fixed value of α. Such tests are called *most powerful.*

For a random sample x drawn from a distribution characterized by a parameter θ, the Neyman-Pearson lemma shows that there exists a most powerful test of size α of the simple hypothesis $H:\theta = \theta_0$ against the simple alternative $K:\theta = \theta_1$, and that this test is given by the prescription:

$$\text{reject } H \text{ if } \quad \lambda^* \equiv \frac{P(x\,|\,H)}{P(x\,|\,K)} \le k^* ,$$

or

$$\text{accept } H \text{ if } \quad \lambda^* > k^* ,$$

where k^* is given implicitly by the requirement that $P(\lambda^* \le k^*\,|\,H) = \alpha$.

In general, whether λ^* is greater than k^* or not depends on θ_1. If it does not, that is, if the ordering of points in the measurement space according to their values of λ^* does not depend on θ_1, then the test is said to be *uniformly most powerful* (UMP) and can decide between composite hypotheses, e.g., $H:\theta \ge \theta_0$ and $K:\theta < \theta_0$. (Note that the test is the same as before, but the distributions satisfy additional requirements, and stronger theorems apply. We use the generic expression "likelihood ratio tests" rather than "Neyman-Pearson tests" to emphasize this distinction.)

Given our assumption of Gaussian sky fluctuations, we can calculate λ^* for the measured $\Delta T_i \pm \sigma_i$:

$$\lambda^*(\Delta T) = \frac{\prod_{i=1}^{7} p(\Delta T_i\,|\,\sigma_i, \theta_{\rm sky} = \theta_0)}{\prod_{i=1}^{7} p(\Delta T_i\,|\,\sigma_i, \theta_{\rm sky} = \theta_1)}$$
$$= \prod_{i=1}^{7} \left(\frac{\sigma_i^2 + \theta_1^2}{\sigma_i^2 + \theta_0^2}\right)^{1/2} \exp\left\{\frac{\Delta T_i^2}{2}\left[\frac{\theta_0^2 - \theta_1^2}{(\sigma_i^2 + \theta_0^2)(\sigma_i^2 + \theta_1^2)}\right]\right\} .$$

To find k^* we must know the distribution of λ^* under H. It is simpler, and involves no loss of information about θ, to calculate the distribution under H of

$$\lambda = \sum_i \frac{x_i^2}{(\sigma_i^2 + \theta_0^2)(\sigma_i^2 + \theta_1^2)} , \qquad (5)$$

where x_i is Gaussian-distributed with variance $\sigma_i^2 + \theta_0^2$, and the sign has been chosen for the case $\theta_0 > \theta_1$. That is, λ is *sufficient for* θ. The observed value of λ is given by

$$\lambda(\Delta T) = \sum_i \frac{\Delta T_i^2}{(\sigma_i^2 + \theta_0^2)(\sigma_i^2 + \theta_1^2)} .$$

Then the test of size α is as follows: reject H if $\lambda(\Delta T) \le k$, and accept H if $\lambda(\Delta T) > k$, where k is found from $P(\lambda \le k\,|\,H) = \alpha$. To calculate the power β of the test, we calculate the distribution of λ under $K:\theta = \theta_1$, where this time x_i is Gaussian distributed with variance $\sigma_i^2 + \theta_1^2$. Then $\beta(\theta_1) = P[\lambda \le k\,|\,\theta = \theta_1]$.

We want to use the test to find an upper limit to $\theta_{\rm sky}$ at a certain value of α. To do this, we fix α, then vary θ_0 until $P[\lambda \le \lambda(\Delta T)] = \alpha$. In other words, we find θ_0 such that if we sample randomly from seven Gaussian distributions with variance $\sigma_i^2 + \theta_0^2$, the probability of finding λ no larger than we have measured it $[\lambda(\Delta T)]$ is only α.

It turns out that for the distribution in equation (5), the question of whether $\lambda(\Delta T) \le k$ or not is independent of the value of θ_1. Therefore the likelihood ratio test specified above is UMP.

Figure 13 shows the results of these calculations for the data of Table 4. On this basis, we reject $H:\theta_{\rm sky} \ge 52.5$ μK at the 95% confidence level (i.e., $\alpha = 0.05$), and reject $H:\theta_{\rm sky} \ge 107$ μK at the 99.87% confidence level. The power of the test β is 0.72 (independent of α) for $\theta_1 = 0$, and decreases monotonically until $\beta = \alpha$ at $\theta_1 = \theta_0$.

Under appropriate assumptions, likelihood ratio tests are "most powerful." This means only that the power is greater than that of any other test at the same level of significance: it does *not* mean that the power is close to unity. Results of likelihood ratio tests should always be regarded with suspicion unless the power is stated along with the level of significance.

The inclusion of measurement errors in the likelihood ratio test has important consequences. While these have been pointed out by others, we restate them here for emphasis. Consider the following. The term $\sigma_i^2 + \theta_0^2$ in equation (5) comes from the combination of the measurement errors with the sky fluctuations, so that, physically, $\sigma_i^2 + \theta_0^2 \ge \sigma_i^2$. Formally, however, the term can be treated as a single quantity that satisfies only $\sigma_i^2 + \theta_0^2 \ge 0$. In effect, this "allows" sky fluctuations to compensate for measurement errors, reducing the width of the overall distribution. The likelihood ratio test requires $P(\lambda \le \lambda(\Delta T)\,|\,H) = \alpha$. Suppose that the measurements

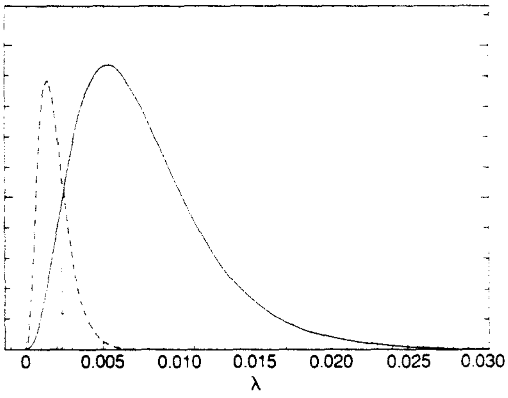

FIG. 13.—Distribution of $\lambda = \sum_i x_i^2/(\sigma_i^2 + \theta_0^2)(\sigma_i^2 + \theta_1^2)$ with $\theta_0 = 52.48$, $\theta_1 = 0$ from a Monte Carlo simulation. Each x_i was assumed to be Gaussian-distributed with variance $\sigma_i^2 + \theta_0^2$ (*solid line*) or $\sigma_i^2 + \theta_1^2$ (*dashed line*). In each case, 300,000 sets of x_i were generated. The curves are independently normalized. A vertical line marks $\lambda(\Delta T) = 0.00233$. The area under the solid curve to the left of this line is $\alpha = 0.05$, while the area to the left under dashed curve is $\beta(\theta_1 = 0) = 0.72$.

are much closer to zero than expected for the size of the measurement errors *alone* (i.e., $\chi_\nu^2 \ll 1$), and that $P[\lambda \leq \lambda(\Delta T) | \theta_0 = 0] < \alpha$. Even with $\theta_0 = 0$, the requirements of a test of size α cannot be satisfied. If, however, $\sigma_i^2 + \theta_0^2$ is treated as a single quantity that can be reduced to arbitrarily small values, a test of size α always exists (see Partridge 1980*b* for an example), even though it is physically absurd. By imposing the condition $\theta_0^2 \geq 0$ in the algorithm that performs the test, we can avoid this absurdity. But in less extreme cases the test will still implicitly treat $\sigma_i^2 + \theta_0^2$ as a single quantity and will underestimate θ_0 to compensate for scatter in the measurements that is unexpectedly small given the errors alone (see Lawrence, Readhead, and Myers 1988 for an example). Fortunately, the power of the test against the alternative $\theta_1 = 0$ immediately shows the existence of this problem. Consideration of how Figure 13 would look for various θ_0 and θ_1 shows that as θ_0 goes to zero, $\beta_{\max} = \beta(\theta_1 = 0)$ goes to α. When the power is low, a high confidence level is meaningless.

iii) *Comparison of Statistical Tests*

The OVRO data do not have the problem of $\chi_\nu^2 \ll 1$, and we therefore expect (and obtain) results from the two statistical methods that are in close agreement. It is instructive, however, to compare the performance of the methods on data sets with $\chi_\nu^2 \approx 1$, as may be obtained in practice either by chance or through misestimation of measurement errors. Such a comparison can be made at small computing cost for the idealized case in which the measurement errors for all fields are equal. Then the likelihood function is simple, and λ (see eq. [5]) has a χ^2 distribution.

Let $\sigma_{\rm true}$ and $\sigma_{\rm assumed}$ be the true (in practice unknown) and assumed measurement errors, respectively, for N fields. Suppose that $\sum_{i=1}^N \Delta T_i^2/\sigma_{\rm true}^2 = N$ for the measurements, and that $\theta_{\rm sky} = 0$. Consider first the case where $\chi_\nu^2 \neq 1$ because the errors are misestimated. Figure 14 and 15 show the upper limits produced by the two methods for $\frac{1}{3}\sigma_{\rm true} \leq \sigma_{\rm assumed} \leq 3\sigma_{\rm true}$ (corresponding to $9 \geq \chi_\nu^2 \geq \frac{1}{9}$). As the assumed error decreases, the 95% upper limit (as previously defined) given by both tests increases slowly. This is desirable; however, as shown by the lower set of curves in Figure 14, with a 30% to 40% underestimate in errors the value of the likelihood function at $\theta_{\rm sky} = 0$ is only ~0.1, and for even lower values of $\sigma_{\rm assumed}$ *both tests would support claims of detections, rather than upper limits.* Underestimation of errors is thus a serious problem, but one to which both statistical methods are equally susceptible.

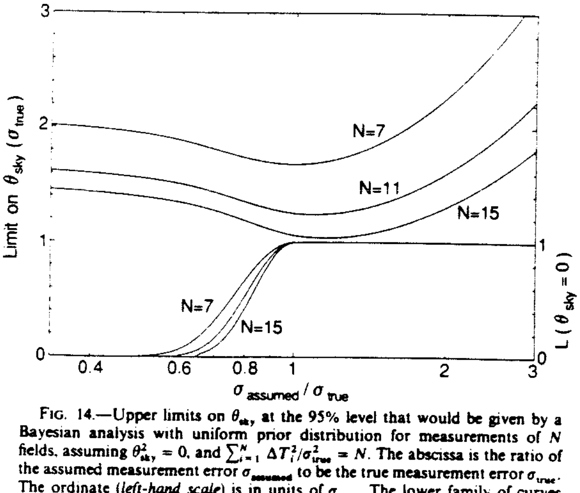

FIG. 14.—Upper limits on $\theta_{\rm sky}$ at the 95% level that would be given by a Bayesian analysis with uniform prior distribution for measurements of N fields, assuming $\theta_{\rm sky}^2 = 0$, and $\sum_{i=1}^N \Delta T_i^2/\sigma_{\rm true}^2 = N$. The abscissa is the ratio of the assumed measurement error $\sigma_{\rm assumed}$ to be the true measurement error $\sigma_{\rm true}$. The ordinate (*left-hand scale*) is in units of $\sigma_{\rm true}$. The lower family of curves gives the value of the likelihood function at $\theta_{\rm sky} = 0$ (*right-hand ordinate*). Values of $L(0)$ less than about 0.1 suggest (false) detection of fluctuations.

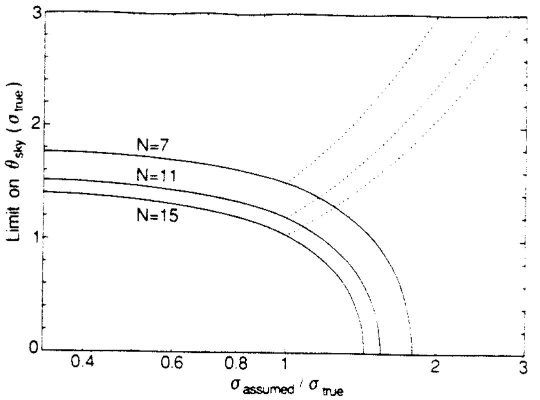

FIG. 15.—Same as Fig. 14, but for a likelihood ratio test. Dotted curves show limits given by a modified likelihood ratio test in which the power of the test is specified in advance, as described in the text. In this case the power for each N is set to the power of the "normal" likelihood ratio test for $\chi_\nu^2 = 1$. For $N = 7$, $\beta = 0.57$, while for $N = 15$, $\beta = 0.55$.

As the assumed error increases, on the other hand, the two tests behave quite differently. The 95% limit given by the Bayesian method increases, while the limit given by the likelihood ratio test *decreases to zero.* For $\sigma_{\rm assumed}$ large enough, the requirements of the likelihood ratio test cannot be satisfied for $\theta_{\rm sky}^2 > 0$. This dramatic difference between the two methods arises because the likelihood ratio test compares the measured values to what "should" have been measured given the errors, and ascribes any discrepancy to sky fluctuations, while the Bayesian method compares only changes in likelihood as $\theta_{\rm sky}$ varies. The likelihood ratio method is in some sense absolute, while the Bayesian method is relative.

The behavior of both statistical methods when data values (rather than errors) are arbitrarily changed (corresponding to the chance occurrence of larger or smaller measurements than expected from the parent distribution) follows at once, since a change of the data values alone can be thought of as a change of both data values and errors by a given factor, which changes the limits by the same factor, followed by a change of the errors while leaving the data values fixed. For example, with $N = 7$ the limits given by the Bayesian method increase by a factor of 1.12 when errors alone are multiplied by 1.5. When means are divided by 1.5, therefore, the limit will change by 1.12/1.5; i.e., the Bayesian method leads to underestimation by a factor of 1.3. For the likelihood ratio method, the limit changes by 0.66 when the errors change by 1.5, so when means are divided by 1.5 the limit will change by 0.66/1.5, i.e., the likelihood ratio method leads to underestimation by a factor of 2.3.

To summarize, underestimation of errors, or measured values by chance larger than expected given the true parent distribution, leads to higher limits or spurious detections with both statistical methods. Overestimation of errors leads to higher limits with the Bayesian method, but lower limits or failure for the likelihood ratio test. Measured values by chance smaller than expected for the parent distribution lead to moderately lower limits for the Bayesian method, but dramatically lower limits for the likelihood ratio method. Neither method is able to extract "truth" from faulty or statistically unlikely data sets, but the results of the Bayesian method for data sets with low values of χ_ν^2 are much less misleading than those of the likelihood ratio method.

As we noted in § VIII*a*(ii), when $\chi_\nu^2 \ll 1$ the distributions of λ under $\theta_{\rm sky} = \theta_0$ and $\theta_{\rm sky} = 0$ are not very different, since both are dominated by the measurement errors, and the power of the likelihood ratio test will be low. This problem can be avoided by using the test in a different way (G. Bernstein and D. Cottingham, private communication). Rather than finding the value of θ_0 for which $\lambda_{\rm observed}$ is equal to λ at the α point of the distribution (see Fig. 13), one could find θ_0 so that the α point in the distribution of λ for $\theta_{\rm sky} = \theta_0$ coincides with the β point in the distribution of λ for $\theta_{\rm sky} = 0$. Call this value of λ $\lambda_{\alpha\beta}$. In effect, the choice of β fixes the minimum value of $\theta_{\rm sky}$ that we believe can be distinguished from zero, given the measurement errors. After specifying α and β in advance, we compare $\lambda_{\rm observed}$ with $\lambda_{\alpha\beta}$: if $\lambda_{\rm observed} \leq \lambda_{\alpha\beta}$ we reject $\theta_{\rm sky} = \theta_0$, and θ_0 can be taken as an upper limit to sky fluctuations.

The dotted curves in Figure 15 show how the limits on $\theta_{\rm sky}$ found by this method depend on the assumed errors when errors are overestimated ($\chi_\nu^2 < 1$). For each value of N the power is chosen to be the power of the likelihood ratio test in its "normal" form when $\chi_\nu^2 = 1$. For example, $\beta_{N=7} = 0.57$, $\beta_{N=15} = 0.55$, and $\lim_{N\to\infty} \beta = 0.5$. Such a modified likelihood ratio test is clearly safe for $\chi_\nu^2 > 1$, in the sense that it does not give misleadingly low limits.

The OVRO data set has roughly equal measurement errors for all fields and $\chi_\nu^2 \approx 1$, thus we obtain limits from the two statistical methods that are in close agreement: $\theta_{\rm sky} < 58\ \mu$K (95% confidence) from a Bayesian analysis with a prior density uniform in $\theta_{\rm sky}$ for $\theta_{\rm sky}^2 \geq 0$, and $\theta_{\rm sky} < 52\ \mu$K (95% confidence, $\beta = 0.72$) from a UMP likelihood ratio test. We will use 58 μK as our 95% limit.

b) Limits on the Temperature Autocorrelation Function

The statistical properties of a Gaussian random field, which we assume describes the microwave background fluctuations, are fully specified by the two-point correlation function. Over small angles, we can use the familiar Fourier expansion in rectangular coordinates for $T(x, y)$, the radiation temperature on the sky. The corresponding correlation function,

$$C(\phi) = \langle T(\boldsymbol{x}_1)T(\boldsymbol{x}_2)\rangle , \tag{6}$$

depends only on the angular distance $\phi \equiv |\boldsymbol{x}_1 - \boldsymbol{x}_2|$ between sampled points.

For physically reasonable fields, the maximum values of $C(\phi)$ occurs at $\phi = 0$, with zero first derivative. The *coherence angle* is defined by

$$\phi_c \equiv \left[-\frac{C(0)}{C''(0)} \right]^{1/2} .$$

Many examples of autocorrelation functions computed for models of interest can be found in the literature (e.g., Vittorio and Silk 1984; Vishniac 1987; Bond and Efstathiou 1987). Baryonic models with $0.1 \leq \Omega \leq 1$ and standard recombination (Peebles 1968) typically have coherence angles of 4′–8′ for adiabatic fluctutations (Gouda, private communication) and 2′–12′ for isocurvature modes (Efstathiou and Bond 1987). Models with lower values of Ω have smaller ϕ_c but larger amplitudes, as required by normalization with the observed galaxy-galaxy correlation function. Cold dark matter (CDM) models with $\Omega = 1$ have coherence angles of $\sim 10'$ for adiabatic fluctuation modes and 50′ for isocurvature modes (Bond and Efstathiou 1987). The effect of early reionization is to erase the fluctuations on small scales, effectively increasing ϕ_c and reducing the amplitude $C(0)^{1/2}$ (see, e.g., Efstathiou and Bond 1987), while generating new fluctuations on intermediate and small scales. Seond-order effects over the extended last scattering surface appear with amplitude $\leq 10^{-5}$ on scales $\phi_c \approx 1\rlap{.}'5$ (CDM) and 15′ (hot dark matter) for $\Omega = 1$ adiabatic models (Vishniac 1987). In isocurvature scenarios, for which early reionization or nonstandard recombination is most plausible, the reimposed perturbations appear with $C(0)^{1/2} \approx 10^{-5}$, again on arcminute scales (Efstathiou 1988).

In practice, we observe the sky with an antenna whose response pattern $B(x, y)$ (normalized to unit power over 4π sr) has nonzero width. The measured sky temperature as a function of position is the cross-correlation of the true temperature with the beam pattern,

$$T_{\rm obs}(x, y) = T \star B .$$

For a symmetric real beam the autocorrelation theorem implies

$$C_{\rm obs}(\phi) = C \star C_{\rm beam} , \tag{7}$$

where $C_{\rm beam}(\phi) \equiv B \star B$.

If, as is often the case, the antenna beams are well-represented by a circularly symmetric Gaussian with dispersion $\phi_0 = 0.4247\phi_{\rm FWHM}$, equation (7) becomes

$$C(\phi_0, \phi) = C(\phi) \star \frac{1}{4\pi\phi_0^2} \exp\left(-\frac{\phi^2}{4\phi_0^2} \right) , \tag{8}$$

where we write $C(\phi_0, \phi)$ in place of $C_{\rm obs}$ as an explicit reminder of the Gaussian approximation. This expansion is analytically tractable for many $C(\phi)$. For the OVRO 40 m telescope, $\phi_{\rm FWHM} = 108''$, so $\phi_0 = 0\rlap{.}'77$.

For switching experiments, one must cross-correlate the smeared temperature field $T_{\rm obs}(x, y)$ with the sampling function $S(x, y)$. For an idealized double switching scheme with three Gaussian beams separated by ϕ_S (see Fig. 3 and eq. [3]), the expected sky variance is

$$\begin{aligned} \langle \Delta T^2 \rangle &= \langle [T_M - \tfrac{1}{2}(T_{R1} + T_{R2})]^2 \rangle \\ &= \tfrac{3}{2}\langle T_{\rm obs}(\boldsymbol{x})^2 \rangle - 2\langle T_{\rm obs}(\boldsymbol{x}_M) T_{\rm obs}(\boldsymbol{x}_R) \rangle \\ &\quad + \tfrac{1}{2}\langle T_{\rm obs}(\boldsymbol{x}_{R1}) T_{\rm obs}(\boldsymbol{x}_{R2}) \rangle , \end{aligned} \tag{9}$$

where $|\boldsymbol{x}_M - \boldsymbol{x}_R| = \phi_S$, and $|\boldsymbol{x}_{R1} - \boldsymbol{x}_{R2}| = 2\phi_S$. Combining equations (6), (8), and (9), we obtain

$$\langle \Delta T^2 \rangle = \tfrac{3}{2}C(\phi_0, 0) - 2C(\phi_0, \phi_S) + \tfrac{1}{2}C(\phi_0, 2\phi_S) . \tag{10}$$

On the 40 m telescope, $\phi_S = 7\rlap{.}'15$. Analytic tractability is often lost when the details of real experiments must be included; however, as discussed in § VIII*c* below, equation (10) turns out to be quite accurate for the OVRO measurements. (See also Boynton 1980 for discussion of the manipulation of autocorrelation functions.)

If $\phi_c \ll \phi_S$, equation (10) reduces to

$$\langle \Delta T^2 \rangle \approx \tfrac{3}{2}C(\phi_0, 0) .$$

If in addition $\phi_c \gg \phi_0$, then beam smearing is unimportant, and

$$\langle \Delta T^2 \rangle \approx \tfrac{1}{2} C(0) . \tag{11}$$

In real experiments, the ratio ϕ_S/ϕ_0 must usually be restricted in order to minimize certain systematic errors, and both inequalities cannot be satisfied simultaneously. Nevertheless, equation (11) is often a good approximation for $\phi_c \approx \sqrt{\phi_0 \phi_S}$, and it has been used widely in the past to derive limits from switching experiments (e.g., Uson and Wilkinson 1984*a*, *b*; Boynton and Partridge 1973). In § VIII*a* we derived an upper limit on the sky dispersion from the OVRO measurements, assuming Gaussian fluctuations, of $\theta_{\rm sky} < 58$ μK. In the approximation of equation (11), then,

$$\frac{``\delta T"}{T} = \frac{C^{1/2}(0)}{T} = \frac{\sqrt{2/3}\,\theta_{\rm sky}}{2.78} < 1.7 \times 10^{-5} .$$

As noted above, many models have large-scale power, with coherence angles outside the range where equation (11) is a reasonable approximation. To put our results in a form that can be compared with a wide range of model predictions, we assume that the temperature autocorrelation function can be approximated by a Gaussian,

$$C(\phi) = C_0 \exp\left(-\frac{\phi^2}{2\phi_c^2}\right) .$$

In this case equation (8) becomes

$$C(\phi_0, \phi) = C_0 \frac{\phi_c^2}{2\phi_0^2 + \phi_c^2} \exp\left[-\frac{\phi^2}{2(2\phi_0^2 + \phi_c^2)}\right] . \tag{12}$$

This approximation has been used only occasionally in the past to present results of observations (Davies *et al.* 1987), but usually produces results in good agreement with those obtained from the detailed model autocorrelation functions. Figure 16 shows the OVRO limits on C_0 for this model as a function of ϕ_c, obtained by combining equations (10) and (12), and using the OVRO experimental limit of 58 μK derived in the previous section. Note the reduced sensitivity to fluctuations with coherence angles smaller than the beam size due to averaging over many independent fluctuations, and to fluctuations with large-scale power where we sample only the curvature of a single fluctuation.

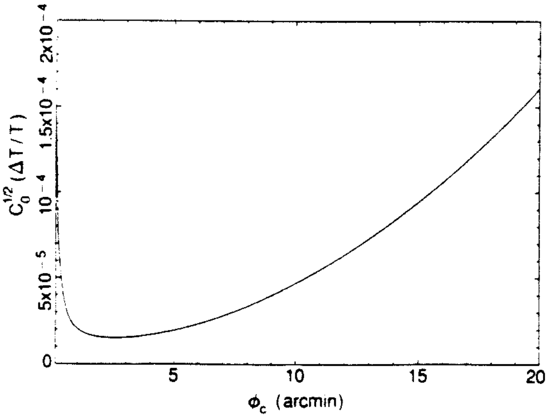

FIG. 16.—Limits on $\Delta T/T$ for a Gaussian correlation function, assuming Gaussian beams in both center and reference fields, for $\theta_{\rm sky} = 58$ μK.

In the case of non-Gaussian statistics for the temperature field, such as those produced by models involving cosmic strings (Ostriker, Thompson, and Witten 1986; Bouchet, Bennett, and Stebbins 1988) and decaying massive particles (Daly 1987), the correlation function and hence $\theta_{\rm sky}$ is a poor discriminator between theories. Such models predict relatively rare signals of large amplitude. As discussed in the Appendix, the proper method to search for these fluctuations is to cover a large portion of sky less deeply, trading sensitivity for area. The effective beam area of the 40 m at 20 GHz is $2\pi\phi_0^2 = 3.72$ arcmin^2, giving a total of 61 arcmin^2 for the eight fields and 16 reference positions. More sophisticated analyses such as $P(D)$ distribution tests used in source count studies (Scheuer 1957, Condon 1974) can also provide useful limits on non-Gaussian source distributions, especially those of power-law form. Note that by increasing the search area the survey becomes more susceptible to contamination by discrete radio sources, which have just the power-law–number flux distribution to which this test is particularly sensitive. In this case, it is necessary to interlock the main and reference fields or to map a contiguous region of the sky to allow discrimination and identification of features.

c) Model Comparisons and Corrections for the True Beam

If a model of MWB fluctuations has Gaussian fluctuations, the results can be given in terms of an autocorrelation function. Then equation (7) shows how to compare the model with our observations. The beam correction depends on both the autocorrelation function and the detailed shape of the beam shown in Figure 4. Clearly, an analytic approximation for Figure 4 would be useful for this purpose. Since the instantaneous beams of the 40 m are reasonably close to Gaussian, the simplest function that could represent Figure 4 consists of one positive Gaussian of unit height straddled by two negative Gaussians half as high and 7.′15 away, all of FWHM 1.′8.

We have estimated the error that would be introduced by using this simplified beam in comparisons with models, in the following way. Bond and Efstathiou (1987) calculated the rms angular power spectrum for two CDM models. Using these power spectra (supplied by Bond), we made several realizations of maps of the microwave background radiation according to each model. We convolved these maps with two "beams": the effective beam of Figure 4, based on measurements of the true telescope beams; and the Gaussian approximation mentioned above. The value of the convolution at a given point is just the mean temperature ΔT that we would measure on the model sky in the absence of instrumental noise, so that the rms value of the convolved map is just $\theta_{\rm sky}$. For both models, the differences between the results with the true beam and the Gaussian approximation were less than 2%.

This close agreement depends to some extent on the models, and we cannot generalize the results to arbitrary power spectra. However, any model whose power spectrum is not drastically different from those of the Bond and Efstathiou models can be compared with the OVRO results using a simple three-Guassian analytic beam without fear of significant error.

We can test the independence of our observed fields in a similar fashion, by comparing the convolution with a single effective beam to the convolution with seven beams appropriately spaced around a 1° ring. For both adiabatic and isocurvature models the convolutions differed by the factor of $7^{1/2}$ expected if the measurements are truly independent.

IX. COMPARISON WITH OTHER OBSERVATIONS

A number of sensitive observations on the isotropy of the microwave background radiation have been made. It is often difficult to compare results made with different instruments, on different angular scales; however, if the autocorrelation function of the background fluctuations is smooth, anisotropy limits from measurements on one angular scale can be extrapolated to other angular scales (e.g., Fig. 16). In this section we discuss the most recent results on four different angular scales.

On scales of 1′ or less, the most sensitive published measurements are the VLA results of Martin and Partridge (1988) and Fomalont *et al.* (1988). Martin and Partridge report a detection of fluctuations at levels of 1.7×10^{-4} and 1.3×10^{-4} on scales of 36″–160″ and 18″–80″. Fomalont *et al.* derive a 95% confidence limit of $\delta T/T < 6 \times 10^{-5}$ on a scale of 1′, and other limits on smaller scales as shown in Figure 17. The results and techniques of the two groups are compared in some detail by Partridge (1989), who concludes that the cause of this apparent contradiction is not fully understood. As will be seen below, under certain assumptions the OVRO results favor interpretation of the VLA measurements as upper limits rather than detections, but our comparisons should not be taken as a resolution of the interesting questions raised by Partridge (1989).

On scales of a few arc minutes, the most sensitive previous measurement is that of Uson and Wilkinson (1984*a*, *b*, *c*), who used an experimental setup similar to our own. They found that $\delta T/T < 2.1 \times 10^{-5}$ at the 95% confidence level, using a likelihood ratio test as described in § VIII*a*(ii). Unfortunately, the power of the likelihood ratio test applied to their measurements is only 0.13, a result of the fact that their measurements were closer to zero than expected from the measurement errors. The Bayesian analysis of § VIII*a*(i) applied to their data (given in Lasenby 1988) yields $\delta T/T < 3.8 \times 10^{-5}$ for a uniform prior distribution. However, the simulations described in § VIII*a*(iii) suggest that this is still an underestimate, given that $\chi_\nu^2 = 0.67$ for their data, and that 4.7×10^{-5} is more consistent with their error estimates.

On scales from a few arc minutes up to $2\overset{\circ}{.}5$, the lowest published upper limits are those of Parijskij and his coworkers (Parijskij 1973*a*, *b*; Parijskij, Petrov, and Cherkov 1977; Berlin *et al.* 1983, 1984). Their early results range from 1.3×10^{-5} to 8.0×10^{-5}. These have been converted to 95% confidence upper limits by Partridge (1980*a*, *b*; 1983), but not corrected for possible errors in statistical analysis. Including such factors, Lasenby (1981) calculates 95% confidence upper limits ranging from 5.4×10^{-5} on a scale of 75′ to 1×10^{-4} on a scale of 10′. Recent preliminary results from this group (Berlin *et al.* 1983) give $\delta T/T < 1 \times 10^{-5}$ ($1\ \sigma$ level) on scales from $4\overset{\prime}{.}5$ to $9\overset{\prime}{.}5$, and $\delta T/T < 3 \times 10^{-5}$ ($1\ \sigma$ level) on a scale of 1°. These observations were made with the Ratan 600 m telescope at a frequency of 3.9 GHz. Observations at this frequency with this telescope require substantial corrections for background sources. Amirkhanyan (1987) has estimated that due to the effects of confusion the reported upper limits are optimistic by a factor of 10, but his analysis has been challenged by Parijskij, Petrov, and Cherkov (1987). As yet we do not have enough details of the observing and analysis procedures to compare these results directly with our own, and we do not, therefore, consider them further here.

On a scale of $8\overset{\circ}{.}3$, with a beam dispersion of $\phi_0 = 3\overset{\circ}{.}5$, Davies *et al.* (1987) report the detection of anisotropies at a level of 3.7×10^{-5}, corresponding to a triple-beam $\theta_{\rm sky}$ of 2.9×10^{-5}. They are now following up this 10.4 GHz detection with observations at other frequencies to determine whether this anisotropy is intrinsic or galactic in origin. The Relikt experiment on the *Prognoz 9* satellite yielded a residual rms temperature fluctuation of 0.2 mK after convolution with a 7° (FWHM) Gaussian (Klypin *et al.* 1987). Analysis of these data based on an assumed fractal perturbation spectrum gives $\delta T/T < 5.6 \times 10^{-6}$ on a scale of 6°. However, the Relikt observations are consistent with the Davies *et al.* result for a power-law spectrum with index $n > 1$ (Scaramella and Vittorio 1988).

In Figure 17 we compare our results with those of Fomalont *et al.* and Davies *et al.*, assuming a Gaussian autocorrelation function. The curve for the Davies *et al.* observations was computed in the same manner as that in Figure 16 for the OVRO limit, also reproduced in Figure 17. The appropriate expression to allow inclusion of the VLA results of Fomalont *et al.* was obtained using the autocorrelation function $C(\theta_0, \theta)$ (see § VIII*b*) for a synthesized beam of dispersion θ_0, the Fourier transform relationship between the autocorrelation function and the power spectrum, and the effective truncation of the measured power spectrum for interferometer spacings less than the VLA telescope diameter. Curves are plotted for $\theta_{\rm sky} < 8.3 \times 10^{-4}$, 1.2×10^{-4}, 7.8×10^{-5}, and 5.8×10^{-5}, with synthesized beams of FWHM 12″, 18″, 30″, and 60″, respectively. The OVRO results provide the most stringent limits on $C_0^{1/2}$ on all scales smaller than 26′, while those of Davies *et al.* provide the most stringent limits on larger scales. From Figure 17, it is clear that if the Davies *et al.* anisotropy turns out to be intrinsic to the microwave background, and the autocorrelation function is Gaussian, then $\phi_c > 26'$.

X. DISCUSSION

Proposed theories of galaxy formation can be classified as linear perturbation theories, which rely on linear growth of small density fluctuations until the density contrast approaches unity and objects condense out of the Hubble flow (Lifschitz 1946), or nonlinear theories in which galaxy formation is driven by something other than the gradual growth of perturbations. Most linear theories assume either adiabatic fluctuations (e.g., Peebles and Yu 1970; Sunyaev and Zel'dovich 1972; Doroshkevich, Zel'dovich and Sunyaev 1978; Silk and Wilson 1980; Wilson and Silk 1981; Kodama and Sasaki 1986; Bond and Efstathiou 1987), or entropy fluctuations (e.g., Peebles 1974; Gott and Rees 1975; Silk and Wilson 1980; Vittorio and Silk 1984; Efstathiou and Bond 1986; Bond and Efstathiou 1987; Efstathiou and Bond 1987; Gouda, Sasaki, and Suto 1987). A variety of nonlinear mechanisms have been considered, including explosions of primordial stars (Doroshkevich, Zel'dovich, and Novikov 1967; Ikeuchi 1981; Ostriker and Cowie 1981), cosmic strings (Ostriker, Thompson, and Witten 1986; Stebbins 1988), and mock gravity (Hogan and White 1986). These scenarios are further complicated by the possibilities of early reionization (Hogan 1980, 1984; Kaiser 1984*a*; Ostriker and Vishniac 1986; Peebles 1987*a*; Vishniac 1987; Silk and Vittorio 1987; Efstathiou 1988), baryonic and nonbaryonic dark matter (White and Rees 1978; Vittorio and Silk 1984; Efstathiou and Bond 1986; Bond and Efstathiou 1987), and biased galaxy formation (Kaiser 1984*a*, *b*, 1986).

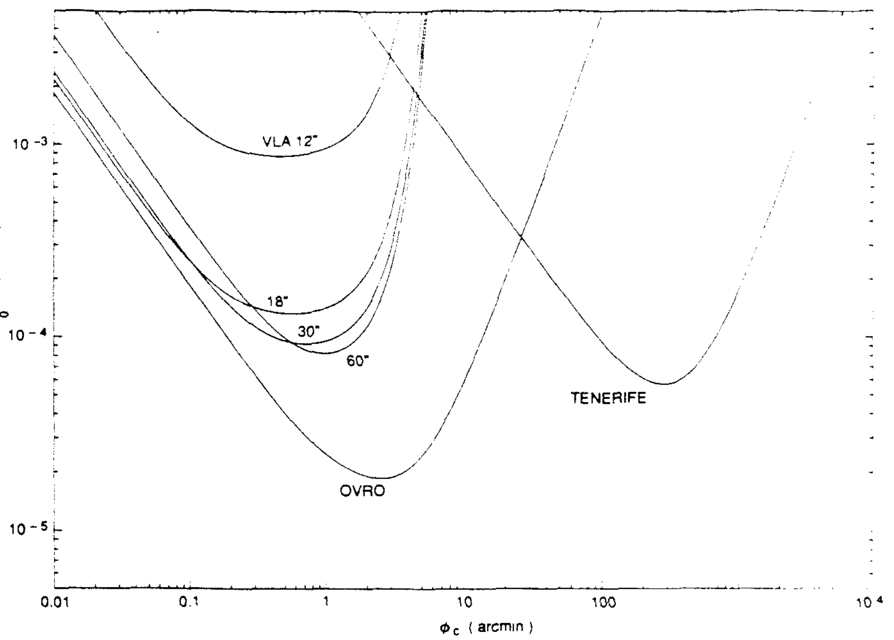

FIG. 17.—Comparison of limits placed on a Gaussian autocorrelation function by the OVRO measurements, with those placed by the measurements of Fomalont *et al.* (1988) and Davies *et al.* (1987).

For convenience, we will refer to models in which the dominant matter constituent of the universe is baryonic and the reionization of the intergalactic medium occurred comparatively recently (i.e., after the epoch at which it would obliterate intrinsic anisotropy on small scales) as "conventional" models. Models based on nonbaryonic matter, early reionization, biased galaxy formation or explosions will be termed "unconventional." No great significance is attached to these labels. It will be seen that the new anisotropy limits place interesting constraints on the conventional models, but do not strongly constrain unconventional models.

It is well known that the intergalactic medium is highly ionized back to the redshifts of distant quasars (see, e.g., Steidel and Sargent 1987 for a recent discussion). Intrinsic fluctuations are not erased by plasma at a given redshift on angular scales greater than the horizon scale at that redshift. It is easy to show that for all plausible values of the density parameter intrinsic fluctuations on angular scales of arc minutes will be erased only if reionization occurs before redshift 10. Since there is no evidence of the existence of compact objects at redshifts greater than 10, reionization earlier than that seems unlikely. Thus conventional scenarios embrace those models in which reionization of the intergalactic medium is due, for example, to ultraviolet radiation from quasars and occurs after redshift 5 (e.g., Donahue and Shull 1987).

The growing conflict between observations and theoretical predictions of conventional models has spurred interest in unconventional models. Numerous models, both linear and nonlinear, have invoked various combinations of early reionization, nonbaryonic matter and biased galaxy formation to reconcile this conflict. Many of these models have not been developed to the point where they make detailed predictions about expected levels of anisotropy, so they cannot yet be tested against our new limit. Those cases for which estimates have been given are discussed below.

There are many predictions of the temperature anisotropy of the microwave background radiation in the literature. As discussed in § VIII*b*, a precise comparison of experimental results with model predictions must take account of both beamwidth and sampling effects. This is possible only when the model autocorrelation function (or, equivalently, the power spectrum) is given. Unfortunately, models are often given in the literature without this information. Sometimes enough information is given to permit an approximate reconstruction of the autocorrelation function or power spectrum, and a fairly accurate prediction for our experimental arrangement can be determined.

Table 6 gives the levels of $\delta T/T \times 10^5$ predicted by various models after adjustment for the parameters of our observations. The models assume a power-law initial spectrum of the form $|\delta_k|^2 \propto k^n$, where δ represents the fluctuation of density or entropy as appropriate. The corrections that we have made are given in the footnotes. Values in the table can be compared directly with the OVRO limits of 2.1×10^{-5} (95%) or 4.6×10^{-5} (equivalent 3 σ).

Clearly, one should be cautious in accepting or rejecting models based on fine distinctions. Nevertheless, there are some clear results:

1. Most of the predictions of conventional adiabatic models are well above our equivalent 3 σ limit, and are therefore definitively ruled out. The lowest predictions of $\delta T/T$ are

TABLE 6

PUBLISHED MODEL PREDICTIONS OF "$\delta T/T$" × 10^5, CORRECTED WHERE POSSIBLE FOR OVRO BEAM AND BEAM SEPARATION†

MODEL PARAMETERS‡						FLUCTUATIONS†					
Ω	Ω_b	Ω_{nb}	Ω_{vac}	h	n	Adiabatic	Adiabatic + Early Reionization	Isocurvature	Isocurvature + Early Reionization	Explosions	COMMENTS
.1	.1	0	0	.5	0				1.5 *c* A		
.1	.1	0	0	.5	−1	72 *k* G			3.2 *c* A		
.1	.1	0	0	.5	0	100 *k* G			0.1 *d* D		
.1	.1	0	0	.5	−1				0.9 *d* D		
.1	.1	0	0	.5	+1	87 *k* G		55 *e* E			
.1	.1	0	0	1	+1			80 *e* E			
.1	.1	0	0	.5	?					>5.2 *f* F	
.1	.1	0	0	1	?					> 10 *f* F	
.2	.2	0	0	.5	0			10.0 *c* I	0.5 *c* I		
.2	.2	0	0	.5	−1			16.5 *c* I	1.7 *c* I		
.2	.2	0	0	.5	0				2.3 *c* A		$z < 200$
.2	.2	0	0	.5	−1				2.3 *c* A		$z < 200$
.2	.2	0	0	.5	0				1.2 *c* A		$z < 200$, $\chi_e = 0.1$
.2	.2	0	0	.5	−1				2.7 *c* A		$z < 200$, $\chi_e = 0.1$
.2	.2	0	0	1	0			10 *c* A			
.2	.2	0	0	1	−1			17 *c* A			
.4	.4	0	0	.5	0				0.9 *d* D		
.4	.4	0	0	.5	−1				1.7 *d* D		
.4	.4	0	0	.5	+1			14 *e* E			
1	1	0	0	.5	0				3.0 *d* D		
1	1	0	0	.5	0	4.3 *l* G		11.0 *c* I	8.5 *c* A		
1	1	0	0	.5	−1	2.4 *l* G		11.1 *c* I	3.0 *c* A		
1	1	0	0	.5	−1				1.4 *d* D		
1	1	0	0	.5	−2			5.3 *c* A			
1	1	0	0	.5	+1	4.4 *l* G		1.9 *e* E			
1	1	0	0	1	+1			4.0 *e* E			
.2	.03	.17	0	.5	+1	13 *a* I					
.2	.1	.1	0	.75	+1	17 *a* B					
.2	0	.2	0	.5	+1	17 *i* G					
.4	0	.4	0	.5	+1	5.4 *i* G					
.4	0	.4	0	1	+1	2.0 *i* G					
1	0	1	0	.5	+1	1.3 *i* G					
1	0	1	0	1	+1	0.7 *i* G					
.4	.03	.37	0	.5	0	4.4 *j* E					Biased
.4	.03	.37	0	.5	+1	3.8 *j* E					Biased
1	.03	.97	0	.5	0	0.9 *j* E					Biased
1	.03	.97	0	.5	+1	0.9 *j* E					Biased
1	.03	.97	0	.5	+1	0.5 *b* B					Biased 1.7
1	.1	.9	0	.5	+1	0.7 *a* B	.03 *m* I				Biased 1.7
1	.2	.8	0	.4	+1	0.9 *a* I					Biased 1.7
1	.5	.5	0	.5	+1	1.7 *a* I					Biased 1.7
1	.1	.9	0	.5	...					> 15 *f* F	
1	.1	.9	0	1	...					> 30 *f* F	
1	.1	.9	0	.5	+1		0.5 *h* G				
1	.1	.9	0	1	+1		0.8 *h* G				
1	.1	.9	0	.5	+1		0.1 *h* H				Biased
1	.1	.9	0	1	+1		0.1 *h* H				Biased
1	.1	.9	0	.5	0		1.3 *h* G				Biased HDM
1	.1	.9	0	1	0		1.6 *h* G				Biased HDM
1	.1	.9	0	.5	+1	2.5 *a* I					Antibiased massive neutrinos
1	.03	.17	.8	.75	+1	1.7 *m* I					$\Lambda \neq 0$
1	.03	.17	.8	.5	+1	3.5 *a* I					$\Lambda \neq 0$
1	.1	.1	.8	.5	+1	1.5 *a* B					$\Lambda \neq 0$
1	~0	~1	0	.75	?			0.4 *m* I			Biased 1.7 Axions
1	~0	~1	0	.5	+1	3.6 *g* G					Massive neutrinos

obtained for high-density models ($\Omega_b \approx 1$). However, even these are well above our 95% confidence limit.

2. Conventional isocurvature models by Efstathiou and Bond (1987) and Gouda, Sasaki, and Suto (1987) also produce fluctuations above our 95% limit for $\Omega_b \leq 1$. Models with $\Omega_b \leq 0.8$ are difficult to reconcile with our present limit, and an improvement of a factor of 2 in our limit would provide strong constraints over a large region of the Ω_b–n plane.

3. Nonbaryonic models with early reionization predict anisotropy levels up to a factor of 3 below our present limit.

4. Many isocurvature baryonic models with early reionization predict anisotropy levels slightly below our limit, but much of the Ω_b–n plane would be excluded if no anisotropy were detected at half the present limit (Efstathiou 1988).

5. The lowest predictions come from models with biased galaxy formation, nonbaryonic matter and early reionization, and are as much as a factor of 10 below our present sensitivity limit.

6. Some massive neutrino models are excluded (Silk 1984), but not all (Bond 1988).

Based on most theories suggested thus far, a modest improvement in the present sensitivity level would lead to the detection of anisotropy. We regard it as encouraging that most theories of galaxy formation, including not only linear theories with early reionization or nonbaryonic matter, but also nonlinear theories, such as those based on superconducting cosmic strings (Ostriker and Thompson 1987), are within reach with only modest extensions of present techniques. If no anisotropy is detected within a factor of 3 of the present limits, most present theories of galaxy formation will be in jeopardy. Possibly those invoking nonstandard reionization and nonbaryonic matter and biased galaxy formation will still be tenable, particularly if further relaxation of the normalization requirements is justified.

We believe that sensitivity 3 or 4 times better than that of the present work should be achievable on arcminute scales with ground based observations at centimeter wavelengths. Discrete source confusion and low-level systematic errors are likely to be the limiting factors. If no anisotropy is detected at this level, alternative methods will probably be needed. Two promising possibilities are instruments designed to image the microwave background radiation on angular scales up to 20°, and a space antenna designed to measure microwave background radiation anisotropy on angular scales down to $\frac{1}{2}$° with a sensitivity of 1 μK.

We would like to thank R. Bond and N. Kaiser, organizers of a workshop at the Canadian Institute of Theoretical Astrophysics, and the other participants in that workshop, for many useful discussions about the microwave background radiation. E. Turner, S. Boughn, D. Cottingham, A. Lasenby, and N. Kaiser contributed significantly to our statistical education. We are grateful to R. Bond and G. Efstathiou for sharing the results of their calculations before publication, and to P. Crane for the VLA observations of NCP 9 on short notice. We thank C. Hogan and B. Partridge for useful criticisms of an early version of this paper, and G. Bernstein, R. Bond, P. Boynton, G. Efstathiou, A. Lasenby, J. Uson, and D. Wilkinson for useful discussions. This work would not have been possible without the help of a number of our colleagures in developing the maser, particularly R. Moore, and R. Clauss, G. Resch, S. Petty, and D. Neff at the Jet Propulsion Laboratory. We are particularly indebted to R. Vogt for this help and encouragement at a crucial time, without which the Microwave Background Program at the Owens Valley Radio Observatory would likely have foundered, and to M. Cohen for his support of this program over many years. We also thank the staff of the OVRO, particukarly T. Seling, M. Hodges, C. Giovanine, W.

Notes to Table 6

† The letters following the predictions refer to the lists of references and corrections given in the notes. Values in the table should be compared directly with the OVRO limits of 2.1×10^{-5} (95%) or 4.6×10^{-5} (equivalent 3 σ).

‡ Total mass-energy density; its constituents in baryons; nonbaryons; and the vacuum; the Hubble constant in units of 100 km s^{-1} Mpc^{-1}; and the spectral index of the initial fluctuations, given by $|\delta_k^2| \propto k^{3+n}$.

References.—Key to references following the predictions:

a Bardeen, Bond, and Efstathiou 1987.
b Bond 1988.
c Efstathiou and Bond 1987.
d Efstathiou 1988.
e Gouda, Sasaki, and Suto 1987.
f Hogan 1984.
g Silk 1986.
h Vishniac 1987.
i Vittorio and Silk 1984.
j Vittorio, Materrese, and Lucchin 1988.
k Wilson 1983.
l Wilson and Silk 1981.
m Bond 1988 (private communication).

Corrections.—Model predictions are often given for particular beam sizes, beam separations, and switching schemes. Where possible we have multiplied published values by a factor f so that the predictions correspond to the OVRO beam arrangement and switching scheme.

A Prediction given for Uson and Wilkinson beam size and separation. Corrected to OVRO using ϕ_c given by or estimated from reference. $1.1 \leq f \leq 2.5$.
B Predictions from reference *a* were modified for OVRO observations in reference *b*. Predictions from reference *b* given for OVRO observations. No correction needed.
C Prediction given for Uson and Wilkinson experiment. Corrected by $f = 2$ under the assumption $\phi_c \geq 6'$ (note $\phi_c \approx 12'$ for the $\Omega = 1, \Omega_b = 0.03$, $h = 0.75$ CDM models of Bond and Efstathiou 1987). If $\phi_c \geq 20'$, then $f = 2.5$.
D Prediction given for OVRO. No correction needed.
E Prediction given for OVRO ϕ_s, but $\phi_0 = 0.64$ (the Uson and Wilkinson value). No correction made.
F Fluctuations have no angular scale. No correction made.
G Prediction given in terms of ϕ_s, but $\phi_0 = 1'.5$. Not corrected to $\phi_0 = 0'.78$, the OVRO value. Corrected from single to double switching if necessary.
H Prediction given in terms of a biasing factor. Biasing at 2.7 σ peaks assumed, $f = 0.17$. Otherwise same as G.
I Prediction for OVRO from reference *m*. No correction needed.

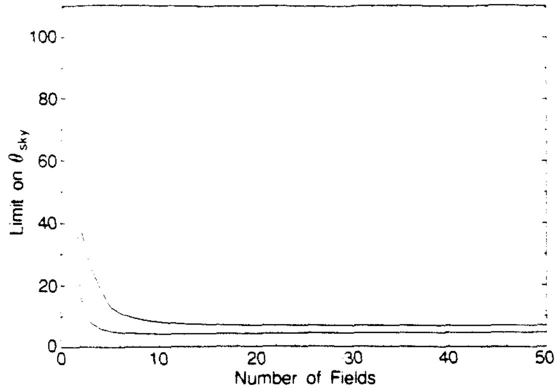

FIG. 18.—Relative upper limits that would be placed on $\delta T/T$ for measurements with a given total integration time divided among N fields, assuming Gaussian fluctuations and using the Bayesian method of § VIII*a*(i) with a uniform prior distribution. The upper curve gives 0.9987 probability, the lower 0.95.

Hutton, W. Schaal, L. Wiley, and C. Lackore. We gratefully acknowledge the support of the National Science Foundation, the James Irvine Foundation, the IBM Research Fund, and the Caltech President's Fund. This work has been supported by the National Science Foundation under grants AST 79-13249, AST 80-24119, AST 82-10259, AST 85-09822, and AST 86-10693.

This paper is dedicated to the memory of Alan Moffet, who contributed much to this work before his untimely death on 1987 August 20.

APPENDIX

In this appendix, we discuss the optimum number of fields to observe, given a limited available integration time τ. The optimum number depends on the relationship between integration time and sensitivity, the spectrum of fluctuations we are trying to measure, and on various instrumental factors.

For the reasons given in § V, we are confident that the sensitivity of our measurements with the 40 m telescope is approximately proportional to the square root of integration time. Thus if a total integration time τ is split between N fields, and σ is the error for $N = 1$, the error σ_N in time τ/N is given by $\sigma_N^2 = N\sigma^2$.

The fluctuation spectrum, on the other hand, is unknown, so we can only answer the question conditionally. For Gaussian fluctuations, the answer is best found using the Bayesian analysis of § VIII*a*(i). As before, we assume that the fluctuations have dispersion θ_{sky}. With a uniform prior distribution $[p(\theta_{sky}) = \text{constant}]$, $p(\theta_{sky} | \{\Delta T_i\}) \propto L(\{\Delta T_i\} | \theta_{sky})$. To estimate the limit that an N-field experiment could place on θ_{sky}, we assume that the measured values ΔT_i are determined entirely by the measurement errors, that is, $\theta_{sky} = 0$. Then the ΔT_i are normally distributed with variance $N\sigma^2$. From the posterior distribution, we determine θ^*_{sky} such that $\int_0^{\theta^*_{sky}} p(\theta_{sky} | \{\Delta T_i\}) d\theta_{sky} = c$, where $c = 0.95$, 0.9987, or some other favorite value. θ^*_{sky} is the 95% or equivalent 3 σ upper limit that we would place on θ_{sky} from our measurements. Figure 18 shows that as N increases, θ^*_{sky} decreases sharply at first, then levels out with an extremely broad minimum at $N \approx 14$ for $c = 0.95$ and $N \approx 25$ for $c = 0.9987$. For $c = 0.95$, θ^*_{sky} is almost constant for $N \gtrsim 10$, while for $c = 0.9987$, θ^*_{sky} is almost constant for $N \gtrsim 17$.

Thus, for Gaussian fluctuations and thermal noise, there is no clear choice of N, except that it not be too small. However, three additional considerations favor moderate values of N over large ones. First, the smaller N, the closer to the celestial pole the fields can lie, minimizing systematic errors from differential ground pickup. Second, for moderate values of N the errors in each field are small. Low-level systematic effects that are detectable in measurements of individual fields with small errors might be undetectable in observations of many fields with much larger individual errors, yet still distort the overall result. Finally, when N is large fewer observations will be made of each individual field, making it difficult to estimate the errors, particularly those due to long-term atmospheric fluctuations. As we have shown in § VIII*a*(iii), both under- and overestimates of the true errors have serious consequences in the statistical analysis of data.

Similar calculations could be done for any assumed distribution of sky fluctuations. Few methods with non-Gaussian fluctuations have been proposed, so we restrict ourselves here to a general consideration. Suppose that the density of fluctuations of temperature ΔT is given by $\rho(\Delta T) \propto \Delta T^{\beta}$. If $\beta = -2$, the probability of finding *one* source in N fields at some fixed multiple of the noise level σ (proportional to $N^{1/2}$ from above) is independent of N. For $\beta > -2$, large fluctuations will be detected with higher probability in an experiment with large N.

REFERENCES

Aaronson, M., Bothun, G., Mould, J., Huchra, J., Schommer, R. A., and Cornell, M. E. 1986, *Ap. J.*, **302**, 536.
Aaronson, M., Huchra, J., Mould, J., Schechter, P. L., and Tully, B. 1982, *Ap. J.*, **258**, 64.
Amirkhanyan, V. R. 1987, *Soob. Spec. Astrofiz. Obs.*, **53**, 96.
Baars, J. W. M., Genzel, R., Pauliny-Toth, I. I. K., and Witzel, A. 1977, *Astr. Ap.*, **61**, 99.
Bahcall, N. A. 1987, *Comments Ap.*, **1**

Bahcall, N. A., and Soneira, R. M. 1982, *Ap. J.*, **262**, 419.
Bardeen, J. M., Bond, J. R., and Efstathiou, G. 1987, *Ap. J.*, **321**, 28.
Bardeen, J. M., Steinhardt, P., and Turner, M. S. 1983, *Phys. Rev. D*, **28**, 679.
Berger, J. O. 1985, *Statistical Decision Theory and Bayesian Analysis* (New York: Springer).
Berger, J. O., and Wolpert, R. L. 1984, *The Likelihood Principle* (Hayward: Institute of Mathematical Statistics).
Berlin, A. B., Bulaenko, E. V., Vitkovsky, V. V., Kononov, V. K., Parijskij, Yu. N., and Petrov, Z. E. 1983, in *IAU Symposium 104, The Early Evolution of the Universe and Its Present Structure*, ed. G. Abell and G. Chincarini (Dordrecht: Reidel), p. 121.
Berlin, A. B., Gassanov, L. G., Gol'nev, V. Ya., Korol'kov, D. V., and Parijskij, Yu. N. 1984, *Soob. Spec. Astrofiz. Obs.*, **41**, 5.
Bertschinger, E., and Watts, P. W. 1988, *Ap. J.*, **328**, 23.
Birkinshaw, M., Gull, S. F., and Hardebeck, H. E. 1984, *Nature*, **309**, 34.
Bond, J. R. 1988, in *IAU Symposium 130, Evolution of Large Scale Structures in the Universe*, ed. J. Audouze, M. C. Pelletan, and A. Szalay (Dordrecht: Kluwer), p. 93.
Bond, J. R., and Efstathiou, G. 1987, *M.N.R.A.S.*, **226**, 655.
Bond, J. R., Szalay, A. S., and Silk, J. 1988, *Ap. J.*, **324**, 627.
Bouchet, F. R., Bennett, D. P., and Stebbins, A. 1988, *Nature*, **335**, 410.
Boynton, P. E. 1980, in *IAU Symposium 92, Objects at High Redshift*, ed. G. O. Abell and P. J. E. Peebles (Dordrecht: Reidel), p. 293.
Boynton, P. E., and Partridge, R. B. 1973, *Ap. J.*, **181**, 243.
Brandenberger, R., Albrecht, A., and Turok, N. 1986, *Nucl. Phys. B*, **277**, 605.
Condon, J. J. 1974, *Ap. J.*, **188**, 279.
Daly, R. A. 1987, *Ap. J.*, **322**, 20.
Danese, L., De Zotti, G., and Mandolesi, N. 1983, *Astr. Ap.*, **121**, 114.
Davies, R. D., Lasenby, A. N., Watson, R. A., Daintree, E. J., Hopkins, J., Beckman, J., Sanchez-Almeida, J., and Rebolo, R. 1987, *Nature*, **326**, 462.
Donahue, M., and Shull, M. J. 1987, *Ap. J.* (*Letters*), **323**, L1.
Donnelly, R. H., Partridge, R. B., and Windhorst, R. A. 1987, *Ap. J.*, **321**, 94.
Doroshkevich, A. G., Zel'dovich, Ya. B., and Novikov, I. D. 1967, *Soviet Astr.*, **11**, 233.
Doroshkevich, A. G., Zel'dovich, Ya. B., and Sunyaev, R. A. 1978, *Soviet Astr.*, **22**, 523.
Dressler, A., Faber, S. M., Burstein, D., Davies, R. L., Lynden-Bell, D., Terlevich, R. J., and Wegner, G. 1987, *Ap. J.* (*Letters*), **313**, L37.
Edwards, A. W. F. 1984, *Likelihood* (Cambridge: Cambridge University Press).
Efstathiou, G. 1988, in *Large-Scale Motions in the Universe*, ed. V. C. Rubin and G. V. Coyne (Princeton: Princeton University Press), p. 299.
Efstathiou, G., and Bond, J. R. 1986, *M.N.R.A.S.*, **218**, 103.
———. 1987, *M.N.R.A.S.*, **227**, 33P.
Fomalont, E. B., Kellermann, K. I., Anderson, M. C., Weistrop, D., Wall, J. V., Windhorst, R. A., and Kristian, J. A. 1988, *A.J.*, **96**, 1187.
Fomalont, E. B., Kellermann, K. I., and Wall, J. V. 1984, *Ap. J.* (*Letters*), **277**, L23.
Franceschini, A., Toffolatti, L., Danese, L., and De Zotti, G. 1989, *Ap. J.*, **344**, 35.
Gamow, G. 1935, *Ohio J. Sci.*, **35**, 406.
Gott, J. R., and Rees, M. J. 1975, *Astr. Ap.*, **45**, 365.
Gouda, N., and Sasaki, M., and Suto, Y. 1987, *Ap. J.* (*Letters*), **321**, L1.
Guth, A. H., and Pi, S.-Y. 1982, *Phys. Rev. Letters*, **49**, 1110.
Harrison, E. R. 1970, *Phys. Rev.*, **1**, 2726.
Hawking, S. W. 1982, *Phys. Letters*, **115B**, 295.
Hogan, C. J. 1980, *M.N.R.A.S.*, **192**, 891.
———. 1984, *Ap. J.* (*Letters*), **284**, L1.
Hogan, C. J., and Bond, J. R. 1988, in *Proc. NATO Advanced Study Institute, The Post-Recombination Universe*, ed. A. N. Lasenby and N. Kaiser (Dordrecht: Kluwer), p. 141.
Hogan, C. J., and White, S. D. M. 1986, *Nature*, **321**, 575.
Ikeuchi, S. 1981, *Pub. Astr. Soc. Japan*, **33**, 211.
Ikeuchi, S., Tomisaka, K., and Ostriker, J. P. 1983, *Ap. J.*, **265**, 583.
Kaiser, N. 1984*a*, *Ap. J.*, **282**, 374.
———. 1984*b*, *Ap. J.* (*Letters*), **284**, L9.
———. 1986, *M.N.R.A.S.*, **222**, 323.
Kirschner, R. P., Oemler, A., Schechter, P. L., and Shectman, S. 1981, *Ap. J.* (*Letters*), **248**, L57.
Klypin, A. A., Sazhin, M. V., Strukov, I. A., and Skulachev, D. P. 1987, *Soviet Astr. Letters*, **13**, 104.
Kodama, H., and Sasaki, M. 1986, *Internat. J. Mod. Phys.*, **A1**, 265.
Lake, G., and Partridge, R. B. 1980, *Ap. J.*, **237**, 378.
Lasenby, A. N. 1981, Ph.D. thesis, University of Manchester.
———. 1988, in *Large-Scale Motions in the Universe*, ed. V. C. Rubin, G. V. Coyne (Princeton: Princeton University Press), p. 278.
Lasenby, A. N., and Davies, R. D. 1983, *M.N.R.A.S.*, **203**, 1137.
Lawrence, C. R., Readhead, A. C. S., and Myers, S. 1988, in *Proc. NATO Advanced Study Institute, The Post-Recombination Universe*, ed. A. N. Lasenby and N. Kaiser (Dordrecht: Kluwer), p. 173.
Lehmann, E. L. 1986, *Testing Statistical Hypotheses* (New York: Wiley-Interscience).
Lemaitre, G. 1927, *Ann. Soc. Sci. Brux.*, **A47**, 49.
Lifshitz, E. M. 1946, *Zh. Eksper. Teoret. Fiz.*, **16**, 587.
Martin, H. M., and Partridge, R. B. 1988, *Ap. J.*, **324**, 794.
Matsumoto, T., Hayakawa, S., Matsuo, H., Murakami, H., Sato, S., Lange, A. E., and Richards, P. L. 1988, *Ap. J.*, **329**, 567.
Moore, C. R. 1980, *IEEE Trans.*, **MTT-28**, 149.
Moore, C. R., and Clauss, R. C. 1978, *IEEE Trans.*, **MTT-27**, 249.
Ostriker, J. P., and Cowie, L. L. 1981, *Ap. J.* (*Letters*), **243**, L127.
Ostriker, J. P., and Thompson, C. 1987, *Ap. J.* (*Letters*), **323**, L97.
Ostriker, J. P., Thompson, C., and Witten, E. 1986, *Phys. Letters*, **B180**, 231.
Ostriker, J. P., and Vishniac, E. T. 1986, *Ap. J.* (*Letters*), **306**, L51.
Parijskij, Yu. N. 1973*a*, *Ap. J.* (*Letters*), **180**, L47.
———. 1973*b*, *Soviet. Astr.*, **17**, 291.
Parijskij, Yu. N., Berlin, A. B., and Vitkovskij, V. V. 1987, *Soob Spec. Astrofiz. Obs.*, **53**, 99.
Parijskij, Yu. N., Petrov, Z. E., and Cherkov, L. N. 1977, *Soviet. Astr. Letters*, **3**, 263.
Partridge, R. B. 1980*a*, *Phys. Scripta*, **21**, 624.
———. 1980*b*, *Ap. J.*, **235**, 681.
———. 1983, in *Proc. NATO Advanced Study Institute, The Origin and Evolution of Galaxies*, ed. B. L. T. Jones and J. E. Jones (Dordrecht: Reidel), p. 121.
———. 1989, in *Proc. 3d ESO/Cern Symposium, Astronomy, Cosmology, and Fundamental Physics*, ed. M. Caffo, R. Fanti, G. Giacomelli, and A. Renzini (Dordrecht: Kluwer), p. 105.
Pauliny-Toth, I. I. K., Witzel, A., Preuss, E., Baldwin, J. E., and Hills, R. E. 1978, *Astr. Ap. Suppl.*, **34**, 253.
Peebles, P. J. E. 1968, *Ap. J.*, **153**, 1.
———. 1974, *Ap. J.* (*Letters*), **189**, L51.
———. 1987*a*, *Ap. J.* (*Letters*), **315**, L73.
———. 1987*b*, *Ap. J.*, **317**, 576.
Peebles, P. J. E., and Yu, J. T. 1970, *Ap. J.*, **162**, 815.
Rees, M. J. 1972, *Phys. Rev. Letters*, **28**, 1669.
Rephaeli, Y. 1981, *Ap. J.*, **245**, 351.
Rubin, V. C., Thonnard, N., Ford, W. K., and Roberts, M. S. 1976, *A.J.*, **81**, 719.
Scaramella, R., and Vittorio, N. 1988, *Ap. J.* (*Letters*), **331**, L53.
Scherrer, R. J. 1987, *Ap. J.*, **320**, 1.
Scheuer, P. A. G. 1957, *Proc. Camb. Phil. Soc.*, **53**, 764.
Silk, J. 1986, in *Inner Space/Outer Space*, ed. E. W. Kolb, M. S. Turner, K. Olive, D. Seckel, and D. Lindley (Chicago: University of Chicago Press), p. 126.
Silk, J., and Vittorio, N. 1987, *Ap. J.*, **317**, 564.
Silk, J., and Wilson, M. L. 1980, *Phys. Scripta*, **21**, 708.
Starobinsky, A. A. 1982, *Phys. Letters*, **117B**, 175.
Stebbins, A. 1988, *Ap. J.*, **327**, 584.
Steidel, C. C., and Sargent, W. L. W. 1987, *Ap. J.* (*Letters*), **318**, L11.
Sunyaev, R. A. 1977, *Pis'ma Astr. Zh.*, **3**, 491.
———. 1978, *Soviet Astr. Letters*, **3**, 268.
Sunyaev, R. A., and Zel'dovich, Ya. B. 1972, *Astr. Ap.*, **20**, 189.
Uson, J. M., and Wilkinson, D. T. 1984*a*, *Ap. J.* (*Letters*), **277**, L1.
———. 1984*b*, *Ap. J.*, **283**, 471.
———. 1984*c*, *Nature*, **312**, 427.
Vishniac, E. T. 1987, *Ap. J.*, **322**, 597.
Vishniac, E. T., and Ostriker, J. P. 1985, in *Proc. 3d Rome Meeting on Astrophysics, The Cosmic Background Radiation and Fundamental Physics*, ed. F. Melchiorri (Bologna: Italian Physical Society), p. 137.
Vittorio, N., and Silk, J. 1984, *Ap. J.* (*Letters*), **285**, L39.
White, S. D. M., and Rees, M. J. 1978, *M.N.R.A.S.*, **183**, 341.
Wilson, M. L. 1983, *Ap. J.*, **273**, 2.
Wilson, M. L., and Silk, 1981, *Ap. J.*, **243**, 14.
Zel'dovich, Ya. B. 1967, *Soviet Phys. Usp.*, **9**, 602.
———. 1972, *M.N.R.A.S.*, **160**, 1P.
———. 1980, *M.N.R.A.S.*, **192**, 663.

H. E. Hardebeck, C. R. Lawrence, S. T. Myers, A. C. S. Readhead, and W. L. W. Sargent: California Institute of Technology, Mail Code 105-24, Pasadena, CA 91125

A. T. Moffet: Deceased

CHAPTER 4
The RING Experiment

4–1 Overview

The object of the microwave background program at Owens Valley is to detect and characterize spatial fluctuations in the temperature of the cosmic background radiation. Because the patterns we are searching for are expected to be the result of a Gaussian random process in a linear phase of evolution, the standard approach is to tune the parameters of the experiment to maximize sensitivity for a Gaussian random field. However, especially in light of the failure to confirm the predictions of the simplest galaxy formation scenarios, it is important to explore the possibility that non-Gaussian processes are involved either at the time of the generation of the density fluctuations at inflation or at the time of decoupling of matter and radiation. While in the case of a Gaussian random field the sufficient statistic is the two-point correlation function (or autocorrelation function) of the two-dimensional temperature field on the sky, the non-Gaussian case has no such guaranteed sufficient statistic; the results of an observation must be compared on a case-by-case basis with specific models. To this end, an experiment should cover a large fraction of the sky compared to the resolution of the telescope with the aim of both providing sufficient information for statistical tests and searching for 'rare' large fluctuations that can arise in scenarios such as cosmic strings and decaying particles. However, as one increases the area covered, the time spent on any given field must decrease and sensitivity is lost. The details of this calculation are presented in § 2–4. Specifically, for Gaussian and nearly Gaussian statistics, on the order of 14–25 fields should be observed (for 95%–99.87% HPD limits); more than this results in using large numbers of degrees of freedom to probe below the uncertainty level in any given field and an overall slight loss in sensitivity. Also, the loss in individual field sensitivity may lead to a situation where it is not possible to 'detect' at a significant level any of the data points contributing to a significant anisotropy or variance.

The RING program was designed with the intention of extending the Owens Valley observing program to cover a significantly larger area of the sky providing increased sensitivity to non-Gaussian fluctuation models and allowing distribution oriented statistical analyses while not dividing the integration time between too many fields and degrading the overall sensitivity to more standard Gaussian perturbation models. The number of target fields finally chosen was 96, thus providing an order of magnitude increase in the area coverage over the previous programs yet allowing us to reach the level 5×10^{-5} in approximately 100 hours of integration time. The locations of the 96 fields were chosen such that they form a uniform ring around the north celestial pole with a spacing of 15^{m} in right ascension equivalent to the $7'.15$ separation between beams on the switched receiver (Figure 4–1). Field i has celestial coordinates Right Ascension (α) and Declination (δ) given by

$$\alpha = (i - 1)\ 15^{\mathrm{m}} \qquad \delta = 88^\circ\ 10'\ 42''$$

in mean coordinates of epoch 1987. This arrangement has the feature that the reference beams in the double switching pattern for one field are the in the main beams for adjacent fields. With this scheme, real sources will show up with a characteristic minus-plus-minus pattern in consecutive fields. In addition, the overall sum of field levels should be nearly zero, giving an added check on systematic errors. Because the fields are located on a circle of constant declination while the switching is done in azimuth, the true position of the reference beams is $0'.24$ south of the adjacent field centers. As this is a small fraction of a beam width, the RING interlock error will have little effect on sources near the center of the beams and extended sources, but poses potential problems for point sources outside the half power response level.

4–2 Observations and Editing

2.1 Experimental setup and observing

As in the previous work presented as Chapter 3 (Paper 1, hereafter denoted as the NCP experiment), the 40-meter radio telescope at the Owens Valley Radio Observatory (OVRO) was used with the K-Band maser receiver at an observing frequency of 20 GHz. The observing mode was similar to that used in the NCP experiment, and the reader is referred to Chapter 3 for the details of the antenna, receiver, and switching schemes. We now describe the features unique or particularly important to the RING.

To minimize telescope movement and thus differential ground spillover, each field was observed for only 12 minutes centered at transit on any given day. Slightly less than one-half of the total solid angle of the antenna reception pattern is in the main and reference beams, leaving us with a significant sidelobe contribution from the 300 K ground (about 11 K of system temperature as measured in December 1988). This level of ground spillover varies with the zenith angle of the telescope, increasing as the instrument is pointed closer to the horizon. The FLUX measurements were taken in a double switching pattern with Dicke switching between the horns at 10 Hz followed by moving of the antenna on the sky by the beam separation. The second switching was performed in the standard off-on-on-off pattern with a single FLUX measurement completed in a total cycle time of 40 seconds, a rate twice as fast as that used previously. This change was made to obtain a reasonable number of samples during a single 12 minute scan to define noise statistics. As before, noise was injected in the main beam side of the signal path to compensate for a slight imbalance in the noise levels in the two arms; the amplitude was periodically adjusted to produce equal power output at the radiometer in the two channels. During the observations reported here, the magnitude of the added noise was nearly 5 K, or 19% of the large calibration diode used as the injection source. This level varies diurnally by 0.1–0.4 K, and is a possible source of systematic error. As shown in Chapter 3–2, the effect should be negligible as diurnal signals are reduced by a factor of $\sim 4 \times 10^6$ by the switching, leaving a maximum effect of only 0.1 μK.

The observing schedule was set up so that a cycle consists of a nearby pointing and calibration source (1637+826) followed by three RING fields. Every hour, a pointing scan on the calibrator was substituted for one of the RING field observations, and each day a different field was replaced. Thus, in four days, each of the RING fields would be observed three times. A scan on a field began with integrations of the output from the total power and Dicke-switched outputs (for later diagnostics on the level of the signals) and a record of the wind speed. A 40 second off-on-on-off measurement of the LCAL was made, followed by a series of FLUX measurements. The scan was aborted 6 minutes after transit and the observations on the next field (or calibrator) begun.

2.2 Calibration

There are several quantities that need to be measured to ensure proper calibration of the data. These are the equivalent temperatures of the noise diodes, the aperture and beam efficiencies, the system temperatures of the various components of the receiver, and the gain of the telescope as a function of zenith angle. Because the system gain was monitored using the small calibration diode (LCAL) and the temperature scale from hot and cold absorbers was referenced to the large noise source (HCAL), the ratio of large to small diodes was monitored frequently. Also, the flux densities of a set of reference radio sources relative to the CAL sources were measured regularly. Finally, the absolute calibration of the system was performed several times using hot and cold absorbing loads. A summary of these calibration results is presented in Table 4–1. For calibration purposes, we split the observations into 3 separate time ranges : 1 December 1986–23 April 1987, 26 November 1988–3 January 1989 (plus calibration sessions during 30 August–1 September and 6–9 October 1988), and the period from 18 January 1989 onward. The division into these intervals was necessitated by the work done on the maser receiver package in 1987–1988 and the installation of a new second stage amplifier and refrigerator overhaul (requiring disassembly of the noise source injection assembly) in January 1989, both of which apparently caused changes in the coupling of the HCAL and LCAL into the waveguides. First, we calculated the equivalent temperature of the HCAL in the 1988–89 and 1989 sessions from hot and cold absorbing load measurements. We will assume that the relative strengths of the HCAL and LCAL remained constant at the level measured in 1989, giving us the temperature of the LCAL. The equivalent flux density of the LCAL was determined in all three sessions using observation of two standard radio sources. From the flux and temperature of the LCAL in 1988–89 and 1989, we find the sensitivity of the system in Jy/K, and thus the aperture efficiency. Finally, using the flux of LCAL in 1986–1987, we deduce the LCAL temperature in the first session. For the propagation of errors, we assume that the quantities in question are constant within the intervals considered and that the scatter among the observed values is due to measurement error, and we propagate errors using the standard deviation in the mean. We have no reason to expect that the fundamental parameters of the system vary during the sessions and the changes between sessions are understood to be the consequence of the engineering changes noted above.

The typical procedure for measurement of the HCAL/LCAL ratio R_{HL} was to set the radiometer gain to a low enough value such that the output of the large noise tube was within the acceptable range of the detector, and then alternate 5 second integrations with the two diodes. We measured the ratio of the HCAL and LCAL noise sources in this manner during the calibration sessions in the 1986–87 season and monitored it regularly throughout the 1988–89 season. The determined values are listed in Table 4–1. It is apparent that the ratio is relatively stable for long periods of time, although the scatter in the measurements (6%) is larger than expected from the individual uncertainties (0.3%). This prompted a careful investigation of the ratio measurement procedure and revision thereof in October 1989. It was found that insufficient time was being allowed for recovery of the radiometer after firing of the HCAL and a 10 second delay was incorporated into the ratio routine. We thus use only the 11 measurements in Table 4–1 from the 16 October 1989 and later to obtain $R_{HL} = 25.33 \pm 0.06$.

The most difficult measurement was the determination of the absolute temperature scale using the hot and cold absorbers. For this calibration, ambient and liquid nitrogen soaked Eccosorb loads were alternately placed over the horns while the telescope was parked in the horizontal service position; it was demonstrated that the loads covered the horn apertures sufficiently to not require the tests to be performed with the antenna pointed closer toward the zenith where the sky and ground contaminations are less. It was also decided after testing that the thin Mylar protective window covering the feed assemblies could be left in place during the calibration procedure without detriment to either the measurement or the integrity of the window. Because the boiling off of the liquid nitrogen on the cold load leads to a gradual increase of temperature as a function of time, a long series of 2-second integrations were performed to allow the measurement of the true liquid nitrogen baseline. The hot and cold load observations were alternated with measurements of the zero-point of the total power, (the voltage output when full attenuation was applied at the input to the radiometer). For the purposes of the system temperature measurement, the Dicke switch was locked in the MAIN position. The hot and cold load measurements were performed with the large calibration diode both on and off. From these observations, the equivalent temperature of the HCAL noise source was then calculated, allowing calibration of the rest of the data, both calibrator and microwave background. The only reliable measurements using this method were obtained during the autumn of 1988 and winter 1989 yielding the figures in Table 4–1. In 1988 the calibration was performed three times giving a weighted mean of $T_{HCAL} = 21.47 \pm 0.43$ K. In 1989 we have the single determination $T_{HCAL} = 26.16 \pm 0.14$ K. Using our value for the R_{HL}, we obtain $T_{LCAL} = 0.848 \pm 0.017$ K and 1.033 ± 0.006 K respectively.

To find the sensitivity of the K-Band system on the 40-meter telescope (in Jy/K), and the T_{LCAL} in the first session, we use the measured flux densities of two standard sources, summarized in Table 4–2. The primary calibrator is DR21, and the secondary NGC7027 and both are nonvariable galactic objects. The flux density of DR21 is derived using the scale near $\lambda = 1$ cm from Klein and Gulkis (1978)

$$S = 26.70 - 5.62 \log \left(\frac{\nu}{1 \text{ GHz}} \right) \text{ Jy} \tag{4.1}$$

with an estimated error of 3% (1σ) giving us a value of 19.4 ± 0.6 at 20 GHz. The flux density of NGC7027 is given as 5.9 ± 1.3 Jy (Baars *et al.* 1977) but we choose to refer directly to DR21. We have measured both NGC7027 and DR21 on five occasions, giving the ratios listed in Table 4–1. We obtain NGC7027/DR21 $= 0.315 \pm 0.004$

giving 6.11 ± 0.20 Jy for the flux density of NGC7027, in agreement with the Baars *et al.* value. The primary reason that NGC7027 was included as a calibrator is that no adjustment of the radiometer gain is required to prevent saturation of the A/D converters, unlike DR21. From the error bars on the two values, we estimate a 3% overall uncertainty in the flux density scale.

The gain of the 40-meter antenna as a function of zenith angle was determined by tracking a bright radio source such as DR21 or 3C84 over a large range of zenith angles and performing FLUX and CAL cycles. A polynomial was then fitted to the flux versus zenith angle and normalized to unity at the peak. This procedure was performed at least once each season, usually near the calibration period. The gain information was then used to correct FLUX measurements of a set of standard radio sources to establish the flux of the HCAL and LCAL diodes. The parameters used in fitting are listed in Table 4–3. The polynomial as a function of zenith angle θ_{ZA} is given by

$$g(z) = c_0 + c_1 \cdot \theta_{ZA} + c_2 \cdot \theta_{ZA}^2 + \dots \tag{4.2}$$

Also listed is the zenith angle at peak gain. These gain curves were applied to the standard source observations when deriving the values listed in Table 4–2.

For the period November 1986 until April 1987, we use the calibration information from December 1, 1986 on NGC7027. From this we derive the value

$$S_{LCAL} = 7.29 \pm 0.10 \text{ Jy}.$$

There were other monitoring runs during this period but their results were not included due to problems with weather and equipment. The error bar on the one measurement has been determined from the scatter among measurements in the 1989 session, as the uncertainties estimated from the individual points making up the measurement appear woefully inadequate (there are significant systematic effects at the several percent level such as pointing). During the 1988–1989 session, from August 1988 to January 1989, we obtain $S_{LCAL} = 6.72 \pm 0.12$ Jy. Finally, for the session 18 January–17 March 1989, the value $S_{LCAL} = 8.26 \pm 0.09$ Jy is derived. These numbers were arrived at by compiling the mean value of LCAL flux for each day and then the unweighted mean and error in mean for those in each session. The figures in Table 4–2 are corrected for atmospheric absorption. We calculate the transfer of the thermodynamic sky temperature

$$J(T) = \frac{(h\nu/k)}{\exp(h\nu/kT) - 1} \tag{4.3}$$

through the mean atmosphere (*e.g.*, Ulich *et al.* 1980). As a function of 'airmass' $A = \sec(\theta_{ZA})$

$$J(T_{sky}) = J(T_{atm})\,(1 - e^{-\tau A}) + J(T_{3K})\, e^{-\tau A}. \tag{4.4}$$

In the Rayleigh-Jeans region where we work, $J(T) \approx T$ and for $\tau \ll 1$

$$T_{sky} \approx T_{3K} + \tau A \cdot (T_{atm} - T_{3K}). \tag{4.5}$$

By performing a tip curve, we can measure the antenna temperature as a function of airmass A, the slope of which should give us τT. If we assume T_{atm} = 298 K and use a typical slope of 10 ± 3 K/A, we find τ = 0.034 ± 0.010. Since the gain curves are normalized to their maximum, which occurs at around a zenith angle of 39° (A = 1.29), we find an attenuation factor for the microwave background signal T_{3K} and the flux of point sources of $e^{\tau A} = 1.045 \pm 0.013$. The uncertainty in the correction factor has not been folded into the errors listed in the table. It represents the variation in atmospheric water vapor content and should decrease with increasing number of observations.

If we now use the results of the absolute temperature calibration for T_{LCAL} , we find a sensitivity ξ = 7.93 ± 0.21 Jy/K and 8.00 ± 0.10 Jy/K for the 1988–89 and 1989 sessions respectively. We take as our fiducial number the weighted mean 7.99 ± 0.09 Jy/K. Because of the overall 3% uncertainty in the flux density scale, we choose

$$\xi = 7.99 \pm 0.26 \text{ Jy/K}.$$

We can relate this to the physical area A_{phys} of the antenna using the standard formula (see Kraus 1982 for a discussion of radio astronomy fundamentals)

$$S = \frac{2kT}{\eta_a A_{phys}} \tag{4.6}$$

for the equivalent temperature of radiation T from a source of flux density S. For the 40-meter telescope, with a diameter of 130 feet, $A_{phys} = 1.23 \times 10^7$ cm^2 and from ξ and (4.6) we calculate an aperture efficiency of

$$\eta_a = \frac{2.24}{\xi} = 0.280 \pm 0.009$$

consistent with the 0.27 ± 0.01 adopted in Paper 1. We can use the sensitivity ξ along with the derived S_{LCAL} in the first session to calculate the appropriate values for noise diode temperatures. We find $T_{LCAL} = 0.912 \pm 0.016$ K and $T_{HCAL} = 23.10 \pm 0.41$ K. Our final calibrated equivalent temperatures along with important system parameters are summarized in Table 4–4.

2.3 Data

The observations were carried out beginning in November 1986 and completed in March 1989. With the exception of November 1987 to May 1988, which was completely lost due to equipment malfunction, a total of 173 days on the telescope were used to obtain 554 hours of integration time. The data were edited based on weather, telescope performance monitoring, and noise analysis to produce a final data set consisting of 49898 FLUX measurements in 4195 12 minute scans or an average of 44 scans per field. This leaves us a total of 554.4 hours out of the original 173 days for an efficiency of 13%. A breakdown of actual telescope and final integration times is presented in Table 4–5. We find that 48% of the final data originated in the last season from January to March 1989 during which the efficiency was 18%; the excellent weather and system operation during this time, on a par with that during the first season in December 1986, was a welcome respite from the bleak performance in the previous three seasons.

In the spring of 1987, it was noticed that the Backward Wave Oscillator (BWO), the source of pumping radiation for the maser, was losing efficiency and sporadic interference spikes were seen in the chart record. This effect worsened in the beginning of the 1987–88 winter season and in January of 1988 the BWO was replaced. The interference remained and was eventually traced to a failure in the delay-line voltage modulator, which at that time was mounted at the focus cage of the 40-meter in a position exposed to the elements; this problem was corrected in May 1988. Unfortunately, the whole of the 1987–88 season was lost. After extensive system checkout prior to the 1988–89 observations, it was discovered that the maser gain was only 21 db instead of the nominal 30 db figure. It was then decided that system temperatures could be improved by nearly 10 K by installation of a low-noise second stage and this was effected in December 1988. After repeated cryogenic failures in late 1988 and early 1989, the refrigerator was replaced in January. The system then performed admirably until the completion of observations in March 1989. It was during these two repair intervals that the discontinuities in calibration occurred as detailed in the previous section.

The application of the calibration (by dividing the data by measurements of the LCAL and scaling by the appropriate equivalent temperature) and calculation of the parallactic angle of the FLUX measurements were done using the FORTRAN program SUMMARY. This routine also calculated the scan statistics for later use in the editing stage. The output data file from this program (.SUM file) consists of a series of records, one for each FLUX measurement of a RING field, tagged with the date and time of observation, the scan to which it belongs, calibrated flux value and error, and the parallactic angle of the observation. This data can then be passed to any of various programs that bin by time of day, parallactic angle, or do distribution tests, and to the next stage of the reduction.

At this point we would like to elaborate on the various definitions of noise. The maser receiver itself, the associated electronics, the waveguides and feed horns, the column of atmosphere in the view of the antenna, stray radiation from the ground, and the cosmic microwave background itself introduce signal that is measured by our system. Although the origin of much of this is thermal in nature anyway, we can in any event equate the power detected from these sources to the power received from a fictitious thermal bath at some temperature T_{sys} in which the entire antenna is immersed. The equivalent temperature T_{sys} of the excess noise power we denote as *system temperature*. If this were the only signal or we were to observe an unvarying celestial object, then the noise characteristics would be thermal (white) and the relation for our double switching becomes[1]

$$\sigma = \frac{4T_{sys}}{\sqrt{\tau \Delta \nu}}. \tag{4.7}$$

This could then be used to measure T_{sys} from the variance σ^2 in integrations of length τ of the detector output. However, the power received from the atmosphere varies with time and position in the sky, and this also causes the detected output to vary. The atmospheric noise (as well as receiver gain variations) do not have a white noise spectrum, but if enough samples are taken over a long enough time period, then the statistics are Gaussian with a definable variance that can again be equated to a *noise temperature* T_{noise} through our above relation. Note that this $T_{noise} > T_{sys}$, as it includes the thermal contribution, but (especially in the case of the spatial fluctuations) the level is not equivalent. Consider, for example, a screen of 1 mK *rms* variations on top of 15 K of smooth atmosphere and background. Inversion of our equation would tell us that we have an increased T_{noise} over T_{sys} of

$$\Delta T_{noise} = 0.001 \text{ K } \times \frac{\sqrt{\tau \Delta \nu}}{4} \tag{4.8}$$

which can be substantially larger than the static 15 K component. For our OVRO system running the RING program, $\Delta\nu = 400$ MHz, $\tau = 40$s, and $\Delta T_{noise} = 31.6$ K or equivalently the 15 K of atmosphere contributes only 0.47 mK to the *rms* of the 40s integrations. In this example, fluctuations that are 7×10^{-5} of the smooth background cause more than twice the variation in the measurements than the water vapor column itself. This is the crucial distinction to be made between T_{sys} and T_{noise}. The exact contribution of the atmospheric inhomogeneity to the scatter in our observations depends upon the filtering afforded by the switching (see Chapter 2–3), or more specifically, the amplitude and scale of the fluctuations in the 'screen' that the telescope sees depends upon the filtering of the true distribution of irregularity by the beam and switching procedure.

---

[1] The factor 4 is due to the Dicke switching and second differencing effectively reducing the integration time on a single patch of sky to $\tau/4$ and including only 1/4 the number of samples in the average. Another way to think of this is that for every difference there is a factor of 2 correction so that a source in one beam enters with unity gain.

The data set was first edited by removing the points from periods when conditions were known to be unfavorable such as excessive clouds, high winds, ice on the dish surface, and equipment malfunction. Second, individual FLUX measurements were excised if the associated error was larger than 2.66 mK, a cutoff corresponding to $T_{noise} > 84$ K, twice an assumed system temperature of 42 K. Next, a T_{noise} was calculated for two hour blocks of data, typically involving 6 different fields but providing a sufficient number of samples to define a variance, and the data in this period was noted as suspect if the noise temperature thus inferred was higher than 84 K. The interfield variations (approximately 0.3 mK peak, 0.1 mK *rms*) should not significantly bias the flagging process, being a small fraction of the 2.66 mK cutoff noise level, but in any event we have adopted a procedure (see below) to safeguard against this.

With reference to Table 4–5, the 'final' 554 hours refer to data that has passed all the tests above. A breakdown of the figures is given in Table 4–6. The resulting efficiency of 13% is the same as that in the NCP experiment, even though slightly different rejection criteria were used. The automatic editing procedure used in the NCP survey was not implemented during reduction of the RING because the small number of FLUX measurements ($\sim$ 10) comprising a typical scan is insufficient to define a mean and standard deviation for reliable rejection. This is in contrast to the previous observations where the $\sim$ 60 data points per scan provided ample statistics for identification of bad measurements. In addition to the editing of compromised data, measurements taken more than 6.6 minutes from transit (parallactic angles of greater than $1^\circ.65$) were also removed. These are FLUXes taken when the field in question was observed directly following the pointing calibrator, which in general takes less than the allotted 15 minutes, and are not included in the interest of maintaining as much symmetry and consistency in the experiment as possible. At this stage we are left with 43977 FLUX points (488.6 hours integration, 5.1 per field) bringing our efficiency to 12%.

If a two hour block was deemed suspect under the criteria outlined above, the individual scans comprising the time in question were examined and those with internal standard deviations greater than 2.66 mK were checked. If this increased noise was due to a single FLUX measurement with a value more than 3.98 mK (equivalent to 3 times the 42 K system) away from the scan mean then the offending point was removed. If more than a single FLUX was suspect, then the entire scan was discarded. This is one of only two points in the selection procedure where points were rejected based on the deviation from a mean value. Use of a sample mean (in this case the average for the scan) ensures that no bias toward a particular value is generated while the removal of only single measurements or entire scans prevents improper 'weeding' out of measurements on the Gaussian noise tail and underestimation of the noise level. If none of the constituent scans had abnormal noise levels, then all data were left in under the assumption that the scatter was due to the differences between the mean values of the scans. If more than a couple of scans in a questionable two hour block had large errors, then all scans in that block were thrown out. There was an amount of subjectivity in deciding whether to discard single scans, the entire block, or to leave the data in the set, but great care was taken to avoid the introduction of bias in the data through the editing process. The use of the internal scatter as the primary standard for rejection and minimization of the use of mean values was chosen to further this end, and we believe we have succeeded in producing a reliable body of measurements.

There are various tests we can perform to assess data quality and robustness of the set as a whole. Monitoring of the equivalent noise and variance of the individual FLUXes, scans, two hour blocks, and the data that comprise the field measurements provides us information on both possible problems in the system but also important knowledge about the effect of the noise contribution from the receiver and atmosphere. The results from this exercise for the RING data are summarized in Table 4–7. We find a 0.80 mK increase in the *rms* noise from timescales of 40 seconds to 12 minutes, and a further increase of 0.05 mK from 12 minutes to the entire dataset. Since the noise is dominated by emission from the atmosphere, water vapor to be specific, and we estimate the path length at the elevation of the north celestial pole to be 13–16 K (a 8–10 K/airmass column at 1.6 airmasses), our switching is filtering the offending noise at a level of 6×10^{-5}. We find our 0.85 mK equivalent to $\Delta T_{noise} = 27$ K , and in fact the dynamic component due to the spatial structure in the water vapor distribution being resolved by the differential horns adds noise at almost the level from the static component. Of course, this same amplification of 3.1×10^4 works in our favor when we look at the spatial fluctuations in the microwave background, while the atmospheric structures will average out as long as they do not persist on timescales of days. Indeed, the fact that the noise level ceases to increase for intervals longer than 2 hours demonstrates that things stabilize by this time. If coherent atmospheric patterns remain on longer timescales, then they should manifest themselves in the form of a bias in the mean level of the RING field fluxes, which are each tracked across the same small region of the sky. Fluctuations intrinsic to the celestial sphere should average to zero on account of the nearly interlocked main and reference beam geometry adopted for this experiment, and any significant residual could be attributed to long-term cloud patterns or other systematic problems.

The 43977 FLUXes are plotted in histogram form in Figure 4–2 along with the best-fit Gaussian ($\sigma = 2.45$ mK) distribution function to the unweighted (but temperature corrected, see below) data. Using the Kolmogorov-Smirnov (KS) test (also see below), we find a probability of 61% for a $D = 3.6 \times 10^{-3}$ or worse. This degree of fit is not surprising given the large number of points; the central limit theorem certainly applies in this case. We merely note that there is no indication of systematic or non-Gaussian behavior in the noise characteristics of the system when the data is considered as a whole. If we bin the data into two hour intervals in Pacific Standard Time (PST) of observation, shown in Figure 4–3(a), we also find no discernable deviation from the expected behavior, obtaining a chi-squared of 8.8 for 11 degrees of freedom in the 12 two hour bins. Note that since the observing season lasts from November until April, any given field is observed over nearly 12 hours in PST (field NPR0000 covers the range 10:00–22:00 PST), and each PST bin fairly samples half of the fields. Also shown in Figure 4–3(b) is the scatter among the FLUX measurements in the PST bins, with no significant trend seen.

To obtain the final value for each field, the mean and uncertainty of the FLUXes in a given field were computed using weights given by the FLUX errors ϵ_i. For field

k, with FLUXes $\{x_i^k, \epsilon_i^k\}, i = 1, \ldots, n_k$:

$$T_k = \frac{1}{W_k} \sum_{i=1}^{n_k} \frac{x_i^k}{(\epsilon_i^k)^2} \tag{4.9}$$

$$\sigma_k^2 = \frac{n_k}{n_k - 1} \cdot \frac{1}{W_k} \sum_{i=1}^{n_k} \frac{(x_i^k - T_k)^2}{(\epsilon_i^k)^2} \tag{4.10}$$

$$\epsilon_k^2 = \frac{1}{n_k} \sigma_k^2 \tag{4.11}$$

$$W_k = \sum_{i=1}^{n_k} \frac{1}{(\epsilon_i^k)^2} \tag{4.12}$$

The choice of the FLUX error as a weighting parameter was occasioned by the fact that the preferred statistic, the scan variance, which we have shown is a much better estimate on average of the increase in T_{noise} due to the water vapor structures in the atmosphere, is not sufficiently determined with only 7 FLUXes within the acceptable parallactic angle range. For a set of n measurements, the variance about the mean itself has a variance

$$\sigma_{\sigma^2}^2 = \frac{2}{n-1} \tag{4.13}$$

leading to an estimated error of 58% in the weighting factor for 7 points. Though an underestimate of the true noise level, the FLUX error should be relatively stable, being made up of 80 half-second integrations, and is an acceptable estimate of T_{sys} and rapid fluctuations in the atmosphere. It is also desirable to remove the FLUX measurements that lie on the tail of the distribution (Figure 4–2); we test against the mean for the field (k) and reject a point x_i^k if

$$|x_i^k - T_k| \geq q\sigma_k$$

for cutoff parameter q. This is the second and last time where the mean value is used as a criterion for acceptance of data, and is justified by the desire to remove grossly discrepant measurements (perhaps due to interference). In fact, examination of Figure 4–2 shows that the tail is well behaved and no problems or systematic bias should arise from the inclusion of this step. In practice, we will adopt the conservative value $q = 4$, and we find that only a very small number of FLUXes are excluded during this stage.

Before analysis, the temperature scale of the data has been corrected for atmospheric absorption, beam efficiency, and blackbody function. The attenuation factor (1.045 ± 0.013) was derived in the previous section for the flux density calibration, and also applies here. We also need to correct for the fact that only the main beam is considered when measuring antenna temperatures, while one receives radiation from sky and ground through the sidelobes. Let Ω_{MB} be the main beam solid angle and Ω_B the total beam solid angle. The beam efficiency is defined as

$$\eta_B \equiv \frac{\Omega_{MB}}{\Omega_B} \tag{4.14}$$

and in practice measured by observations of the antenna temperature T_a of planets such as Venus, Mars, and Jupiter with known brightness temperatures T_b and sizes Ω_S and noting that

$$T_a = \frac{\Omega_S}{\Omega_B}\, T_b = \frac{\Omega_S}{\Omega_{MB}}\, \eta_B\, T_b. \tag{4.15}$$

The main beam angle Ω_{MB} can be measured from observations of strong radio sources; for the OVRO 40-meter at 20 GHz we find $\Omega_{MB} = 3.2 \pm 0.1 \times 10^{-7}$ sr and $\eta_B = 0.47 \pm 0.02$ (Paper 1). We assume the sidelobes $\Omega_B - \Omega_{MB}$ see only some constant combination of background and ground T_{junk}. Then for our *main* beam response $B(\Omega)$ to an on-sky temperature field $T(\Omega)$ we measure the convolution

$$T_a = \eta_B\, T(\Omega) \star B(\Omega) + (1 - \eta_B)\, T_{junk} \tag{4.16}$$

of which the second term on the right-hand side contributes to the static T_{sys} and is removed in the differencing. Another correction factor arises from the actual differencing scheme used in the RING observations. An individual FLUX measurement is actually made up of $4N$ 0.5 second integrations y_j

$$x_{flux} = -\frac{1}{N}\sum_{j=1}^{N} y_j^{(off1)} + \frac{1}{N}\sum_{j=1}^{N} y_j^{(on1)} + \frac{1}{N}\sum_{j=1}^{N} y_j^{(on2)} - \frac{1}{N}\sum_{j=1}^{N} y_j^{(off2)} \tag{4.17}$$

where the *off* integrations are the difference between the main horn pointed at reference field R1 and the reference horn at MAIN and the *on* integrations are the difference between the main horn pointed at field MAIN and the reference horn at R2 (see Figure 3 in Paper 1). This arrangement is used so that if the receiver were used in non-switching mode we would recover $y^{(on)} - y^{(off)}$. However, because of the Dicke switching, the main field enters twice and we actually measure after calibration

$$x_{flux} = 2T(MAIN) - T(R1) - T(R2) \tag{4.18}$$

which is precisely twice the quantity that we wish to measure. This is purely a matter of convention as we wish to define our measured quantity such that a temperature fluctuation filling the main beam in the main field enters with a coefficient of unity.

Finally, we correct for the Rayleigh-Jeans approximation to the blackbody function $J(T)$, or more correctly, the difference between our temperature scale referenced to thermal loads at 72 K and 298 K and the difference in power received, and fluctuations in the temperature of the cosmic background. It is true that this is a small and ultimately insignificant correction factor but it is still useful, if only philosophically, to make a clear distinction in temperature definitions. We first note the power emitted by a blackbody at physical temperature T_{phys}

$$P(T_{phys}) = k\,\Delta\nu\,T_{phys}\,j(T_{phys}) \tag{4.19}$$

with (see 4.3)

$$j(T) = \frac{J(T)}{T} = \frac{(h\nu/kT)}{\exp(h\nu/kT) - 1}. \tag{4.20}$$

When we calibrate the power from the HCAL diode against the power from hot and cold eccosorb loads, we derive an equivalent temperature

$$T_{HCAL} = \frac{P_{HCAL}}{P_{hot} - P_{cold}}\,(T_{hot} - T_{cold}). \tag{4.21}$$

For $T_{hot} = 298$ K and $T_{cold} = 78$ K, we find a negligible effect from (4.21) using (4.19,4.20)

$$k\,\Delta\nu\,T_{HCAL} - P_{HCAL} \simeq 3 \times 10^{-6}. \tag{4.22}$$

Now, when we measure the fluctuations in the microwave background, we relate differences in received power to fluctuations in temperature of the cosmic background. For example, our FLUX procedure (after correcting for the effects discussed above) is equivalent to measuring

$$\Delta t = \frac{P_{on} - P_{off}}{P_{HCAL}}\,T_{HCAL} \tag{4.23}$$

with for small temperature deviations ΔT

$$\begin{aligned} P_{on} &= P(T_{mwb}+\Delta T) \approx P(T_{mwb}) + \Delta T \cdot \left.\frac{dP}{dT}\right|_{T_{mwb}} \\ P_{off} &= P(T_{mwb}). \end{aligned} \tag{4.24}$$

Thus, we have

$$\begin{aligned} \Delta t &\approx \Delta T \frac{T_{HCAL}}{P_{HCAL}} \cdot \left.\frac{dP}{dT}\right|_{T_{mwb}} \\ &= \Delta T \, \frac{k\,\Delta\nu\, T_{HCAL}}{P_{HCAL}} \, \exp(h\nu/kT_{mwb})\, j^2(T_{mwb}) \\ &\simeq \Delta T \, \exp(h\nu/kT_{mwb})\, j^2(T_{mwb}) \\ &= 0.9901\ \Delta T \end{aligned} \tag{4.25}$$

for $T_{mwb} = 2.74$ K at $\nu = 20$ GHz. Our correction factor is then

$$\frac{\Delta T}{\Delta t} = 1.010.$$

We combine all of the correction factors detailed above into a single multiplicative factor applied to the FLUX measurements (after division by the LCAL voltage and multiplication by T_{LCAL} from Table 4–4)

$$\kappa = \frac{1.010 e^{\tau A}}{2\eta_B} = 1.12.$$

4–3 Results

The entire data set of 49898 FLUXes was collated into the 96 fields and analyzed using the FORTRAN program FIELDS. At this point, 10 FLUXes with errors greater than 2.98 mK (after correction to MWB temperature) were discarded. Of the remainder, 43977 lie within the parallactic angle range $\pm 1^\circ.65$. The distribution with parallactic angle is shown in Figure 4–4 in histogram form, with 0.1° bins corresponding to the resolution of the PA calculation used in the analysis. We see that the distribution is uniform out to 1.6° (hence our choice of acceptance range), and there is a surplus of points at negative angles due to the early acquisition of the RING fields following observation of the pointing calibrator. Note that parallactic angles are computed at the midpoint of the FLUX measurement and last about 50 seconds or 0.2 degrees in

PA, with some small variation in dead time, giving us the discrete peaks in Figure 4–4. Finally, 6 more FLUX points were rejected as having values more than $4 \times \sigma_k$ away from T_k, leaving us with 43971 FLUXes in 4195 scans.

We have first broken the results down by the epoch of observation in Table 4–8. The values of $\overline{T} \pm \sigma_{\overline{T}}$ were computed for the n_{tot} FLUX measurements within individual data intervals using the method detailed below. The maximum likelihood estimator for the excess standard deviation $\hat{\theta}$ was also calculated in the manner also described subsequently. We find no *strong* evidence for aberrant sections of data, although the deviation of some means from zero is uncomfortably larger, especially the 3.5σ excursion of the 1987 value. This behavior is reminiscent of that exhibited in December 1985 during the NCP observations. The fact that the mean for the entire dataset is consistent with zero leads us to conclude that any postulated bias mechanism may operate over timescales of several months but must average to zero over our $3\frac{1}{2}$ year baseline. Therefore, we will consider the behavior of the 1987 average to be somewhat alarming, but not ultimately damaging to our final results (only 17% of the data originate from the 1987 season). The possibility of a long period tail to the noise spectrum (presumably atmospheric) will be noted and provide a cautionary remark upon our presumed knowledge of the noise statistics.

The results for the 96 fields are plotted in Figure 4–5 and tabulated in Table 4–9. The first thing to note is that there are no detections above the 4.1σ level. The second is that those fields that show significant signal are flanked by fields with means of the opposite sign, as expected for real signals with our switching scheme. If we form the weighted mean of the 96 fields in a manner similar to that used to calculate the field values (4.9–4.12),

$$\overline{T} = \frac{1}{W} \sum_{k=1}^{96} \frac{T_k}{\epsilon_k^2} \tag{4.26}$$

$$\sigma_{\overline{T}}^2 = \frac{1}{W} \tag{4.27}$$

$$\sigma_{tot}^2 = \frac{96}{95W} \sum_{k=1}^{96} \frac{(T_k - \overline{T})^2}{\epsilon_k^2} \tag{4.28}$$

$$W = \sum_{k=1}^{96} \frac{1}{\epsilon_k^2} \tag{4.29}$$

$$\overline{\epsilon}_{fld} = \frac{1}{96}\sum_{k=1}^{96}\epsilon_k \tag{4.30}$$

we obtain the values

$$\begin{aligned}\overline{T} &= -6 \pm 12\ \mu\mathrm{K}\\ \sigma_{tot} &= 175\ \mu\mathrm{K}\\ \overline{\epsilon}_{fld} &= 113 \quad (\sigma_\epsilon = 8\ \mu\mathrm{K}).\end{aligned}$$

There is an excess variance in field means above that expected from the uncertainties shown by the error bars; it is easily shown by taking the expectation values of (4.26–4.30) that

$$\begin{aligned}\sigma_{sky}^2 &\simeq \sigma_{tot}^2 - \frac{1}{W}\\ \sigma_{sky} &= 134\ \mu\mathrm{K}\end{aligned} \tag{4.31}$$

neglecting the correlations between the measurements.

We can use the Bayesian formalism of Chapter 2 to place limits on the magnitude of the excess signal in the measurements, neglecting for the time being the correlation properties of any assumed random field or the actual correlations between the interlocked RING fields themselves. If σ_{sky}^2 is the contribution to the variance from sources not attributable to the measurement errors, then the likelihood function for the parameter σ_{sky} with the distribution mean $\mu = 0$ is

$$L(\sigma_{sky}) = \prod_{i=1}^{96} \frac{1}{\sqrt{2\pi(\epsilon_k^2 + \sigma_{sky}^2)}}\ \exp\left[-\frac{T_k^2}{2(\epsilon_k^2 + \sigma_{sky}^2)}\right] \tag{4.32}$$

obtained from (2.56) with diagonal correlation matrix

$$A_{ii} = \frac{1}{\epsilon_i^2 + \sigma_{sky}^2}. \tag{4.33}$$

The likelihood function is plotted in Figure 4-6. The value of σ_{sky} at the maximum likelihood is denoted $\hat{\sigma}_{sky}$, the MLM estimator of the signal *rms*. The width of the likelihood function is very narrow

$$\sigma_{\hat{\theta}}^2 \sim \frac{\hat{\theta}}{\sqrt{2 \cdot 96}} \tag{4.34}$$

and because of this we can dispense with worries about the choice of the Bayesian prior over the range in θ for which L contributes. We can integrate this function in the manner described in §2–3 to obtain the desired HPD credible intervals in θ :

$$\begin{array}{ll} 103 < \sigma_{sky} < 168\ \mu\mathrm{K} & (95\%) \\ 85 < \sigma_{sky} < 195\ \mu\mathrm{K} & (99.87\%). \end{array} \qquad \hat{\sigma}_{sky} = 133\ \mu\mathrm{K}$$

These upper limits are significantly higher than those yielded by the NCP program (58 μK, 127 μK) and those expected assuming a null signal (Figure 2–3) of 61 μK and 89 μK. The subtraction of the mean ($\overline{T} = -6\ \mu$K) changes these limits by less than 1 μK and therefore all calculations will be for $\mu = 0$.

We can also test the distribution of RING field values, an option not available with the NCP sample as it lacks a sufficient number of points. If we divide the field means by their associated errors

$$\chi_k = \frac{T_k}{(\epsilon_k^2 + \sigma_{sky}^2)^{1/2}} \tag{4.35}$$

and then construct the cumulative distribution function of the $\{\chi_k\}$ ranked in ascending order

$$S(\chi) = \begin{cases} 0 & \chi < \chi_1 \\ \dfrac{i}{n} & \chi_i \leq \chi < \chi_{i+1} \\ 1 & \chi \geq \chi_n \end{cases} \tag{4.36}$$

which we will compare to the model cumulative distribution function $F(\chi)$. The Kolmogorov-Smirnov (KS) test (see Kendall and Stuart 1979, §30.49–30.55) is a well known nonparametric test of the statistic for a sample of n points

$$D_n = \max_{-\infty<\chi<\infty} |S(\chi) - F(\chi)| \tag{4.37}$$

which measures the maximum deviation of the step-like function S from the theoretical distribution function F. For Gaussian errors and signal, the parent distribution of χ is a normal N(0,1). If we wish to test against the hypothesis of no signal, then we set $\sigma_{sky} = 0$ in (4.35) and compute D. Because of the large number of fields in the sample, the significance of D is easily assessed using the asymptotic formula (Press *et al.* 1986, pp. 472-474)

$$P(> D_n) = Q(n^{1/2} D_n)$$
$$Q(d) = 2 \sum_{j=1}^{\infty} (-1)^{j-1}\, e^{-2j^2 d^2}. \tag{4.38}$$

In Figure 4–7 (a), both S and F are shown for $\sigma_{sky} = 0$, which yields a probability $P(> D) = 0.064$. A histogram of the χ values and the test Gaussian is shown in Figure 4–7(b). If we increase the excess variance to $\sigma_{sky} = 133\ \mu$K, we find a K-S probability of 0.90 with the distribution function shown in Figures 4–7(c) and 4–7(d). The significance of the KS test result of 6.4% against a null signal is lower than one might have expected given the extremely strong rejection of zero by the Likelihood or Bayesian method above, due to the weighting of the standard tests toward the tail of the distribution. Because a parametric test such as the Bayesian HPD method is designed to extract the maximum amount of information available in the data about the parameter under consideration, it is more powerful than a general nonparametric method such as the Kolmogorov-Smirnov test. The failure of the KS test to produce a strong result should, however, warn us that our detection of excess variance is likely to be based on a few large values on the tail of the distribution. We will now inspect the dataset carefully and look for the specific fields containing the signal.

4–4 Matched Filtering and Reconstruction

The prime candidate for the source of excess variance is radio source confusion. The NCP observations detected 1 out of 8 fields with a level around 200μK due to a known radio source, and simple extrapolation would lead us to expect contamination of the RING experiment by around 3–12 such sources. The confirmation of this is contingent upon the results of the VLA survey reported later. Armed with independent information on source confusion, the RING dataset can be edited to produce a 'clean' set of fields to be used in comparison with theoretical models. However, since VLA data is not available at the same frequency and concurrent with the OVRO observations, it can only place limits on this contamination. In any event, it is necessary to identify the specific RING fields in which there are suspected sources, microwave background or otherwise. The interlocked sampling geometry of the RING experiment was chosen so that the reconstruction would be possible on a field by field basis by deconvolution of the switching pattern. The closure of the RING compensates for the loss of the gradient information in the individual double-differences and the mean level remains as the only undetermined parameter. Of course, this means that there is information on the correlation function of the MBR on scales up to the RING diameter, and should be taken into account in our Bayesian analysis of variance. Also it should be remembered that the RING fields do not interlock exactly nor are the beams perfectly symmetric: there is a 14.4″ difference between the circles of azimuth and declination at the adjacent field positions and significant irregularities in the OVRO primary beam below the 20% power level. The import of these nonuniformities will be discussed more fully in Chapter 5 in relation to the point source contribution, but there is no significant effect on the results expected for distributed signal such as the microwave background anisotropy.

The first thing we can do to locate those fields in which there are significant detections is to convolve the RING with the switching pattern (as opposed to deconvolution). This is an application of 'matched filtering', where the filter that produces the highest signal-to-noise for detection is the signal that is being searched for itself (see Robinson 1967 for an obtuse discussion of the principle). The result of this method for the RING is shown in Figure 4–8. We find that our procedure has picked out ten fields with filtered levels above the 3σ level (positive or negative): NPR0415, NPR0700, NPR1015, NPR1130, NPR1345, NPR1700 and the negative fields NPR0645, NPR1145, NPR1715, and NPR1945. We can reasonably associate the negative fields except NPR1945 as the result of positive signal in the adjacent reference beam. Note that only NPR0700 and NPR1015 of the positive and NPR0645 and NPR1145 of the negative are above 3σ in the raw RING data, the increased sensitivity attributed to the matched filtering. These seven fields are the prime candidates for containing real sources, microwave background or otherwise. Our statistical tests may show the presence of anisotropy, but only in these fields is it reasonable to pursue the identification of the source, based on the RING data alone. This important distinction between statistical inference of anisotropy and detection of anisotropy will be stressed as we proceed in our analysis of the experiment. If all seven fields and their adjacent references are removed from the RING, then in the 75 remaining fields we are left with HPD limits and MLM estimate

$$\begin{aligned} 38 < \sigma_{sky} < 125\ \mu\text{K} \quad (95\%) \\ \sigma_{sky} < 146\ \mu\text{K} \quad (99.87\%). \end{aligned} \qquad \hat{\sigma}_{sky} = 83\ \mu\text{K}$$

By removal of these fields, we have eliminated the lower limit at the 3σ level and reduced the MLM amplitude by 38%.

Because we have a (nearly) interlocked ring, it is possible to reconstruct the temperatures of the individual fields from our difference observations to within an arbitrary mean level. We can attempt direct inversion of the equation (2.18)

$$\mathbf{y} = S\ \mathbf{x}$$

where x_j is the true temperature of the sky in beam j, and y_i is the measured temperature for the RING field with pointing center at x_i (neglecting noise), and the sampling matrix

$$S_{ij} = \delta_{ij} - \frac{1}{2}\,\delta_{ij-1} - \frac{1}{2}\,\delta_{ij+1} \tag{4.39}$$

where the indices i and j are taken modulo 96. The matrix S is singular, as any row is the negative of the sum of the other rows; this is just a consequence of the closure of the RING and the insensitivity to a mean level. If we solve subject to the constraint that $\sum x_k = 0$ perhaps by using the modified matrix

$$S'_{ij} = S_{ij} + \lambda\,\delta_{i1} \tag{4.40}$$

obtained by adding our constraint to (4.39), then we get a literal and unique but unacceptable result for $\{x_k\}$, shown in Figure 4–9. The double-differencing FLUX procedure is a second-difference method, and small deviations from zero propagate into large changes in slope as we attempt our inversion. We would like to associate the values that lie within one or two times the error bar of zero with zero, otherwise the cumulative effect of many small curvatures is to give a large scale spurious structure to our literal solution (12 mK peak-to-peak for the RING in Figure 4–9). By inspection of the data we see that the signal is of the same order as the noise in the measurements, and any acceptable reconstruction must supply reliable error estimates as well as a solution for $\mathbf{x}$.

When developing the Bayesian formalism for statistical inference in §2–3, we made a point to indicate the possibility for generalization from probabilities to any positive additive distribution. If we are only considering the contribution from discrete radio sources to our microwave background data, then the intensity of the radio sky containing these sources can be considered to be just such a field. Therefore, our Bayesian statistical procedure, or some modification of it, should provide the 'correct' method for reconstruction of the RING in the presence of noise, with the same caveats expressed during the discussion of said method. These are the justifications for the use of the deconvolution algorithm known as the Maximum Entropy Method (MEM), extensively applied to image processing and data analysis in a variety of applications such as radio astronomical interferometry, medical imaging, and optical 'deblurring' in law enforcement and satellite surveillance (Gull and Skilling 1984). Although the method does not lend itself well to the problem of measurement of positive and negative fluctuations in the cosmic background, we can use it to identify the positive source component in the RING. The program used for the RING reconstruction is that provided by Gull and Skilling in the MEMSYS-3 [1] package, of which the mechanics as well as the theory are explained in Skilling 1989 and Gull 1989. The details of the procedure will not be discussed here, except to note that as the name implies, it seeks to maximise the entropy in the image $\mathbf{x}$, as defined by

$$S(\mathbf{x}) = \sum_{i=1}^{96} [x_i - m_i - x_i \log(x_i/m_i)] \tag{4.41}$$

where $\mathbf{m}$ is a model or default image, subject to any constraints imposed by the measurement procedure. The end result of this is that if a default model that is flat is chosen, then the output image in some sense will be the smoothest image consistent with the noise characteristics and constraints. A by-product of this is that it is entropically advantageous for MEM to reduce source intensities and transfer the flux into the noise estimate; the bias of intensities in this method is well known and in our RING solution where the signal-to-noise ratio is of order unity the underestimation of amplitudes is expected to be significant. The reconstructed RING produced by MEMSYS-3 is shown in Figure 4–10 along with MEM (Bayesian) estimated error

---

[1] S.F. Gull and J. Skilling, Maximum Entropy Data Consultants Ltd., Royston, England.

bars. We find four fields above the 3σ level: NPR0415, NPR0700, NPR1130, and NPR1700. If we delete these fields and their adjacent references from our dataset, and perform our Bayesian HPD analysis as above, then we obtain the HPD credible intervals

$$\begin{aligned} 66 < \sigma_{sky} < 137\ \mu\mathrm{K} \quad (95\%) \\ 41 < \sigma_{sky} < 165\ \mu\mathrm{K} \quad (99.87\%). \end{aligned} \qquad \hat{\sigma}_{sky} = 101\ \mu\mathrm{K}$$

Although the entire signal is not removed, we find that around one-quarter of our signal is due to these fields and the lower limit falls by more than one-third by their removal. For the MEM method to provide reliable reconstruction for high noise and low signal datasets where the image can assume positive and negative values, further development is required, likely involving a reformulation of the entropy-like quantity S.

The reduction phase of our data analysis has now been completed, leaving us with a set of calibrated measurements and estimated error bars. After a series of tests aimed at probing the robustness and quality of the data, we conclude that there is no evidence for systematic error although there is the possibility of a weak non-Gaussian tail to the noise distribution at microKelvin levels. During preliminary analysis of variance, we detect an overall excess standard deviation of 133μK over that expected from the instrumental and atmospheric noise. Matched filtering selects seven fields above the 3σ level as candidates for detection of fluctuations. Four of these fields are identified in the MEM reconstruction at 3σ. After removal of these four and the eight adjacent fields from the RING, we still have a residual excess $\hat{\theta} = 101\mu$K. We now turn to the tasks of identification of the detected sources and a more thorough statistical analysis of the data, with the aim of comparison with theoretical models. In Chapter 5 we study the problem of radio source contamination and present the results of a survey of the RING region. Then, in Chapter 6, we discuss the detailed predictions of current galaxy formation scenarios and methods of statistical inference to compare these models with the RING. This work concludes with a discussion of the implications of our results and speculation upon the future directions in observational and theoretical cosmology.

TABLE 4–1

SUMMARY OF CALIBRATION

Date	HCAL/LCAL	NGC7027/DR21	T_{HCAL} (K)
04 Feb 1987	25.86 ± 0.04		
30 Aug 1988	26.26 ± 0.03		
31 Aug 1988	26.85 ± 0.05		
01 Sep 1988	26.70 ± 0.12	.301	22.3 ± 0.4
06 Oct 1988	24.78 ± 0.05		
07 Oct 1988	26.74 ± 0.04		19.1 ± 0.6
08 Oct 1988		.321	
09 Oct 1988	25.30 ± 0.04		
09 Oct 1988	24.53 ± 0.08		
26 Nov 1988	22.59 ± 0.11		
26 Nov 1988	22.71 ± 0.10		
26 Nov 1988	22.60 ± 0.20		
07 Dec 1988	24.25 ± 0.16		21.5 ± 0.2
07 Dec 1988	24.56 ± 0.10		
19 Jan 1989	24.54 ± 0.06		
21 Jan 1989		.321	
22 Jan 1989		.314	
02 Feb 1989	24.71 ± 0.05		
22 Feb 1989	24.66 ± 0.06		
16 Oct 1989	25.31 ± 0.22		
17 Oct 1989	25.32 ± 0.38		
18 Oct 1989	25.19 ± 0.06		
19 Oct 1989	25.60 ± 0.06		
20 Oct 1989	25.23 ± 0.07		
23 Oct 1989	25.38 ± 0.08		
24 Oct 1989	25.07 ± 0.07		
25 Oct 1989	25.23 ± 0.08		
26 Oct 1989	25.20 ± 0.08		
27 Oct 1989	25.41 ± 0.10		
16 Dec 1989	25.72 ± 0.08	0.320	26.16 ± 0.14

TABLE 4–2

STANDARD SOURCE CALIBRATION OF LCAL

Source ▷	DR21	NGC7027	Mean
Flux (Jy) ▷	19.4 ± 0.6	6.11 ± 0.20	
01 Dec 86[a]		7.29 ± 0.18 (160)	7.29 ± 0.10[†]
01 Sep 88[b]	6.42 ± 0.22 (129)	6.71 ± 0.03 (9)	6.56 ± 0.14
07 Oct 88[b]	6.31 ± 0.15 (23)		6.31 ± 0.03
09 Oct 88[b]	6.91 ± 0.06 (4)		6.91 ± 0.03
26 Nov 88[c]	6.73 ± 0.04 (5)		6.73 ± 0.02
21 Dec 88[c]	7.20 ± 0.36 (98)		7.20 ± 0.04
23 Dec 88[c]	6.64 ± 0.15 (124)		6.64 ± 0.01
Mean ▷	6.70 ± 0.13	6.71 ± 0.01	6.72 ± 0.12
18 Jan 89[d]	8.34 ± 0.13 (59)		8.34 ± 0.02
21 Jan 89[d]	7.93 ± 0.06 (18)	7.78 ± 0.04 (9)	7.86 ± 0.17
22 Jan 89[d]	7.91 ± 0.08 (9)	7.94 ± 0.08 (9)	7.92 ± 0.08
02 Feb 89[d]		8.19 ± 0.11 (9)	8.19 ± 0.04
11 Feb 89[d]		8.00 ± 0.03 (8)	8.00 ± 0.01
14 Feb 89[d]		8.21 ± 0.06 (9)	8.21 ± 0.02
21 Feb 89[d]		8.47 ± 0.05 (9)	8.47 ± 0.02
22 Feb 89[d]		8.78 ± 0.22 (9)	8.78 ± 0.07
03 Mar 89[d]		8.51 ± 0.24 (95)	8.51 ± 0.02
16 Dec 89[d]	8.35 ± 0.11 (22)	8.22 ± 0.05 (24)	8.28 ± 0.07
Mean ▷	8.13 ± 0.12	8.23 ± 0.10	8.26 ± 0.09

[†] Error estimated from 1989 data

[a] Gain curve 01 December 1986

[b] Gain curve 07 October 1988

[c] Gain curve 23 December 1988

[d] Gain curve 03 February 1989

TABLE 4–3

SUMMARY OF GAIN CURVES

Date ▷	01 Dec 1986	07 Oct 1988	23 Dec 1988	22 Feb 1989
θ_{ZA} (max)	40°	34°	39°	36°
c_0	3.27×10^{-1}	4.90×10^{-1}	5.60×10^{-1}	3.58×10^{-1}
c_1	3.33×10^{-2}	1.27×10^{-2}	2.26×10^{-2}	4.02×10^{-2}
c_2	-4.12×10^{-4}	1.24×10^{-3}	-2.90×10^{-4}	-7.44×10^{-4}
c_3		-5.87×10^{-5}		3.38×10^{-6}
c_4		8.63×10^{-7}		
c_5		-4.38×10^{-9}		

TABLE 4–4

SUMMARY OF SYSTEM CALIBRATION

Observing Session			T_{HCAL} (K)	T_{LCAL} (K)
01 December 1986	-	23 April 1987	23.10 ± 0.41	0.912 ± 0.016
30 August 1988	-	3 January 1989	21.47 ± 0.43	0.848 ± 0.017
18 January 1989	-		26.16 ± 0.14	1.033 ± 0.006

Other parameters :

HCAL/LCAL $= 25.33 \pm 0.06$
$\xi = 7.99 \pm 0.26$ Jy/K
$\eta_A = 0.280 \pm 0.009$
$\eta_B = 0.47 \pm 0.02$

TABLE 4–5

BREAKDOWN OF RING OBSERVING TIME

Observing Season	Telescope Time	Useful Time	Final Integration[a]
1986 Dec 8 - 31	24 days	21 days	131 hours
1987 Jan 1 - May 11	40 days	21 days	94 hours
1987 Nov - 1988 May	>100 days	0 days	0 hours
1988 Nov 26 - 1989 Jan 11	47 days	16 days	65 hours
1989 Jan 12 - 1989 Mar 17	62 days	43 days	264 hours
Total[b]	173 days	101 days	554 hours

[a] Integration time after preliminary editing (see text).
[b] Season 1987 Nov - 1988 May not included.

TABLE 4–6

SUMMARY OF RING EDITING

weather, equipment, real-time monitoring	42%
post-observation noise based rejection	45%
outside transit period	2% (15% of remainder)

TABLE 4–7

TIMESCALE OF NOISE

Timescale	σ (mK)	T_{noise} (K)
40^s FLUX point	1.30 ± 0.18	41.1 ± 5.7
12^m scan	2.10 ± 0.52	66.4 ± 16.4
> 2 hour blocks	2.15 ± 0.07	67.8 ± 2.2

TABLE 4–8

RING RESULTS BY EPOCH

Observing Season	$\overline{T} \pm \sigma_{\overline{T}}$ (μK)	$\hat{\theta}$ (μK)	n_{tot}
8 - 29 December 1986	22.0 ± 23.5	174.3	10375
1 January - 22 April 1987	-93.9 ± 26.9	188.4	7441
26 November 1988 - 3 January 1989	-50.9 ± 34.3	270.6	5204
12 January - 17 March 1989	14.9 ± 16.5	148.8	20951

TABLE 4–9

RESULTS OF RING OBSERVATIONS

Field	α (1950)	δ (1950)	T_k (μK)	ϵ_k (μK)	σ_k (mK)	n_k
NPR0000	235812.1	875820.5	4.7	130.0	2.42	349
NPR0015	001140.7	875821.7	91.4	129.3	2.37	336
NPR0030	002509.6	875825.8	240.8	128.1	2.53	389
NPR0045	003839.1	875832.8	-223.8	114.1	2.46	464
NPR0100	005209.3	875842.5	-151.2	120.0	2.35	384
NPR0115	010540.7	875855.0	31.5	125.0	2.39	366
NPR0130	011913.5	875910.3	-103.5	117.3	2.41	422
NPR0145	013247.9	875928.3	16.5	116.3	2.40	425
NPR0200	014624.3	875948.9	148.8	111.6	2.30	425
NPR0215	020002.9	880012.1	-111.8	120.5	2.49	428
NPR0230	021344.0	880037.8	83.1	110.7	2.33	442
NPR0245	022728.0	880105.9	53.7	116.9	2.40	422
NPR0300	024115.0	880136.3	-133.5	115.4	2.39	431
NPR0315	025505.3	880208.9	214.3	129.7	2.55	386
NPR0330	030859.3	880243.7	116.9	117.3	2.46	439
NPR0345	032257.3	880320.4	-138.3	108.3	2.31	457
NPR0400	033659.4	880359.1	-212.9	112.7	2.48	486
NPR0415	035106.0	880439.4	317.6	113.5	2.37	435
NPR0430	040517.3	880521.3	-81.9	111.6	2.47	489
NPR0445	041933.7	880604.7	-88.1	99.4	2.25	514
NPR0500	043355.3	880649.3	-135.1	108.3	2.45	510
NPR0515	044822.4	880735.1	-54.8	114.9	2.40	436
NPR0530	050255.3	880821.8	-126.2	103.5	2.38	529
NPR0545	051734.2	880909.2	-68.3	106.0	2.44	528
NPR0600	053219.3	880957.2	-48.2	106.1	2.47	544
NPR0615	054710.7	881045.5	185.5	109.0	2.37	474
NPR0630	060208.8	881134.0	132.3	116.2	2.54	477
NPR0645	061713.5	881222.5	-339.9	103.9	2.46	559
NPR0700	063225.2	881310.7	439.2	112.6	2.50	494
NPR0715	064743.8	881358.5	-178.3	109.4	2.44	497
NPR0730	070309.4	881445.5	-7.0	102.5	2.45	571
NPR0745	071842.1	881531.7	64.4	96.3	2.42	630

TABLE 4–9 continued

Field	α (1950)	δ (1950)	T_k (μK)	ϵ_k (μK)	σ_k (mK)	n_k
NPR0800	073421.9	881616.7	-71.8	102.0	2.37	538
NPR0815	075008.7	881700.4	-79.2	102.6	2.36	527
NPR0830	080602.4	881742.5	-279.9	108.0	2.45	515
NPR0845	082203.0	881822.9	156.2	100.7	2.40	567
NPR0900	083810.2	881901.2	-37.7	112.0	2.48	492
NPR0915	085423.8	881937.4	144.0	113.9	2.38	435
NPR0930	091043.6	882011.2	-36.9	110.5	2.38	463
NPR0945	092709.1	882042.4	-14.0	105.1	2.46	546
NPR1000	094340.0	882110.9	-24.9	122.9	2.51	418
NPR1015	100015.8	882136.4	374.9	104.4	2.23	456
NPR1030	101656.1	882158.9	-17.0	105.1	2.37	509
NPR1045	103340.3	882218.2	70.1	100.8	2.40	567
NPR1100	105027.9	882234.2	87.0	107.4	2.30	461
NPR1115	110718.2	882246.8	-132.1	112.9	2.45	470
NPR1130	112410.6	882255.9	280.4	114.5	2.56	499
NPR1145	114104.5	882301.5	-416.0	100.5	2.38	561
NPR1200	115759.0	882303.5	-109.2	106.2	2.31	473
NPR1215	121453.6	882301.9	40.4	124.2	2.55	422
NPR1230	123147.6	882256.8	135.8	99.1	2.25	514
NPR1245	124840.2	882248.1	-34.5	105.0	2.38	513
NPR1300	130530.8	882236.0	60.6	110.4	2.42	479
NPR1315	132218.8	882220.4	139.7	125.4	2.49	395
NPR1330	133903.5	882201.5	-28.9	102.2	2.28	499
NPR1345	135544.3	882139.4	270.6	100.9	2.30	518
NPR1400	141220.7	882114.3	-202.2	109.5	2.32	448
NPR1415	142852.3	882046.2	-193.1	118.1	2.47	436
NPR1430	144518.5	882015.3	77.7	104.0	2.39	529
NPR1445	150139.0	881941.8	-194.5	102.7	2.36	526
NPR1500	151753.4	881905.9	200.1	114.4	2.38	434
NPR1515	153401.4	881827.8	125.5	111.8	2.33	435
NPR1530	155002.8	881747.7	9.6	111.6	2.47	488
NPR1545	160557.5	881705.8	-131.9	114.9	2.55	492

TABLE 4–9 continued

Field	α (1950)	δ (1950)	T_k (μK)	ϵ_k (μK)	σ_k (mK)	n_k
NPR1600	162145.1	881622.3	301.1	111.3	2.44	479
NPR1615	163725.8	881537.5	199.8	114.8	2.39	432
NPR1630	165259.4	881451.4	-154.7	114.8	2.48	468
NPR1645	170825.9	881404.5	-220.2	104.7	2.33	496
NPR1700	172345.4	881316.8	341.5	121.3	2.47	413
NPR1715	173857.9	881228.6	-232.7	115.9	2.30	395
NPR1730	175403.5	881140.2	76.7	119.2	2.37	396
NPR1745	180902.4	881051.7	-213.0	109.5	2.38	473
NPR1800	182354.7	881003.3	-183.4	117.7	2.45	434
NPR1815	183840.6	880915.2	-236.6	120.5	2.43	407
NPR1830	185320.2	880827.7	-51.3	119.8	2.40	400
NPR1845	190753.9	880740.9	44.1	112.5	2.38	447
NPR1900	192221.7	880655.1	-109.9	127.0	2.62	426
NPR1915	193644.0	880610.3	143.2	134.4	2.55	360
NPR1930	195101.0	880526.7	5.7	118.4	2.51	449
NPR1945	200513.0	880444.6	-306.6	104.4	2.31	491
NPR2000	201920.2	880404.1	192.2	116.3	2.46	446
NPR2015	203322.8	880325.2	79.9	120.9	2.37	385
NPR2030	204721.3	880248.2	-173.9	123.1	2.57	436
NPR2045	210115.8	880213.2	252.1	108.4	2.44	505
NPR2100	211506.6	880140.3	-56.3	122.6	2.39	381
NPR2115	212854.0	880109.6	-45.6	132.2	2.58	381
NPR2130	214238.3	880041.2	332.4	115.3	2.30	397
NPR2145	215619.8	880015.2	2.1	115.3	2.40	433
NPR2200	220958.7	875951.7	-122.5	127.0	2.40	358
NPR2215	222335.3	875930.8	-227.1	128.1	2.59	409
NPR2230	223710.0	875912.4	267.3	112.7	2.38	447
NPR2245	225043.0	875856.8	33.7	109.8	2.32	446
NPR2300	230414.5	875843.9	-28.5	122.4	2.31	357
NPR2315	231744.9	875833.8	-88.5	117.8	2.37	405
NPR2330	233114.4	875826.6	-87.9	110.4	2.26	418
NPR2345	234443.4	875822.1	-206.3	115.9	2.43	438

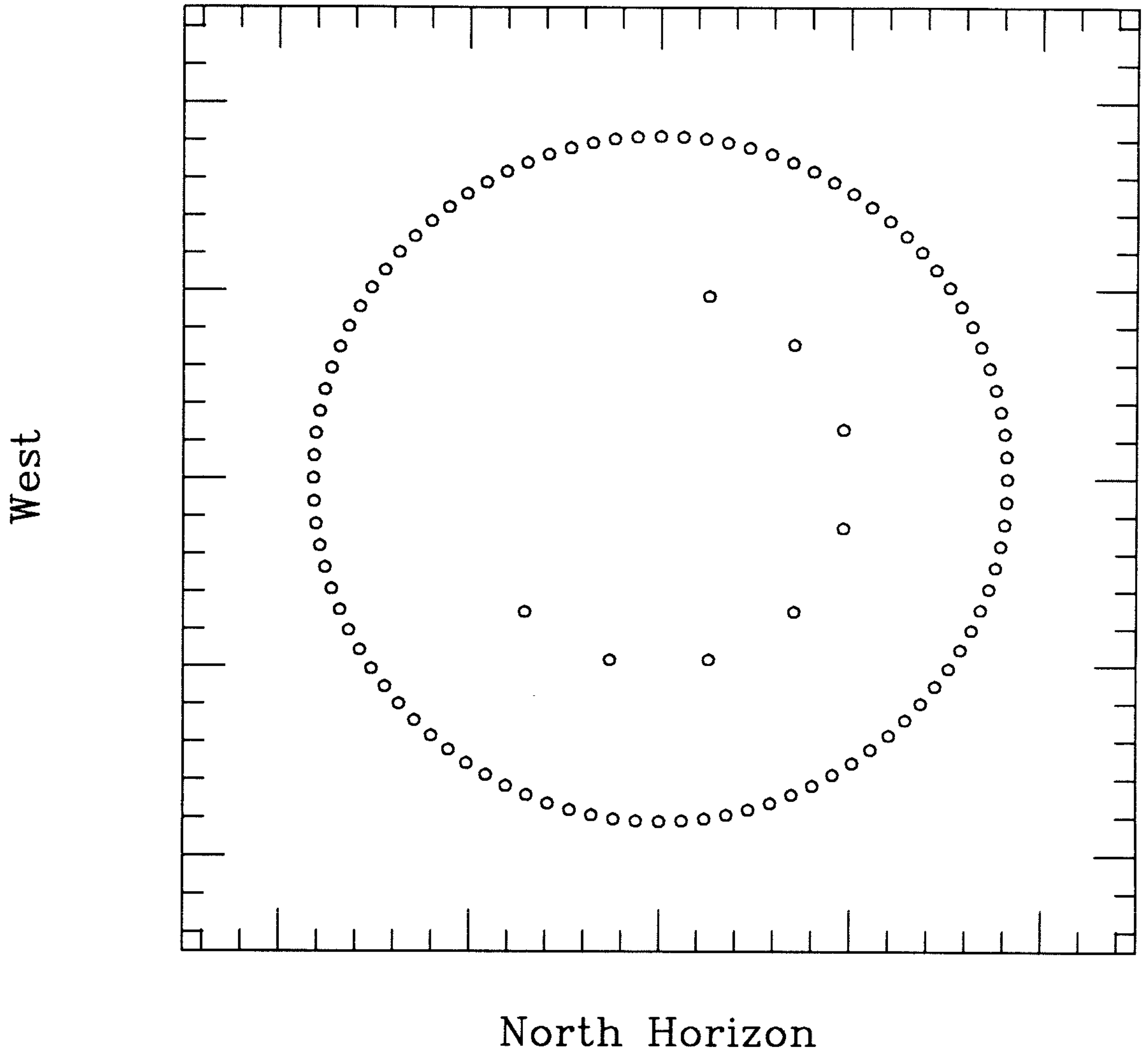

FIGURE 4–1. Approximate projection of RING (outer circles) and NCP (inner circles) field centers on the sky. Orientation is such that the North horizon (Azimuth 0) lies toward the bottom and West is to the left. The spacing between tickmarks is 0°.2. The field NPR0000 is the uppermost in the outer circle, NCP1 is at the top of the inner. Right Ascension increases clockwise. The size of the open circle markers is approximately twice the OVRO primary beam FWHM 1′.8.

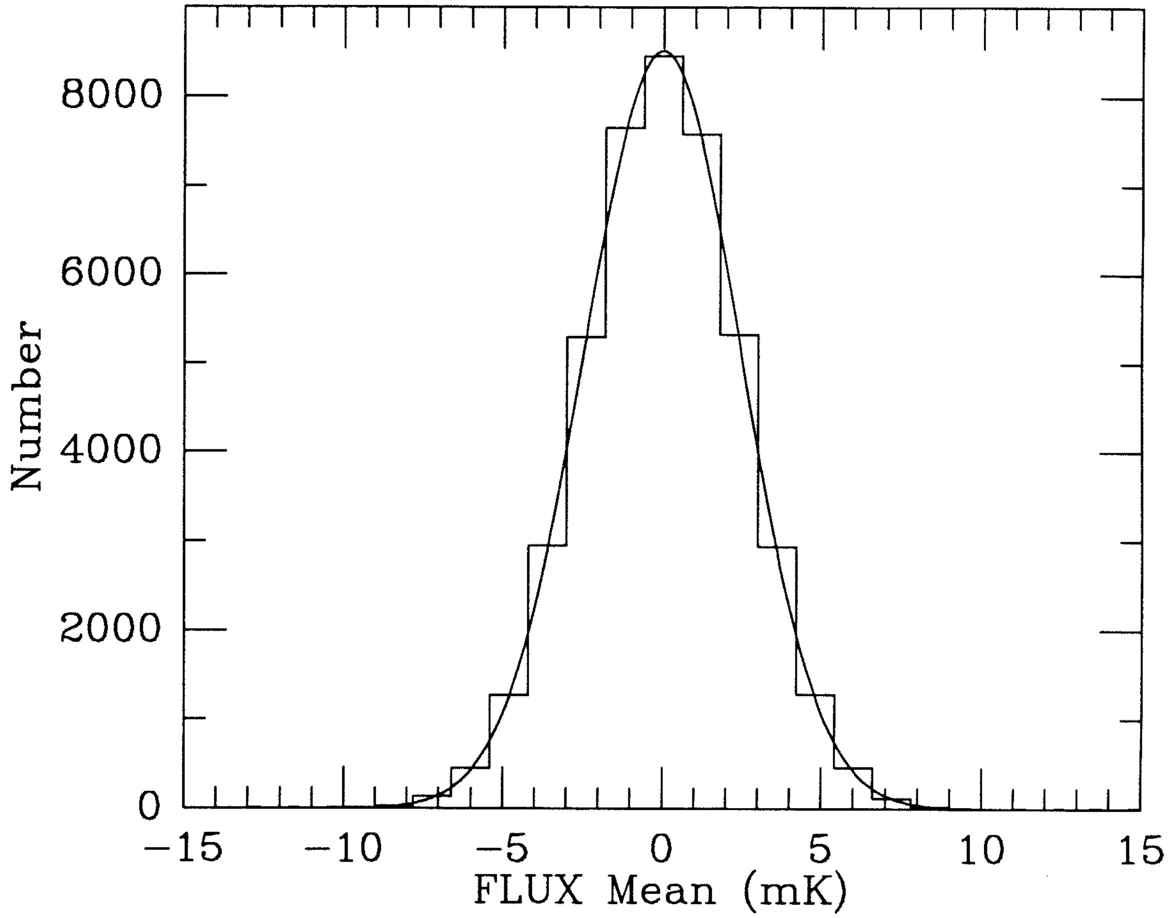

FIGURE 4–2. A histogram of the 43977 calibrated FLUX measurements. The superimposed curve is the number expected in the 0.2 mK bins if drawn from a normal $N(0,\sigma)$ distribution with $\sigma = 2.45$ mK.

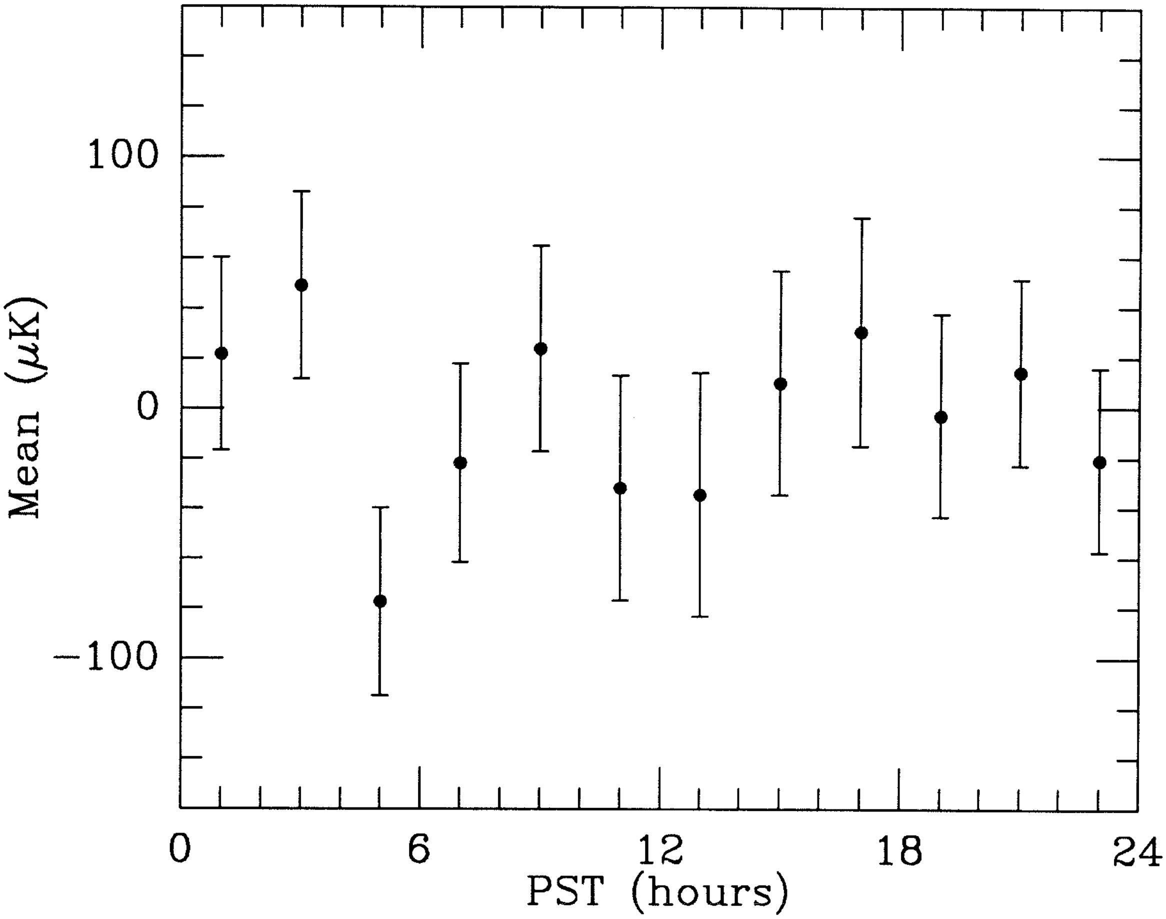

FIGURE 4–3(a). The mean and 1σ error in mean for 43977 RING data points binned into 2-hour intervals in Pacific Standard Time (PST). No significant trend is seen and the value of chi-squared is 8.8 on 11 degrees of freedom for the 12 bins.

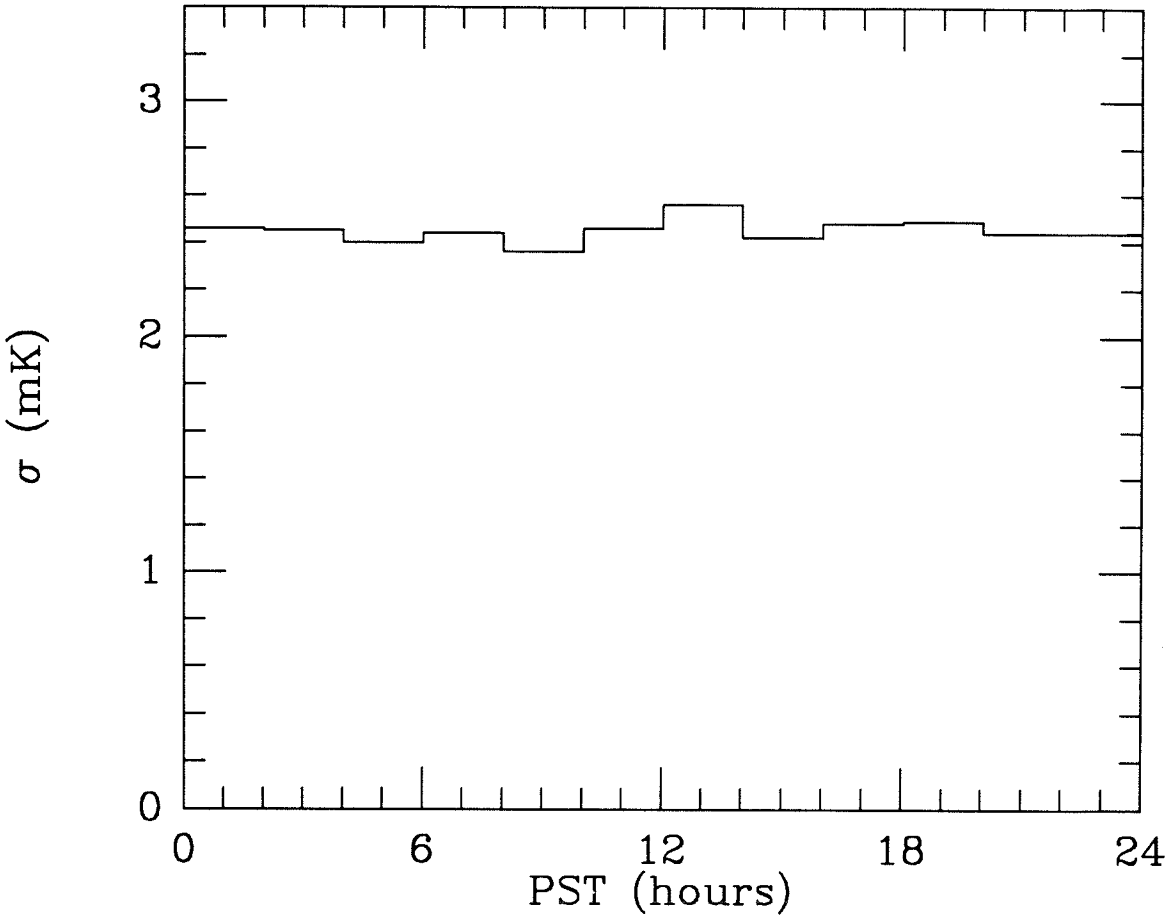

FIGURE 4–3(b). The standard deviation about the mean for the RING data by PST.

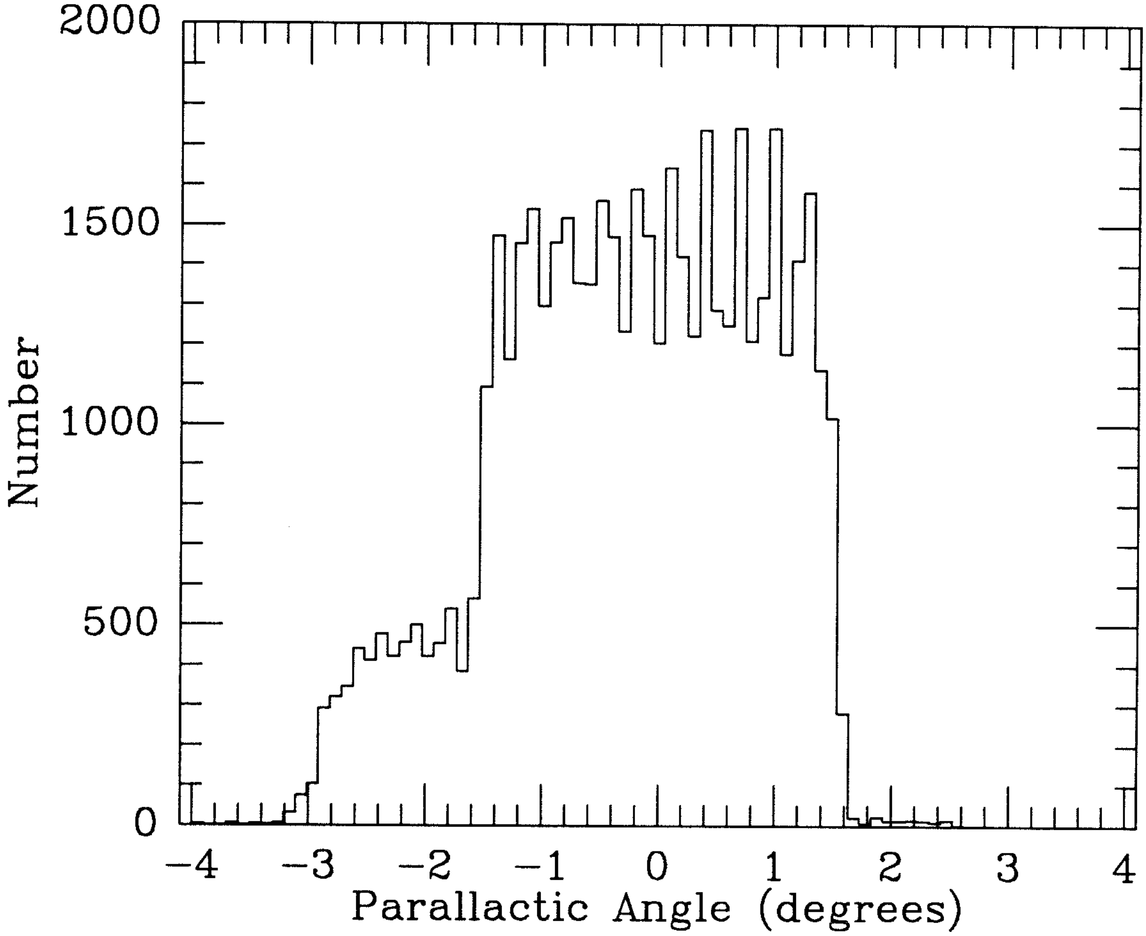

FIGURE 4–4. A histogram of the parallactic angles at the midpoint of 49888 FLUX measurements within ±4° of transit. The bin width is 0°.1 which is the resolution of the parallactic angle calculation. The individual peaks are the mean midpoints of the FLUXes within a scan.

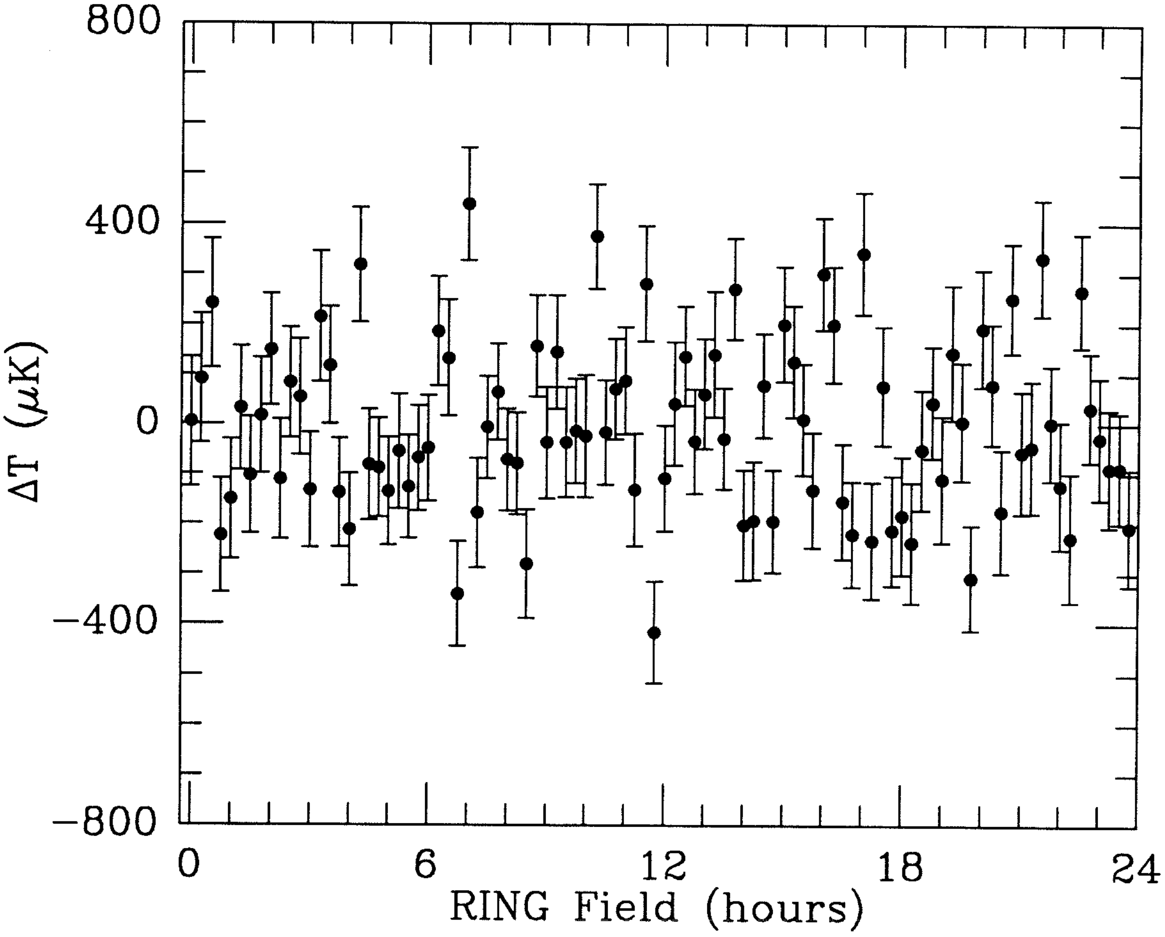

FIGURE 4–5. RING measurements of field values T_k with 1σ error bars. A total of 43971 individual FLUX measurements are included from within the parallactic angle range of $\pm 1^\circ.65$.

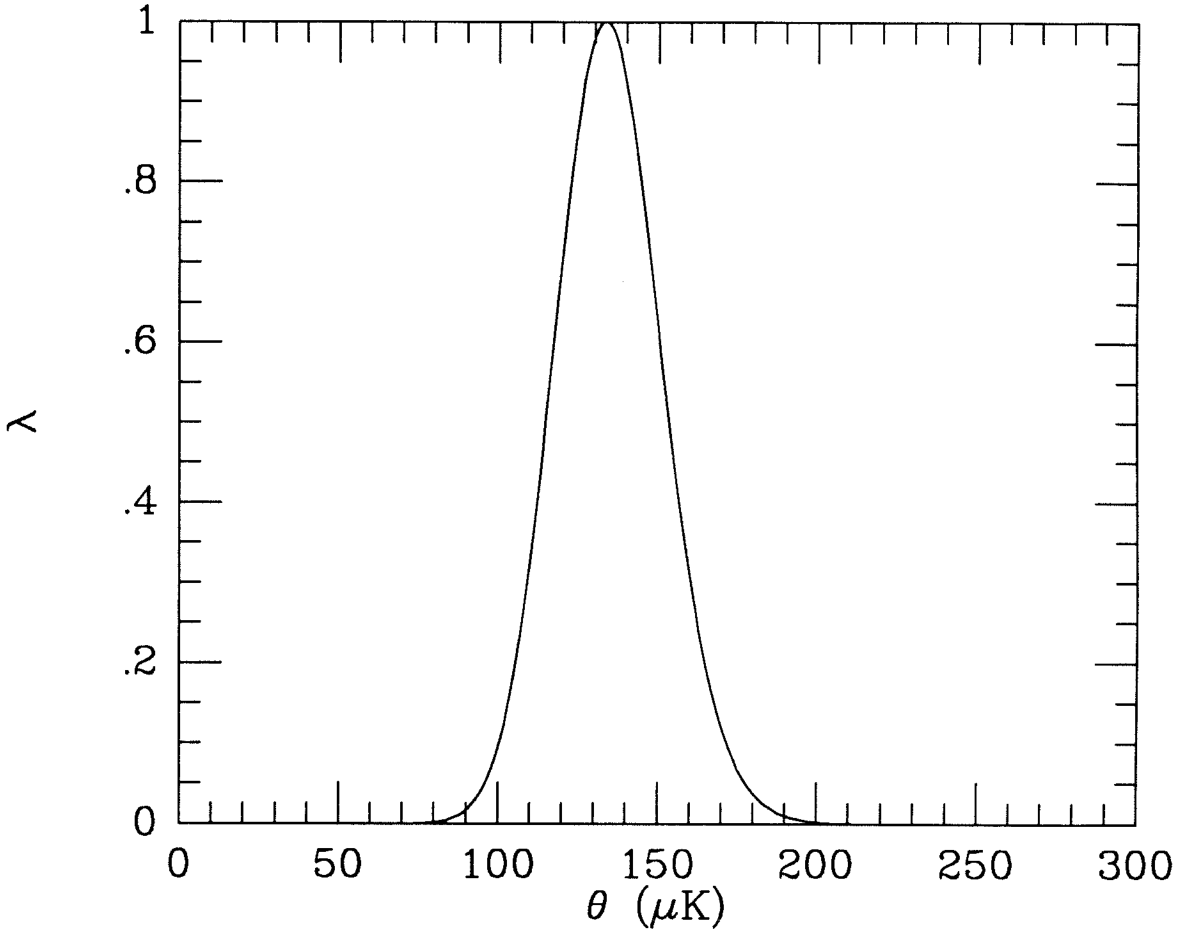

FIGURE 4–6. The likelihood function for $\theta = \sigma_{sky}$ from the RING data, normalized to the maximum at $\hat{\theta} = 134$ μK.

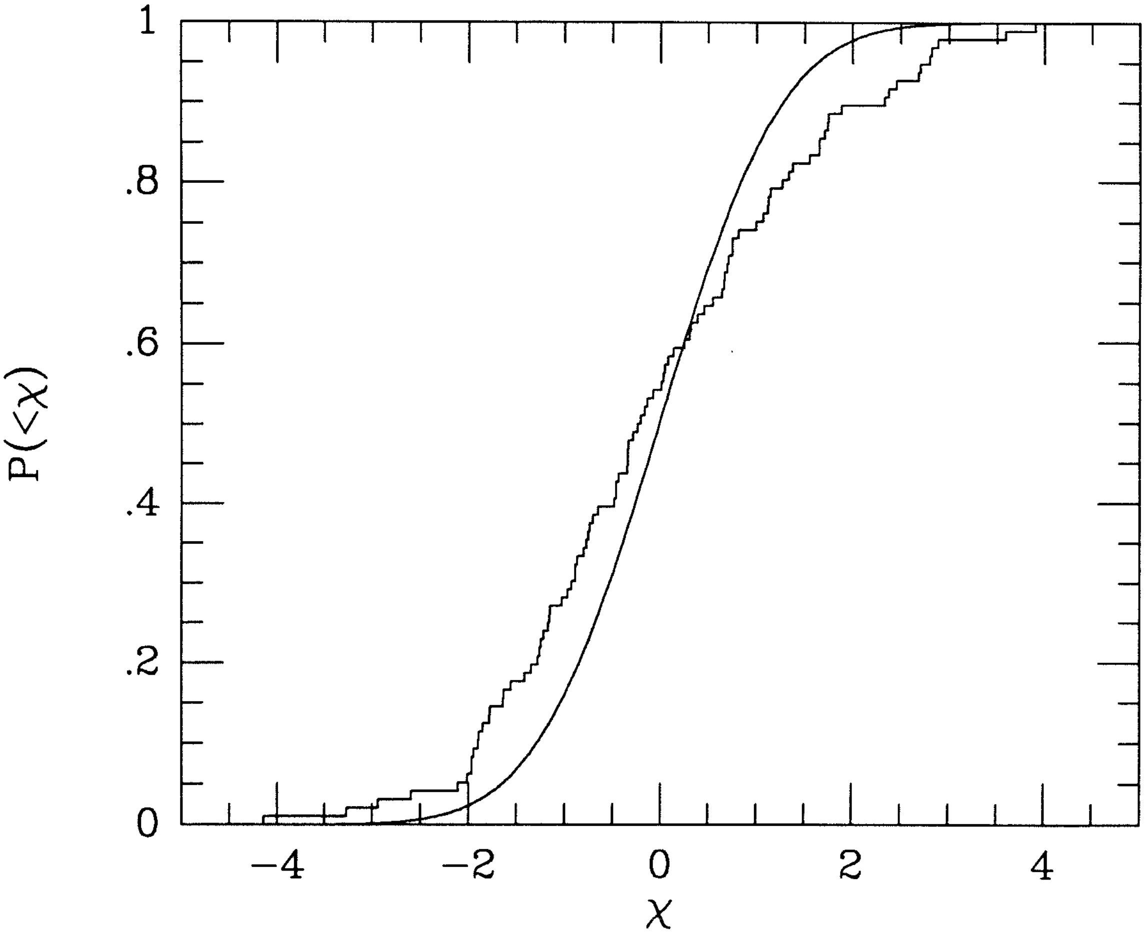

FIGURE 4–7(a). The cumulative distribution function for $\chi_k = T_k/\epsilon_k$ with the normal $N(0,1)$ curve superimposed. The KS probability of a deviation this large or larger is 6.4%.

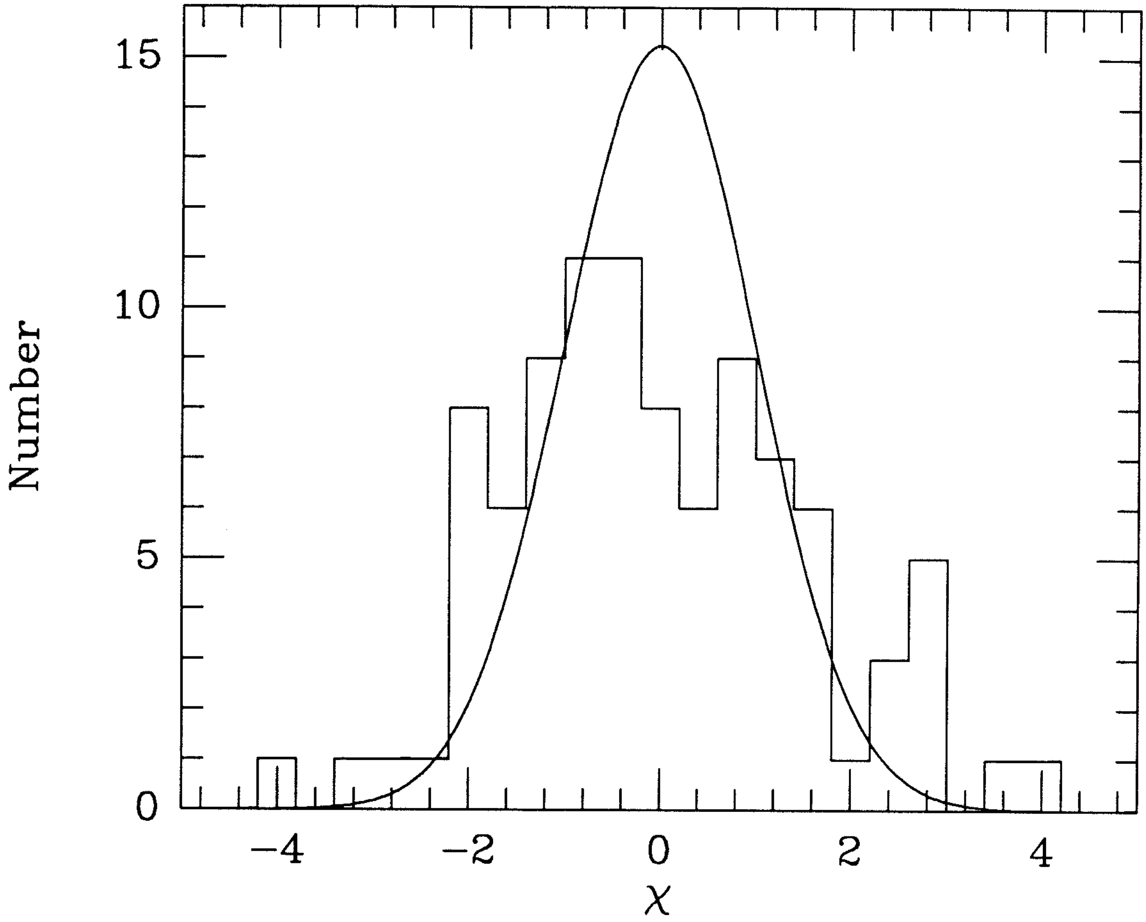

FIGURE 4–7(b). A histogram of the χ values from (a). The curve is the number expected in the $\Delta\chi = 0.4$ bins from the normal $N(0,1)$ distribution.

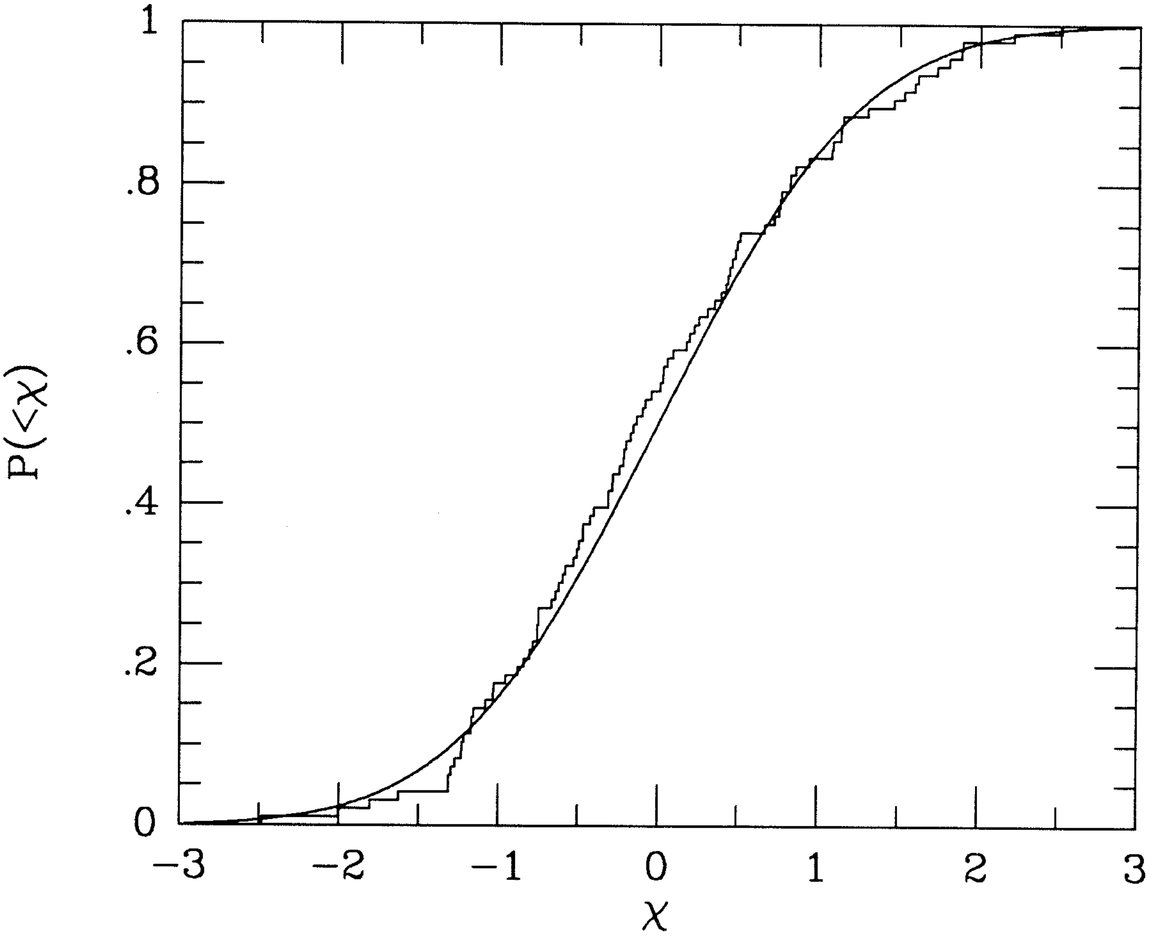

FIGURE 4–7(c). The cumulative distribution function of $\chi_k = T_k/(\epsilon_k^2+\sigma_{sky}^2)^{1/2}$ for $\sigma_{sky} = 134$ μK with the normal $N(0,1)$ curve superimposed. The KS probability of a deviation this large or larger is 90%.

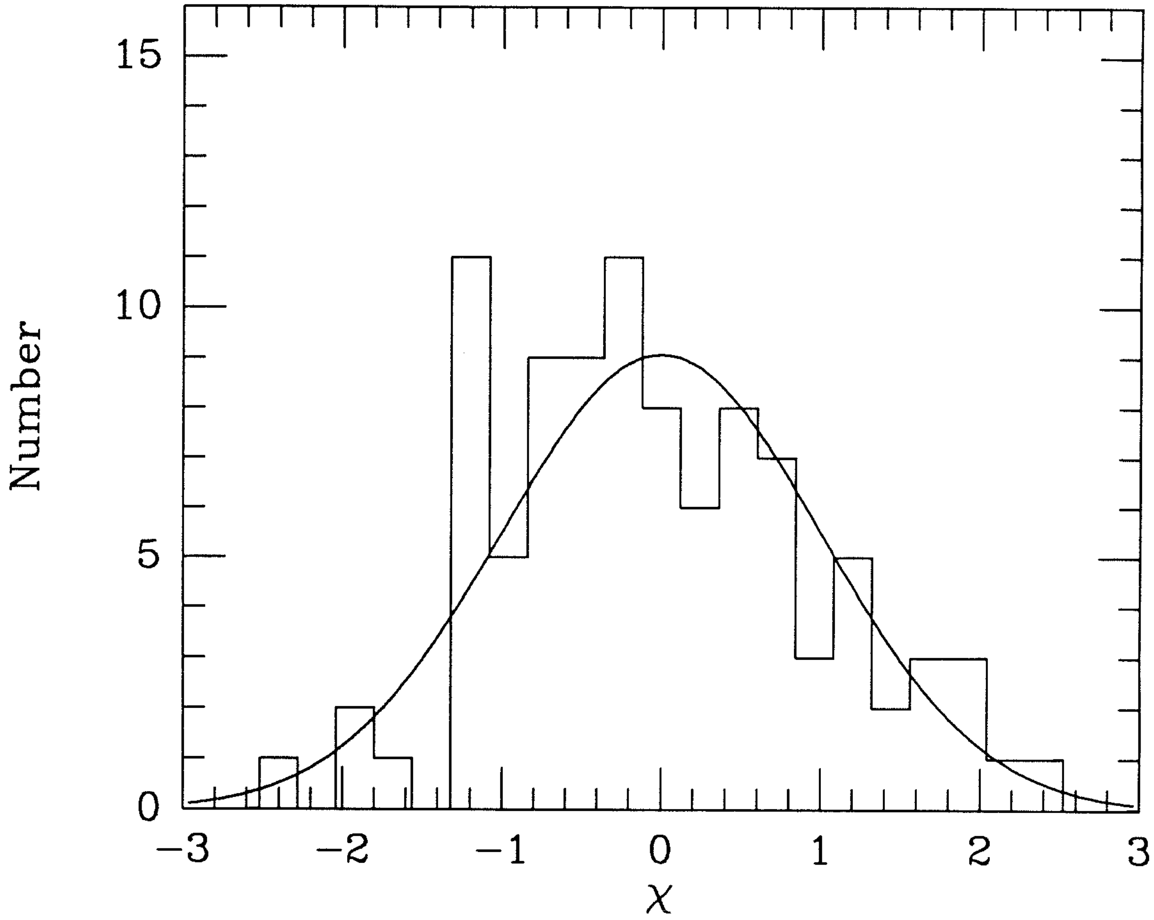

FIGURE 4–7(d). A histogram of the χ values from (c). The curve is the number expected in the $\Delta\chi = 0.24$ bins from the normal $N(0,1)$ distribution.

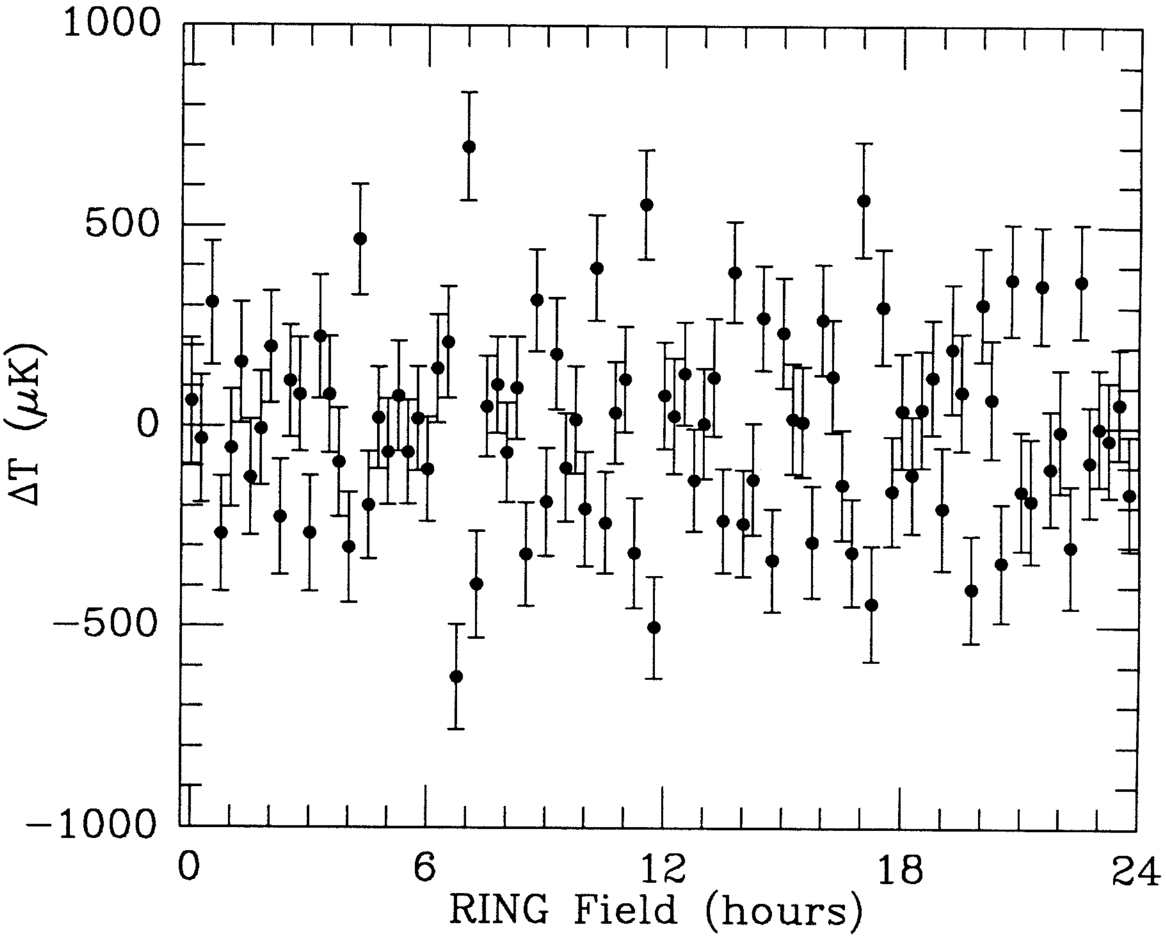

FIGURE 4–8. Results of matched filtering of RING fields. Each point is the convolution of the RING switching with the RING data and provides the highest signal-to-noise discrimination for point sources in the center of fields.

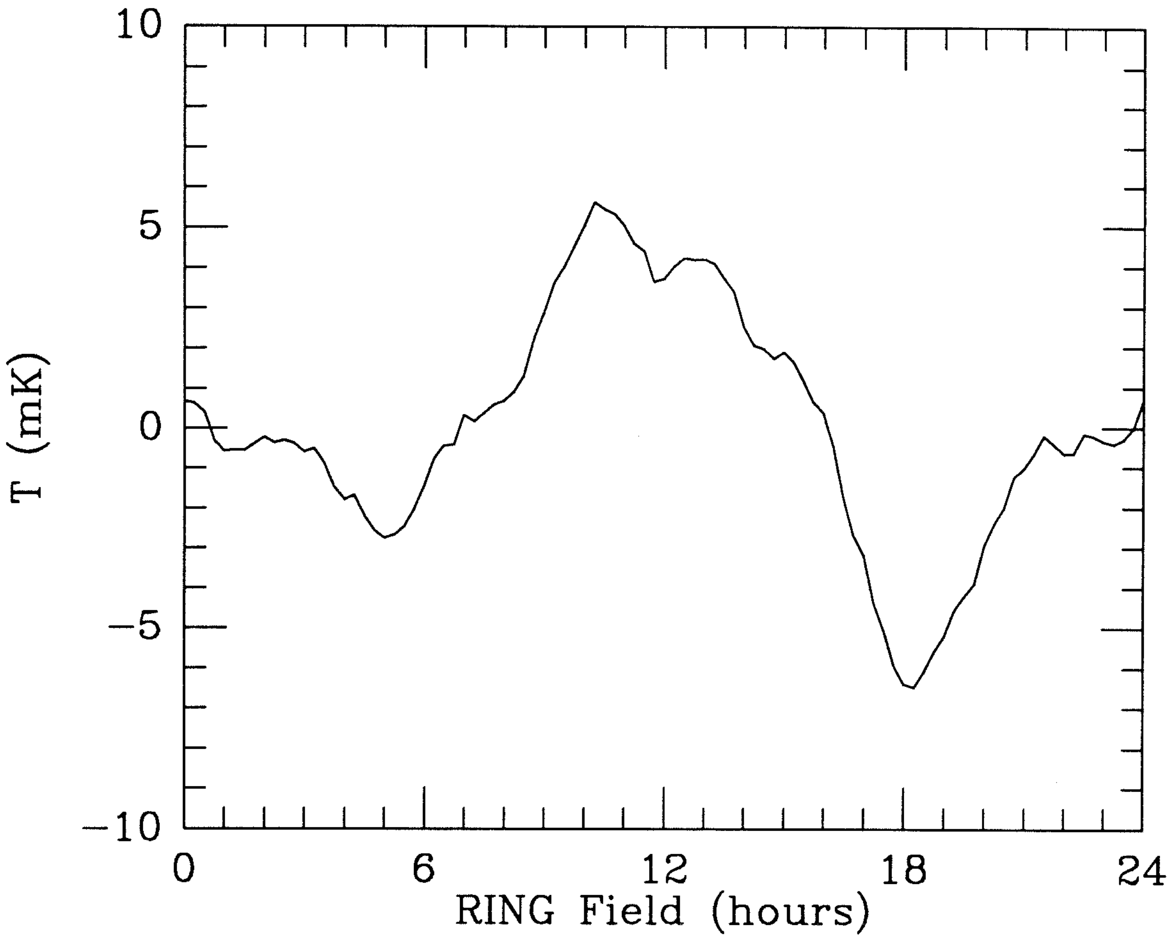

FIGURE 4–9. The reconstruction of RING temperatures using direct inversion with constraint of zero mean. Spurious large-scale structure is generated by noise in the double-differencing measurements.

CHAPTER 5
A VLA Survey of the RING Region

5–1 Overview

The critical topics in a discussion of the results of the RING survey are the statistical significance and the identification of the sources of the signal. We have used the Bayesian formalism to assign a credible interval for the anisotropy, and we now turn to the problem of identification of the individual fields and estimation of the contribution from known non-background objects. We are concerned with two types of contaminating sources, those of angular size much smaller than our beam of $1'.8$ (discrete) and those of size comparable to and larger than our beam (distributed). Discrete radio objects include stars, hot ionized gas in clusters of galaxies, and the dominant contributor, extragalactic radio sources, which we will refer to generically as radio galaxies (RG). Distributed sources include synchotron emission from cosmic ray electrons in our galaxy, free-free emission from ionized hydrogen in the interstellar medium, and thermal radiation from dust associated with molecular clouds in the disk of our galaxy. At frequencies below 90 GHz it is unlikely that dust, as extrapolated from IRAS observations of infrared cirrus, is a source of anisotropy above the level of 10^{-6} and well out of the plane of the galaxy. Likewise, the other distributed sources are not significant on angular scales less than $30'$ and frequencies above 10 GHz. Of the discrete backgrounds, stars are the least significant while the Sunyaev-Zel'dovich (SZ) effect from clusters of galaxies may be significant depending upon the model of cluster evolution adopted; it is likely that the results of the RING can put limits on such models and we will consider the SZ as an interesting signal instead of a contaminating background. Lastly, the primary candidate for contamination is nonthermal emission from radio galaxies associated with active galactic nuclei and star-formation.

The properties and evolution of radio galaxies have been extensively studied, especially at frequencies at and below 5 GHz (see Condon 1988 for a review and references). The spectra of these sources is well explained by the superposition of synchotron emission regions of differing optical depths. For the extended lobe emission from a typical radio galaxy or quasar, we find a power law behavior indicative of optically thin radiation from a power law distribution of electron energies, with flux density decreasing approximately with the 0.75 power of frequency. For cores within extended sources and bright compact objects we find a power law spectrum at high frequencies while the low frequency radiation falls off (again with a power law) due to self-absorption below a turnover wavelength that is a function of the size of and magnetic field strength within the emission zone. We assume a power law spectrum for the RG flux densities over some range of frequencies,

$$S_\nu = S_{\nu_0} \left(\frac{\nu}{\nu_0} \right)^{-\alpha} \tag{5.1}$$

where α is the spectral index. Thus, we can divide our objects into two classes, those with 'steep' spectra where the turnover is below the frequency range considered and 'flat' spectra where the frequency of maximum flux density is within or above our interval considered. The steep spectrum sources typically have $\langle\alpha\rangle \sim 0.7$ between 1.4 and 5 GHz, the best studied frequencies for flux densities below 1 Jansky. For sources selected from flux limited catalogues at 5 GHz, between 1/3 and 1/2 have flat spectra ($\alpha < 0.5$) between 1.4 and 5 GHz at flux densities at and below 1 mJy, the level at which we are interested (Kellerman and Wall 1987). At 5 GHz, the flat spectrum sources have a wide distribution centered at $\langle\alpha\rangle \sim 0.0$. Unfortunately, not much is known about the spectral index properties of faint radio sources selected at higher frequencies, in particular at 20 GHz where we do our work.

The radio source counts at a variety of frequencies can be used to estimate the level of confusion expected from RG confusion, while a survey of the region of the sky containing the RING would allow identification of detections. Both of these efforts, however, are hampered by the fact that there is no available instrument with which to perform the necessary observations to the required level of sensitivity at our observing wavelength, and thus we are led to the prospect of working at lower frequencies and making the extrapolation to the OVRO frequency of 20 GHz. The ideal procedure of contemporaneous coincidental-wavelength observation with both single dish (40-meter) and interferometer (VLA), with complementary sensitivity to extended background and point-like RGs, is still in the future, but we can still hope to use the current state-of-the-art high frequency interferometer arrays, namely the VLA at 8.5 GHz, to place limits on the contribution of these sources to the RING signal.

5–2 Radio Source Counts

The calculation of the contribution of discrete radio sources to microwave background anisotropy experiments has been made by Danese, De Zotti, and Mandolesi (1983) and most recently by Franceschini *et al.* (1989) and their results indicate that for the Owens Valley experiments, confusion can be expected at the level of 44μK (1.6×10^{-5} in $\Delta T/T$) for the contribution to the field *rms* with their different models giving variations of 20% in this value. We have corrected their numbers downward by 6% due to our FLUX procedure and main beam efficiency, atmospheric absorption and blackbody function. However, as noted in these references, the noise distribution from RGs is positive and skewed with a long tail, and the Gaussian estimate of variance can underestimate the true variance. In addition, they use in their calculations of the variance the assumption that the experiments are limited by the confusion noise itself, unlike our case where we are limited by instrumental noise. Since their predicted noise level is less than our RING noise (by a factor of nearly 3), they cut off the source distribution at too low a level, and again underestimate the noise. For example, our largest detection of $\sim$ 400 μK is a 9σ fluctuation with respect to their noise, while they cut off the distribution at 3–5σ. The sensitivity of the calculation to the cutoff level is also worrisome. Perhaps it is reasonable to use these numbers for the contribution of sources to the variance below the detection level; in this case it may account for a little over one-third of our excess anisotropy of 133 μK after removal of the 4 fields NPR0415, NPR0700, NPR1130, and NPR1700 (with their 6 reference fields). On the other hand, the predicted confusion is consistent with the results of the NCP experiment after discarding the 200 μK field NCP7. Here, the instrumental noise levels are nearly equal to the confusion noise level and the 44 μK is comfortably within the 58 μK 95% confidence upper limit on the excess signal.

We conclude from these results that we can account statistically for 44 μK of the signal with the extrapolated radio source counts. Perhaps we should allow ourselves a factor of two leeway in the predicted confusion due to the various problems in the calculation noted above. On the other hand, it seems that there is some level of noise unaccounted for by RG contamination by confusing sources. We now turn to the problem of identification of the brightest RING fields, especially in regards to radio source surveys.

Unfortunately, there is no existing deep radio survey covering the entire region of the sky containing the RING. For the NCP fields, we had found a survey of the 5C9 field at 5 GHz (Pauliny-Toth *et al.* 1978), which we used to identify contaminating sources. To fill in the unexamined regions, we have undertaken a survey of the north celestial polar cap region at 1.4 GHz, of the NCP fields and references at 5 GHz, and of the RING fields at 8.5 GHz. The observations were made at the Very Large Array (VLA) (Thompson *et al.* 1980) in the C array using snapshot mode. The data were taken and reduced using a procedure similar to that in previous VLA snapshot surveys (Condon, Condon, and Hazard 1982). The use of standard VLA reduction and imaging software as well as instrument capabilities and observing techniques is discussed in Sramek and Schwab (1986), Cornwell (1986), and Bridle (1986) and references therein. We will discuss here only the 1.4 and 8.5 GHz observations that are directly relevant to the RING experiment.

5–3 VLA 1.4 GHz Survey

The 1.4 GHz survey fields were arranged in a hexagonal pattern centered upon the north celestial pole in 1988.0 coordinates, as diagrammed in Figure 5–1. The separation between field centers was 26 arcminutes along the principal axes, the distance of a field from each of its six nearest neighbors, and the largest distance of any interior point from a field center occurs at the hexagonal vertices and is $15'.0$. The primary beam of the 25m VLA antennas at the observing frequency of 1.42 GHz is $31'.6$ full width at half-maximum (FWHM) response; the desired region is covered such that all points are within the half-power point of the nearest beam center. This is exactly the same pattern used by Condon, Condon, and Hazard (1982). The observations were made on 14 May 1988, starting at 5:00 Local Sidereal Time (LST) and ending at 15:30 LST, with 26 antennas available at that time. Each field was observed in two 2-minute scans separated by approximately 5 hours, to improve the sampling of the Fourier-transform aperture plane. The integration time per record was 30 seconds. Two intermediate frequency (IF) channels with bandwidth 25 MHz were recorded, with nominal centers at 1.413 and 1.438 GHz respectively. A nearby radio source, 0454+844, was observed once every hour as a phase calibrator. The flux density scale was calibrated using the source 3C286 assumed to have a flux of 14.8 Jy at 1.4 GHz (Baars *et al.* 1977). Calibration and preliminary editing were performed at the VLA site by C.R. Lawrence using the standard DEC-10 software.

The imaging and final phase self-calibration was completed at Caltech using the AIPS software package on the CIT Convex computer by V. Gorjian as part of the Caltech Undergraduate research program. Of the 139 1.4 GHz fields, 30 were selected for reduction as containing the RING 20 GHz fields. Each IF was mapped separately, then averaged together to produce the final image. Our C array observations produced a synthesized beam of $19''$ FWHM within the $32'$ FWHM field-of-view, although there were often significant variations from map to map from differing numbers of points (with 2-minute snapshots, the editing of a relatively small number of points can affect the final sampling and hence the effective resolution). The data were gridded using natural weighting and Fourier transformed to 1024×1024 maps, with a pixel size of $4''$ square, covering nearly the entire primary beam out to the first null in the response.

A theoretical noise level of 21.9 mJy per visibility point was expected, or 0.63 mJy for 1200 visibility records. The data were first edited to remove spurious points with large amplitudes, bad antennas, and discrepant baselines missed during the preliminary editing. Fourier transform and deconvolution were done using the program MX, where the effects of the point response function of the array, or 'dirty beam,' were removed by identification of delta-function sources and successive transforms between the Fourier and image planes to subtract the corresponding amplitude and phase from the data. This procedure and the mechanics of the MX routine are described in Cornwell (1986). The area of the image plane searched for sources was limited to small boxes around objects visible in the map. Deconvolution was performed slowly, with only a small fraction of the source flux removed from the residual image to the 'clean' map at each iteration, to allow the identification of fainter sources as the sidelobe contamination from the brighter objects was removed. This procedure was halted when no new objects brighter than 6σ were found and no residual points inside the search boxes greater than 3σ remained. For fields containing sufficiently bright sources, almost every map at 1.4 GHz, we performed self-calibration of the phases (see Cornwell 1986a) and repeated the deconvolution process. Finally, the two IF images were averaged together. The resolution in the final maps, or the synthesized beam, is typically $18''$, with significant variations from map to map due to the differences in amount of data after editing and thus different sampling of the Fourier plane.

The averaged map was searched for sources above the 6σ noise level and within the 20% response of the primary beam. For 1024×1024 pixels, the probability of a deviation due to the Gaussian noise larger than 6σ is 0.1%. All detected sources were catalogued and measured, both in the averaged map and an image corrected for the primary beam attenuation of the VLA antennas. Two-dimensional Gaussian functions were fitted to objects and components to determine centroid positions, peak intensities, integrated flux densities and sizes. The difference in fitted parameters between the two IF maps was used to estimate error bars. Most sources appear in more than one map, and were used to check on the veracity of the identifications and the u,v-coordinate system integrity. The integrated flux densities from the Gaussian fitting were then recorded, along with estimated errors and estimated deconvolved angular sizes.

The entire set of 30 VLA maps containing the RING fields is shown in Figure 5–2. The locations of the 20 GHz RING field centers are denoted by the crosses, with the arms extending to the OVRO 40-meter half power beam radius. We have catalogued in Table 5–1 the 10 sources identified in the survey as within 2′.5 of a RING field center. In particular, we find two within 1′ in fields NPR1130 and NPR1700 that both show the signature of fluctuations in the RING dataset. The flux densities of these sources at 20 GHz and upper limits on discrete radio source fluxes in those RING fields in which no source is detected from the 1.4 GHz maps are not very accurate, due to unknown spectral indices and the factor of 14 in frequency as well as the relatively poor sensitivity; the noise level in a VLA map at the position of an average RING field is 700 μJy while the error bar on an average RING field at 20 GHz is 480 μJy. Contour maps of the VLA 1.4 GHz sources in Table 5–1 are shown in Figure 5–3 along with the position of 8.5 GHz components (see §5–4 and Table 5–3) represented by crosses. The noise levels in the VLA maps at the positions of the RING field centers are listed in Table 5–2, along with equivalent temperatures for the OVRO system assuming only direct conversion of flux to temperature, $\xi = 7.99$ Jy/K, and a factor

$$\begin{aligned} f &= 2 \times \frac{\kappa \cdot g_{ncp}}{\rho_{atm}} \\ &= \frac{2 \cdot 1.12 \cdot 0.83}{1.045} = 1.78 \end{aligned} \tag{5.2}$$

for antenna gain at north celestial pole g_{ncp}, atmospheric attenuation ρ_{atm}, and correction factor κ (see Chapter 4).

5–4 VLA 8.5 GHz Survey

To gain sensitivity and obtain measurements closer to our observing frequency, we made use of the excellent 8.5 GHz receivers recently installed at the VLA for the Voyager Neptune encounter. On July 3, 1989, we acquired 5 hours of ad-hoc VLA time during which we observed 20 RING fields in two 6 minute scans each. The fields observed were those exhibiting the largest signals in the RING survey and some of those adjacent. We plan to observe all the RING fields at 8.5 GHz in the near future, as is necessary for completeness, but some small subset was needed due to the 5 hour constraint. As in the 1.4 GHz observations, the VLA was in the C configuration.

Phase calibration was applied using the source 0454+844, which was observed every 24 minutes. Due to the extraordinary stability of the 8 GHz system, the default amplitude scale was sufficient for flux density calibration, as verified using several standard sources. Two 50 MHz IF bands were recorded, at center frequencies 8.415 and 8.515 GHz. All calibration, editing, and imaging was done using the AIPS package. The instrumental noise on a single 30-second visibility record was found to be approximately 6.4 mJy, giving us a 1σ level of 79 μJy in a single IF for 6600 visibilities. The maps were made using the same procedure as in the analysis of the 1.4 GHz data; the image size used here was again 1024×1024 with $0''.7$ pixels, again covering nearly the entire $5'.3$ FWHM field-of-view out to the first zero. The synthesized beam of the array was approximately $3''$ FWHM. Only a few of the fields contained sources strong enough for self-calibration, and some of the fields contained no objects above the 6σ detection level. As before, the two IF maps were averaged to produce a final map.

The results for each of the fields are listed in Table 5–2, along with the number of sources found within the VLA 8.5 GHz 20% primary beam above 6σ in the maps. The full 8.5 GHz maps of these fields are shown in Figure 5–4, and contour maps of the individual detected sources are presented in Figure 5–5. The 8.5 GHz source catalogue (objects are denoted NPXnnnn.*m* for source *m* at VLA X-Band in field NPRnnnn) is presented in Table 5–3. The integrated flux densities $S_{8.5}$ and errors are listed, along with the deconvolved Gaussian angular sizes and the angular distance on the sky from the nearest RING field center. Out of the 18 sources found within the 20%

beam, four are found to be double with at least one extended component (NPX0015.1, NPX0415.1, NPX1130.1, and NPX1700.1), and one to be a single extended source (NPX2045.1). Also note that the strong source NPX0045.1 was included in the table even though it was found outside the 20% attenuation level in the beam; the four 8.5 GHz sources with fluxes greater than 3 mJy (NPX0015.1, NPX0045.1, NPX0415.1, NPX2045.1) were later observed at 20 GHz.

In Table 5–4 we have compiled the combined 1.4/8.5 GHz catalogue, using the sources detected above 6σ at 8.5 GHz within the 20% beam and the additional sources detected only at 1.4 GHz but within $2'.5$ of a RING field center, and the additional strong source NPX0045.1. From now on, we will denote these sources by NPRnnnn.m instead of the NPF and NPX designations from the parent survey. The spectral indices are calculated from the flux densities at the two frequencies, when available. All sources at 1.4 GHz were detected at 8.5 GHz when within the field of view, and for the remaining 8.5 GHz sources the 1.4 GHz images were examined at the appropriate positions for sources detected above 3σ (but below the 6σ selection cutoff). For those 8.5 GHz sources not found at 1.4 GHz, a flux density of $3\sigma \pm 1\sigma$ was assumed for purposes of estimating spectral properties and these values should be taken as upper limits. Unfortunately, as examination of Table 5–4 shows, the sensitivity limit of the 1.4 GHz survey is such that we detect mostly the steep spectrum sources of the 8.5 GHz sample and place only upper limits on $\alpha_{1.4}^{8.5}$ for flat spectra. To help alleviate this problem, we have observed the brighter sources at 20 GHz with the results given in the next section.

In Table 5–4, we have also tabulated the extrapolated 20 GHz flux densities S_{20} using the $\alpha_{1.4}^{8.5}$ and limits thereon where available. Where only 1.4 GHz data were available, a spectral index of 0.7 was assumed and the estimated 20 GHz strengths are given in parentheses. The OVRO 20 GHz beam attenuation factor as measured from our beam map is also noted (in the f^{-1} column), and from this the expected equivalent temperature as measured by the RING experiment calculated

$$T_{20} = 2f \times \frac{S_{20}}{\xi} \times \frac{g_{ncp}}{\rho_{atm}} \times \kappa = fS_{20} \times 0.223\ (\pm 0.011). \tag{5.3}$$

We find 6 fields possibly contaminated at the 50 μK level or greater : NPR0415, NPR0630, NPR1130, NPR1200, NPR1700, and NPR2015. The values for NPR0630, NPR1200, and NPR2015 are very uncertain as only 1.4 GHz fluxes are available for the offending RGs. The contributions from the objects in NPR1130 and NPR1700 are very close to the observed temperatures in the RING (see Table 4–9 and Table 5–6) while the source in NPR0415 has an extrapolated strength too low to account for all of the observed signal. In this case, however, the complex structure seen in the maps may indicate that assumption of a single α for both 8.5 GHz components is misleading; it is likely from the possible core-jet morphology that NPR0415.1b has a flat or inverted ($\alpha < 0$) spectrum. As NPR0415.1 is $1'.6$ from the field center and thus likely 10 times stronger than measured at the RING pointing position, direct measurements at 20 GHz will provide the needed information.

5–5 OVRO 20 GHz Observations

In December 1989 we have obtained OVRO 20 GHz direct measurements of four 8.5 GHz sources including NPR0415.1. The results are given in Table 5–5. All four sources were easily detected, with around 6.4 hours of integration time on each. Although all four showed steep spectra between 1.4 and 5 GHz, only three remain steep out to 20 GHz, and only two have slopes consistent with $\alpha_{1.4}^{8.5}$. Most importantly, we find that the worrisome source NPR0415 has a flat spectral index from 8.5 GHz to 20 GHz, as was suggested by the suspicious signal in the RING data. As was mentioned in the last section and is visible in Figures 5–3 and 5–5, this object has a core-jet morphology suggestive of the bright variable superluminal sources.[1] It is thus likely that the 20 GHz flux density is to be associated with the 'core' component NPR0415.1b. Although the direct measurement suggests that all of the signal seen in NPR0415 is due to this source, it is an unfortunate fact that flat spectrum sources (which have necessarily small physical sizes) are nearly all variable sources, and reliable subtraction could prove impossible.

---

[1] These are believed to be relativistic jets emanating from an accretion disk around a supermassive black hole, with the high brightness and variability due to doppler boosting of shocks in the jet plasma (see Bridle and Perley 1984, Kellerman and Owen 1988).

5–6 Final Estimated Contamination Levels

When calculating the contribution of point sources to the RING measurements there are two effects that must be taken into account. As mentioned in Chapter 4, because the OVRO receiver and telescope is designed to perform the beam switching in azimuth, and the RING fields are located on a circle of constant declination, there is a $14''.4$ declination offset of the true reference field at transit from the center of the adjacent RING field. Also, there are departures from a symmetric beam, especially at levels below 10% in the response (see Figure 2 in Paper 1). These effects are sufficiently small that extended sources, such as microwave background fluctuations, are not significantly affected and enter symmetrically into the reference fields at half of the amplitude that they enter into the main beam; we have shown that our experiment is most sensitive to fluctuations on spatial scales between the beam width and the switching angle (on the order of $2'$), and the response to objects of this size is little affected by the small offset or the slight asymmetry as the entire main beam is filled. On the other hand, point sources, especially those located far out in the beam, are significantly affected by these deviations. To estimate the true response of the system to the radio sources, we have used the beam map to obtain the attenuation factor f^{-1}, as in Table 5–4, to obtain the projected RING temperature equivalent T_{est}. The results for the seven sources with $T_{est} > 25\mu\mathrm{K}$ are shown in Table 5–6, for the fields where the object is in the main and reference beams. Also listed are the RING measurements and for those sources with spectral index information, the residual RING temperature after subtraction of the source flux. We find that the three sources NPR0415.1, NPR1130.1, and NPR1700.1 account for the signals seen in these fields, with reasonable residuals (except in NPR1145, which seems to retain an anomalous negative deviation). For NPR0415.1, we have used the 20 GHz measurement of the previous section and placed it at the position of 8.5 GHz component NPR0415.1b, and after subtraction find that we have removed nearly all of the fluctuations in the three fields. Because of our variability arguments presented earlier, it is reasonable to assume that perhaps a T_{est} that is 85% larger would be in order, giving us a residual of 11 μK *rms* among the three fields. It appears that the source NPR1345.1 is too weak to account for the observed RING signal; it would need to be 8 times brighter and then we would overcorrect NPR1330. If we use the corrected values for the four fields, then we find the HPD limits for the *rms* signal

$$\begin{array}{ll} 80 < \sigma_{sky} < 145\ \mu\mathrm{K} \quad (95\%) & \\ & \hat{\sigma}_{sky} = 111\ \mu\mathrm{K} \\ 60 < \sigma_{sky} < 170\ \mu\mathrm{K} \quad (99.87\%). & \end{array}$$

The remaining three 1.4 GHz sources are extrapolated to have interesting temperature contributions, but there is no clear signal in the RING itself to support this. It will be necessary to obtain direct 20 GHz measurements of these objects before attempting to comment further.

We conclude that the fluctuations in fields NPR0415, NPR1130, and NPR1700 are due to the presence of discrete radio sources. Variability of the offending objects could make correction of the RING unreliable, although examination of the residuals in Table 5–6 lends credibility to the estimates of the source strengths. There remain three sources with data at 1.4 GHz only that possibly contaminate the RING, and forthcoming 20 GHz measurements will support or reject this. More significantly, we are left with unexplained signal in NPR0700 and NPR1015 as well as an underlying variance below the detection level for single fields. If we sum the contribution from the detected sources (excluding the three strongly contaminated fields and those with only 1.4 GHz measurements) we can account for only 7 μK *rms*, well below the residual RING anisotropy level of 111 μK and the confusion estimates from source counts; however, because of the 6σ noise level of $\sim$ 80 μK in the 8.5 GHz images, a significant residual source contamination could remain. We will now turn to the problem of quantification of our anisotropy limits, and comparison with theories of galaxy formation.

TABLE 5–1

VLA 1.4 GHz Selected Source Catalogue

Source	R.A. (1950)	Dec. (1950)	1.4 GHz Flux	RING field	θ
NPF038.2	000828.4 $_{\pm 0.5}$	875637.8 $_{\pm 0.2}$	23.1 ± 1.2 mJy	NPR0015	2′.43
NPF063.6a	004151.9 $_{\pm 0.7}$	875819.6 $_{\pm 0.4}$	10.1 ± 1.2	NPR0045	1′.72
NPF063.6b	004122.2 $_{\pm 1.1}$	875814.8 $_{\pm 0.5}$	7.9 ± 1.1	NPR0045	1′.47
NPF042.2a	035411.7 $_{\pm 0.6}$	880456.8 $_{\pm 0.3}$	14.9 ± 0.9[a]	NPR0415	1′.58
NPF042.2b	035446.0 $_{\pm 2.4}$	880514.9 $_{\pm 0.8}$	7.7 ± 1.0	NPR0415	1′.94
NPF070.1	060400.9 $_{\pm 0.5}$	881335.5 $_{\pm 0.2}$	111.3 ± 3.6	NPR0630	2′.21
NPF046.7	071632.8 $_{\pm 0.8}$	881705.5 $_{\pm 0.5}$	7.5 ± 0.9	NPR0745	1′.85
NPF076.3	112216.3 $_{\pm 2.6}$	882252.2 $_{\pm 0.3}$	16.9 ± 1.4[a]	NPR1130	0′.81
NPF050.5	115758.1 $_{\pm 1.7}$	882455.2 $_{\pm 1.9}$	23.4 ± 1.9[a]	NPR1200	1′.86
NPF083.4	172506.4 $_{\pm 1.2}$	881254.7 $_{\pm 0.4}$	29.3 ± 2.3[a]	NPR1700	0′.73
NPF058.1	203641.5 $_{\pm 0.2}$	880158.3 $_{\pm 0.1}$	217.3 ± 2.4	NPR2015	2′.22
NPF091.6	232813.9 $_{\pm 2.4}$	875758.8 $_{\pm 1.2}$	3.3 ± 1.5	NPR2330	1′.66

[a] Extended

TABLE 5–2

VLA 1.4/8.5 GHz SURVEY OF RING FIELDS

RING Field	1.4 GHz 1σ (μJy)	20 GHz 6σ[*] (μK)	8.5 GHz 1σ (μJy)	20 GHz 6σ[*] (μK)	Sources (1.4/8.5)[†]
NPR0000	505	675			0
NPR0015	670	896	69	92	1/1
NPR0030	779	1041	57	76	0/0
NPR0045	549	734	57	76	1/2[a,b]
NPR0100	674	901			0
NPR0115	658	879			0
NPR0130	499	667			0
NPR0145	485	648			0
NPR0200	695	929			0
NPR0215	450	602			0
NPR0230	494	660			0
NPR0245	587	785			0
NPR0300	567	758			0
NPR0315	509	680			0
NPR0330	693	926			0
NPR0345	440	588			0
NPR0400	444	593			0
NPR0415	541	723	56	75	1/1
NPR0430	683	913			0
NPR0445	573	766			0
NPR0500	718	960			0
NPR0515	755	1009			0
NPR0530	537	718			0
NPR0545	526	703			0
NPR0600	727	972			0
NPR0615	1230	1644			0
NPR0630	1120	1497			1
NPR0645	1510	2018			0
NPR0700	1090	1457	60	80	0/1[b]
NPR0715	1010	1350			0
NPR0730	761	1017			0
NPR0745	521	696			1

TABLE 5–2 continued

RING Field	1.4 GHz 1σ (μJy)	20 GHz $6\sigma^*$ (μK)	8.5 GHz 1σ (μJy)	20 GHz $6\sigma^*$ (μK)	Sources $(1.4/8.5)^\dagger$
NPR0800	525	702			0
NPR0815	453	606			0
NPR0830	596	797	58	77	$0/1^{a,b}$
NPR0845	544	727	56	75	$0/1^{c}$
NPR0900	528	706	57	76	$0/1^{c}$
NPR0915	514	687			0
NPR0930	443	592			0
NPR0945	392	524			0
NPR1000	679	908			0
NPR1015	490	655	57	76	0/0
NPR1030	498	666			0
NPR1045	569	761			0
NPR1100	601	803			0
NPR1115	538	719			0
NPR1130	673	900	55	73	$1/2^{c}$
NPR1145	1030	1377	57	76	0/0
NPR1200	816	1091			1
NPR1215	1260	1684			0
NPR1230	969	1295			0
NPR1245	854	1142			0
NPR1300	907	1212			0
NPR1315	772	1032			0
NPR1330	559	747			0
NPR1345	509	680	57	76	$0/3^{b,c,c}$
NPR1400	696	930			0
NPR1415	468	626			0
NPR1430	412	551			0
NPR1445	605	807			0
NPR1500	678	906			0
NPR1515	562	751			0
NPR1530	695	929			0
NPR1545	604	807			0

TABLE 5–2 continued

RING Field	1.4 GHz 1σ (μJy)	20 GHz $6\sigma^*$ (μK)	8.5 GHz 1σ (μJy)	20 GHz $6\sigma^*$ (μK)	Sources (1.4/8.5)[†]
NPR1600	606	810			0
NPR1615	633	846			0
NPR1630	789	1055			0
NPR1645	761	1017			0
NPR1700	754	1008	63	84	1/2[c]
NPR1715	678	906			0
NPR1730	578	773			0
NPR1745	483	646			0
NPR1800	518	692			0
NPR1815	378	505			0
NPR1830	388	519			0
NPR1845	533	712			0
NPR1900	624	834			0
NPR1915	529	707			0
NPR1930	757	1012	57	76	0/0
NPR1945	923	1234	56	75	0/0
NPR2000	862	1152	58	77	0/0
NPR2015	794	1061			1
NPR2030	1010	1350			0
NPR2045	753	1007	60	80	0/1[a,b]
NPR2100	786	1051			0
NPR2115	647	865	58	77	0/0
NPR2130	411	549	55	73	0/2[a,c]
NPR2145	467	624	57	76	0/0
NPR2200	640	855			0
NPR2215	656	877			0
NPR2230	592	791			0
NPR2245	765	1023			0
NPR2300	687	918			0
NPR2315	621	830			0
NPR2330	749	1001			1
NPR2345	661	884			0

[*] Assumes 7.99 Jy/K, and correction factor (see text) of 1.78

[†] Number of sources above 6σ, within $2'.5$ at 1.4 GHz or inside 8.5 GHz beam

[a] 8.5 GHz source outside $2'.5$ from field center

[b] VLA 1.4 GHz source detected at $> 3\sigma$ at 8.5 GHz source position

[c] Source not detected $> 3\sigma$ at 8.5 GHz position at 1.4 GHz

TABLE 5-3

VLA 8.5 GHz SELECTED SOURCE CATALOGUE

Source	R.A. (1950)	Dec. (1950)	8.5 GHz Flux	Size ($''$)	θ
0015.1a	000829.5 ±0.6	875636.8 ±0.3	3.73 ± 0.27 mJy	3.1 x 1.3	$2'.43$
NPX0015.1b	000821.5 ±0.6	875636.6 ±0.2	2.54 ± 0.31	4.4 x 0.8 (< 4.6)	$2'.48$
NPX0045.1	003642.8 ±0.3	875352.7 ±0.9	62.2 ± 2.8	(< 2.4)	$4'.78$[a]
NPX0045.2	004120.1 ±0.6	875815.0 ±0.2	1.15 ± 0.34	(< 1.4)	$1'.45$
NPX0415.1a	035422.3 ±0.6	880502.8 ±0.1	4.15 ± 0.07	1.2 x 0.1 (< 1.3)	$1'.69$
NPX0415.1b	035402.8 ±0.5	880453.1 ±0.1	1.77 ± 0.08	1.4 x 0.6	$1'.50$
NPX0700.1	062943.5 ±0.3	881234.4 ±0.1	0.45 ± 0.18	(< 2.6)	$1'.39$
NPX0830.1	080110.2 ±1.1	881932.0 ±0.6	0.77 ± 0.20	(< 1.8)	$2'.83$
NPX0845.1	082055.4 ±1.1	882132.1 ±0.6	1.08 ± 0.27	(< 2.1)	$3'.19$
NPX0900.1	083906.2 ±0.4	881643.8 ±0.3	0.52 ± 0.17	(< 2.1)	$2'.33$
NPX1130.1a	112215.3 ±0.4	882253.0 ±0.1	2.72 ± 0.10	1.9 x 1.0	$0'.82$
NPX1130.1b	112224.3 ±0.4	882257.0 ±0.1	0.87 ± 0.08	1.8 x 1.2	$0'.75$
NPX1130.2	112254.7 ±0.3	882444.3 ±0.2	0.72 ± 0.08	(< 1.6)	$1'.88$
NPX1345.1	135633.3 ±0.1	882043.1 ±0.3	0.59 ± 0.08	(< 1.7)	$1'.00$
NPX1345.2	135545.8 ±0.1	881919.9 ±0.7	0.91 ± 0.19	(< 2.1)	$2'.33$
NPX1345.3	135159.4 ±2.0	882136.3 ±0.4	0.37 ± 0.18	(< 2.4)	$1'.61$
NPX1700.1a	172455.0 ±0.3	881300.8 ±0.1	2.64 ± 0.36	(< 3.4)[b]	$0'.60$
NPX1700.1b	172521.0 ±0.7	881249.3 ±0.1	1.86 ± 0.22	(< 4.3)[b]	$0'.87$
NPX1700.2	172726.5 ±0.8	881348.0 ±0.1	0.71 ± 0.22	(< 3.1)	$1'.79$
NPX2045.1	210515.1 ±1.0	880520.2 ±0.8	4.90 ± 0.59	3.2 x 1.3	$3'.73$
NPX2130.1	213724.6 ±1.4	875910.6 ±0.3	2.13 ± 0.21	(< 4.2)	$3'.11$
NPX2130.2	214450.2 ±0.3	880049.6 ±0.1	0.38 ± 0.14	(< 1.8)	$1'.15$

[a] Outside 20% primary beam, included for comparison with 20 GHz flux

[b] Extended lobes with bright compact hotspots

TABLE 5–4

VLA-RING 1.4/8.5 GHz SOURCE CATALOGUE

Source	$S_{8.5}$ (mJy)	$S_{1.4}$ (mJy)	$\alpha_{1.4}^{8.5}$	S_{20} (mJy)	f^{-1}	T_{est} μK*
NPR0015.1	6.27 ± 0.41	23.1 ± 1.2	0.73 ± 0.08	3.35 ± 0.48	97 ± 36	8 ± 3
NPR0045.1	62.2 ± 2.8	161.0 ± 2.6	0.53 ± 0.08	39.3 ± 4.6 [a]	-	-
NPR0045.2	1.15 ± 0.34	7.9 ± 1.1	1.08 ± 0.19	0.45 ± 0.23	7.4 ± 1.7	14 ± 8
NPR0415.1	5.92 ± 0.11	22.6 ± 1.3	0.75 ± 0.08	3.11 ± 0.41	12.2 ± 2.4	57 ± 14[b]
NPR0630.1	-	111.3 ± 3.6	(0.7)	(17.5)	25.3 ± 4.7	(154)
NPR0700.1	0.45 ± 0.18	2.2 ± 1.2	0.89 ± 0.38	0.21 ± 0.17	5.1 ± 1.0	9 ± 8
NPR0745.1	-	7.5 ± 0.9	(0.7)	(1.18)	15.4 ± 3.4	(17)
NPR0830.1	0.77 ± 0.20	2.6 ± 0.6	0.68 ± 0.20	0.43 ± 0.17	-	-
NPR0845.1	1.08 ± 0.27	< 1.8	$<0.29 \pm 0.24$	0.84 ± 0.29	-	-
NPR0900.1	0.52 ± 0.17	< 1.7	$<0.66 \pm 0.20$	$> 0.29 \pm 0.13$	257 ± 113	> 0.3
NPR1130.1	3.59 ± 0.13	16.9 ± 1.4	0.87 ± 0.08	1.70 ± 0.25	1.6 ± 0.1	237 ± 40
NPR1130.2	0.72 ± 0.08	< 2.1	$<0.60 \pm 0.20$	$> 0.43 \pm 0.13$	16.1 ± 3.8	> 6
NPR1200.1	-	23.4 ± 1.9	(0.7)	(3.68)	14.1 ± 3.4	(58)
NPR1345.1	0.59 ± 0.08	1.4 ± 0.5	0.48 ± 0.22	0.39 ± 0.12	2.5 ± 0.4	35 ± 12
NPR1345.2	0.91 ± 0.19	< 1.7	$<0.35 \pm 0.23$	$> 0.67 \pm 0.23$	212 ± 79	> 0.7
NPR1345.3	0.37 ± 0.18	< 1.5	$<0.79 \pm 0.34$	$> 0.19 \pm 0.14$	8.2 ± 1.7	> 5
NPR1700.1	4.50 ± 0.42	29.3 ± 2.3	1.05 ± 0.09	1.82 ± 0.39	1.6 ± 0.1	254 ± 58
NPR1700.2	0.71 ± 0.22	< 2.7	$<0.75 \pm 0.26$	$> 0.37 \pm 0.19$	15.6 ± 4.1	> 5
NPR2015.1	-	217.3 ± 2.4	(0.7)	(34.2)	62.1 ± 12.3	(123)
NPR2045.1	4.90 ± 0.59	63.5 ± 3.1	1.44 ± 0.09	1.42 ± 0.41	-	-
NPR2130.1	2.13 ± 0.21	4.7 ± 1.2	0.44 ± 0.16	1.46 ± 0.33	-	-
NPR2130.2	0.38 ± 0.14	< 1.2	$<0.65 \pm 0.28$	$> 0.22 \pm 0.12$	3.3 ± 0.7	> 15
NPR2330.1	-	3.3 ± 1.5	(0.7)	(0.52)	10.3 ± 2.3	(11)

* Expected contribution to RING measurements, not antenna temperature

[a] Outside 20% primary beam, included for comparison with 20 GHz flux

[b] Double source, spectral index extrapolation unreliable (see text)

TABLE 5-5

20 GHz OBSERVATIONS OF VLA 8.5 GHz SOURCES

Source	T_{20} (μK)	S_{20} (mJy)	$\alpha_{8.5}^{20}$
NPR0015.1	833 ± 90	3.74 ± 0.45	0.60 ± 0.20
NPR0045.1	5253 ± 90	23.6 ± 1.2	1.13 ± 0.14
NPR0415.1	1431 ± 92	6.43 ± 0.52	-0.10 ± 0.15 [a]
NPR2045.1	446 ± 89	2.00 ± 0.41	1.04 ± 0.30

[a] Double source at 8.5 GHz, α versus integrated $S_{8.5}$

TABLE 5-6

ESTIMATED CONTAMINATION OF RING FIELDS

Source	Field	f^{-1}	T_{est} (μK)	T_{RING} (μK)	T_{res} (μK)
NPR0415.1[a]	NPR0400	−11.8 ± 2.7	−121 ± 29	−213 ± 113	− 92 ± 117
	NPR0415	8.7 ± 2.5	164 ± 48	318 ± 114	154 ± 124
	NPR0430	−33 ± 12	− 43 ± 16	− 82 ± 112	− 39 ± 113
NPR1130.1	NPR1100	−3.4 ± 0.3	−112 ± 21	−132 ± 113	− 20 ± 115
	NPR1130	1.6 ± 0.1	234 ± 41	280 ± 114	46 ± 121
	NPR1145	−3.1 ± 0.2	−123 ± 21	−416 ± 101	−293 ± 103
NPR1700.1	NPR1645	−2.8 ± 0.2	−147 ± 33	−220 ± 105	− 73 ± 110
	NPR1700	1.6 ± 0.1	254 ± 58	342 ± 121	88 ± 133
	NPR1715	−3.4 ± 0.3	−119 ± 28	−233 ± 116	−114 ± 119
NPR1345.1	NPR1330	−2.9 ± 0.3	− 30 ± 10	− 29 ± 102	1 ± 102
	NPR1345	2.5 ± 0.4	35 ± 12	271 ± 101	236 ± 102
	NPR1400	−4.0 ± 0.6	− 22 ± 8	−202 ± 110	−180 ± 110
NPR0630.1	NPR0615	−88 ± 46	(−44)	186 ± 109	
	NPR0630	25.3 ± 4.7	(154)	132 ± 116	
	NPR0645	−258 ± 174	(−15)	−340 ± 104	
NPR1200.1	NPR1145	−95 ± 36	(−9)	−416 ± 101	
	NPR1200	14.1 ± 3.4	(58)	−109 ± 106	
	NPR1215	−55 ± 20	(−15)	40 ± 124	
NPR2015.1	NPR2000	−51 ± 13	(−149)	192 ± 116	
	NPR2015	62 ± 12	(123)	80 ± 121	
	NPR2030	-	-	−174 ± 123	

[a] 20 GHz source assumed to be at position of NPX0415.1b (see text)

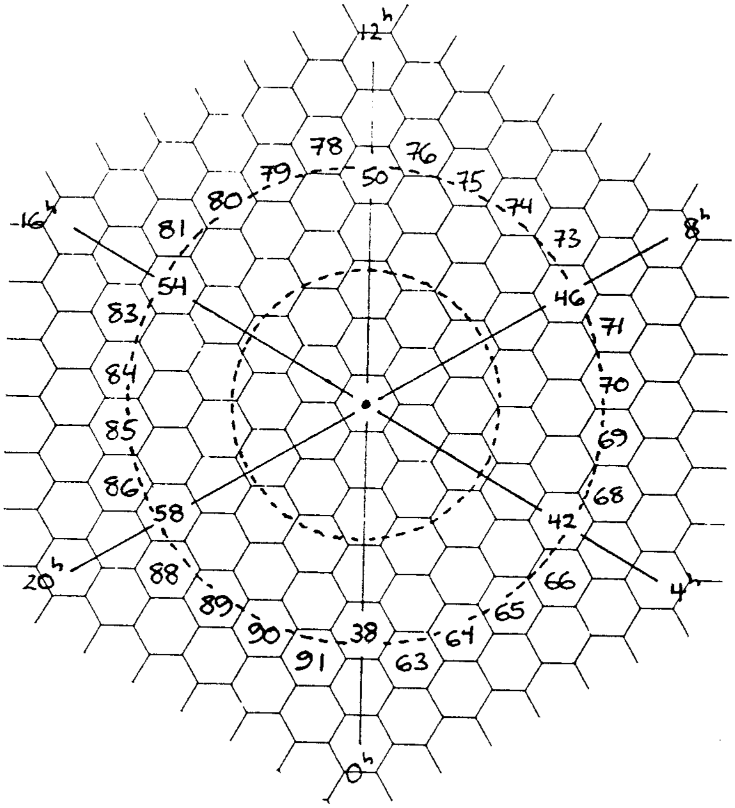

FIGURE 5–1. Geometry of the VLA 1.4 GHz survey map centers. The 30 numbered hexagons are those containing RING fields. The separation between the vertices and the centers is 26′. The inner and outer dashed circles mark the declination of the NCP and RING respectively.

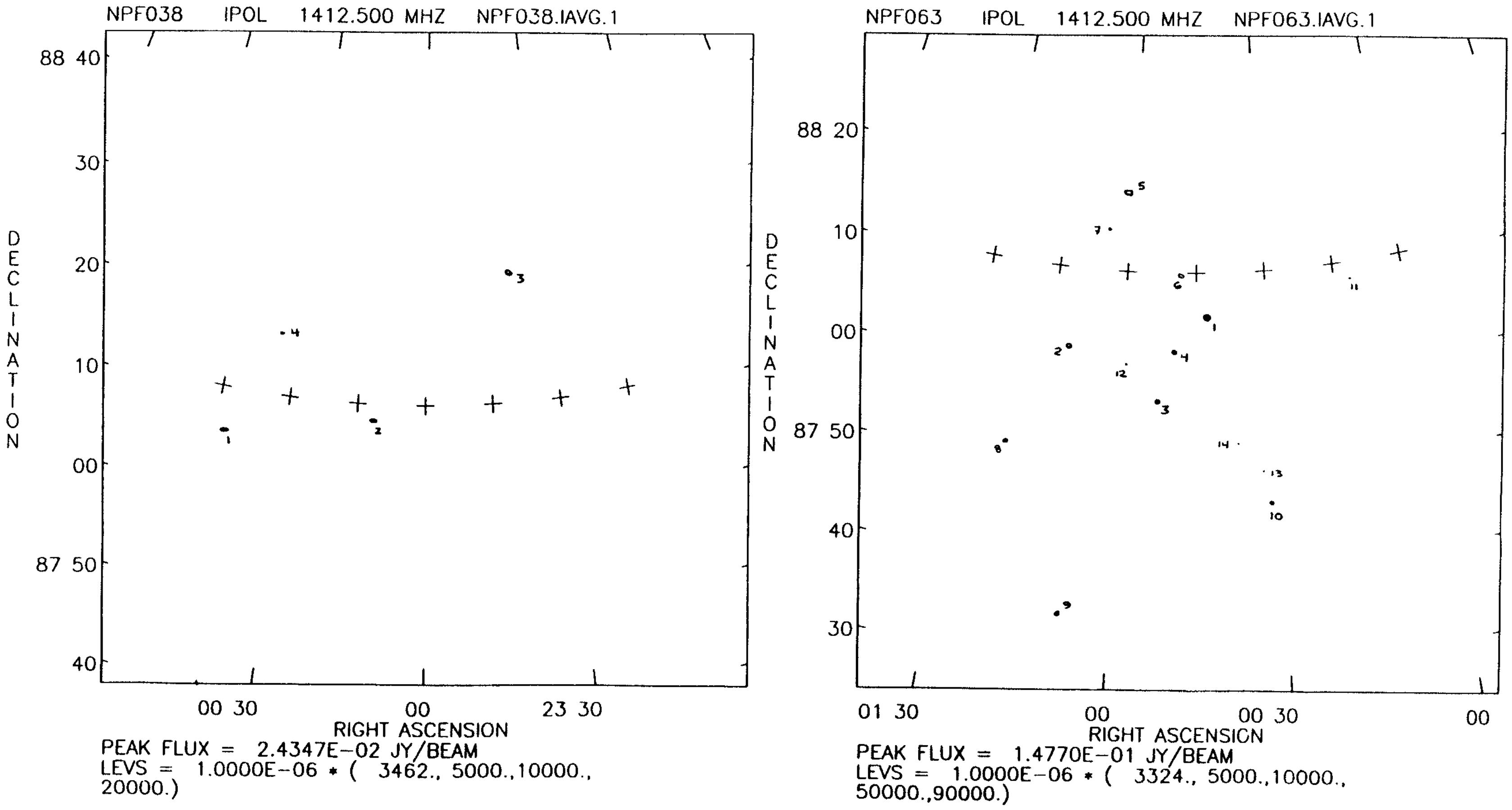

FIGURE 5-2. VLA 1.4 GHz images of RING region. Full 1024 x 1024 area is shown. The VLA primary beam is 32′ FWHM, the OVRO 20 GHz primary beam of 1′.8 FWHM is shown by the crosses at the positions of the RING fields. Sources above the 6σ cutoff in each image are numbered. Coordinates are epoch 1988.0.

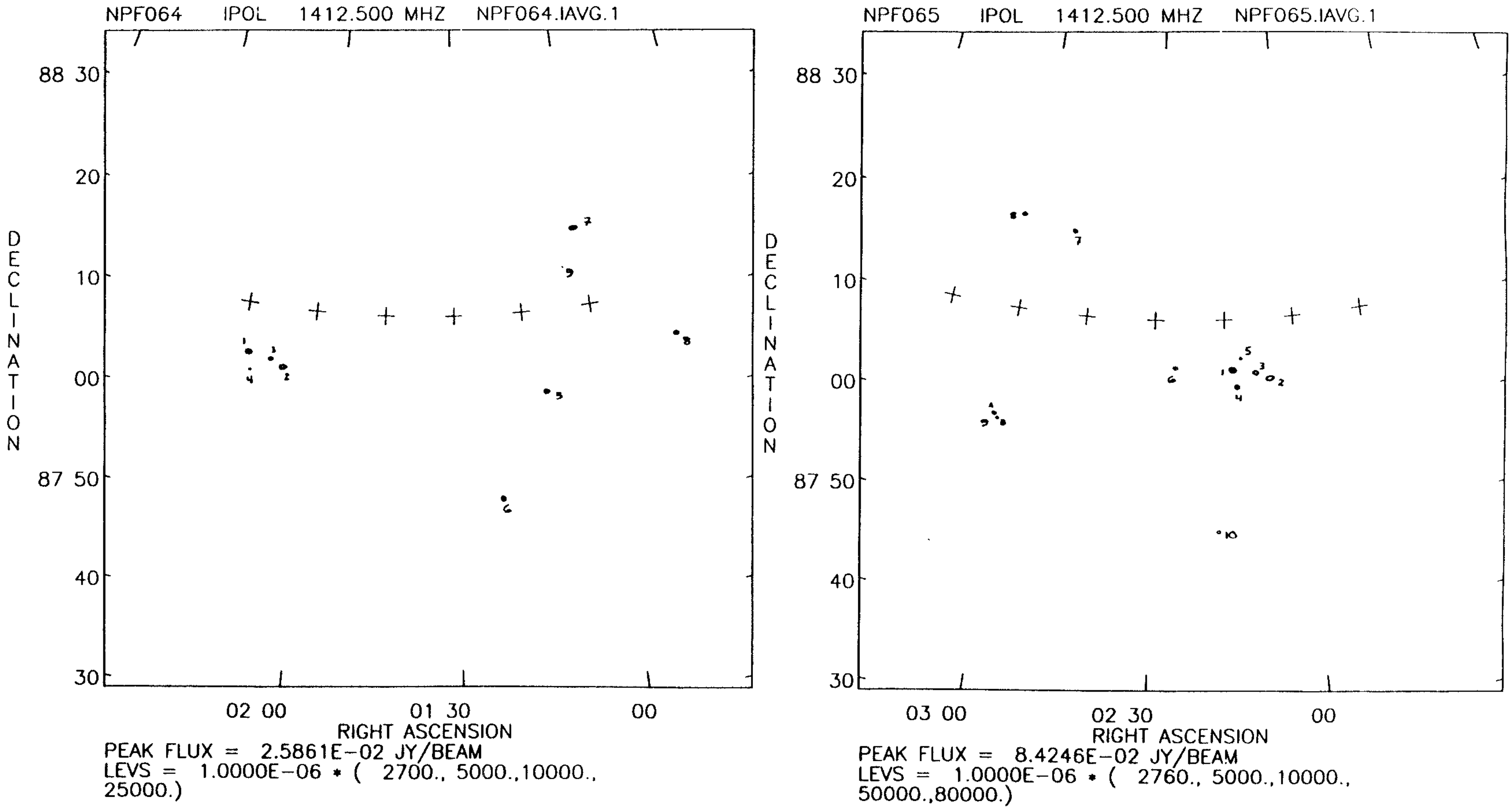

FIGURE 5-2 continued. VLA 1.4 GHz images of RING region.

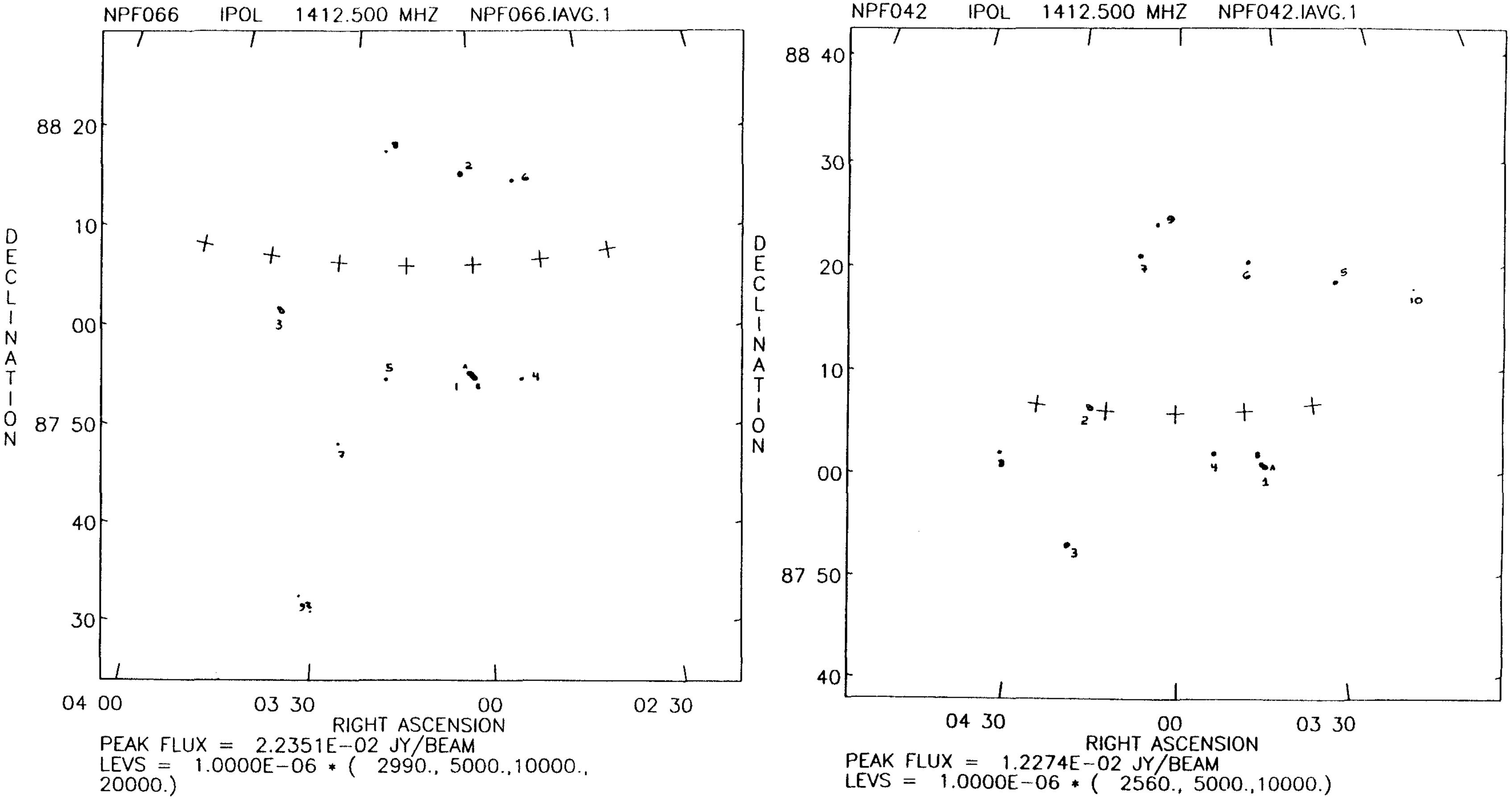

FIGURE 5-2 continued. VLA 1.4 GHz images of RING region.

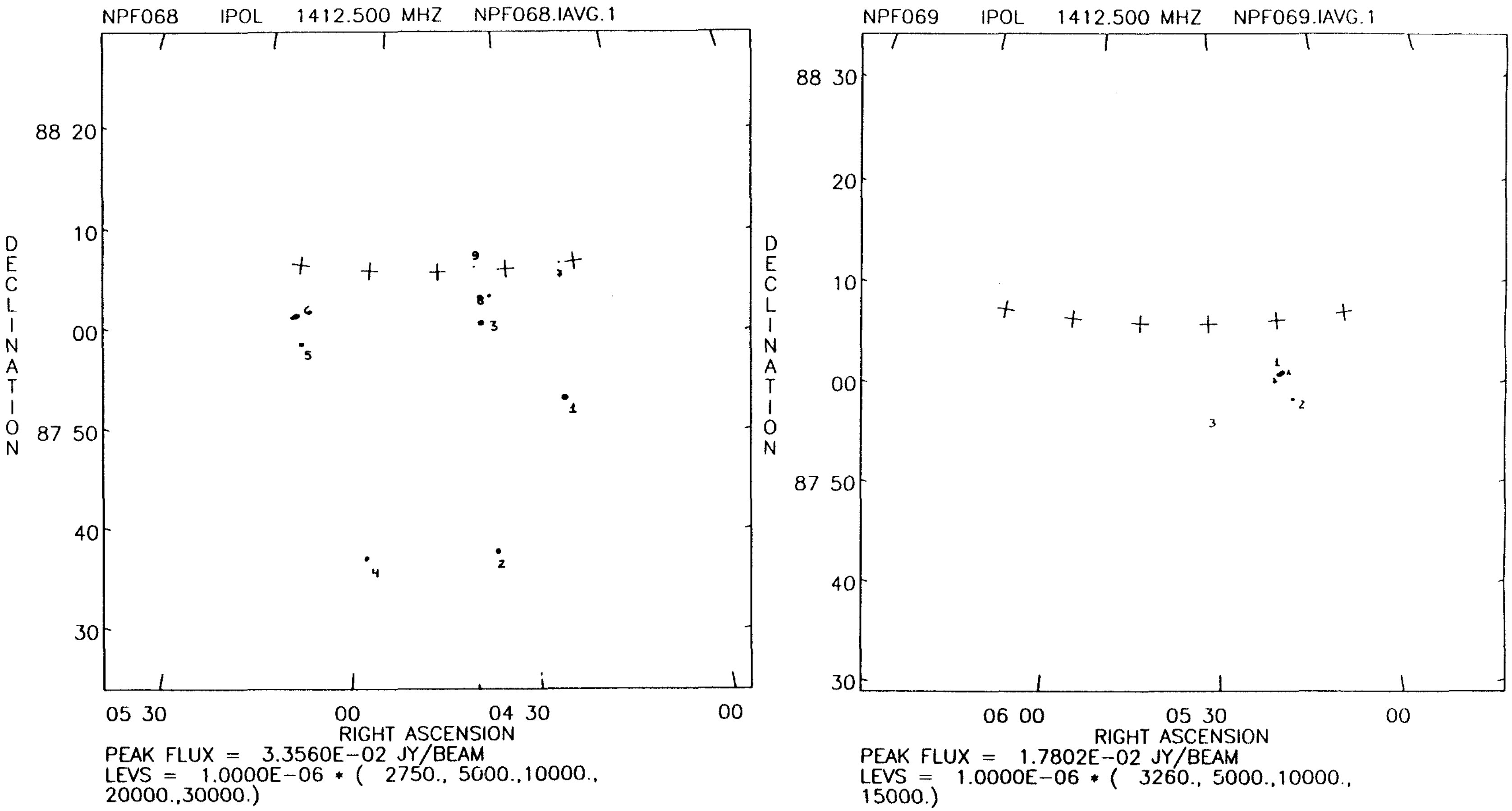

FIGURE 5-2 continued. VLA 1.4 GHz images of RING region.

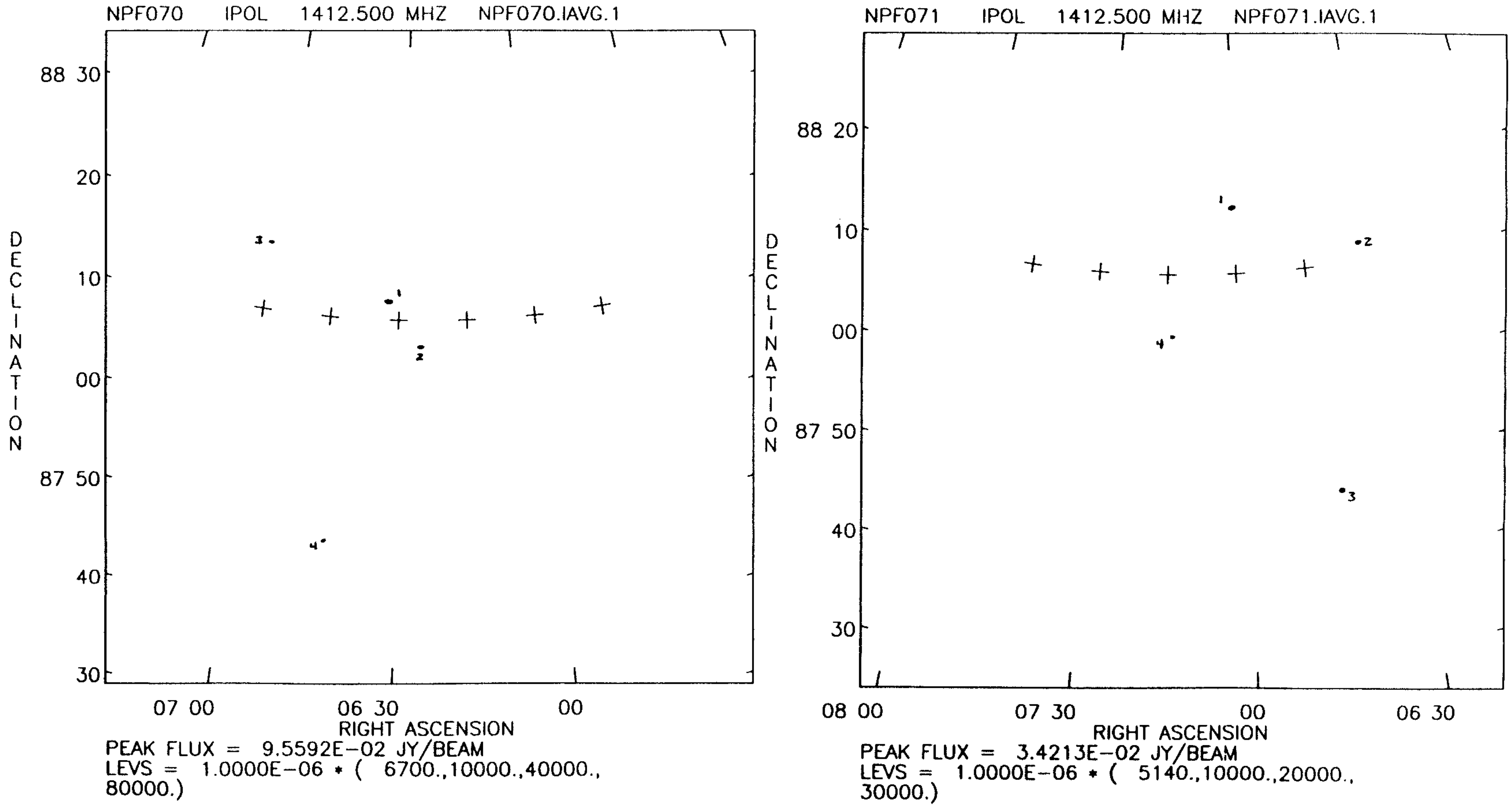

FIGURE 5-2 continued. VLA 1.4 GHz images of RING region.

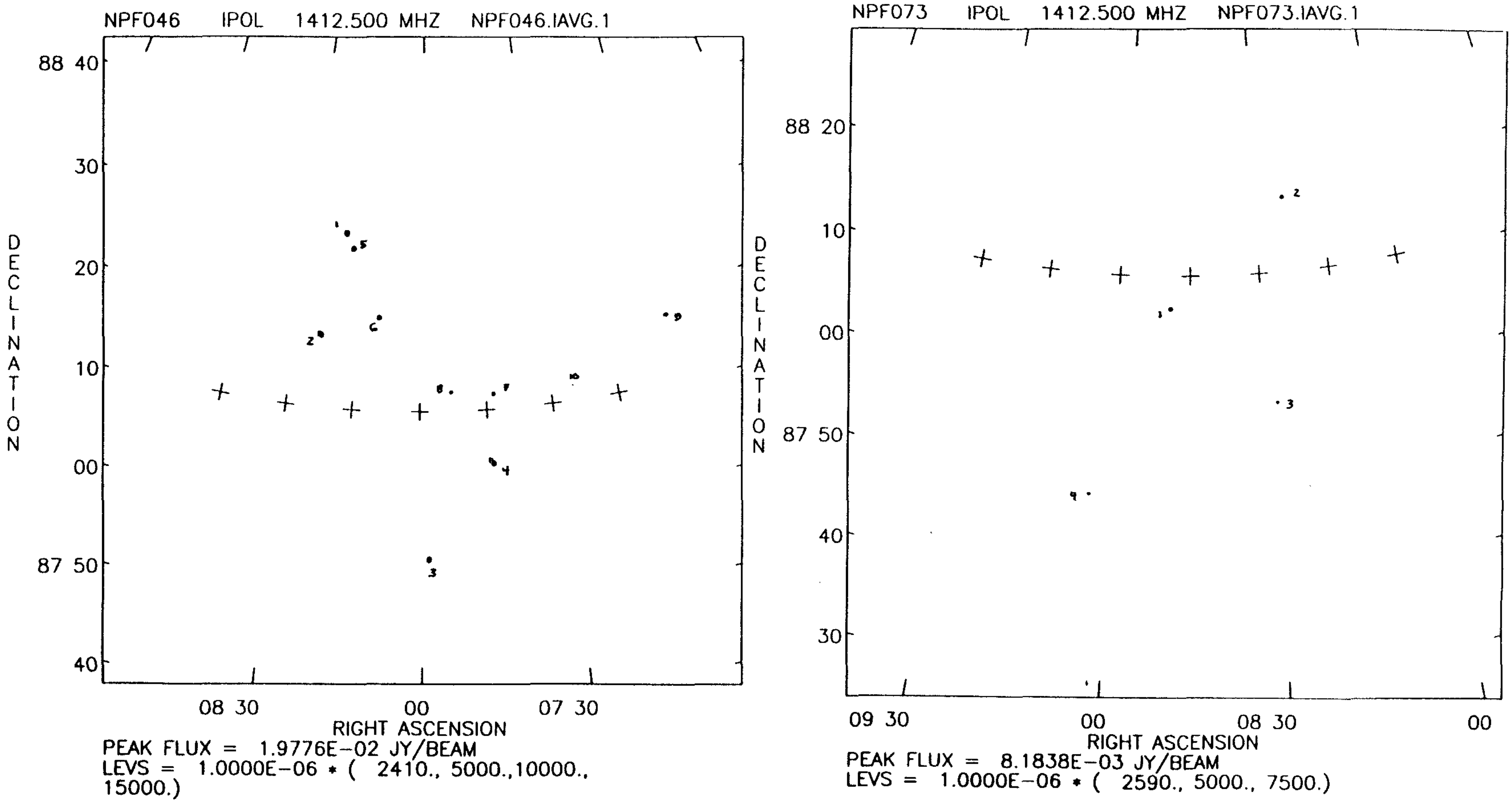

FIGURE 5-2 continued. VLA 1.4 GHz images of RING region.

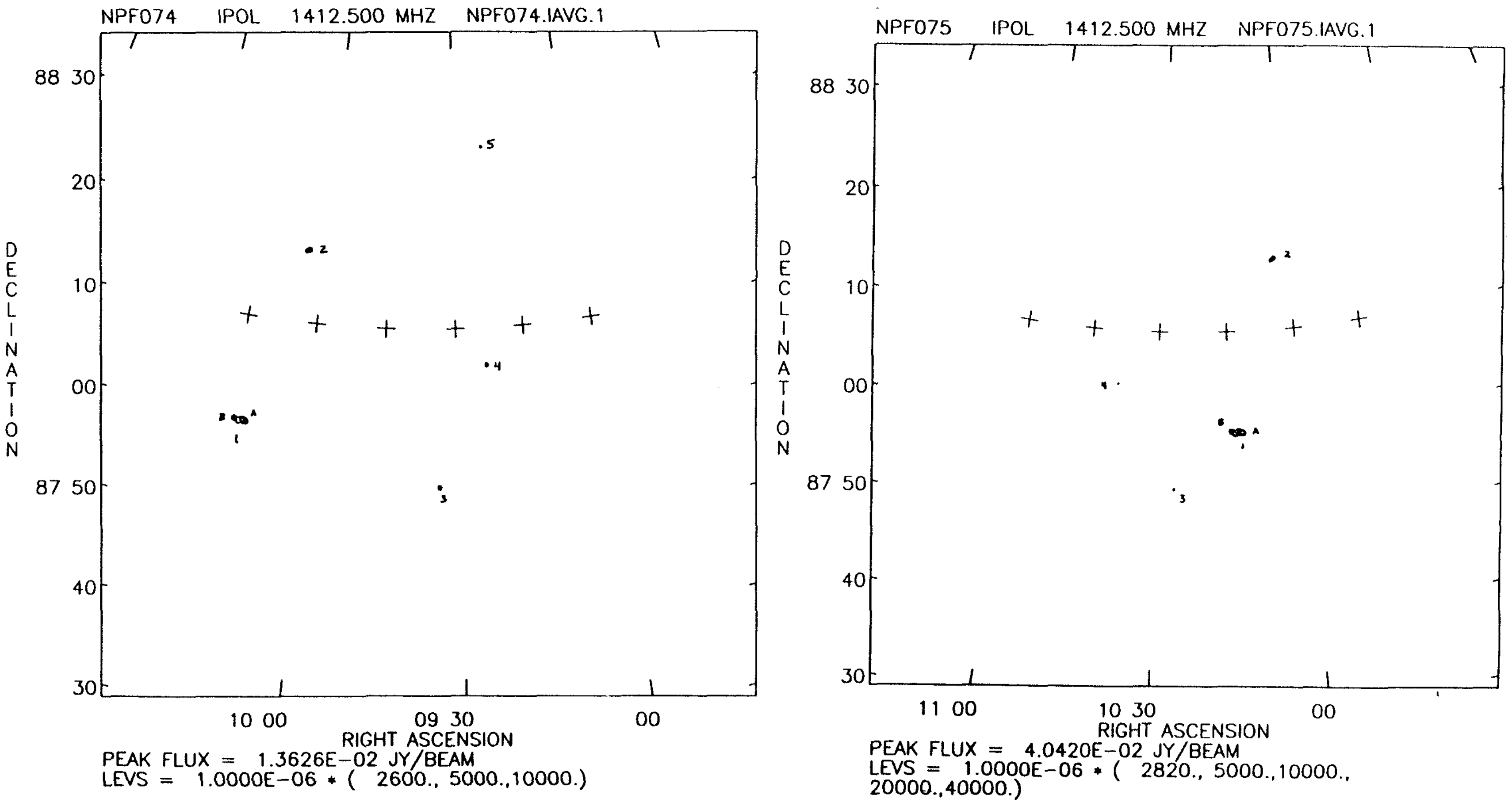

FIGURE 5-2 continued. VLA 1.4 GHz images of RING region.

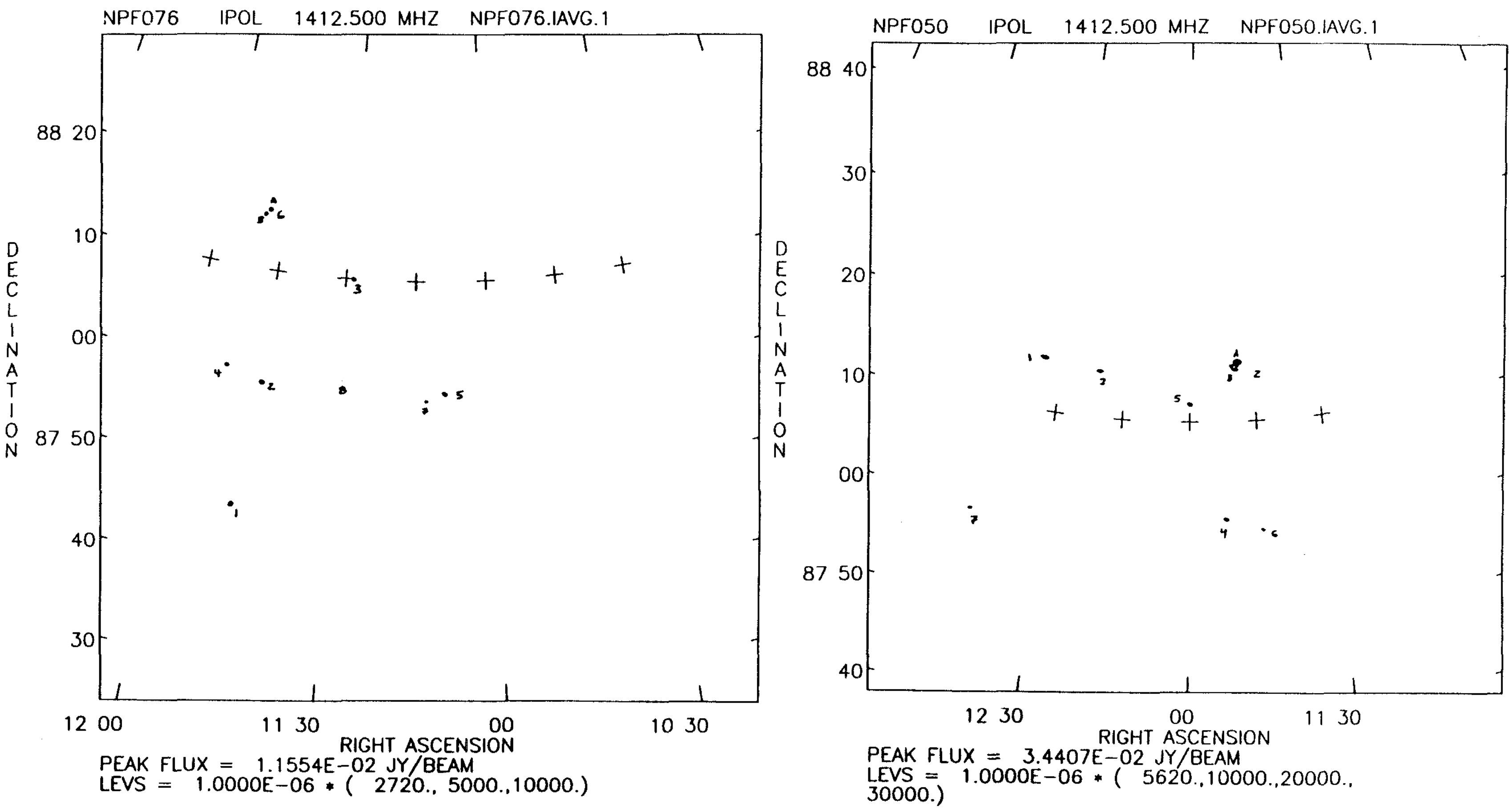

FIGURE 5-2 continued. VLA 1.4 GHz images of RING region.

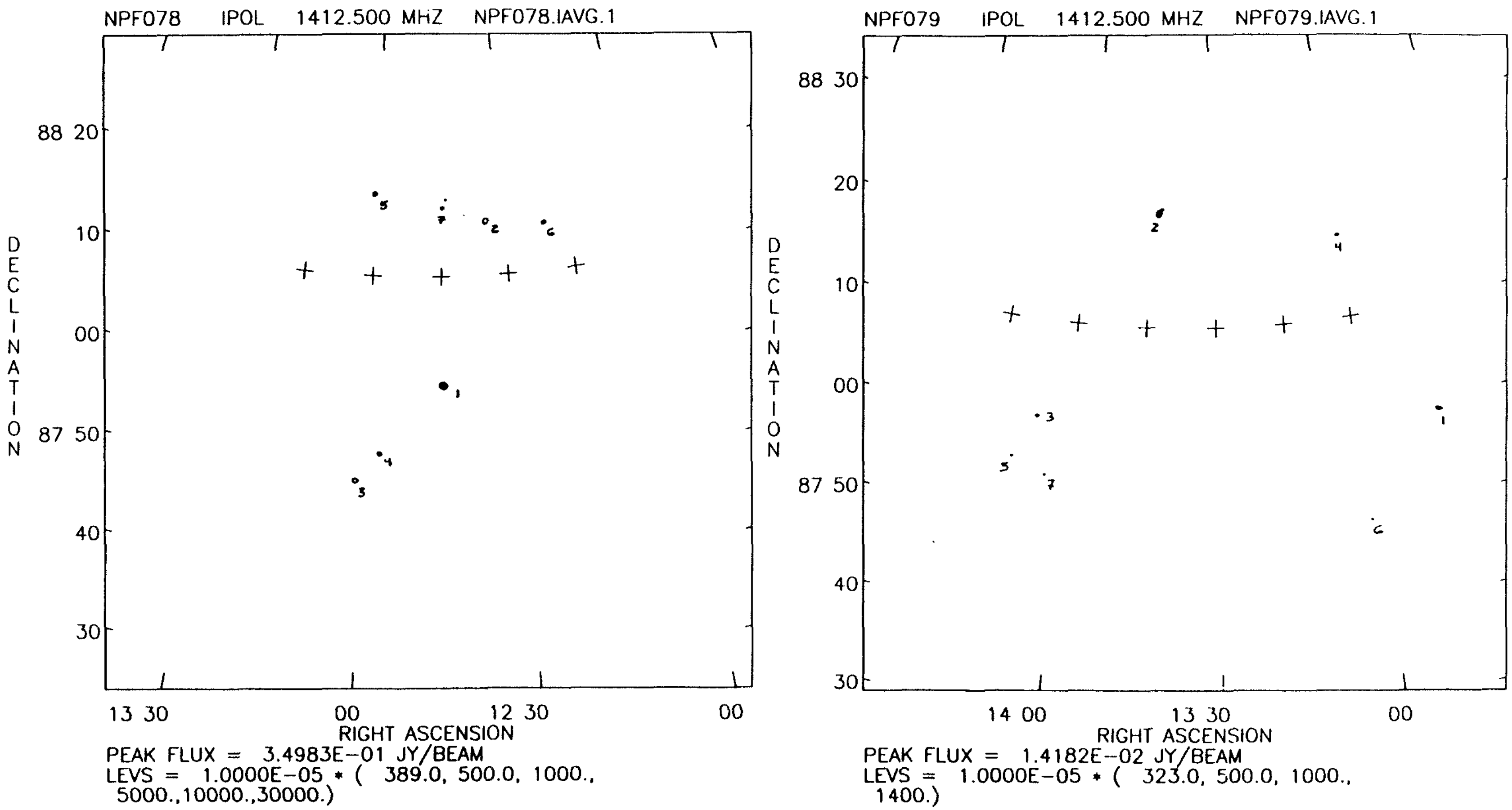

FIGURE 5-2 continued. VLA 1.4 GHz images of RING region.

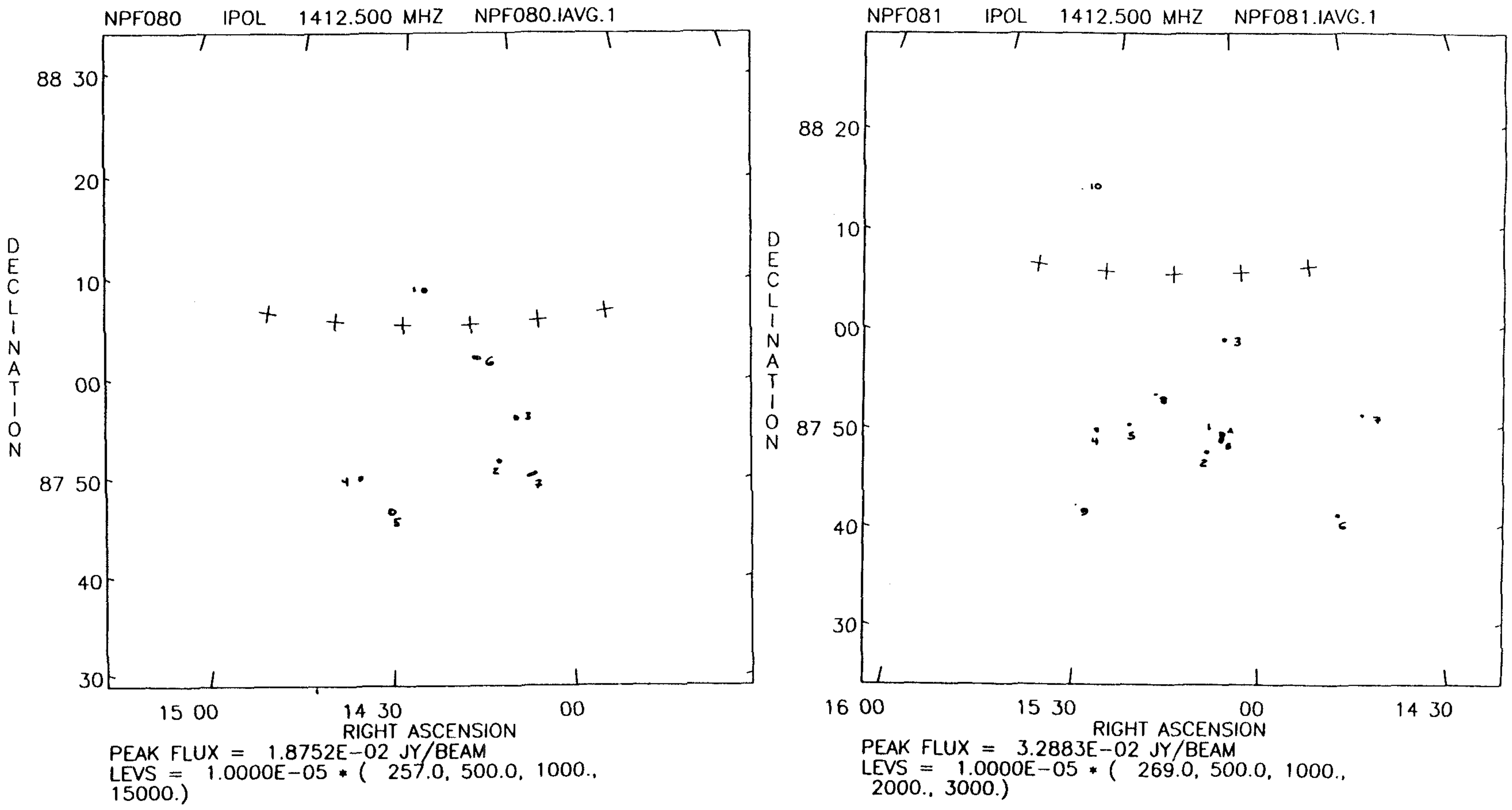

FIGURE 5-2 continued. VLA 1.4 GHz images of RING region.

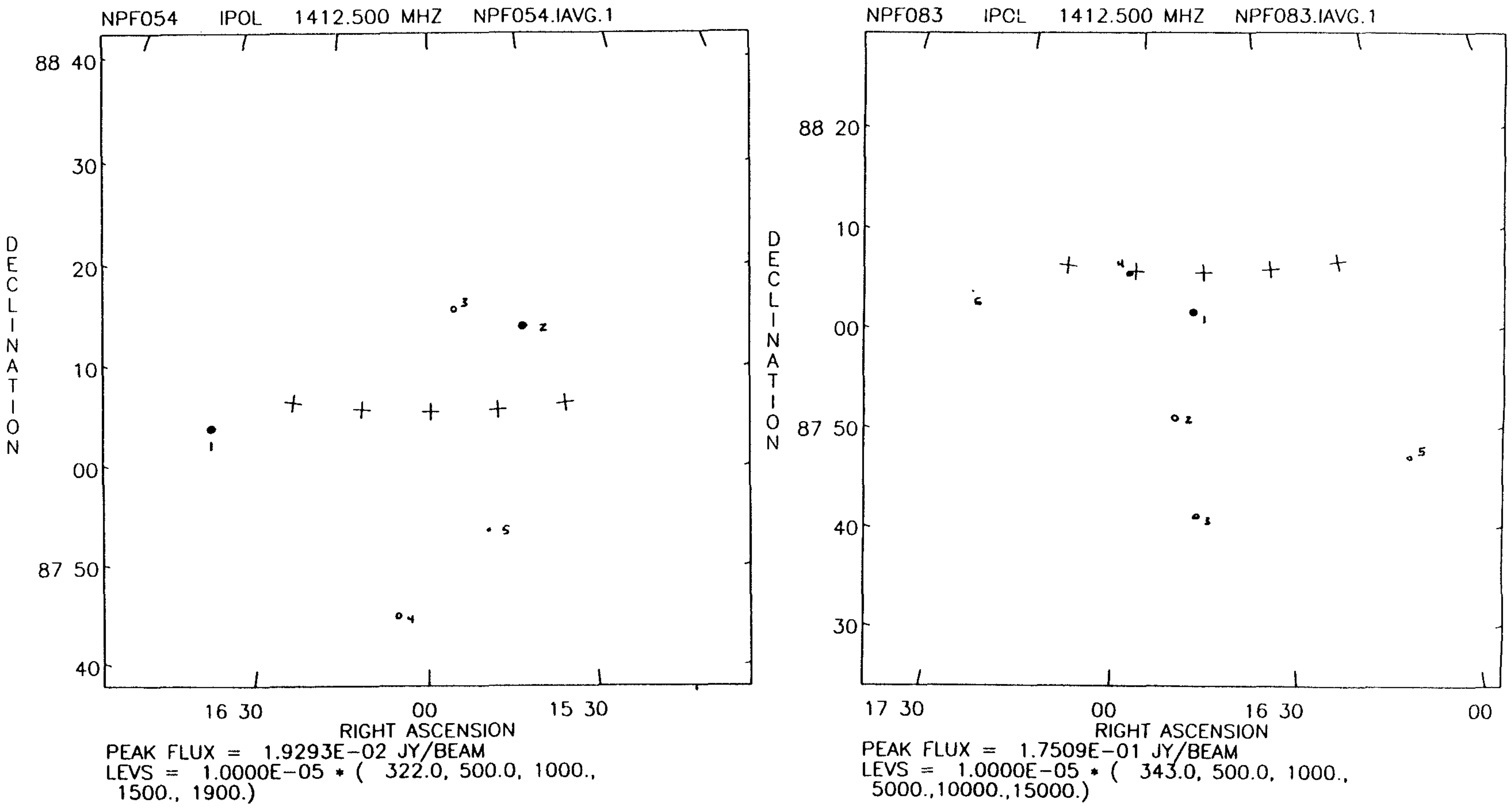

FIGURE 5-2 continued. VLA 1.4 GHz images of RING region.

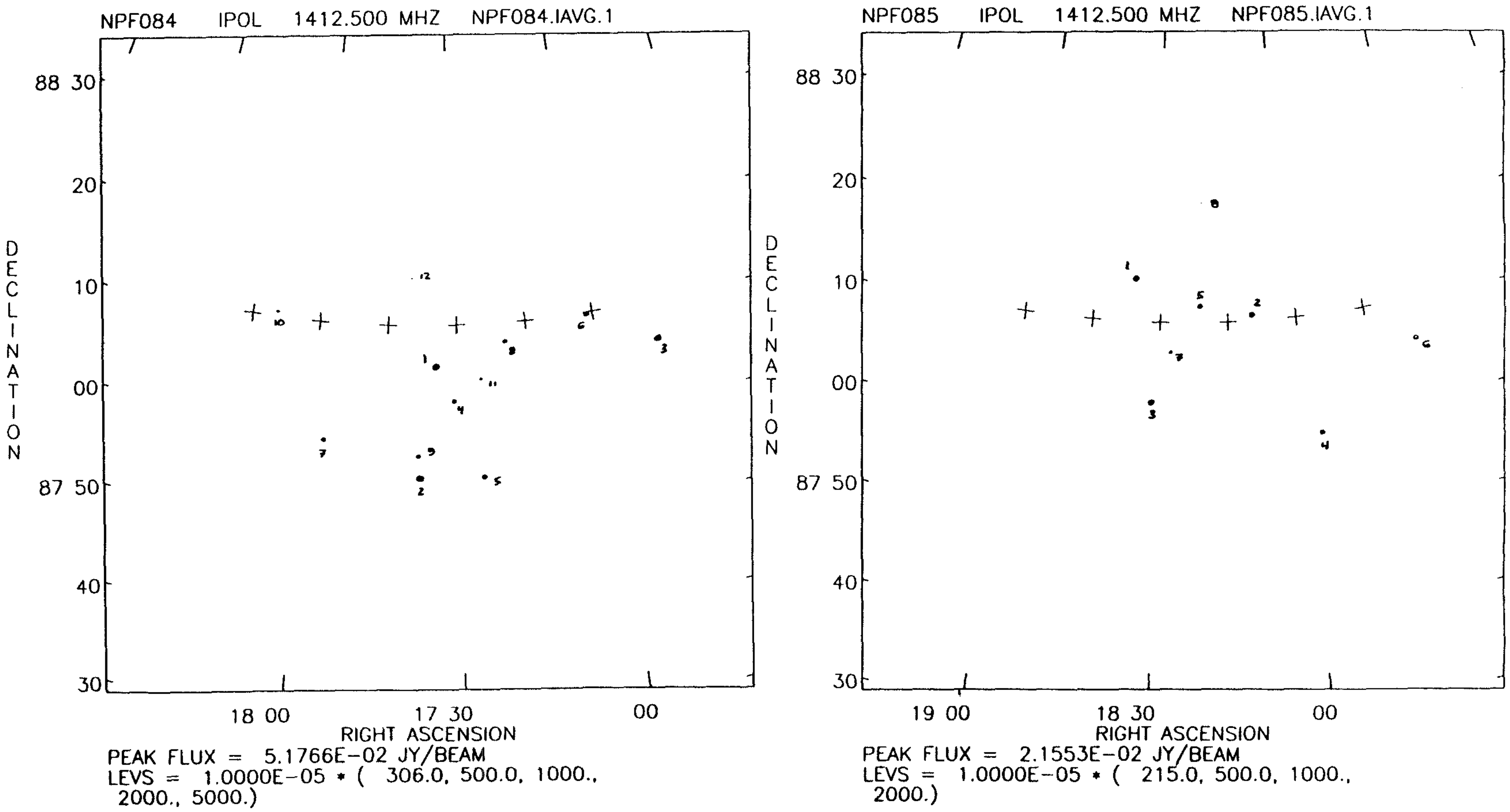

FIGURE 5-2 continued. VLA 1.4 GHz images of RING region.

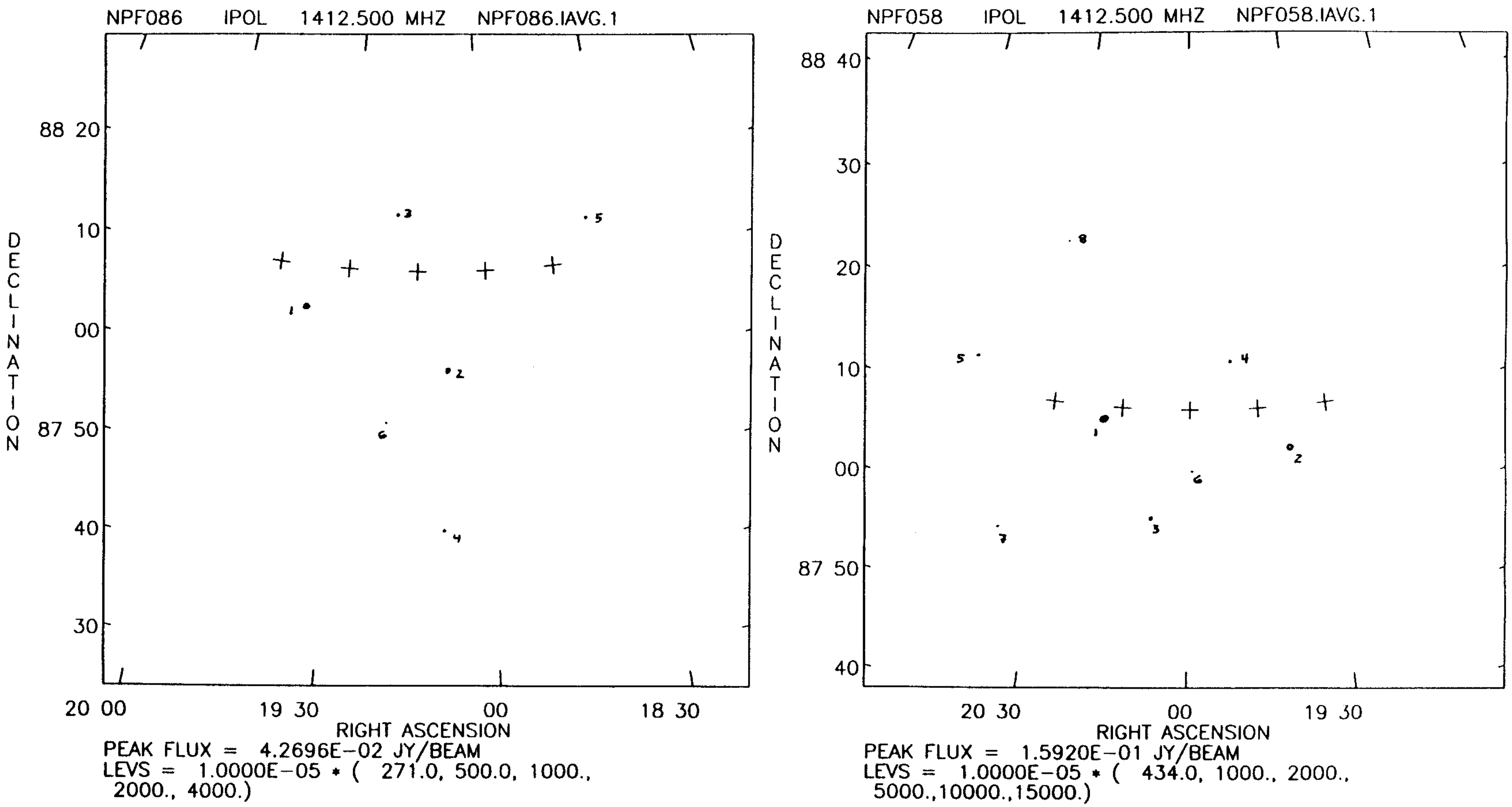

FIGURE 5-2 continued. VLA 1.4 GHz images of RING region.

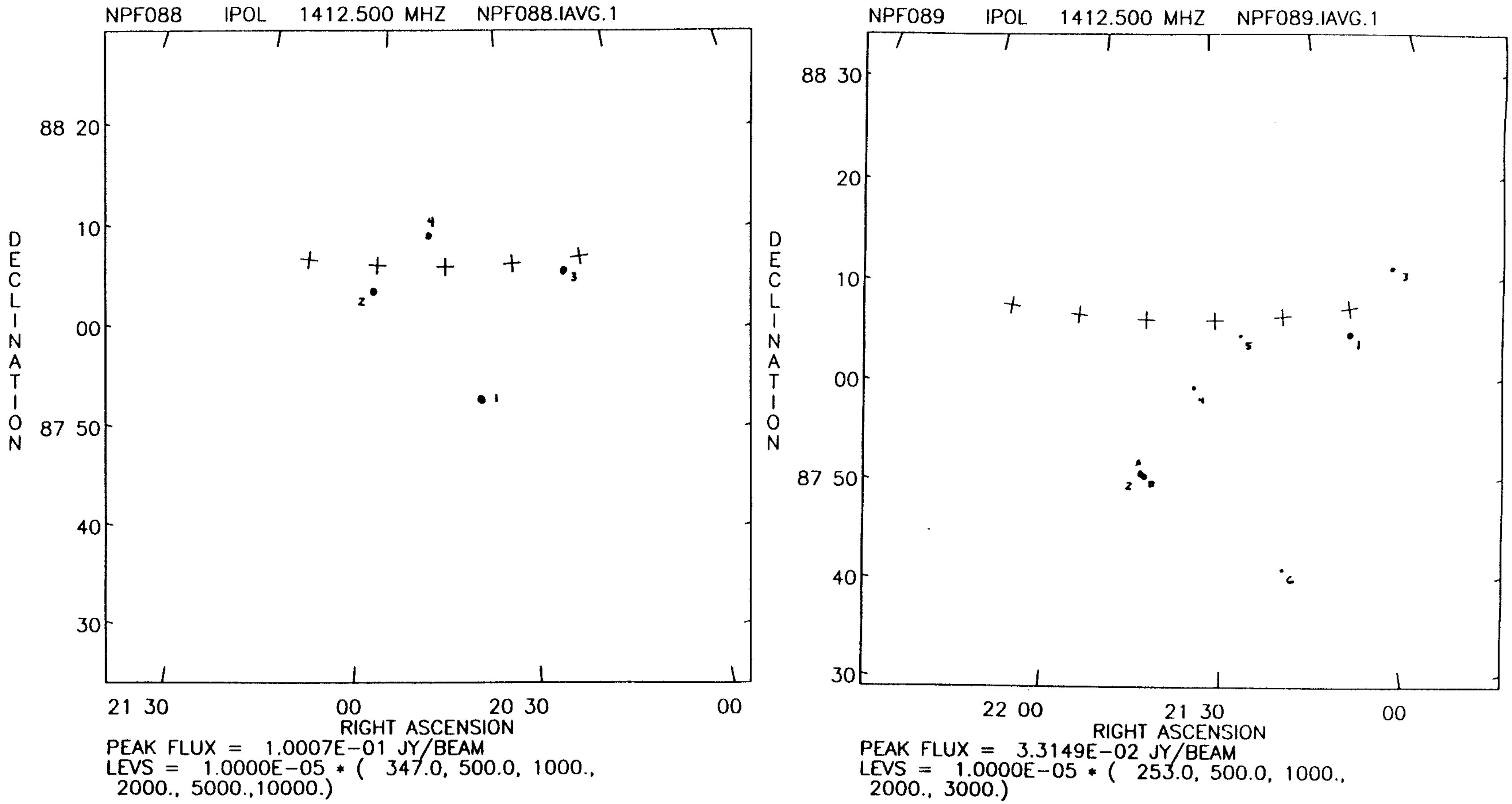

FIGURE 5-2 continued. VLA 1.4 GHz images of RING region.

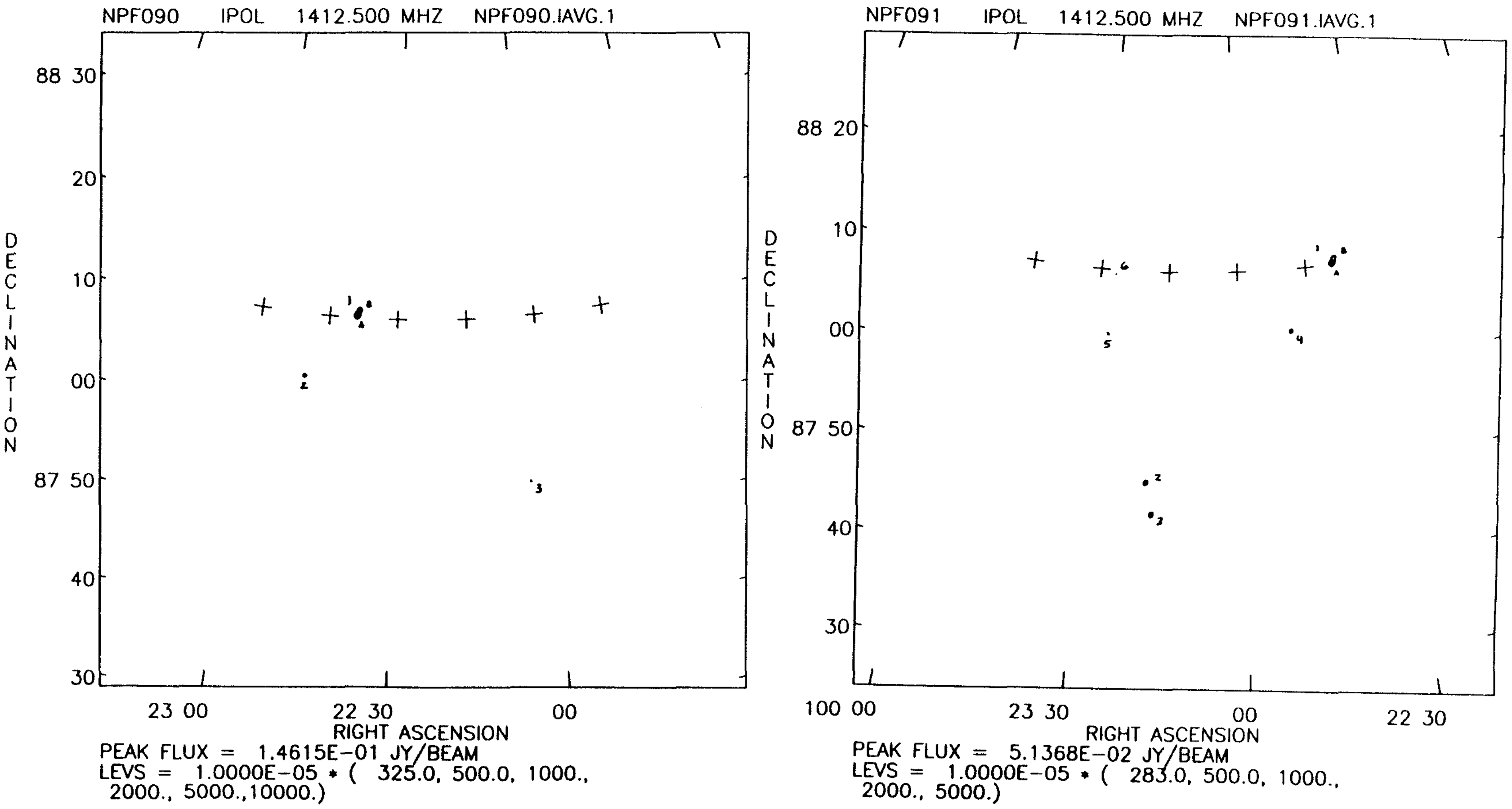

FIGURE 5-2 continued. VLA 1.4 GHz images of RING region.

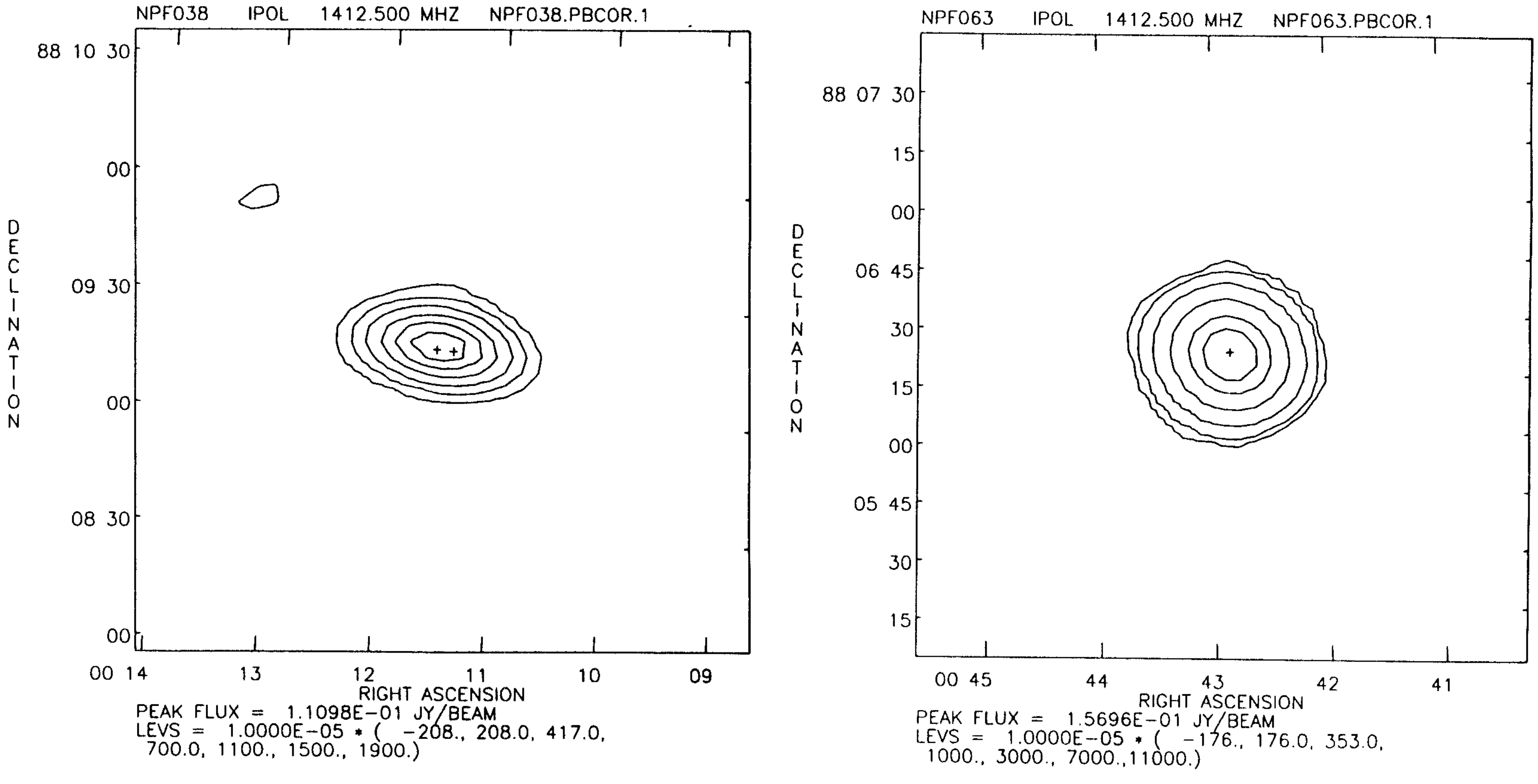

FIGURE 5-3. Contour maps from the 1.4 GHz images of sources detected at 1.4 GHz or 8.5 GHz above the 6σ cutoff. Negative contours are shown as broken lines, and crosses designate the positions of 8.5 GHz components. Shown in this panel are NPR0015.1 (left) and NPR0045.1 (right) with lowest contours $\pm 3\sigma$.

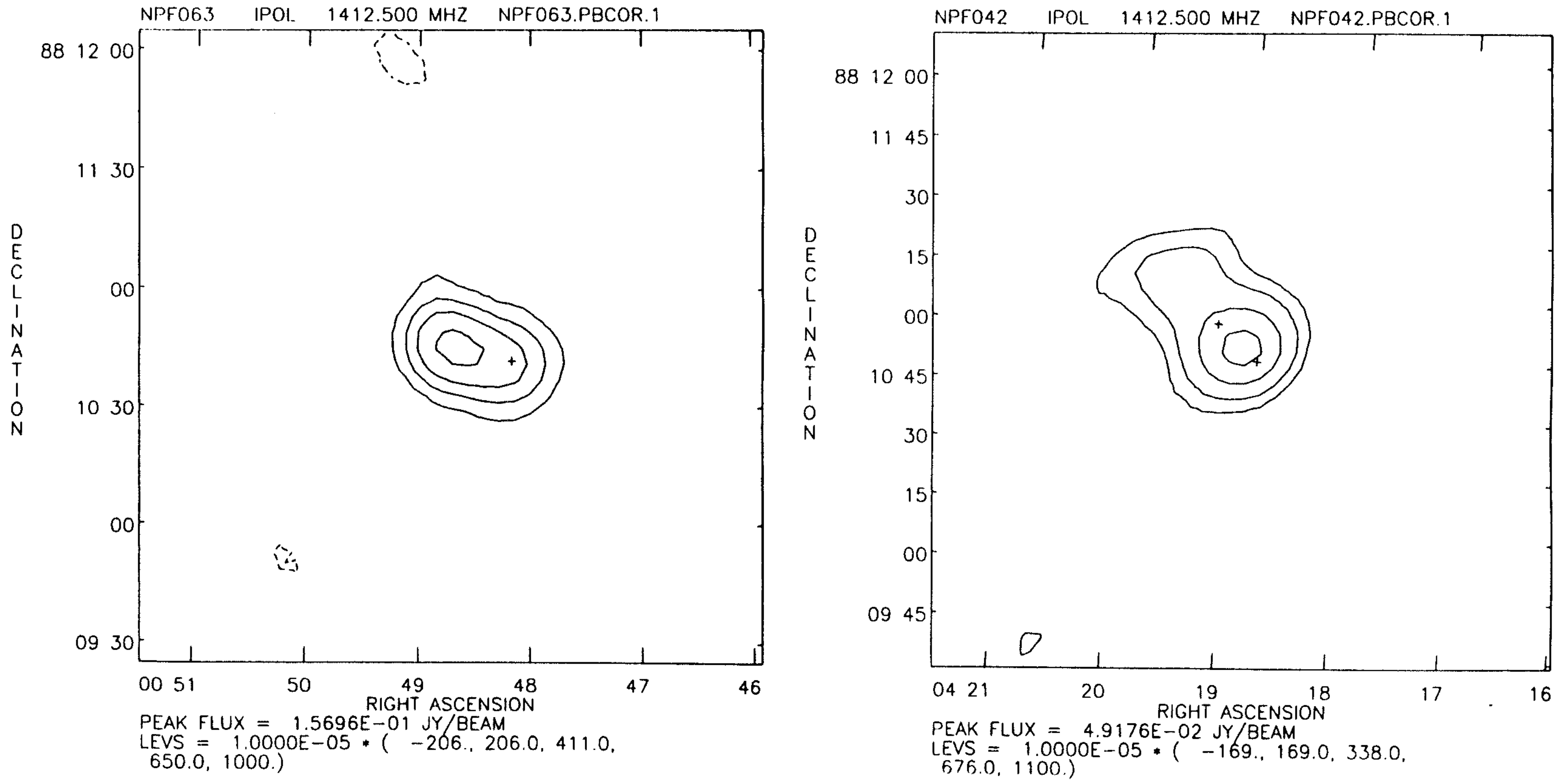

FIGURE 5-3 continued. Contour maps from 1.4 GHz images. NPR0045.2 (left) and NPR0415.1 (right). Lowest contours ±3σ.

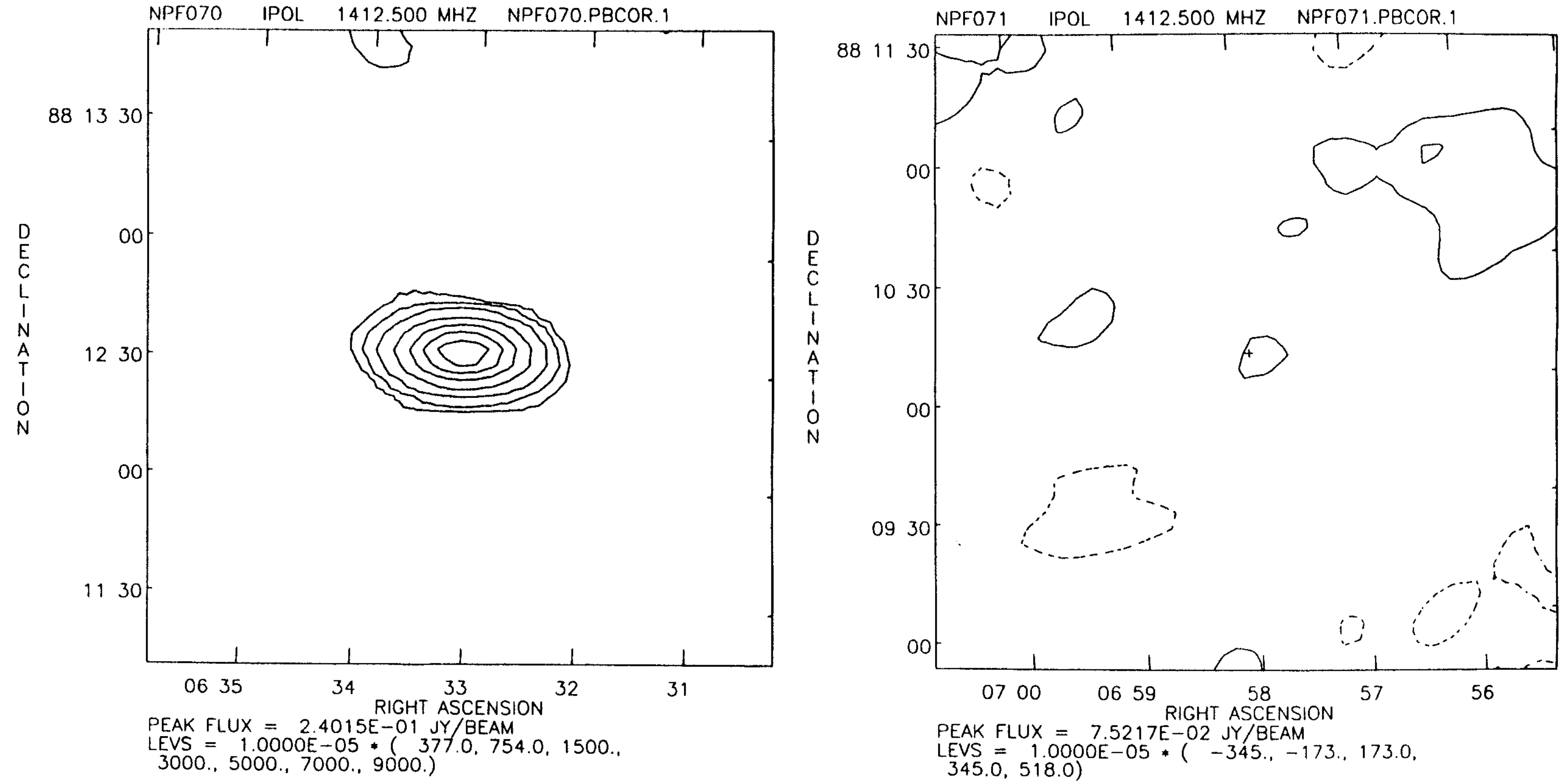

FIGURE 5-3 continued. Contour maps from 1.4 GHz images. NPR0630.1 (left), lowest contours $\pm 3\sigma$, and NPR0700.1 (right), lowest contours $\pm 1.5\sigma$.

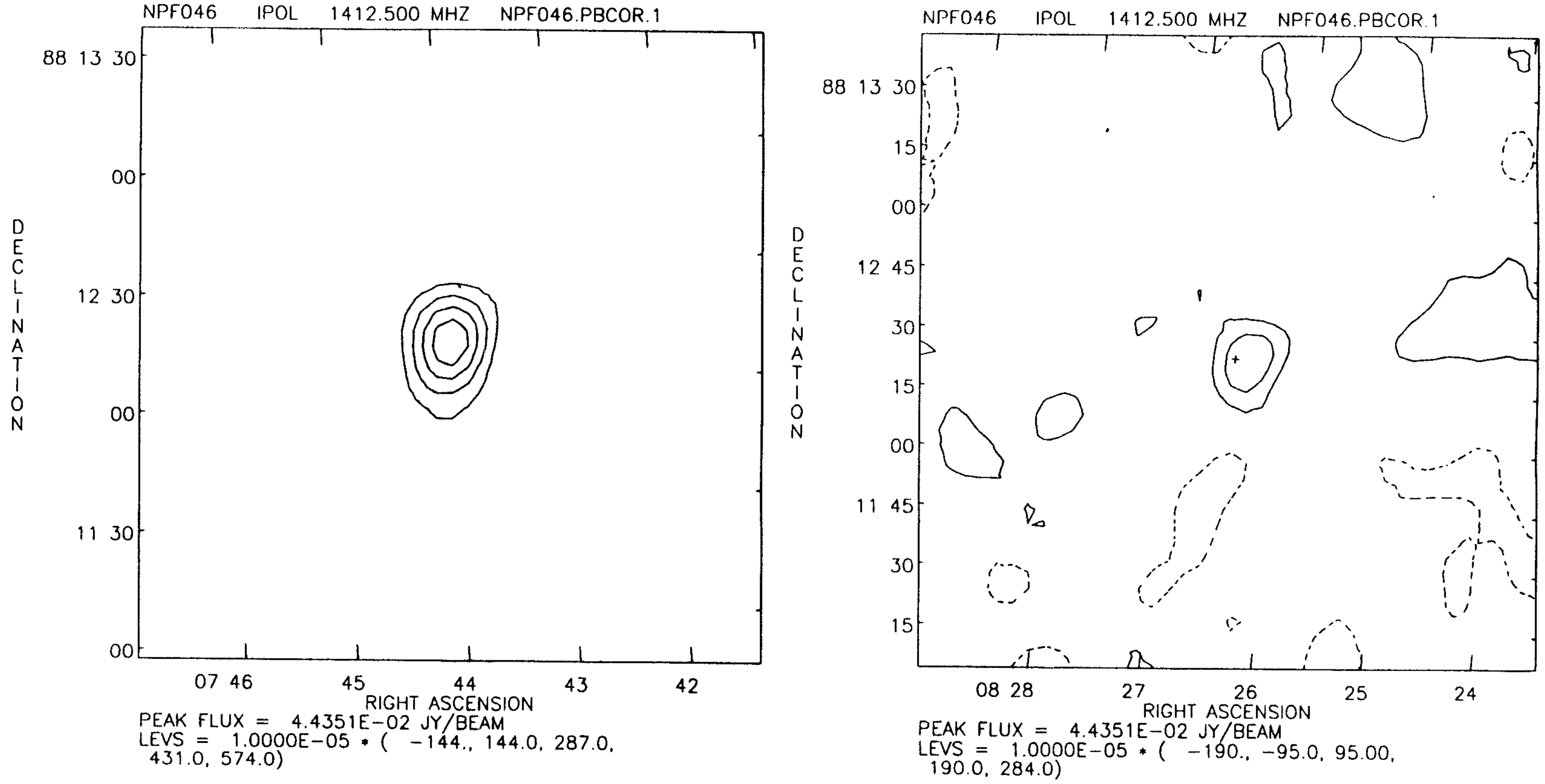

FIGURE 5-3 continued. Contour maps from 1.4 GHz images. NPR0745.1 (left), lowest contours $\pm 3\sigma$, and NPR0830.1 (right), lowest contours $\pm 1.5\sigma$.

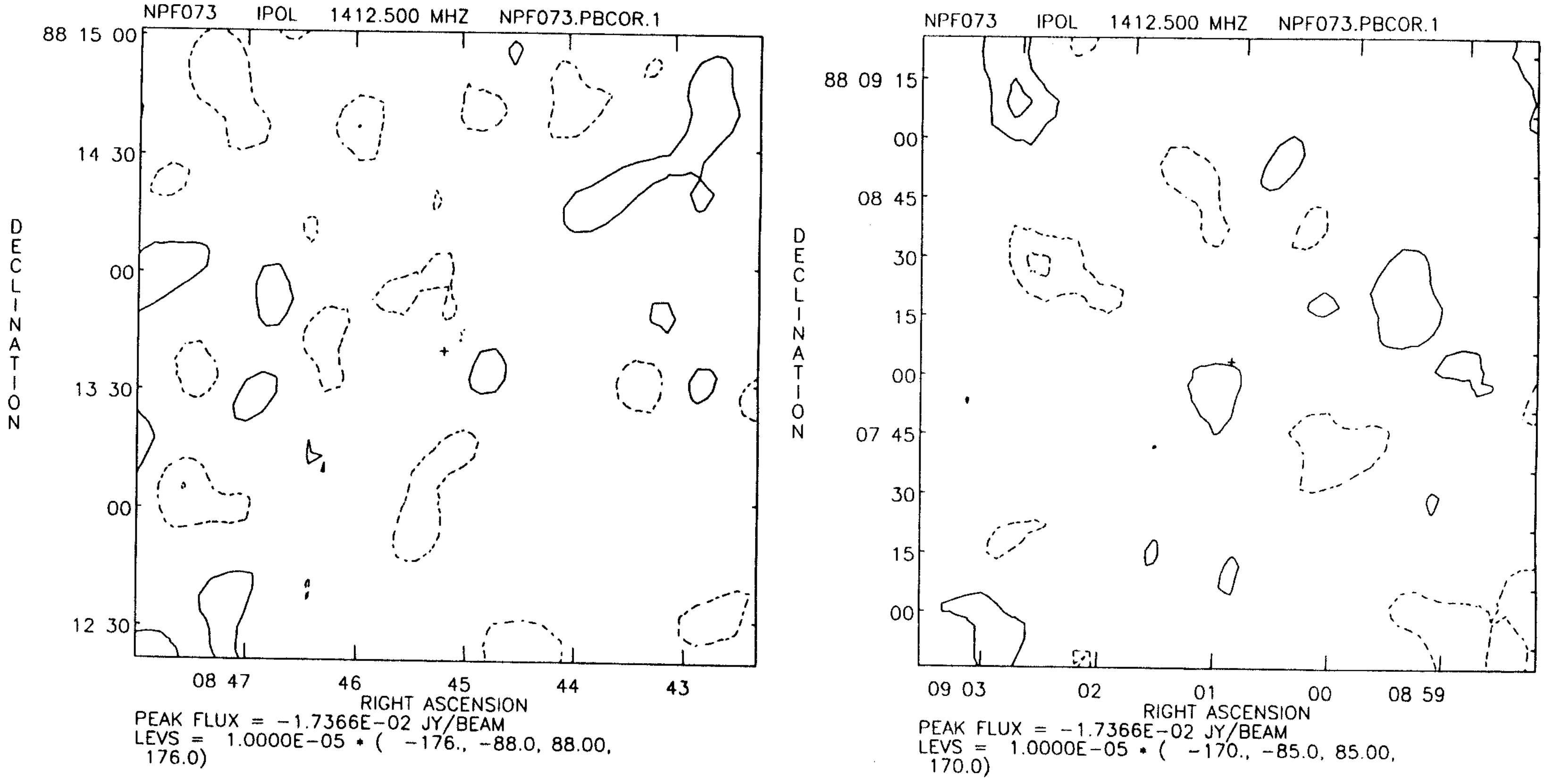

FIGURE 5-3 continued. Contour maps from 1.4 GHz images. NPR0845.1 (left) and NPR0900.1 (right). Lowest contours ±1.5σ.

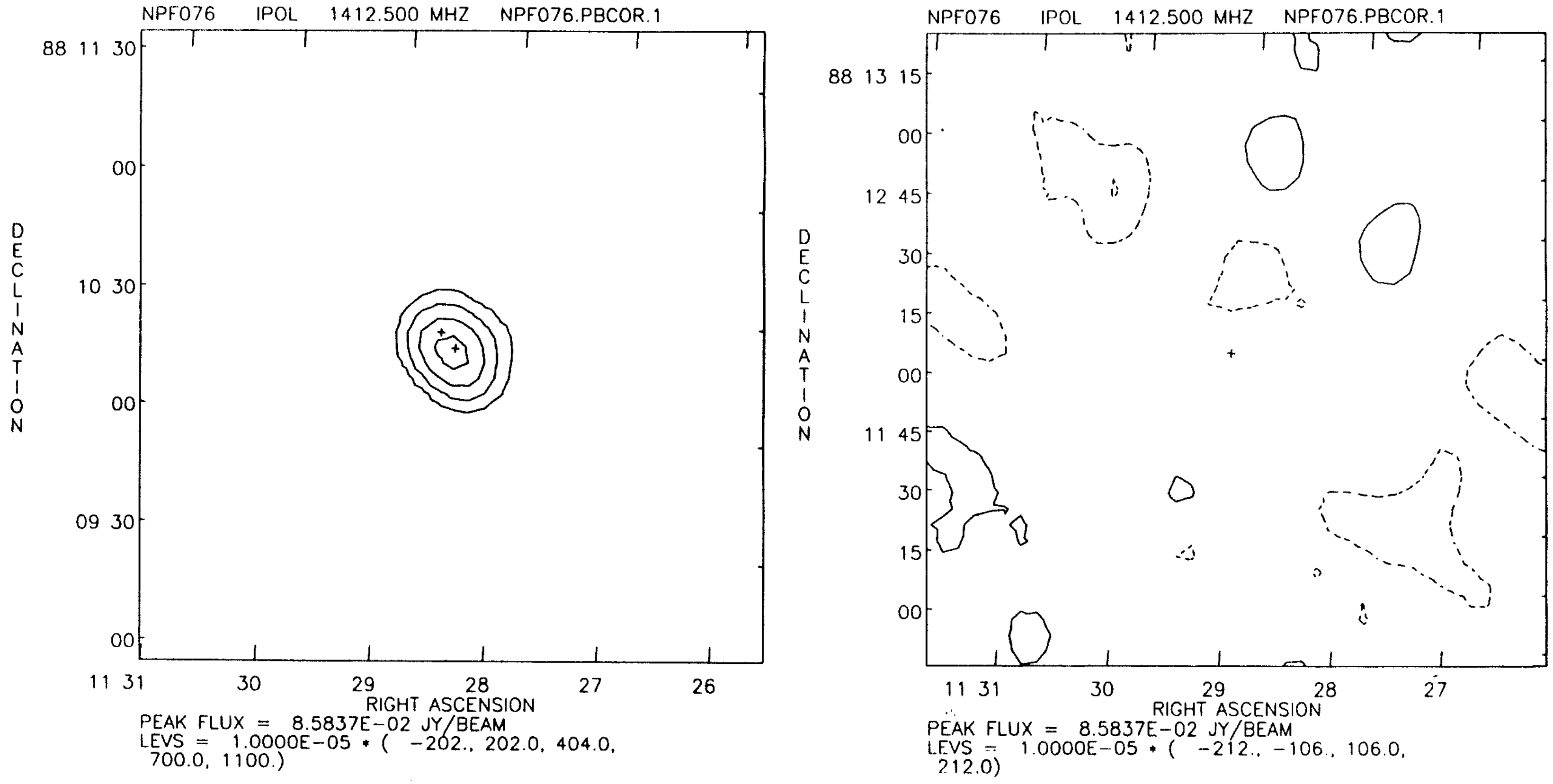

FIGURE 5-3 continued. Contour maps from 1.4 GHz images. NPR1130.1 (left), lowest contour $\pm 3\sigma$, and NPR1130.2 (right), lowest contours $\pm 1.5\sigma$.

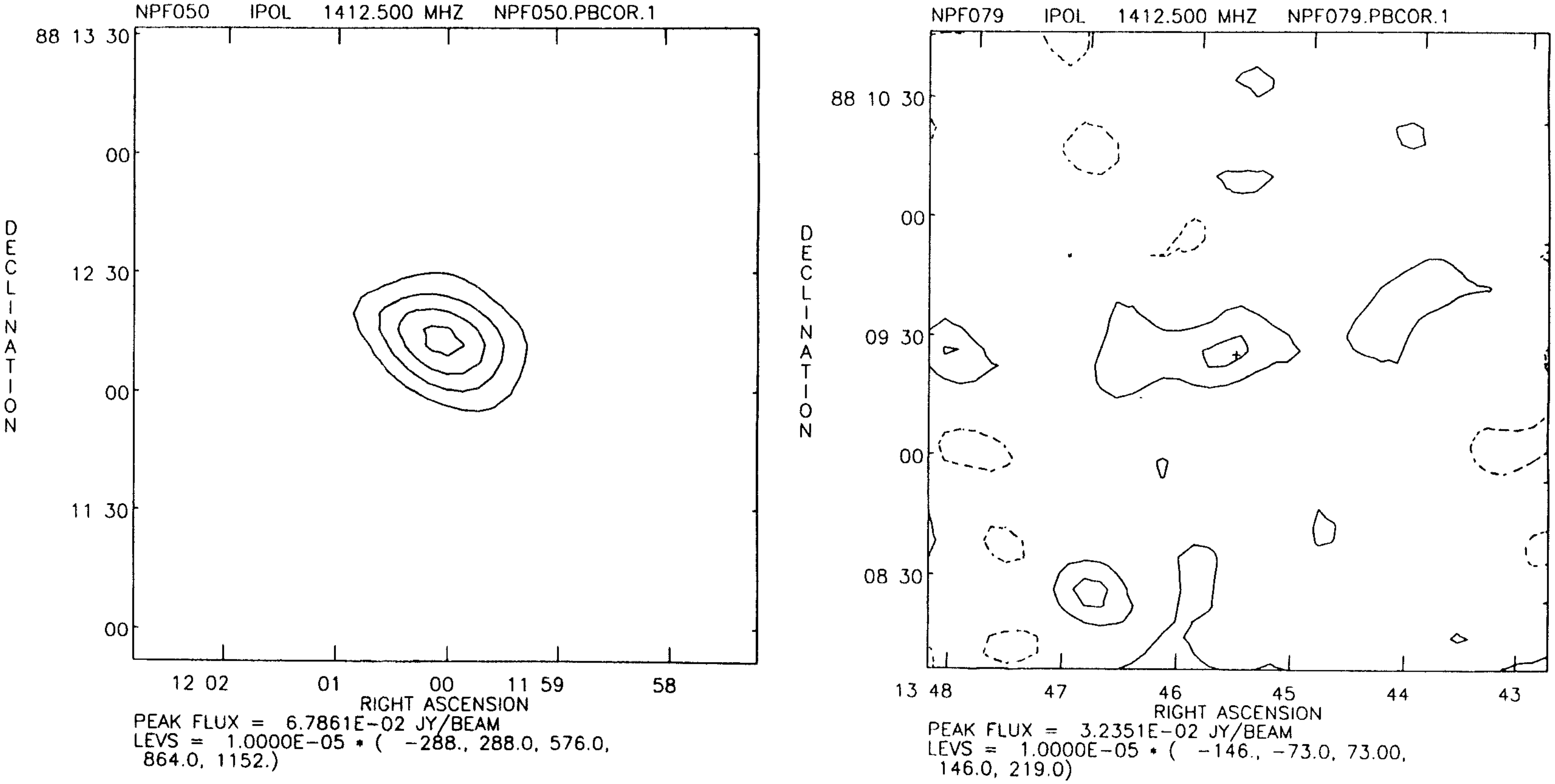

FIGURE 5-3 continued. Contour maps from 1.4 GHz images. NPR1200.1 (left), lowest contours $\pm 3\sigma$, and NPR1345.1 (right), lowest contours $\pm 1.5\sigma$.

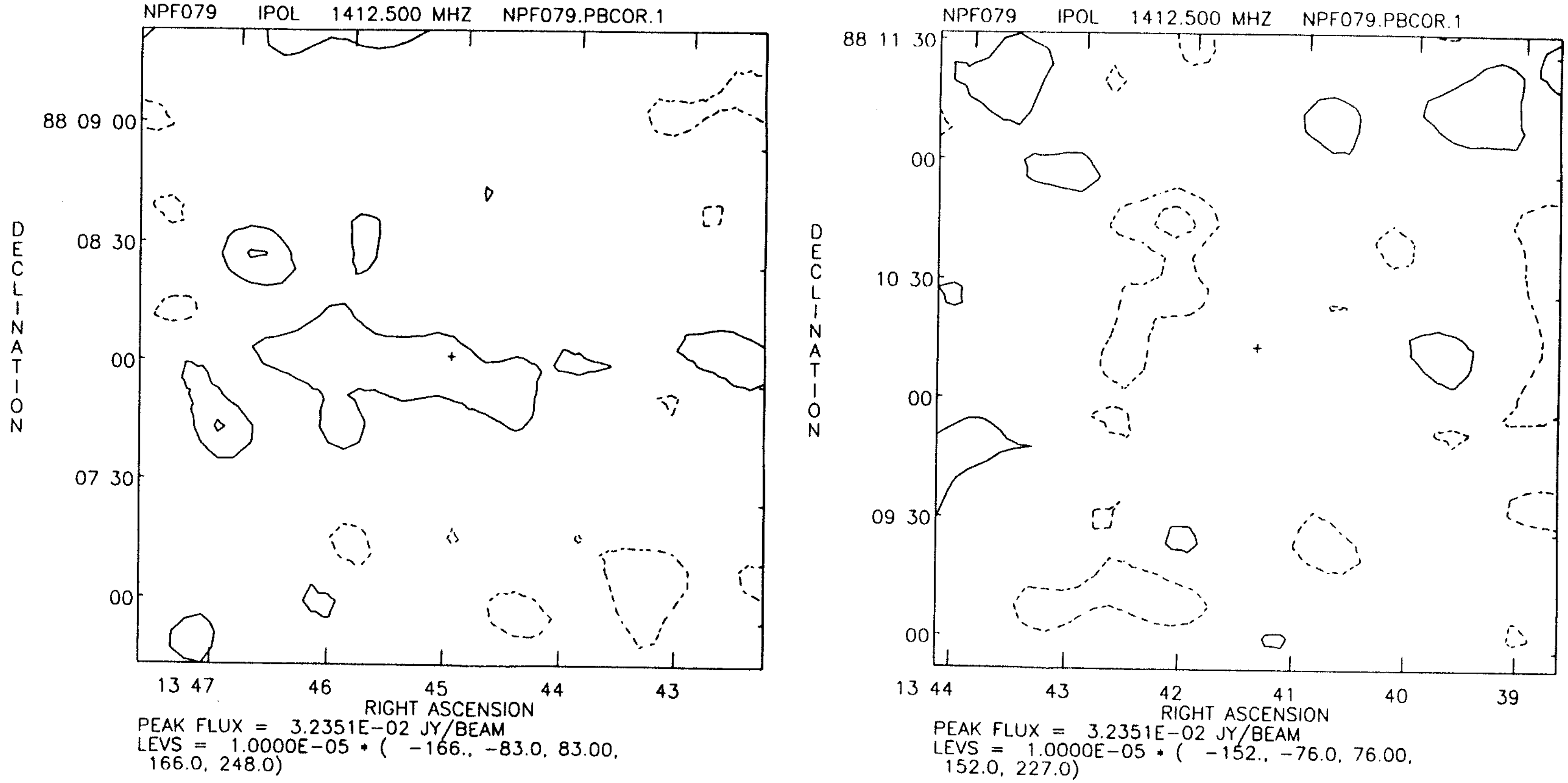

FIGURE 5-3 continued. Contour maps from 1.4 GHz images. NPR1345.2 (left) and NPR1345.3 (right). Lowest contours ±1.5σ.

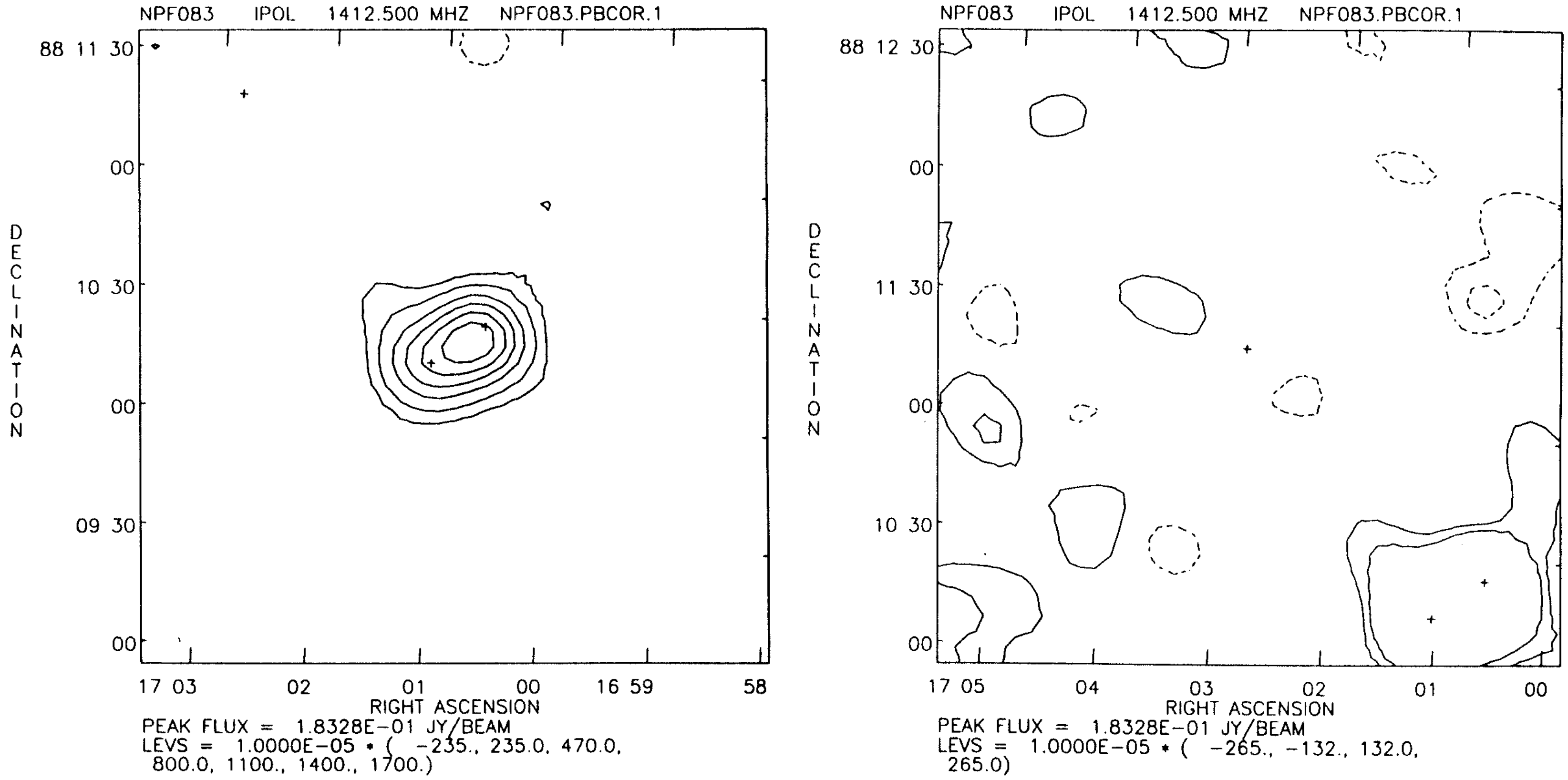

FIGURE 5-3 continued. Contour maps from 1.4 GHz images. NPR1700.1 (left), lowest contours $\pm 3\sigma$, and NPR1700.2 (right), lowest contours $\pm 1.5\sigma$.

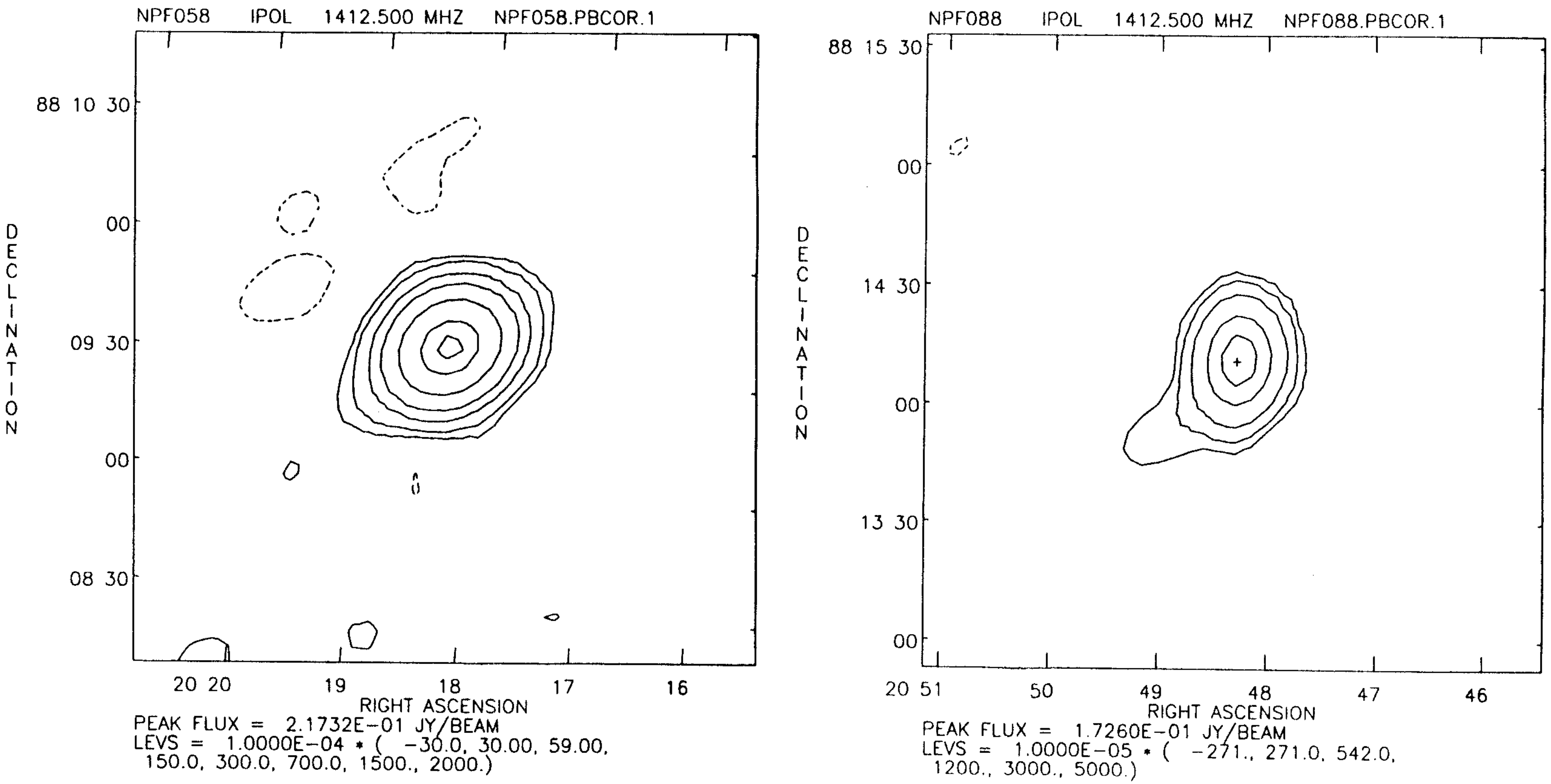

FIGURE 5-3 continued. Contour maps from 1.4 GHz images. NPR2015.1 (left) and NPR2045.1 (right). Lowest contours ±3σ.

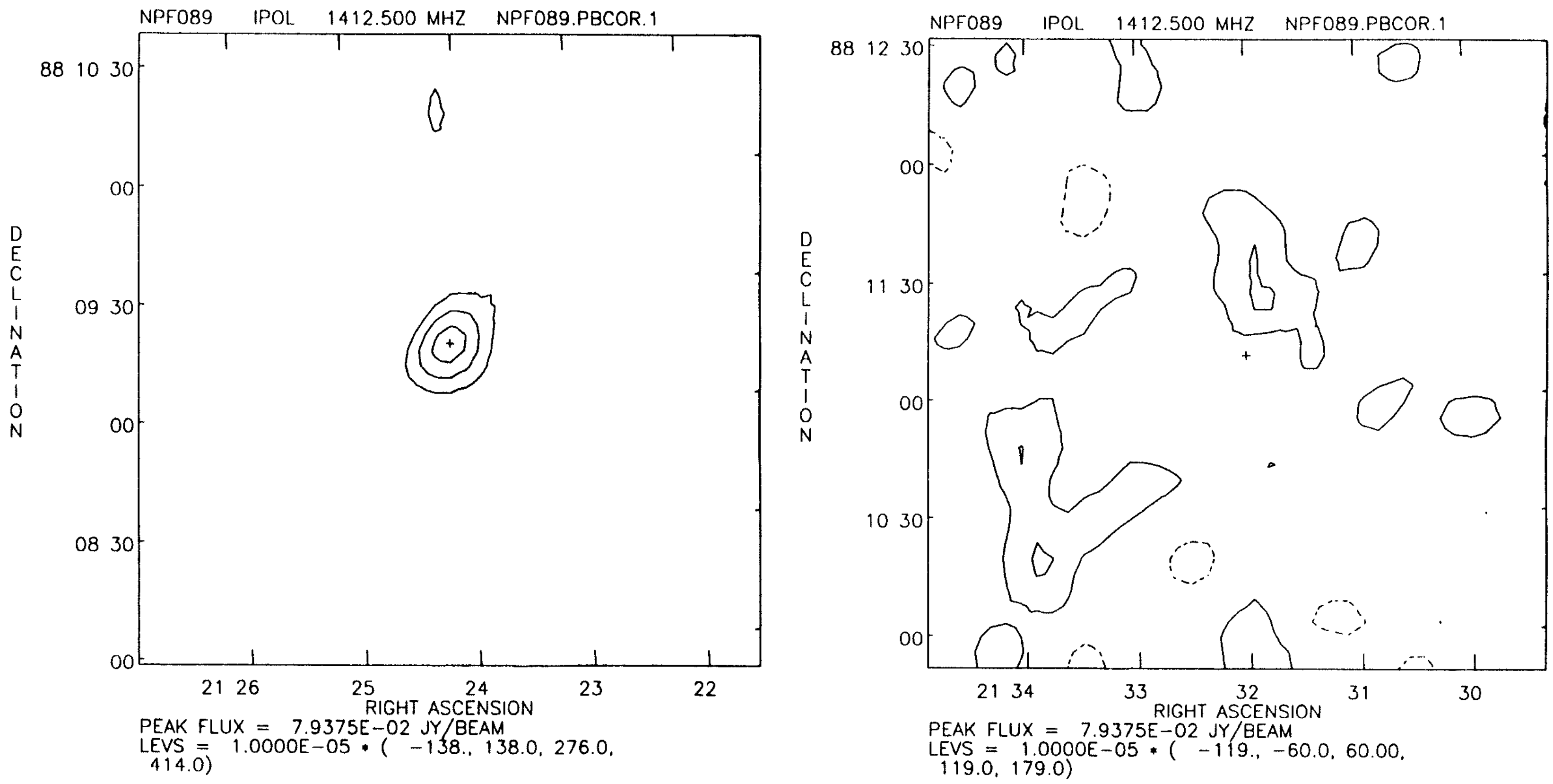

FIGURE 5-3 continued. Contour maps from 1.4 GHz images. NPR2130.1 (left), lowest contours $\pm 3\sigma$, and NPR2130.2 (right), lowest contours $\pm 1.5\sigma$.

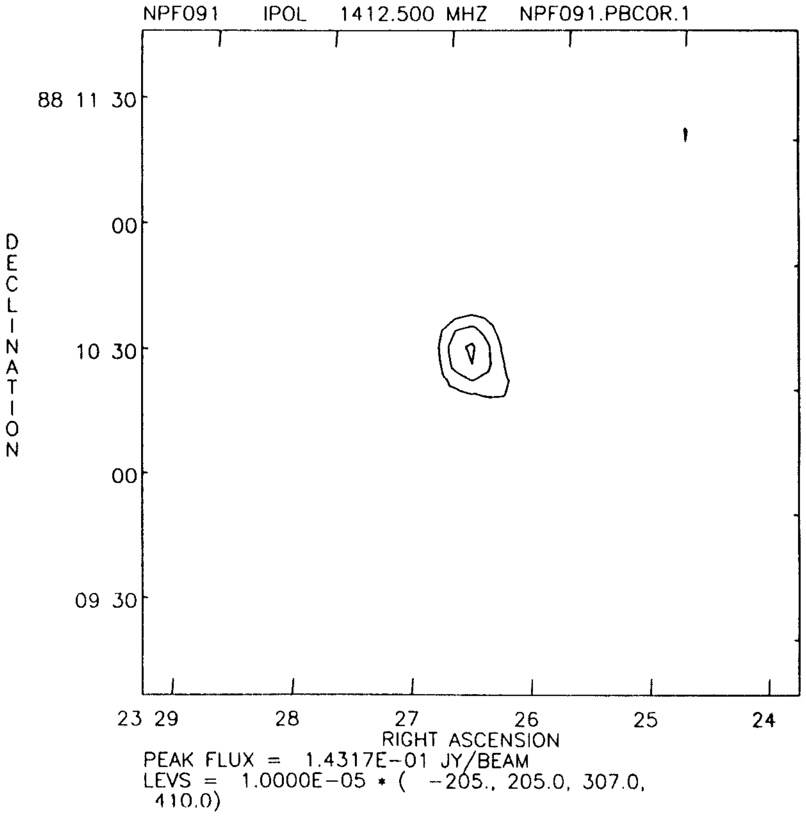

FIGURE 5-3 continued. Contour maps from 1.4 GHz images. NPR2330.1, lowest contours $\pm 3\sigma$.

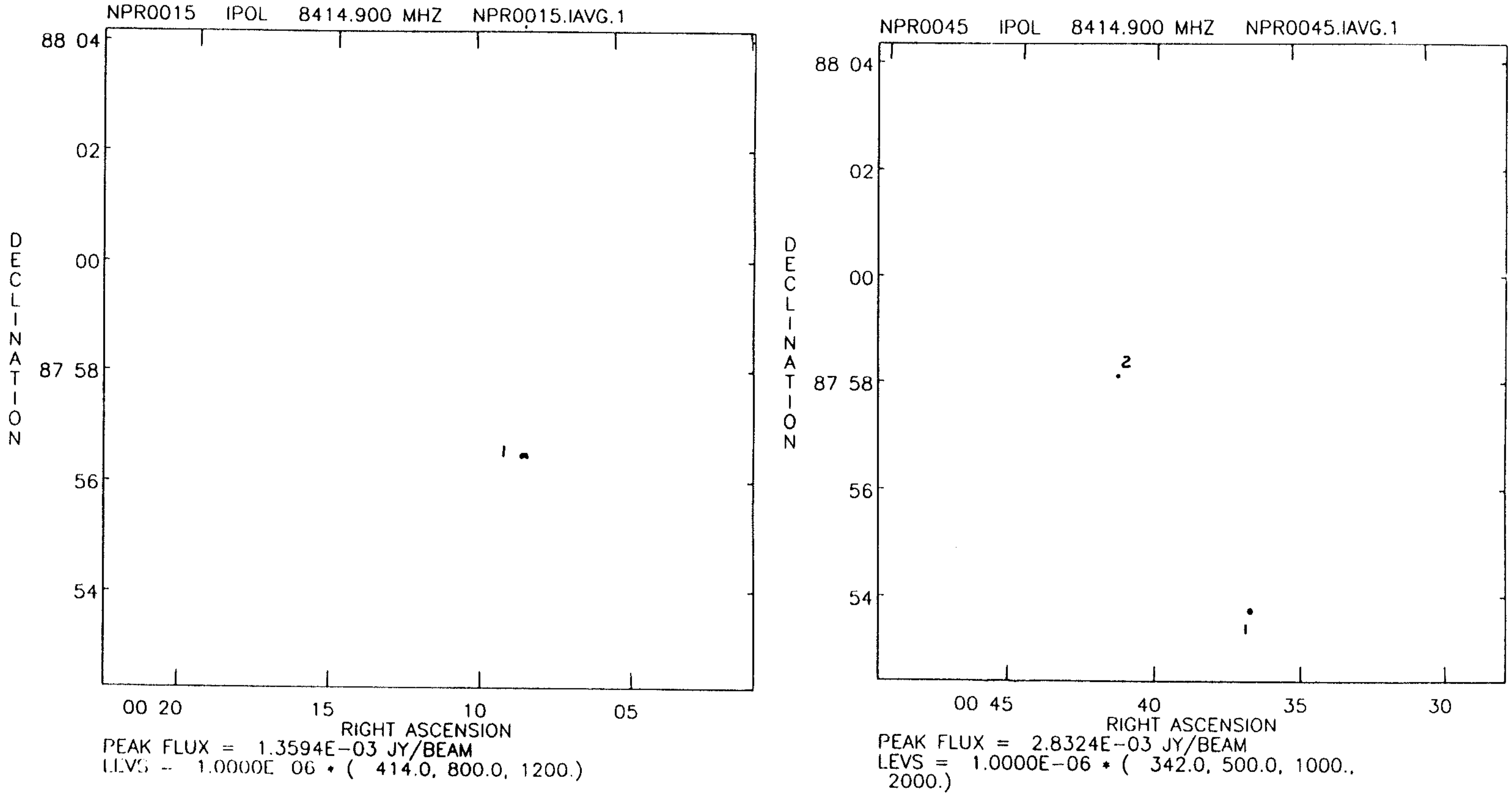

Figure 5–4. VLA 8.5 GHz images of RING region. Full 1024 x 1024 area is shown. The VLA primary beam is 5′.3 FWHM. Sources above the 6σ cutoff in each image are numbered. Coordinates are epoch 1950.0. Only maps containing sources are shown. This panel fields NPR0015 (left) and NPR0045 (right).

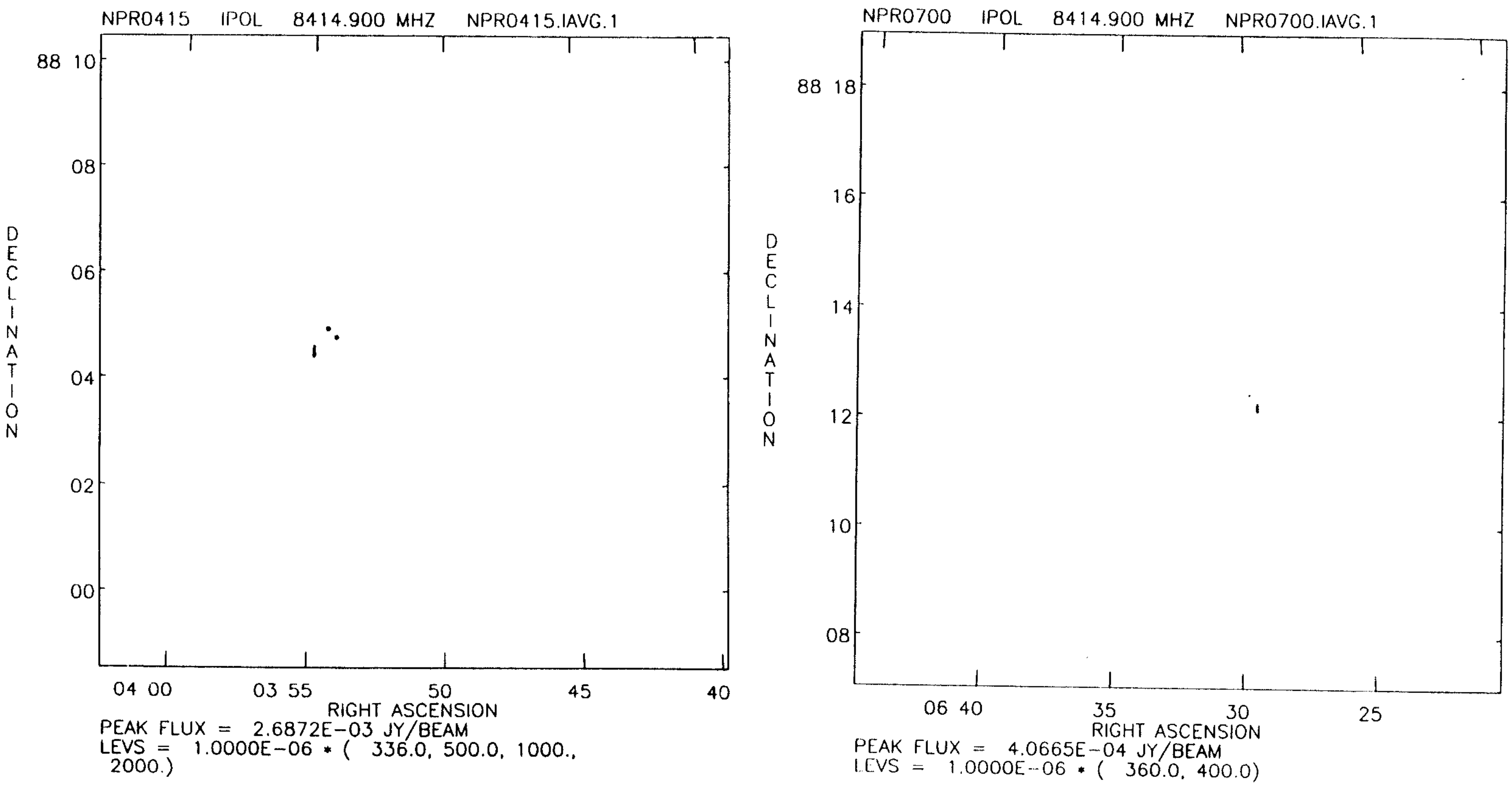

FIGURE 5–4 continued. VLA 8.5 GHz images of RING region. This panel fields NPR0415 (left) and NPR0700 (right).

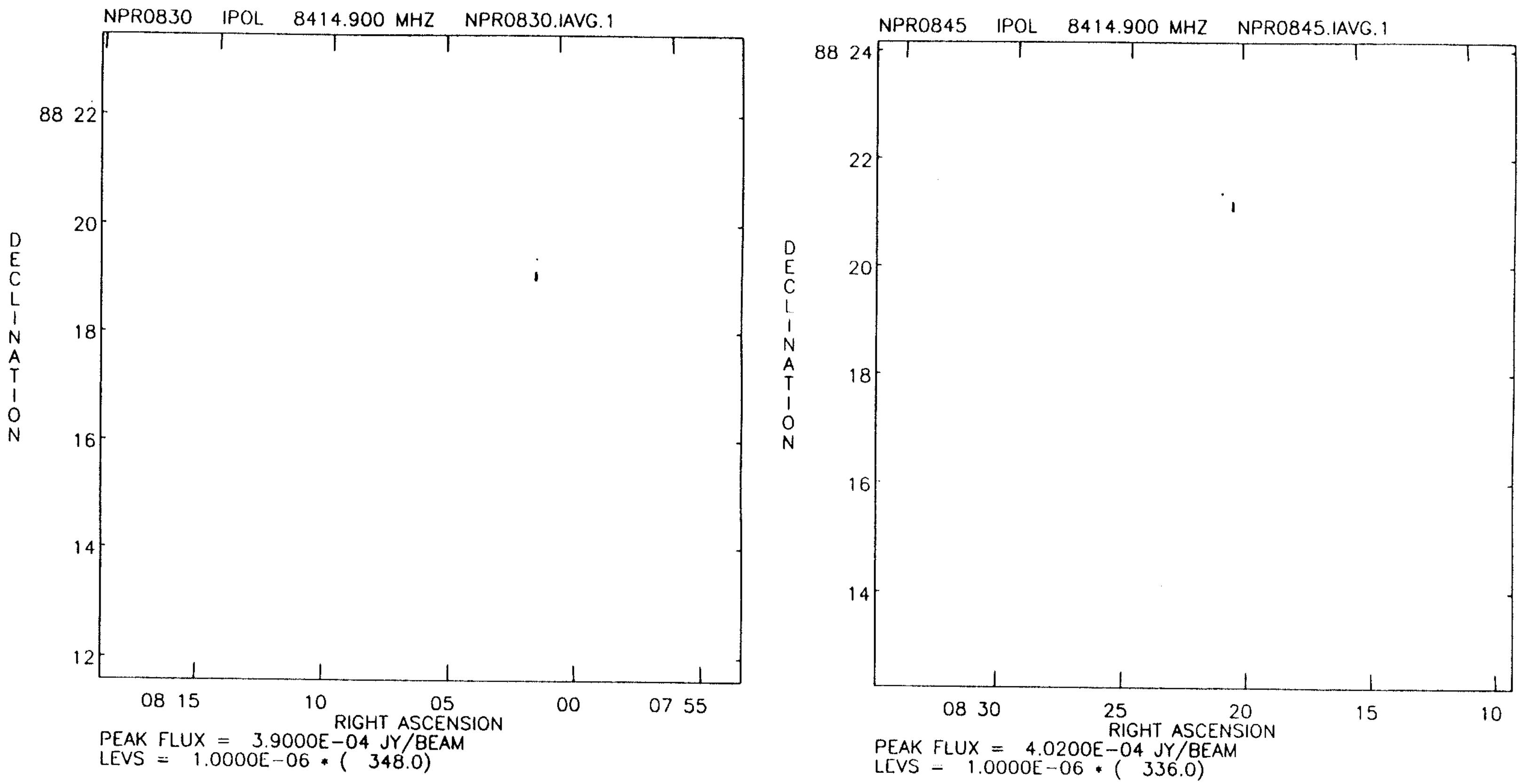

FIGURE 5-4 continued. VLA 8.5 GHz images of RING region. This panel fields NPR0830 (left) and NPR0845 (right).

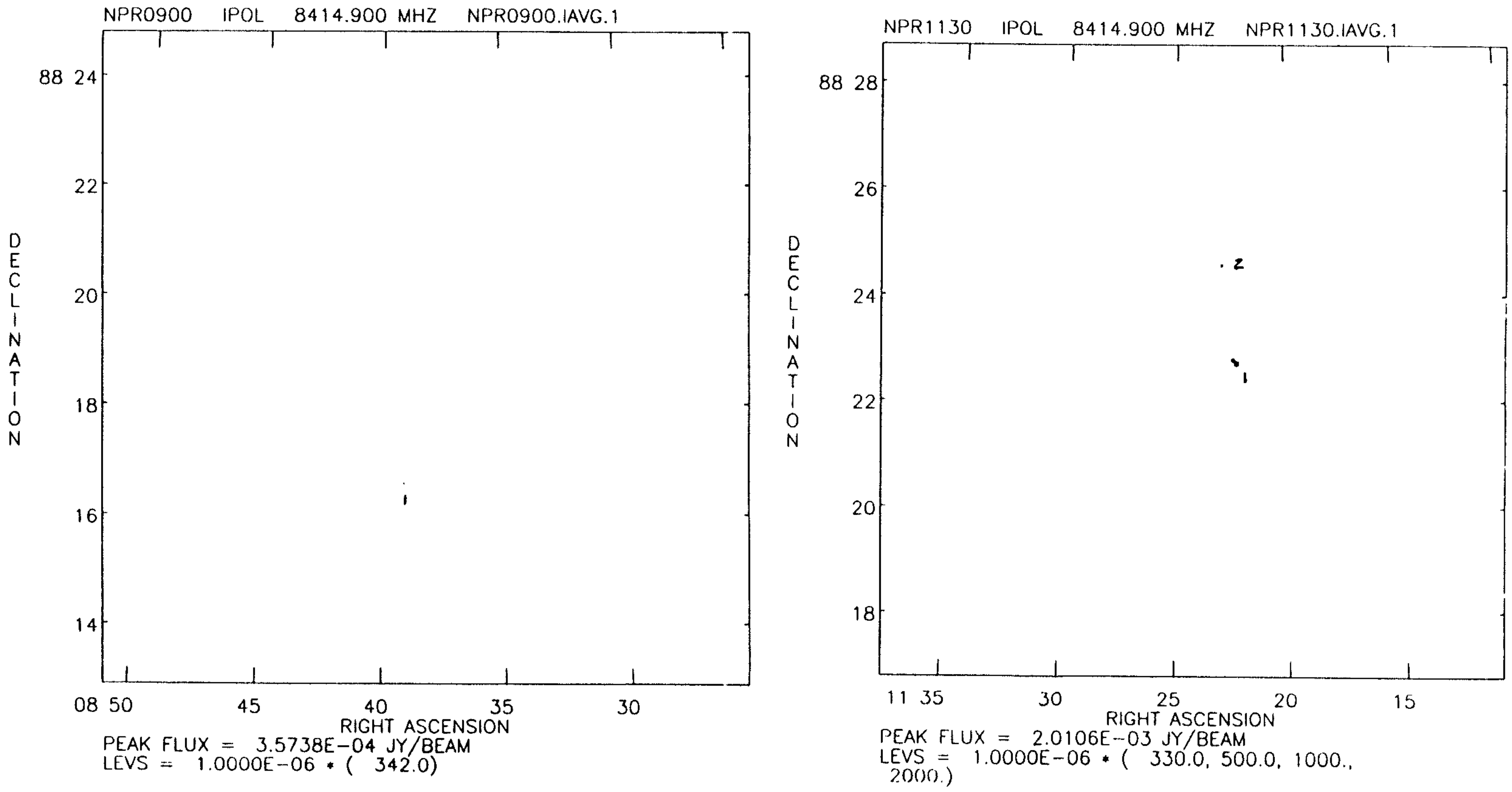

FIGURE 5–4 continued. VLA 8.5 GHz images of RING region. This panel fields NPR0900 (left) and NPR1130 (right).

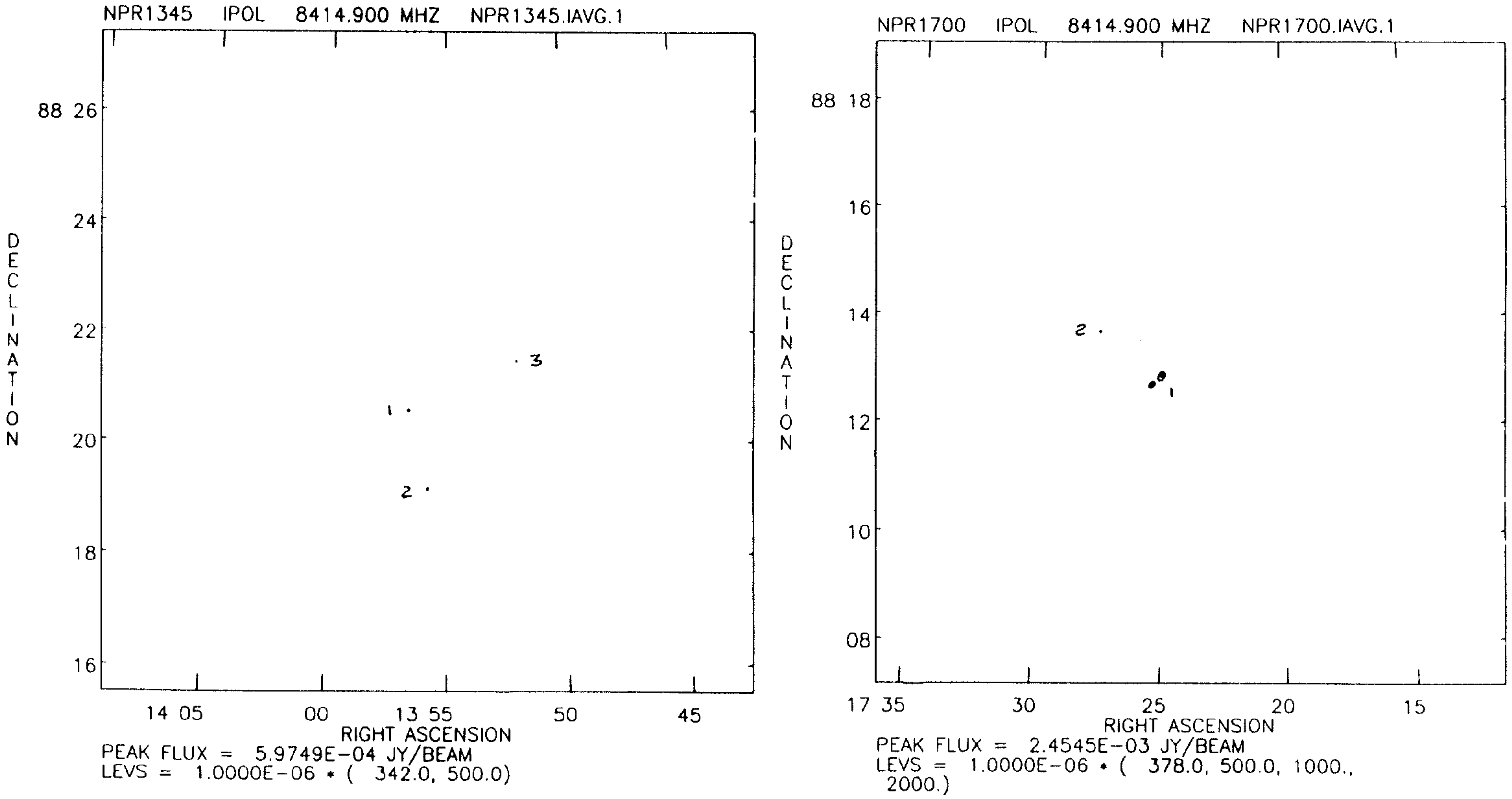

FIGURE 5–4 continued. VLA 8.5 GHz images of RING region. This panel fields NPR1345 (left) and NPR1700 (right).

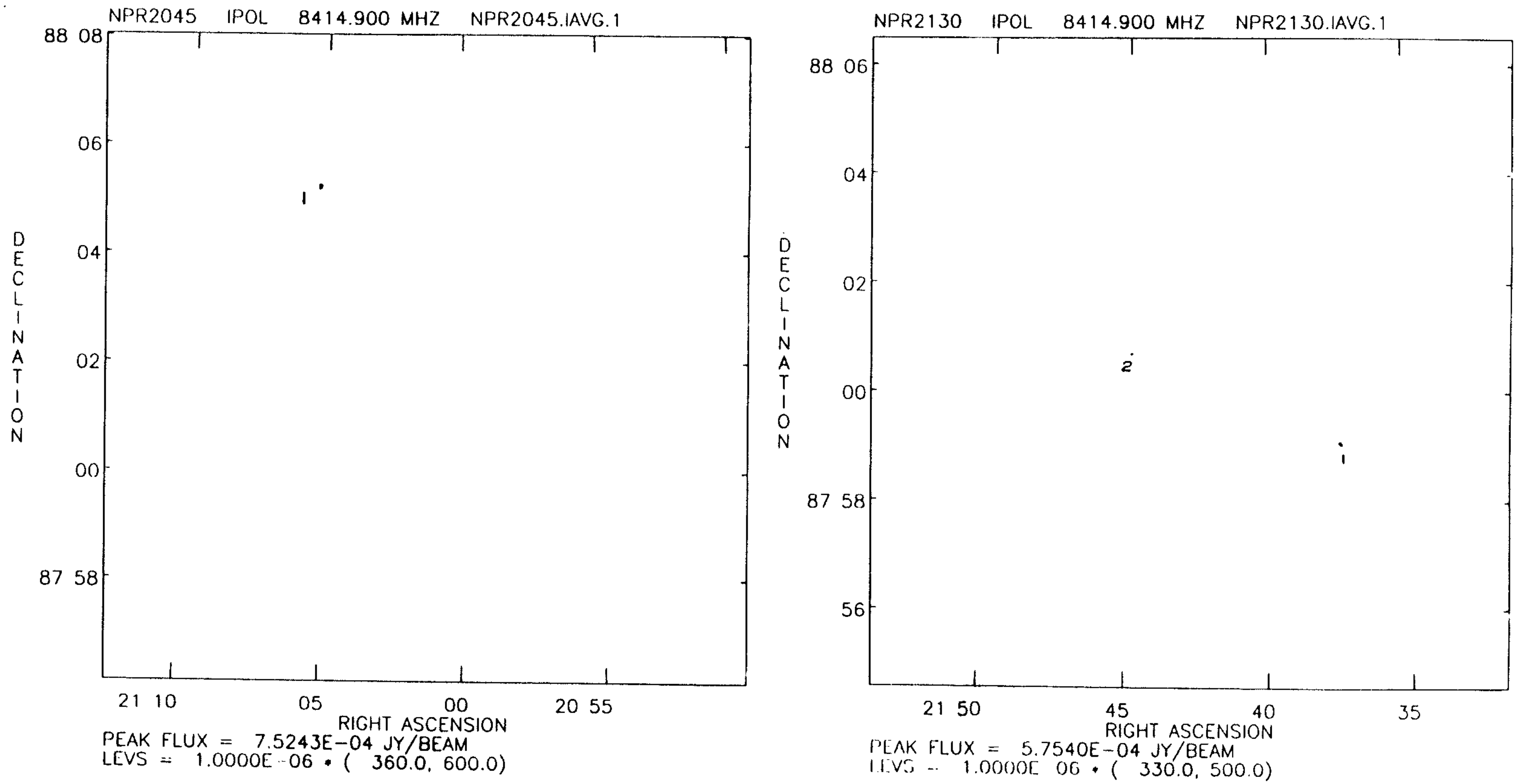

FIGURE 5-4 continued. VLA 8.5 GHz images of RING region. This panel fields NPR2045 (left) and NPR2130 (right).

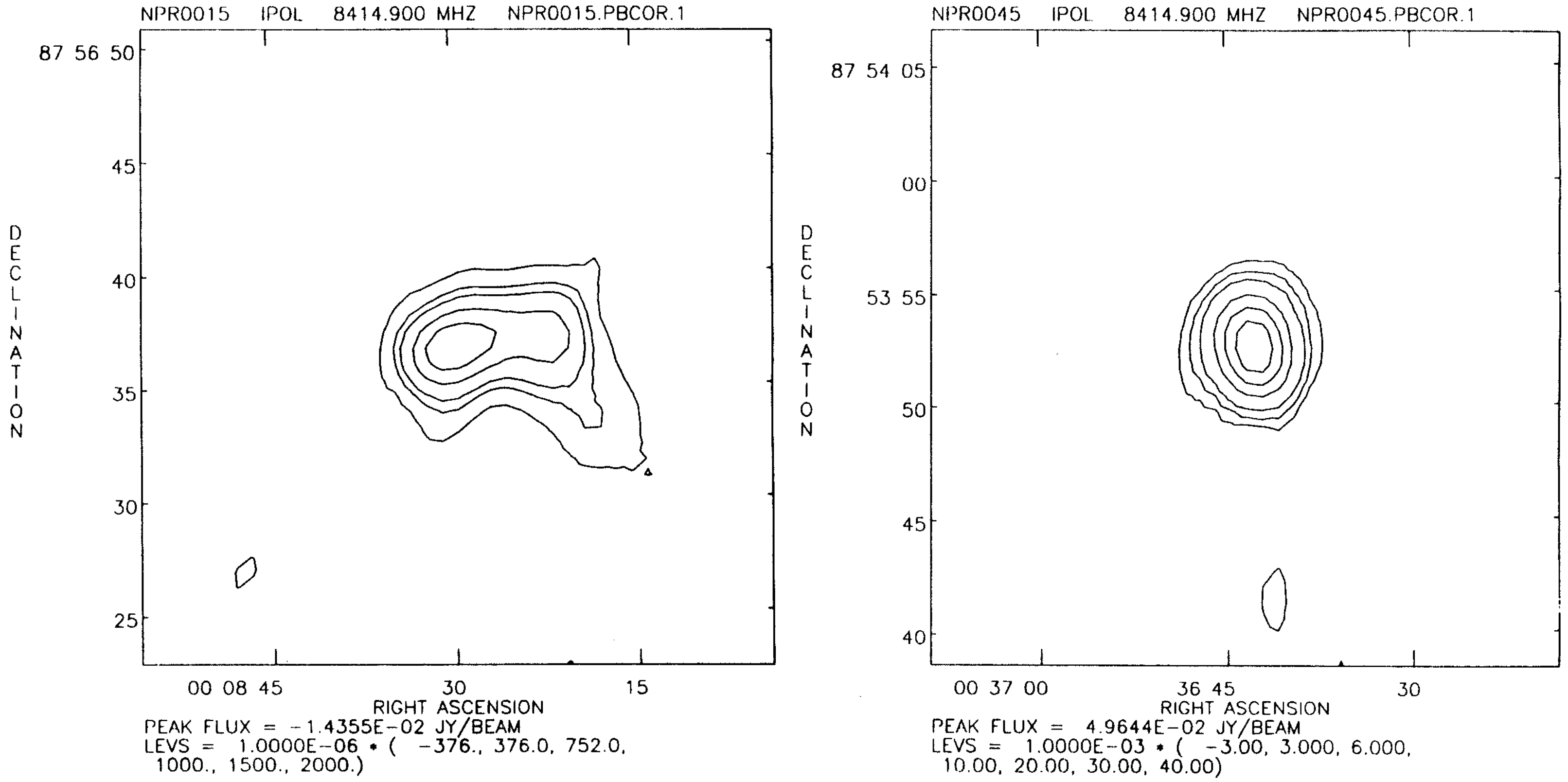

FIGURE 5-5. Contour maps from the 8.5 GHz images of sources detected at 8.5 GHz above the 6σ cutoff. Negative contours are shown as broken lines. Lowest contours are $\pm 3\sigma$. This panel shows NPR0015.1 (left) and NPR0045.1 (right).

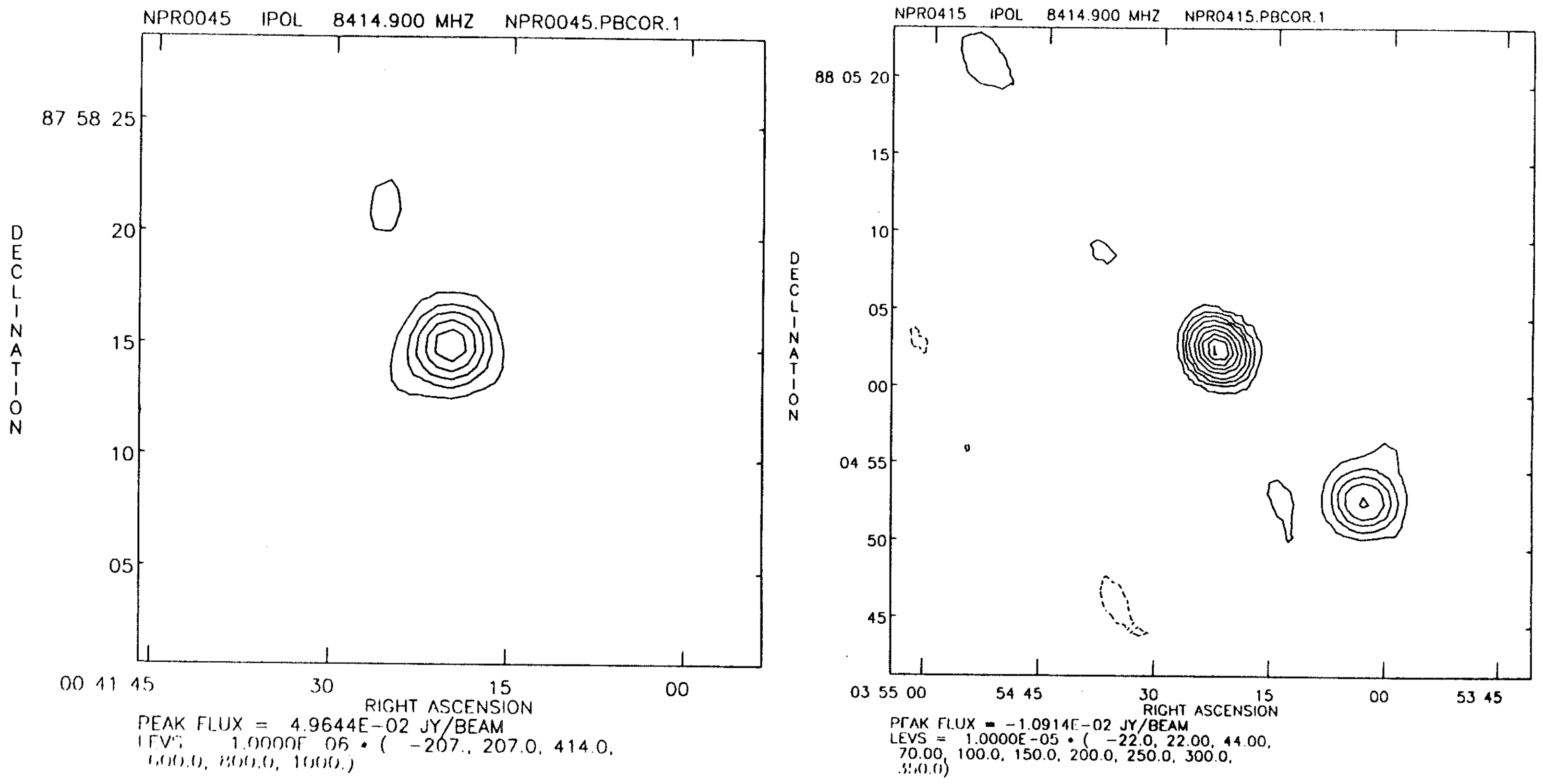

FIGURE 5–5 continued. Contour maps from 8.5 GHz images. NPR0045.2 (left) and NPR0415.1 (right).

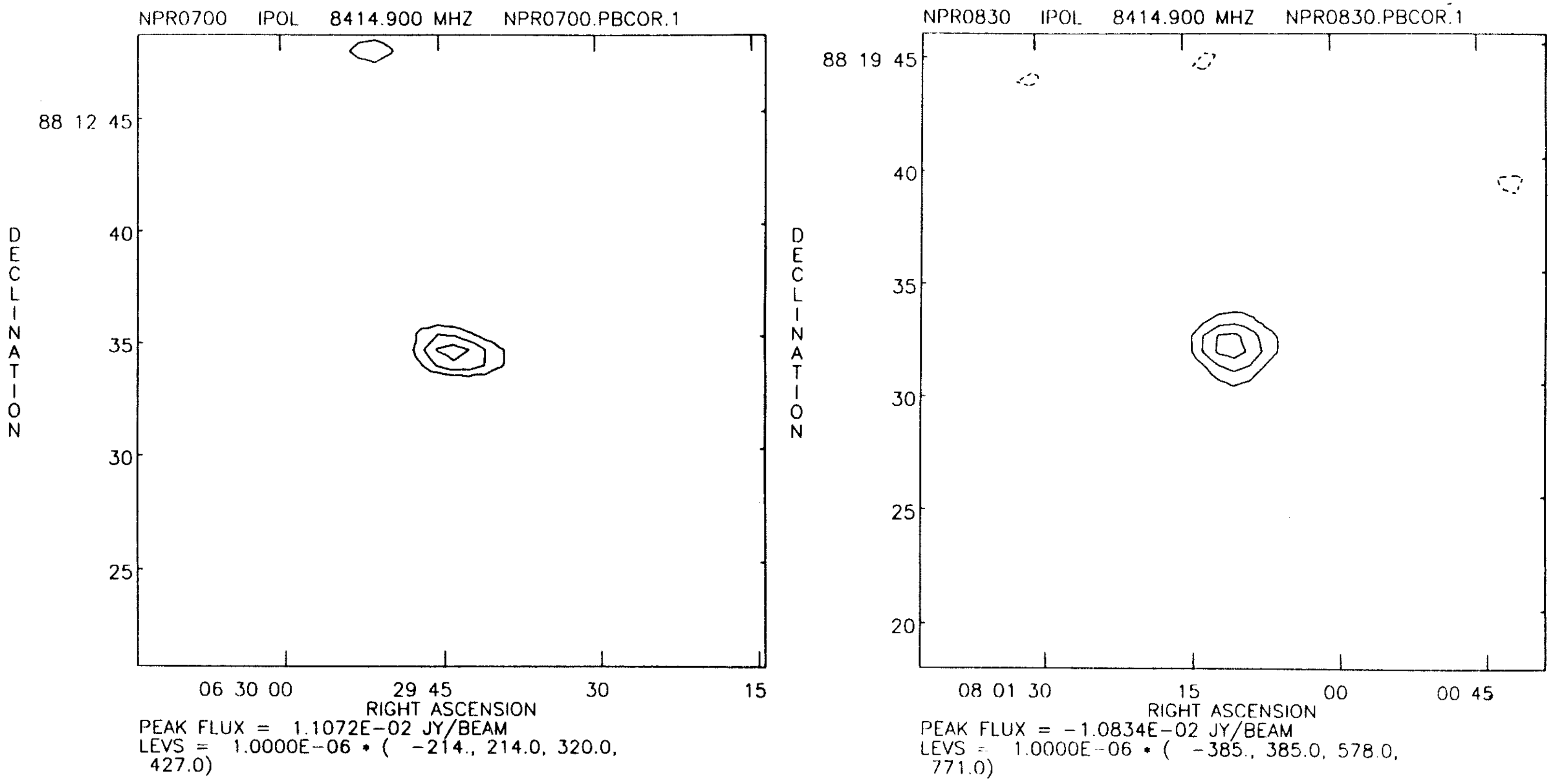

Figure 5–5 continued. Contour maps from 8.5 GHz images. NPR0700.2 (left) and NPR0830.1 (right).

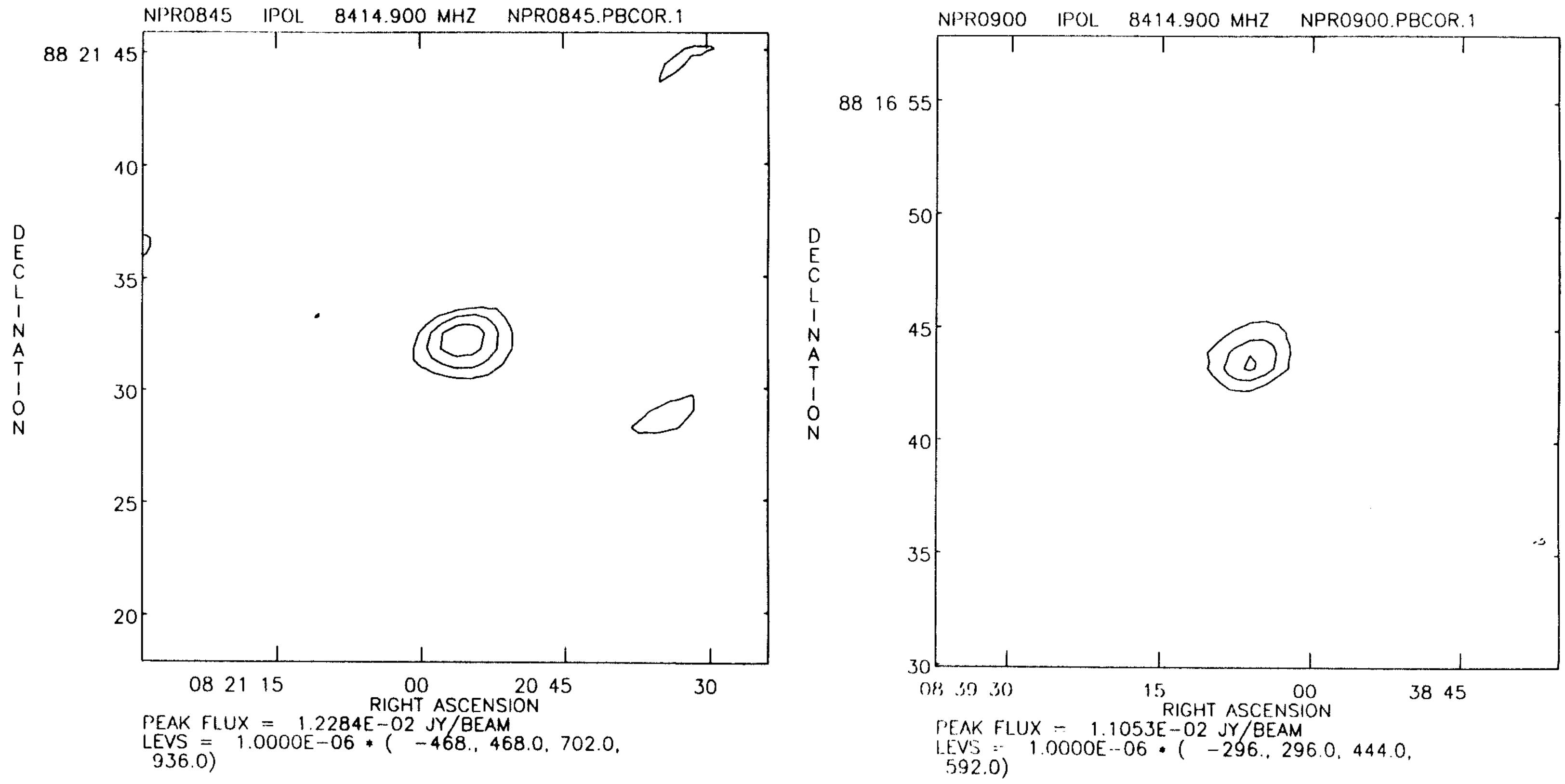

FIGURE 5–5 continued. Contour maps from 8.5 GHz images. NPR0845.1 (left) and NPR0900.1 (right).

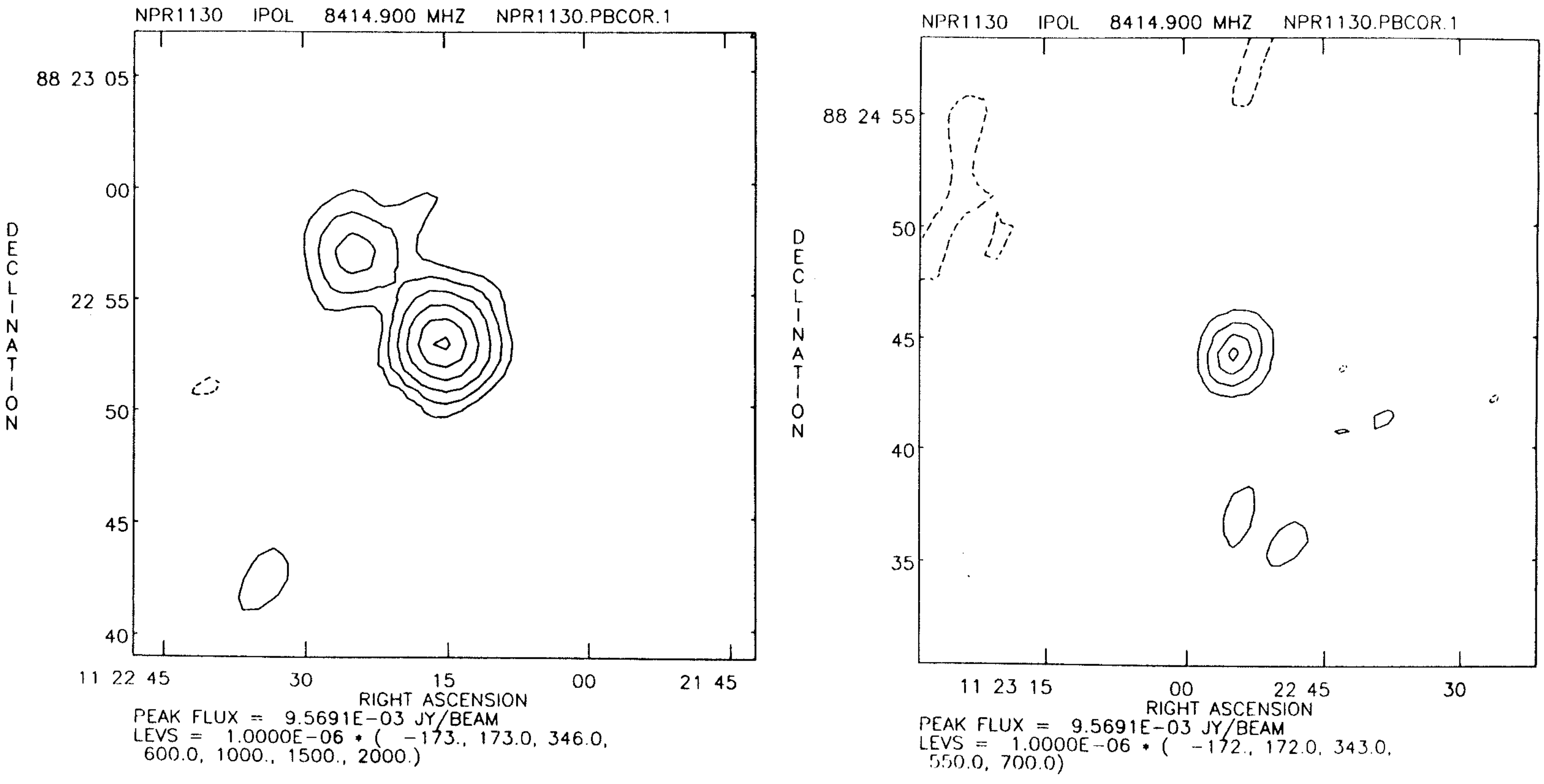

FIGURE 5-5 continued. Contour maps from 8.5 GHz images. NPR1130.1 (left) and NPR1130.2 (right).

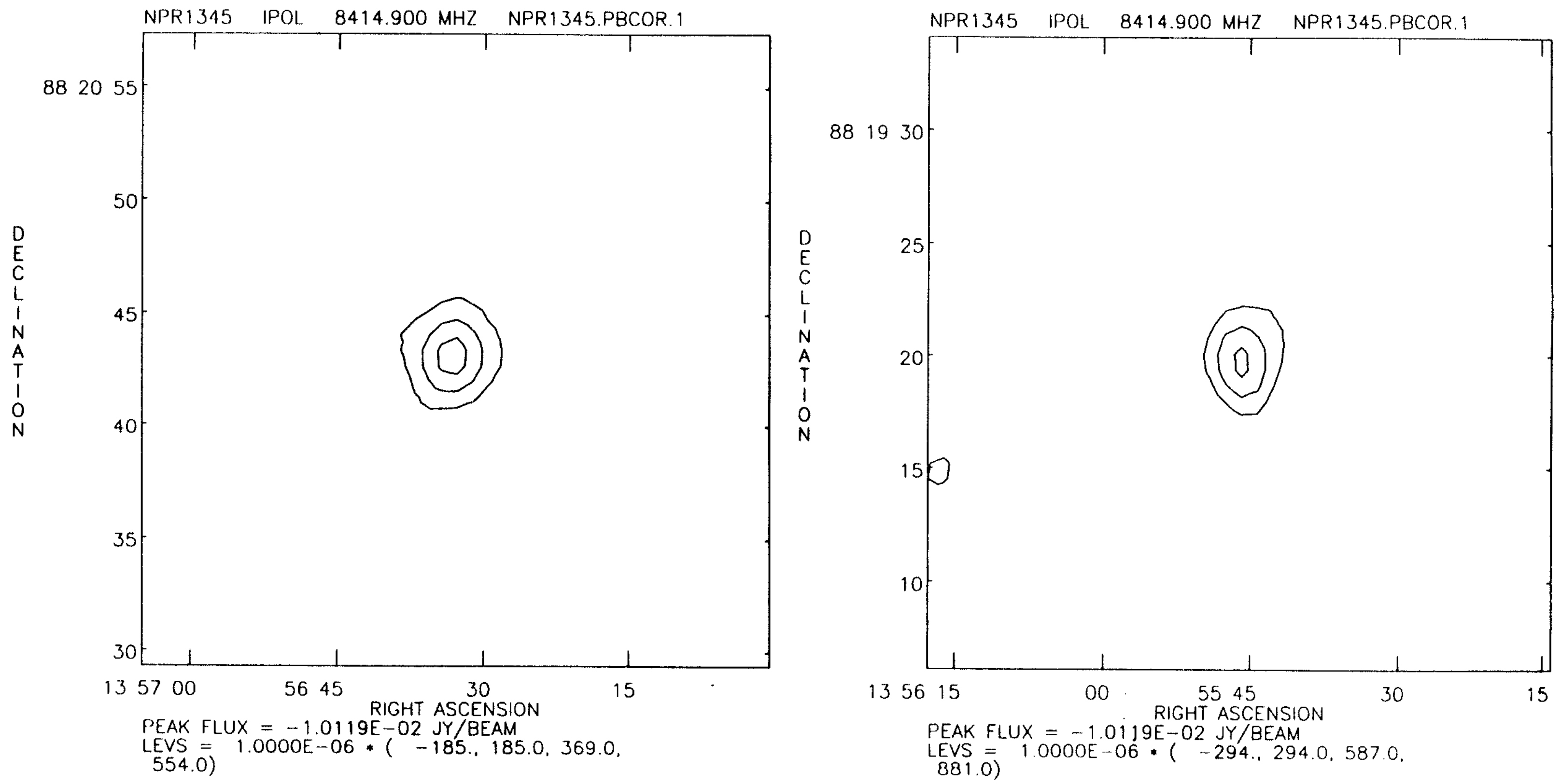

FIGURE 5–5 continued. Contour maps from 8.5 GHz images. NPR1345.1 (left) and NPR1345.2 (right).

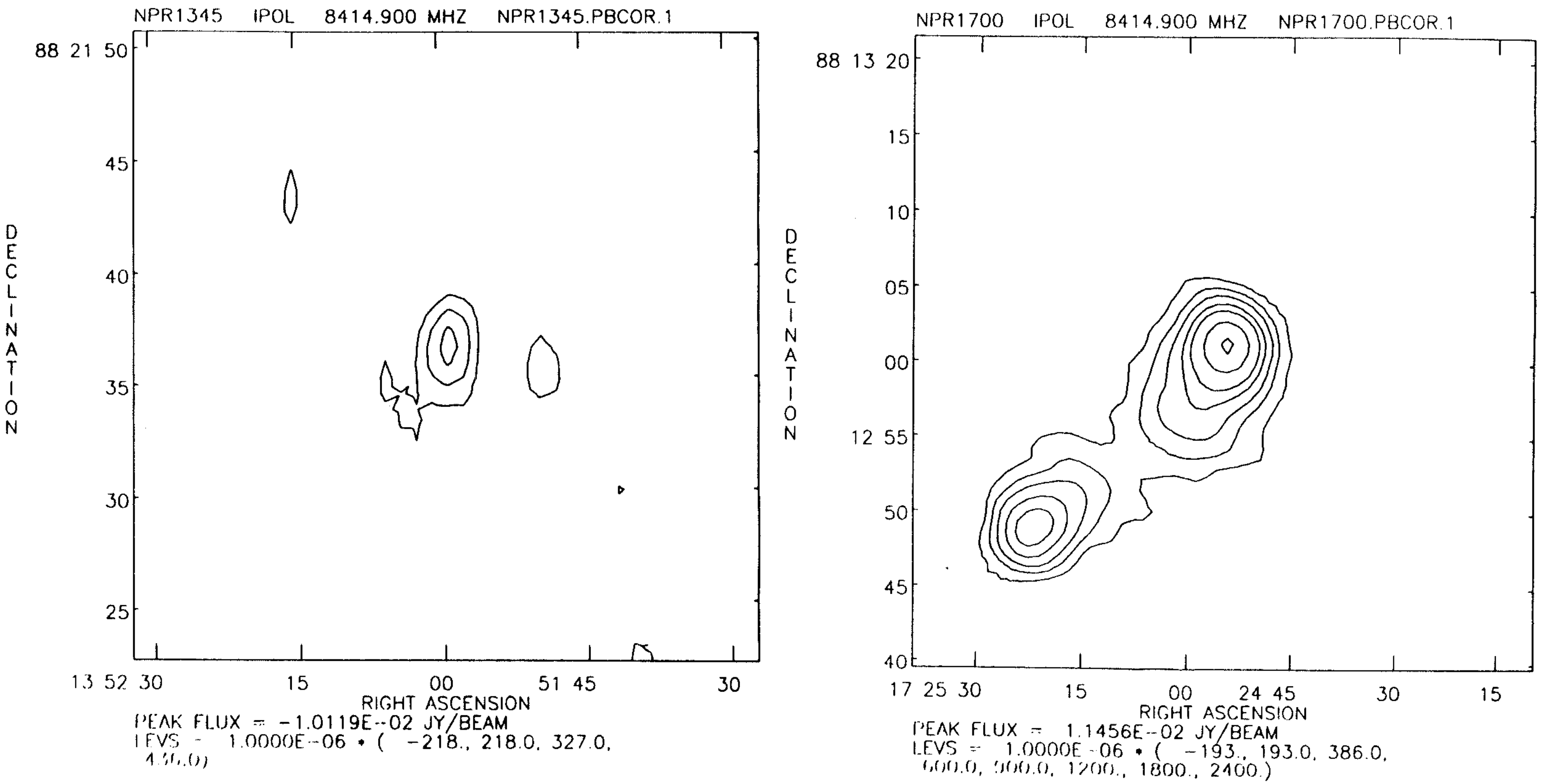

FIGURE 5-5 continued. Contour maps from 8.5 GHz images. NPR1345.3 (left) and NPR1700.1 (right).

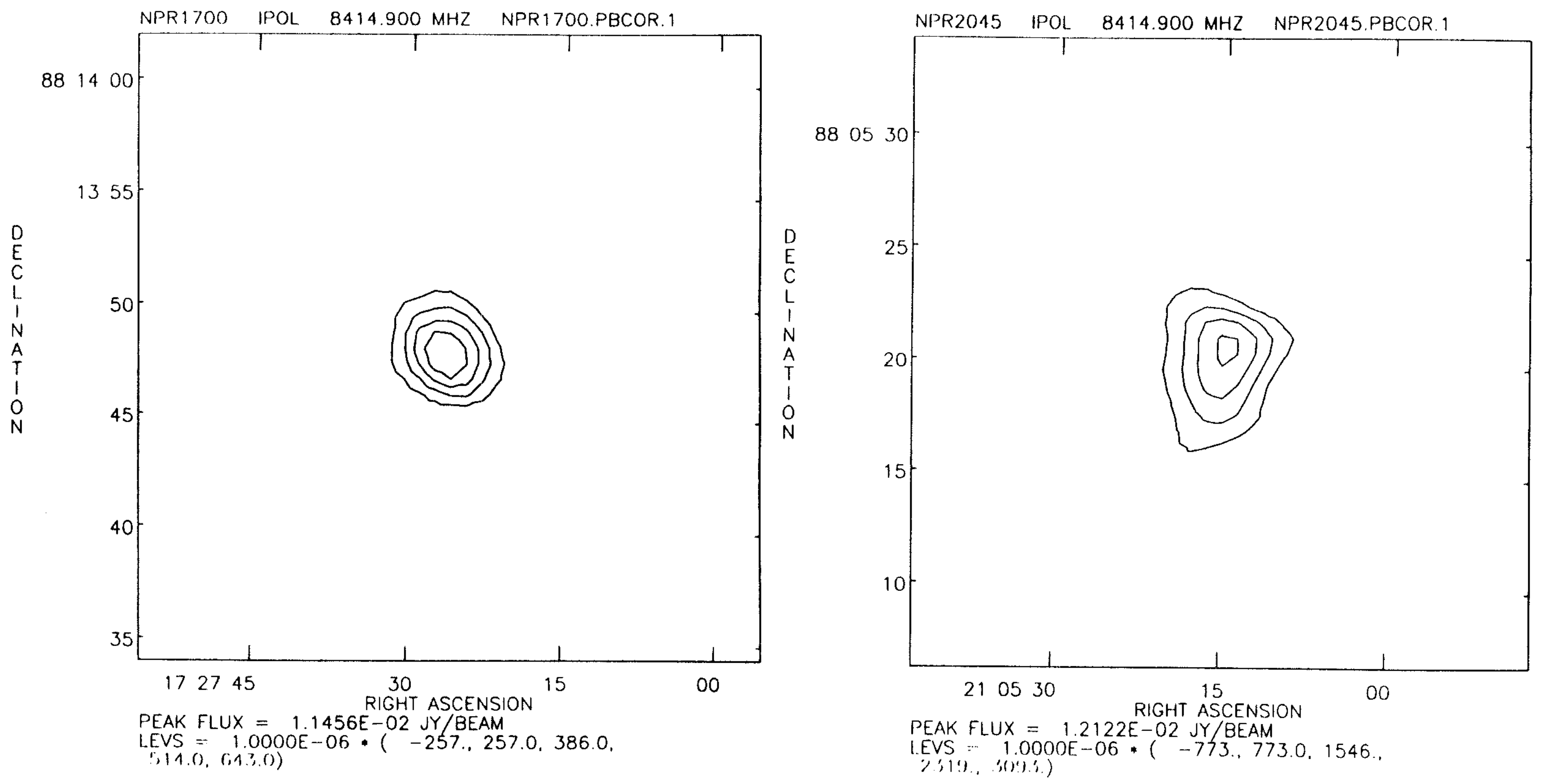

FIGURE 5-5 continued. Contour maps from 8.5 GHz images. NPR1700.2 (left) and NPR2045.1 (right).

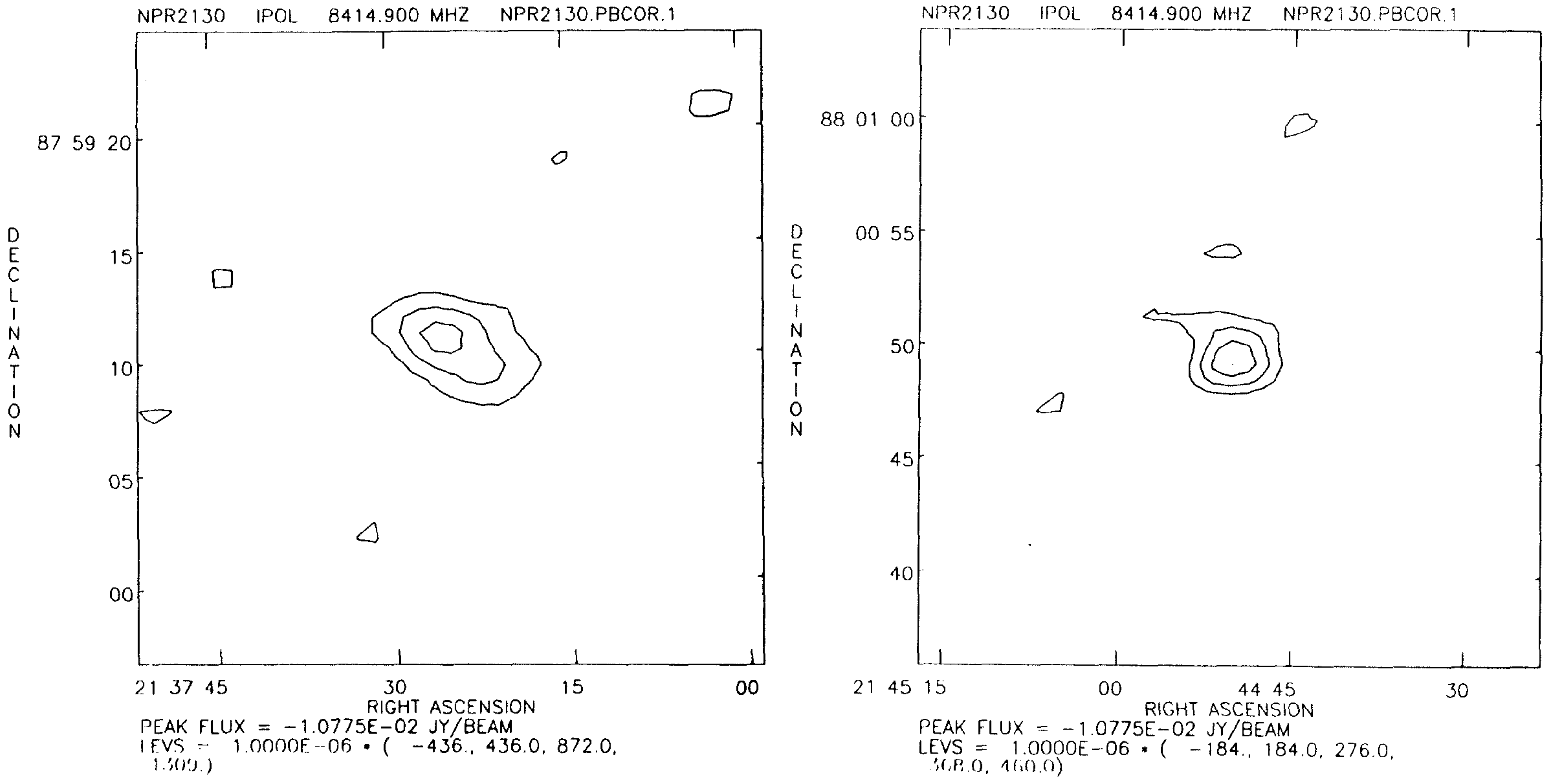

FIGURE 5-5 continued. Contour maps from 8.5 GHz images. NPR2130.1 (left) and NPR2130.2 (right).

CHAPTER 6
Analysis of RING Results

6–1 Overview

In Chapter 4, we have ascertained that the RING dataset contains a signal that has increased the variance among the field values over that expected from the contributions of the instrumental and atmospheric noise alone. The MLM *rms* amplitude of this signal was determined to be $\sigma_{sky} \sim 133\ \mu\mathrm{K}$. Through matched filtering, seven fields with probable fluctuations (above 3σ) were located and of these, four showed significant deviations from zero in the MEM reconstruction. It is now time to apply the full statistical analysis developed in Chapter 2 to the RING results to set limits on the free parameters of Gaussian random distributions generated by theories of galaxy formation. We will first consider the simple model where there is no correlation between the sky fluctuations in the individual beams sampled by the RING; only the correlations between the switched measurements themselves are included in the analysis. Then, we advance to the Gaussian autocorrelation function approximation (§2–2), where the anisotropy field has spatial covariance with a fixed functional form. Following this, implications for actual published models are discussed, with emphasis upon those for which predictions for the OVRO experimental geometry are available. This chapter concludes with preliminary results for non-Gaussian models and the prospects for these theories.

We begin by summarizing the upper limits from the NCP program as presented in Chapter 3. From the results of that experiment, we derived Bayesian credible intervals for fluctuations uncorrelated between beams and for Gaussian autocorrelation function models. Because the NCP fields are separated by over $0^\circ.5$, we can safely assume that there are no correlations between measurements, only between the switched beams within the measurements. The assumptions and calculation method for the two extremes are given in more detail in Paper 1 (§VIIIb) and below. If we assume that there is no correlation between the main and reference beams, we obtain the limits on the amplitude of the root-mean-square (*rms*) fluctuation

$$\begin{aligned} \theta &< 47\ \mu\mathrm{K} \quad (95\%) \\ &< 104\ \mu\mathrm{K} \quad (99.87\%). \end{aligned}$$

Because these are the amplitudes of fluctuations in an assumed random field on the sky, we can express these limits as fractions of the mean microwave background temperature $T_{mwb} = 2.735$ K (Mather *et al.* 1990) :

$$\begin{aligned} \frac{\Delta T}{T} &< 1.7 \times 10^{-5} \quad (95\%) \\ &< 3.8 \times 10^{-5} \quad (99.87\%). \end{aligned}$$

The limits on $C_0^{1/2}$ derived for the generalized Gaussian autocorrelation function are shown in Paper 1 (Figure 16). Also given are the predicted limits from specific galaxy formation theories for the NCP experimental parameters, and the reader is referred to this discussion and the Table 6 included therein.

In Chapter 5 we concluded on the basis of 8.5 GHz VLA observations that at least three RING fields were contaminated significantly by discrete radio sources. In Table 5–6 the estimated strength of this signal was given along with corrected values for the affected RING measurements. On the basis of this, we have generated a source-subtracted RING dataset, which we will designate as the 'corrected' RING; this is our best representative of a clean dataset. The distribution of the field values in the corrected RING is shown in Figure 6–1 where the amplitudes are given in units of the microwave background temperature. Even after the VLA source subtraction, several sources remain with deflections above the 10^{-4} level, most notably NPR0700 and NPR1015.

6–2 Generalized Fluctuation Models

The simplest model for the anisotropic component of the microwave background as measured by the RING experiment is a Gaussian random field without spatial correlation between patches of sky the size of the OVRO 20 GHz primary beam (108″ FWHM), between which there is a variance C_0. In this case, if we denote the single-beam sampled regions corresponding to the main beams of the switched RING fields (equivalent to points in the smeared random field F_{obs} of equation 2.14) as F_k ($k = 1, \ldots, 96$), then a RING field measurement is equal to the sum of the measurement error e_k and the differences between the main and reference beams,

$$T_k = F_k - \frac{1}{2}F_{k-1} - \frac{1}{2}F_{k+1} + e_k \tag{6.1}$$

where the indices are taken to be modulo 96. With the assumption of no spatial correlation

$$\left\langle F_i \; F_j \right\rangle = C_0 \; \delta_{ij} \tag{6.2}$$

and independent Gaussian measurement errors, the matrix A is banded and symmetric

$$A_{ij} = C_0 \left[\frac{3}{2}\delta_{ij} - (\delta_{ij-1} + \delta_{ij+1}) + \frac{1}{4}(\delta_{ij-2} + \delta_{ij+2})\right] + \epsilon_i^2 \; \delta_{ij}. \tag{6.3}$$

We must be careful to note that the indices wrap around at $i = 0$ and $i = 96$ so that there are nonzero entries in the corners of the matrix. We can then perform our calculation of the HPD limits using (2.56) for the likelihood

$$L(\theta) = (2\pi)^{-n/2}[\det A^{-1}]^{1/2} \; \exp\left(-\frac{1}{2}\mathbf{y}^T A^{-1} \mathbf{y}\right).$$

We take as our integration variable the amplitude of the *rms* fluctuation $\theta = C_0^{1/2}$ and obtain the 95% and 99.87% (3σ) HPD limits of

$$\begin{array}{ll} 83 < \theta < 148 \; \mu\text{K} \quad (95\%) & \\ & \hat{\theta} = 111 \; \mu\text{K} \\ 67 < \theta < 177 \; \mu\text{K} \quad (99.87\%). & \end{array}$$

If we use the corrected RING dataset with the estimated contributions from the known VLA sources removed, then the HPD limits are

$$\begin{array}{ll} 62 < \theta < 124 \; \mu\text{K} \quad (95\%) & \\ & \hat{\theta} = 89 \; \mu\text{K} \\ 45 < \theta < 150 \; \mu\text{K} \quad (99.87\%). & \end{array}$$

Expressed as a fraction of the mean microwave background temperature, these are

$$\begin{aligned} 3.0 < \frac{\Delta T}{T} < 5.4 \times 10^{-5} \quad (95\%) \\ 2.4 < \frac{\Delta T}{T} < 6.5 \times 10^{-5} \quad (99.87\%) \end{aligned} \qquad \frac{\Delta \hat{T}}{T} = 4.1 \times 10^{-5}$$

for the full RING data and for the corrected set

$$\begin{aligned} 2.3 < \frac{\Delta T}{T} < 4.5 \times 10^{-5} \quad (95\%) \\ 1.6 < \frac{\Delta T}{T} < 5.5 \times 10^{-5} \quad (99.87\%). \end{aligned} \qquad \frac{\Delta \hat{T}}{T} = 3.3 \times 10^{-5}$$

The limits from the RING corrected data can be compared with the Bayesian upper limits from the NCP experiment noted above and in Chapter 3; we find disagreement between the NCP 95% upper limit of 47 μK and the RING lower limit of 62 μK, but marginal agreement with the 99.87% limits of 104 μK for the NCP and 45 μK for the corrected RING.

If the random field generated by a particular cosmological model has an autocorrelation function $C(\phi)$ of Gaussian form (2.26), or if the correlation function can be approximated as a Gaussian over the angular scales of importance, then we can calculate the limits on the amplitude $C_0^{1/2}$ as a function of the coherence angle ϕ_c. This involves the computation of the function $C(\phi_{ij})$ for the angular distance ϕ_{ij} between the field centers of x_i and x_j

$$\cos \phi_{ij} = 1 - \left[1 - \cos\left(\frac{\pi \Delta_{ij}}{48}\right)\right] \cos^2 \delta \tag{6.4}$$

for RING declination $\delta = 88^\circ\ 10'\ 42''$ with

$$\Delta_{ij} = \begin{cases} |i-j| & 0 \leq |i-j| \leq 48 \\ 96 - |i-j| & 48 < |i-j| \leq 96. \end{cases} \tag{6.5}$$

The correlation matrix A must then be constructed using the smeared autocorrelation function $C(\phi_0, \phi)$ (2.32) for our Gaussian primary beam of dispersion $\phi_0 = 0'.764$. Again, because the reference beams in a given RING switched field measurement are very nearly centered on the adjacent field's main beam (6.1),

$$\begin{aligned} A_{ij} = C(\phi_0, \phi_{ij}) - \frac{1}{2}(C(\phi_0, \phi_{i-1\,j}) + C(\phi_0, \phi_{i\,j-1})) - \frac{1}{4}(C(\phi_0, \phi_{i-1\,j-1}) \\ + C(\phi_0, \phi_{i-1\,j+1}) + C(\phi_0, \phi_{i+1\,j-1}) + C(\phi_0, \phi_{i+1\,j+1})) + \epsilon_i^2\, \delta_{ij} \end{aligned} \tag{6.6}$$

where C is an implicit function of the free parameters $C_0^{1/2}$ and ϕ_c. Because there are significant correlations between the fields, especially for large values of ϕ_c, the matrix A is no longer sparse and inversion is necessary for each evaluation of the likelihood $L(\theta)$. For the full 96 field RING dataset this is computationally expensive; the matrix inversion and manipulation algorithms used must be efficient to allow dense sampling of $(C_0^{1/2}, \phi_c)$ space. Software to calculate the Bayesian HPD limits with the correlation matrix (6.6) was written for the Convex C-1 vectorizing computer of the Caltech Astronomy Data Processing Facility utilizing the optimized FORTRAN compiler and the CONVEX VECLIB subroutines. For each value of the coherence angle, the likelihood function was computed with uniform spacing in $\theta = C_0^{1/2}$,

$$L_j = L(\theta_j) \qquad \theta_j = (j-1)\Delta\theta \quad j = 1, \ldots, J \tag{6.7}$$

with the maximum J chosen such that the likelihood has fallen to e^{-10} of its maximum value

$$L(\theta) \le e^{-10} \cdot \max_{0 \le \theta' < \theta_J} L(\theta') \qquad \text{for all} \quad \theta \ge \theta_J.$$

An array of the integral of the likelihood (with uniform prior) was constructed using the Trapezoidal Method

$$P_j = \sum_{i=2}^{j} \frac{1}{2} \left(L_{i-1} + L_i\right) \Delta\theta \tag{6.8}$$

which approximates the desired integral in the limit

$$\lim_{\Delta\theta \to 0} P_j = \int_0^{\theta_j} L(\theta)\, d\theta. \tag{6.9}$$

This procedure is computationally tractable with sufficient accuracy for reasonable grid spacings $\Delta\theta < 5$ μK. The $(1-\alpha)$ HPD limits $(\theta_{j0}, \theta_{j1})$ were determined by finding the smallest interval $[j0, j1]$ containing the highest values of L,

$$L(j) > L(j') \qquad \text{for all } j \in [j0, j1], \quad j' \notin [j0, j1]$$

for which the integral is greater than or equal to a fraction $(1-\alpha)$ of the total

$$P_{j1} - P_{j0} \ge (1-\alpha)\, P_J \qquad j0 \ge 0, \quad j1 \le J.$$

The results for $(1-\alpha) = 0.95$ and $(1-\alpha) = 0.9987$ are shown for the uncorrected RING data in Figure 6–2(a) and Figure 6–2(b) respectively. The spacing is $0'.1$ in ϕ_C for $0'.1 \leq \phi_C \leq 20'$ and the computational grid resolution $\Delta\theta = 1\ \mu\mathrm{K}$. The solid curves represent the HPD upper and lower limits on the amplitude $C_0^{1/2}$ and the dotted curve represents the MLM value $\hat{\theta}$. Also superimposed on the limits in Figure 6–2 is the upper limit obtained by neglecting the correlations between the RING measurements $\mathbf{y}$, shown as a dashed curve; this is the limit that would be set in an equivalent experiment where the fields were well separated on the sky instead of interlocked. The lower sensitivity of the RING for small coherence angles (due to the reduced amount of sky actually covered) is compensated for by increased sensitivity on scales larger than $10'$, where the linked geometry provides information about the correlations on angular scales larger than the switching angle $\phi_S = 7'.15$. The finite resolution of the numerical grid can be seen in the figure, as well as some possible artifacts, especially where the limit changes from two-sided to one-sided as the value $\theta = 0$ is no longer outside the interval. In Figure 6–3(a) and (b) are the corresponding 95% and 99.87% limits for the corrected RING data.

In Figures 6–4(a) and 6–4(b), the 95% and 99.87% HPD limits are shown for logarithmic spacing in angle ϕ_C and an amplitude grid of $\Delta\theta = 4.0\ \mu\mathrm{K}$ for the original RING data. The solid and dotted contours are the RING limits and ML estimate as in Figure 6–2, and the dashed curve is the corresponding Bayesian upper limit from the NCP experiment. Over most of the range in coherence angle depicted, the NCP limits are lower than the corresponding RING limits, which are excluded from the NCP 95% range in Figure 6–4(a). Because there is a significant radio source contribution to the measurements, Figures 6–5(a) and 6–5(b) show the same limits for the corrected RING observations. The NCP curve is much closer to the RING lower limit, and for coherence angles above $20'$ the linked RING geometry provides lower limits than the sparse NCP sampling, despite the lower sensitivity per field. In Figure 6–5(b) we see that there is much better agreement between the two experiments at the 3σ level, our preferred level of test significance. For the 99.87% limits, the RING provides the better limit for angles $\phi_C > 13'$.

6–3 Comparison with Published Theoretical Models

In the discussion of the predictions of a selection of published galaxy formation models for the NCP experiment given in Paper 1 (§X and Table 6), 56% of the models considered were ruled out at the 95% confidence level, and a further 20% were within a factor of two of exclusion by the NCP results. By and large, the most successful models were those involving $\Omega = 1$ and a dominant Cold Dark Matter (CDM) component, or significant early reionization of the universe after recombination. For adiabatic CDM models, the OVRO NCP limits restrict the free parameter bias b_ρ which is related to the *rms* linear density fluctuation amplitude through the normalization procedure (Bond 1988). For a Hubble constant $H_0 = 50$ and baryon fraction $\Omega_B = 0.03$, the limit is $b_\rho > 0.5$ and increases with increasing Ω_B (to $b_\rho > 0.9$ for $\Omega_B = 0.2$) and decreases for a larger H_0 ($\propto H_0^{-1}$). The isocurvature models with early reionization are also not excluded by our previous 95% limits (see the review in Bond 1988) as rather low ionized fractions ($< 10\%$, see Table 6 in Paper 1 and Bond and Efstathiou 1987, Efstathiou 1988) are needed to affect anisotropies on arcminute scales. A prolonged recombination or subsequent early reionization will enlarge the width of the last scattering surface and thus increase the coherence angle of the fluctuation correlation function. If the universe never recombines, the angular scale increases from $\phi_c \sim 10'$ for standard recombination to $\phi_c \sim 5^\circ$ (Bond 1988). Finally, in the summary of adiabatic and isocurvature CDM and neutrino models without reionization by Holtzman (1989) only the $\Omega = 1$ models with small baryon fractions are not excluded by our results. Recent hybrid models with both hot and cold dark matter are very close to the NCP limit although a correct calculation has not been performed (Schaefer, Shafi and Stecker 1989).

The reason that these theories are able to elude our net is because the coherence angles of the correlation functions predicted by such scenarios are larger than the switching angle of $7'.15$ of our experiments. Unfortunately , the width of the last-scattering surface (the angular scale corresponding to the distance traveled by a photon during the process of recombination, at the redshift of recombination) is $\phi_c \sim 10' h^{-1}$ and density fluctuations smaller than this scale will be washed out due to the superposition of many of these along the photon path through the region of decreasing Thomson optical depth. The enhanced sensitivity to larger scale fluctuations provided by the RING should lead to more stringent limits on nearly all models not excluded by the previous experiment, and an analysis combining the NCP and RING with a single massive correlation matrix will produce the best test of the viability of current and future models by the OVRO experiments. It is true, however, that estimates of the limits on those models with $\phi_C > 10'$ using the Gaussian autocorrelation function approximation will be inaccurate because the correlations over several multiples of the switching angle ϕ_S are likely to be important. In these cases the specific form of $C(\phi)$ must be explicitly used in the calculation of the elements of A if any quantitative comparison is desired.

It should also be stressed once again that the nonzero lower limit indicated by the RING analysis should *not* be taken as conclusive evidence for the detection of microwave background anisotropy. Significant contaminating signals due to nonthermal discrete radio sources have already been subtracted from the measurements and it is certain that there is a non-negligible level of signal remaining in the dataset due to objects missed in the 8.5 GHz VLA survey because of incomplete spatial coverage, inadequate sensitivity, inaccurate extrapolation of spectral energy distributions to 20 GHz, insufficient knowledge of the OVRO primary beam at low levels, and the lingering possibility of a non-Gaussian tail to the instrumental and atmospheric noise distribution at microKelvin levels. In light of these problems, it is advisable to use only the upper limits from the HPD analysis of the RING when investigating the predictions of cosmological models, barring the identification of the 3σ candidate deviations in NPR0700 and NPR1015 as real, extended and attributable to the microwave background. Despite the traditional use of the 95% 'confidence' measure adopted in the literature and practice of the microwave background observational field, it is also prudent to use the more conservative 99.87% limits equivalent to a 3σ deviate from a normal distribution. As discussed in §2–3, there is nothing special about the use of 95% confidence in this field, which makes it more sensible than the 3σ limits adopted as standard in other areas of study such as physics, and we would urge all practitioners to use 99.87% limits in the future.

6–4 Comparison with Non-Gaussian Models

In addition to enhancing the response to Gaussian fluctuations generated by models with large coherence angles, the RING experiment provides increased sensitivity to certain classes of non-Gaussian models, as demonstrated by the greater vulnerability to contamination by discrete radio sources. As discussed in §2–4, random pointlike objects with a power-law differential number count index between 1 and 3 will have an increasing contribution to the variance as the number of fields observed is enlarged. There are a number of theories for the formation of galaxies and large-scale structure that predict some form of non-Gaussian behavior. We can divide these models into three classes : those in which the primary fluctuations themselves are non-Gaussian at the time of their generation (*e.g.*, during the epoch of inflation), those in which the primary or secondary fluctuations are modified or created by gravitational effects from massive particles or structures in the early universe or after recombination, and those in which secondary anisotropies are created or the primary fluctuation spectrum modified by scattering or reprocessing from intervening material after decoupling. We will now briefly discuss the various scenarios contained in each class and the estimates on the contribution to the anisotropy in the RING experiment where available.

The inflationary paradigm has been successful at explaining the flatness of the Universe and why the microwave background is isotropic to at least one part in 10^{-3} (other than the dipole term due to our peculiar velocity in the cosmic background frame), but by no means is it free of loose ends or fine-tuning problems. The generation of fluctuations with Gaussian statistics is taken to be a consequence of the required weak coupling of the 'inflaton' scalar field (see Wise 1988), but problems with the reconciliation of the standard model with the observed properties of large-scale structure have kindled interest in non-Gaussian primordial fluctuations (*e.g.*, Peebles 1983). Inflation with more than a single scalar field may lead to non-Gaussian perturbation statistics in addition to breaking scale invariance (Kofman and Pogosyan 1988), which allows an increased amplitude of long wavelength fluctuations to produce large-scale structure and peculiar velocities. However, since no reliable theories exist that predict a scalar field whose potential surface has the required behavior, Gaussian statistics or not, there are no available quantified models for non-Gaussian fluctuations generated in these scenarios.

On the other hand, a great deal of effort has been put into the investigation of non-baryonic ingredients in the particle mix of the early universe, mostly with an eye toward assisting matter in the collapse into structure without causing excessive anisotropy in the microwave background. In the prevalent models with baryons and a dominant non-baryonic dark matter component the resulting fluctuations in the background remain Gaussian because the density perturbations are still in the linear regime at decoupling. Collapsed objects at moderate to high redshift possibly can alter the microwave background correlation spectrum through gravitational lensing effects (Cole and Efstathiou 1989), though this mechanism is unlikely to be effective on angular scales of interest to us. Topological defects in the vacuum originating from the phase transition in the scalar inflaton field at the end of inflation are inherently nonlinear and the perturbations introduced in the baryonic component at and after recombination are therefore non-Gaussian. The 0, 1, 2, and 3-dimensional defects (boundaries between regions of space with different realized values of order parameters in a broken symmetry) are known as monopoles, strings, domain walls, and texture. The existence of magnetic monopoles is predicted by GUT theories but with a low space density due to dilution during inflation, and the prevention of these unobserved relics from filling space is a triumph of the inflationary model. The density of domain walls separating regions of space containing different degenerate vacua resulting from a GUT transition is similarly diminished by inflation, although there have been recent attempts to enlist walls in the formation of structure (Press, Ryden and Spergel 1989). Texture is a newcomer to the exotic cosmological zoo and consists of regions of space in which the order parameter of a global symmetry has a fixed value (Turok 1989). By far, the most popular defects are cosmic strings, one-dimensional regions of false vacuum that possess a mass per unit length μ (see Vilenkin 1986 and references therein) and closed loops of strings are postulated to form seeds for the formation of galaxies. In addition to the induced density perturbations, cosmic strings act as gravitational lenses to modify directly the microwave background radiation, forming step discontinuities in the background temperature when moving perpendicular to the observer. Numerical simulations of anisotropies induced by string networks have been performed by Bouchet, Bennett and Stebbins (1988) who have constructed maps of the resulting background temperature field. The limits quoted for the NCP experiment using the rms string fluctuations are (from a Gaussian analysis)

$$\frac{G\mu}{c^2} \leq 2 \times 10^{-6},$$

however as noted by the authors, non-Gaussian effects are likely to render this limit unreliable. We are currently involved in a collaboration with this group to perform a detailed comparison between their string models and the RING dataset. Because galaxy formation scenarios using strings as seeds require $G\mu/c^2 \sim 1\text{–}4\times 10^{-6}$, the correct analysis of the RING and NCP limits for these models will provide important constraints on these models.

The presence of dust or ionized gas in the universe after recombination will also modify the fluctuations in the microwave background temperature. The reports of an excess in the submillimeter region of the background spectrum over the 2.74 K blackbody, the latest of which being the Matsumoto *et al.* (1989) rocket experiment, spurred theoretical interest in models with significant amounts of dust at redshifts $z > 10$ (Bond, Carr, and Hogan 1986, Bond, Carr, and Hogan 1989, Djorgovski and Weir 1990) wherein heating of dust by protogalactic objects or active galactic nuclei in the (moderately) early universe causes re-radiation in the infrared bands which is then red-shifted into the submillimeter. The effect of these dusty objects on the anisotropy of the microwave background is dependent upon the Poisson statistics of the number counts of the sources—the OVRO NCP results, among others, place stringent limits on the density ($> 30\, h^3\, \mathrm{Mpc}^{-3}$) or clustering ($< 60\, h^{-1}$ kpc) of these sources (Hogan and Bond 1988, Bond, Carr, and Hogan 1989). However, the immediacy of these results has disappeared along with the submillimeter excess with the measurement of background spectrum by the COBE satellite (Mather *et al.* 1990), which places a limit of 1% of the peak intensity on the deviation from a 2.735 K blackbody over the frequency range 30 GHz to 600 GHz (wavelength 1 cm to 0.5 mm). Explosive galaxy formation scenarios (*e.g.*, Ikeuchi 1981, Ostriker and Cowie 1981), like those involving superconducting cosmic strings (Ostriker and Thompson 1987), also generate non-Gaussian anisotropies, although it has been claimed that there is negligible heating of the pregalactic medium for efficient blast waves. There are no concrete fluctuation distributions predicted by these models and future work will be needed to adapt their predictions to the RING results. Another set of secondary anisotropy generating models are the decaying particle theories (*e.g.*, Daly 1988, Doroshkevich, Klypin and Khlopov 1989) where galaxy formation is prompted either through explosive decay of the massive nonbaryonic particles or through gravitational clustering around these seeds, which later decay and disappear. The work on a condensate scenario by Daly predicts the number of detections for the RING experiment above the $\Delta T/T = 1 \times 10^{-4}$ level; four are found in the corrected dataset. This places an upper limit on the volume filling factor of voids at the current epoch determined by her models of 0.02–0.09, while observations estimate the true value to lie in the range 0.03–0.13. Thus, these models are consistent with the data assuming the identified fields are not due to noise or to discrete radio sources.

Any process that releases significant amounts of energy at an early epoch after recombination will produce secondary anisotropies in the microwave background radiation as well as distort the blackbody spectrum. The limits from COBE on the total Compton parameter are $y < 0.001$, (3σ) where

$$y = \int_{t_0}^{t} \frac{kT_e}{m_e c^2}\, n_e\, \sigma_T\, c\, dt = \int_0^{\tau} \frac{kT_e}{m_e c^2}\, d\tau \tag{6.10}$$

(Zel'dovich and Sunyaev 1969) is a dimensionless variable that is related to the average energy change in a photon along its path through the ionized gas with electron density and temperature (n_e, T_e) due to Thomson scattering for cross-section σ_T, and optical depth along the line-of-sight $\tau = \int n_e\, \sigma_T\, d\ell$. In the Rayleigh-Jeans region of the microwave background spectrum ($h\nu << kT_{mwb}$) the change in the blackbody spectrum induced by scattering the background photons off the electrons in the hot gas is given by

$$\frac{\Delta T}{T} = -2y \tag{6.11}$$

(c.f. Sunyaev and Zel'dovich 1981) causing a decrement in the observed equivalent temperature at frequencies below the blackbody peak as the photons are preferentially scattered up in energy to the Wien region of the spectrum. This process, known as the Sunyaev-Zel'dovich (SZ) effect, has been observed in nearby clusters of galaxies with hot X-ray emitting coronae (Birkinshaw, Gull and Hardebeck 1984, Birkinshaw 1987) with the OVRO 20 GHz system at a level of 600 μK–1 mK. Various estimates of the cumulative effect upon the microwave background by modelling of the formation and evolution of these clusters have been made, although correlation function analyses were not pursued in enough detail to compare with the RING results directly. Schaeffer and Silk (1988) estimate the contribution to the Uson and Wilkinson (1984c) experiment to be

$$\frac{\Delta T}{T} \sim 3 \times 10^{-5}$$

for the NRAO 19 GHz beam dispersion $\phi_0 = 0'.64$ and throw $\phi_S = 4'.5$. Because the estimated correlation angle of the fluctuations was $1'$, the contribution to both OVRO experiments should be slightly less than this, possibly near the level of the NCP limit. Cole and Kaiser (1989), in their CDM model, estimate the *rms* amplitude expected for the NCP experiment to be

$$\frac{\Delta T}{T} \sim 5 \times 10^{-6}$$

although it is not clear from the discussion in the paper whether angular correlations were considered in the calculations. Other models are considered by Bond (1986). Because the distribution of clusters is Poissonian in the absence of clustering, and the distortions to the microwave background are decrements only, the statistics of the fluctuations induced are non-Gaussian with a strong negative tail and predictions for large sample experiments such as the RING are not easily estimated from simple calculations. Numerical simulations of galaxy formation in the popular CDM scenario are now beginning to include the evolution of the baryonic component as well as the dark matter and energy injection by protogalaxies into the gaseous medium, which is seen to lead to non-Gaussian perturbations of the background radiation. Recent work by Ryu, Vishniac, and Chiang (1989) predicts fluctuations at the level

$$\frac{\Delta T}{T} \sim 4 \times 10^{-6}$$

with a log-normal distribution. The prospect of placing limits on these physical models is exciting and should provide important constraints on the nature of the formation process itself as the simulations become more detailed and the observations become more sensitive.

We have outlined a number of theoretical models that predict non-Gaussian fluctuation distributions of possible interest to us for comparison with the RING and NCP experiments. With the exception of Daly's condensate and decay model, none of the scenarios discussed have presented sufficient information on the distributions to permit detailed statistical analyses similar to those given in §6–2. However, we have not yet established the formalism to make such comparisons nor is it clear that sparsely sampled data such as the RING can easily be probed for a non-Gaussian signature particularly in the presence of instrumental noise. The Kolmogorov-Smirnov test of the RING field distribution (§4–3) revealed that the data was marginally inconsistent with a Gaussian distribution with no real signal and very consistent with a Gaussian distribution with a 133 μK *rms*. This may be misleading because the correlation between RING measurements due to the switching and interlocking geometry were not included. Yahil and Vidal (1977) discuss tests of normality in another context, although in their case measurement errors were not significant and it is unlikely that a strong result can be extracted from a low signal-to-noise ratio dataset such as the RING. Geometrical tests of normal and non-Gaussian distributions are discussed in detail in Coles and Barrow (1987) and Coles (1988), with emphasis on measuring the statistics of hotspots. Methods such as theirs may prove powerful if fluctuations are detected and imaged.

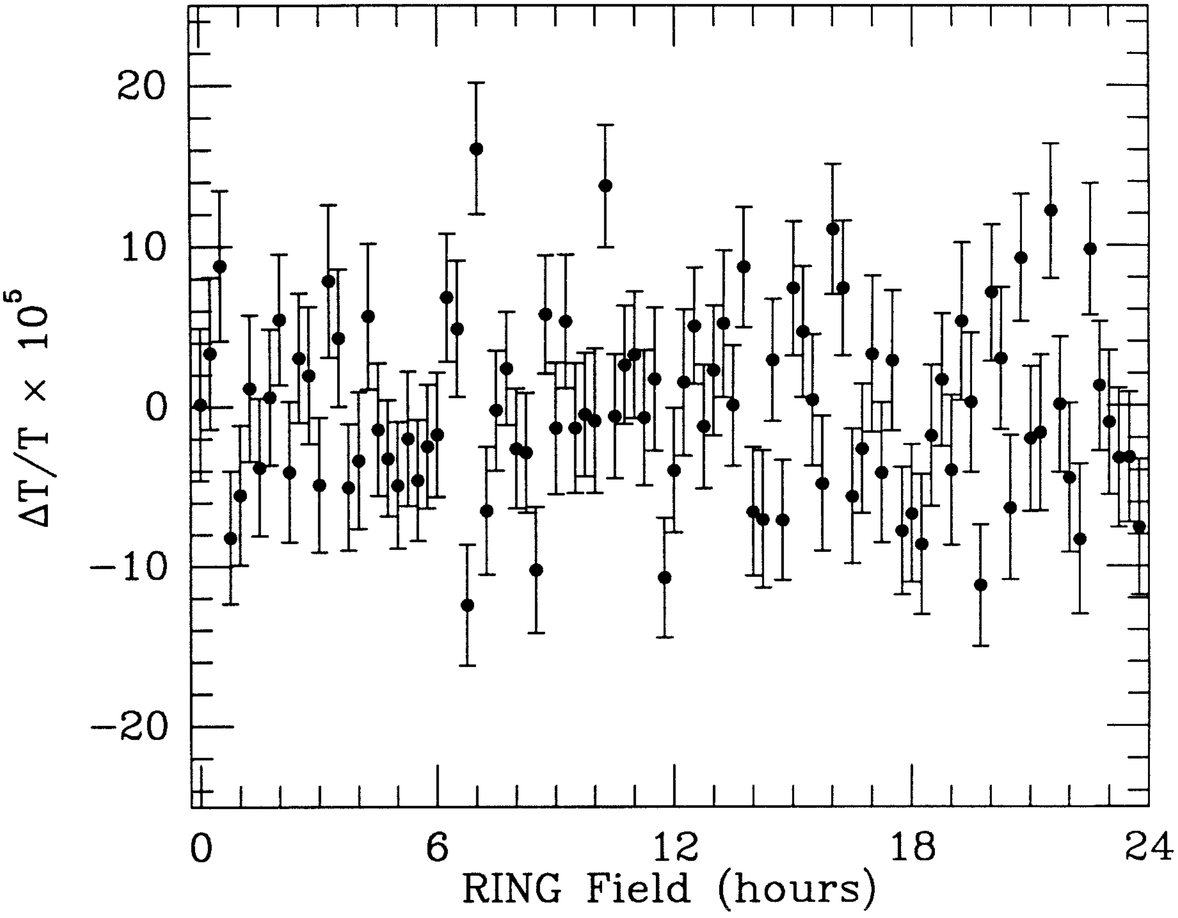

FIGURE 6–1. Corrected RING measurements with estimated contributions from the VLA 8.5 GHz radio sources subtracted, expressed as a fraction of the microwave background temperature $T = 2.735$ K.

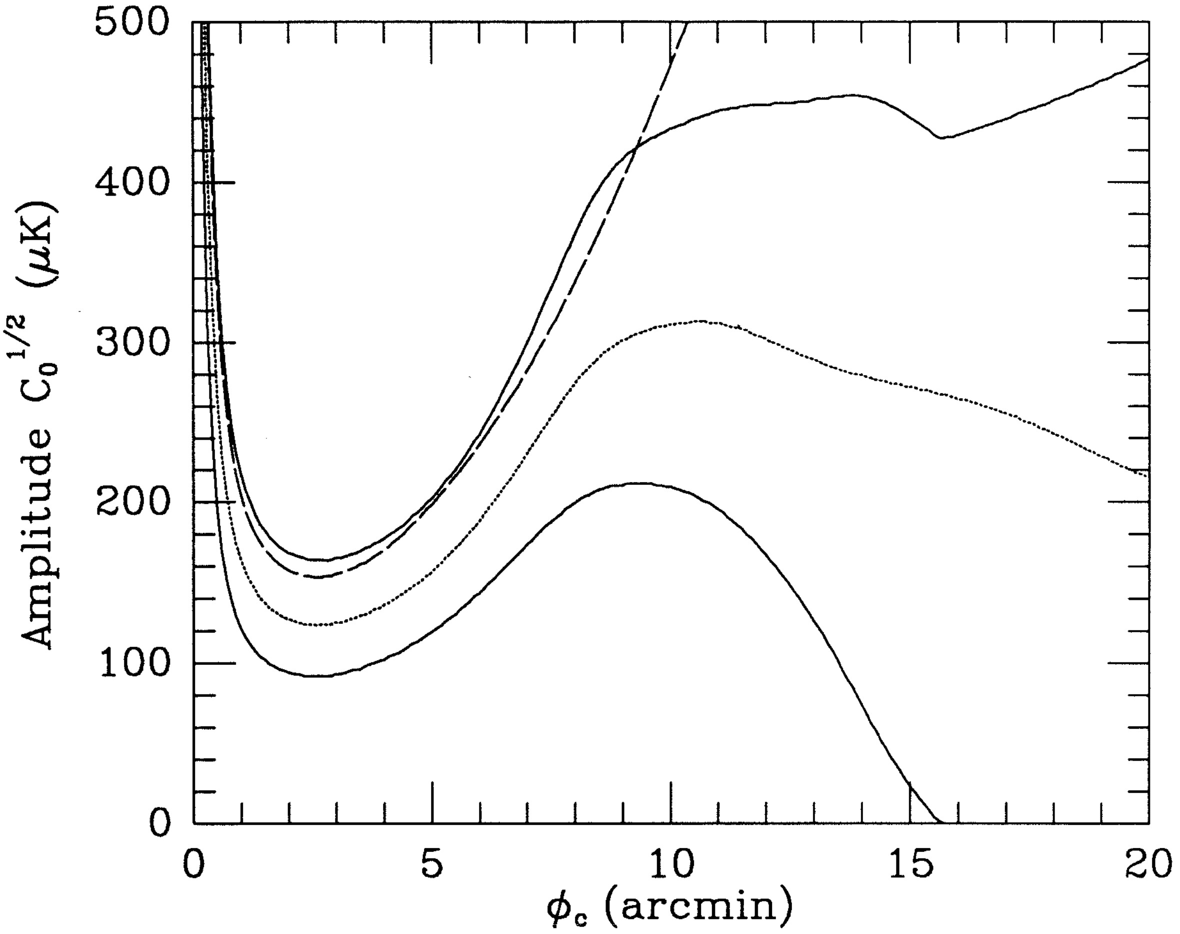

FIGURE 6–2(a). Bayesian 95% HPD limits on the *rms* fluctuation amplitude in the original RING data (solid lines) for the Gaussian autocorrelation function model with coherence angle ϕ_c. Also shown are the Maximum Likelihood estimate (dotted curve) and the corresponding 95% upper limit if it is assumed that the fields are uncorrelated (dashed line).

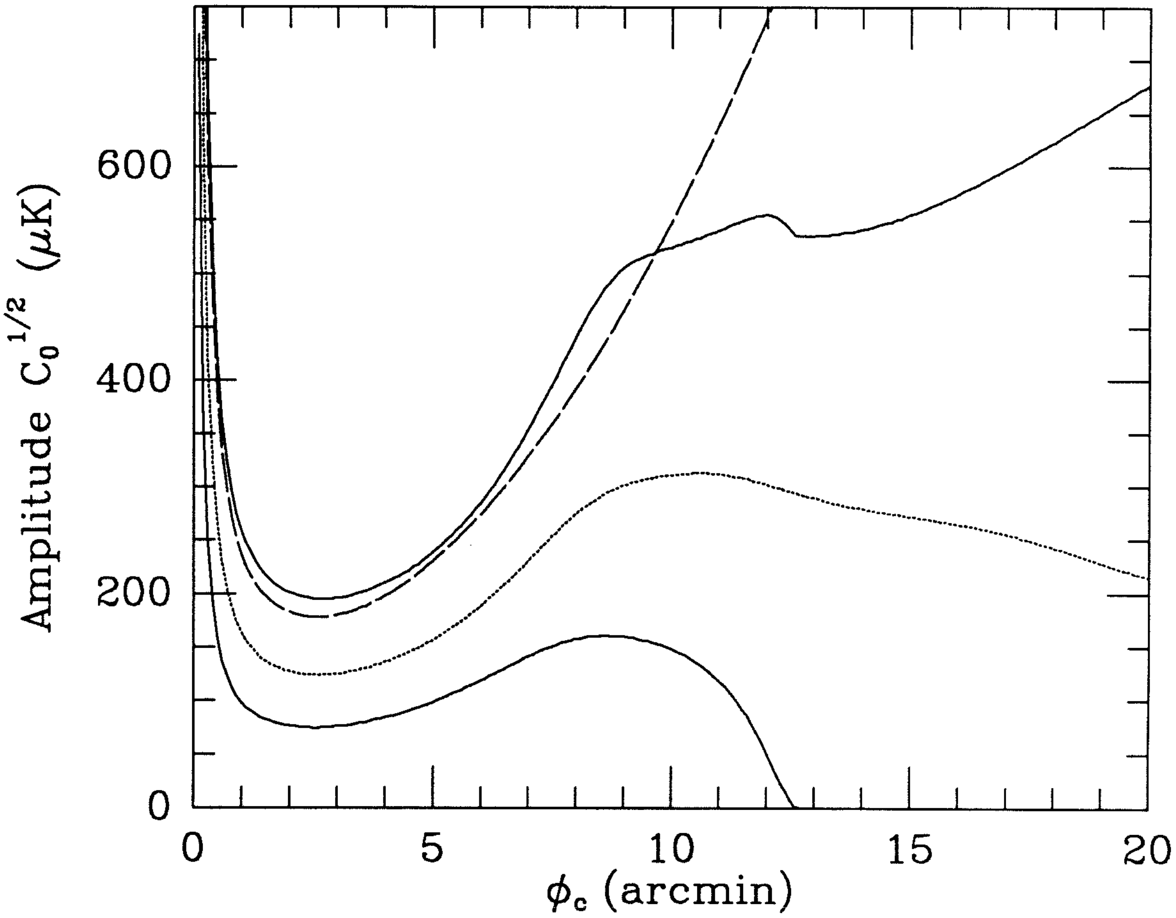

FIGURE 6–2(b). Same as (a) except 99.87% HPD limits (solid and dashed).

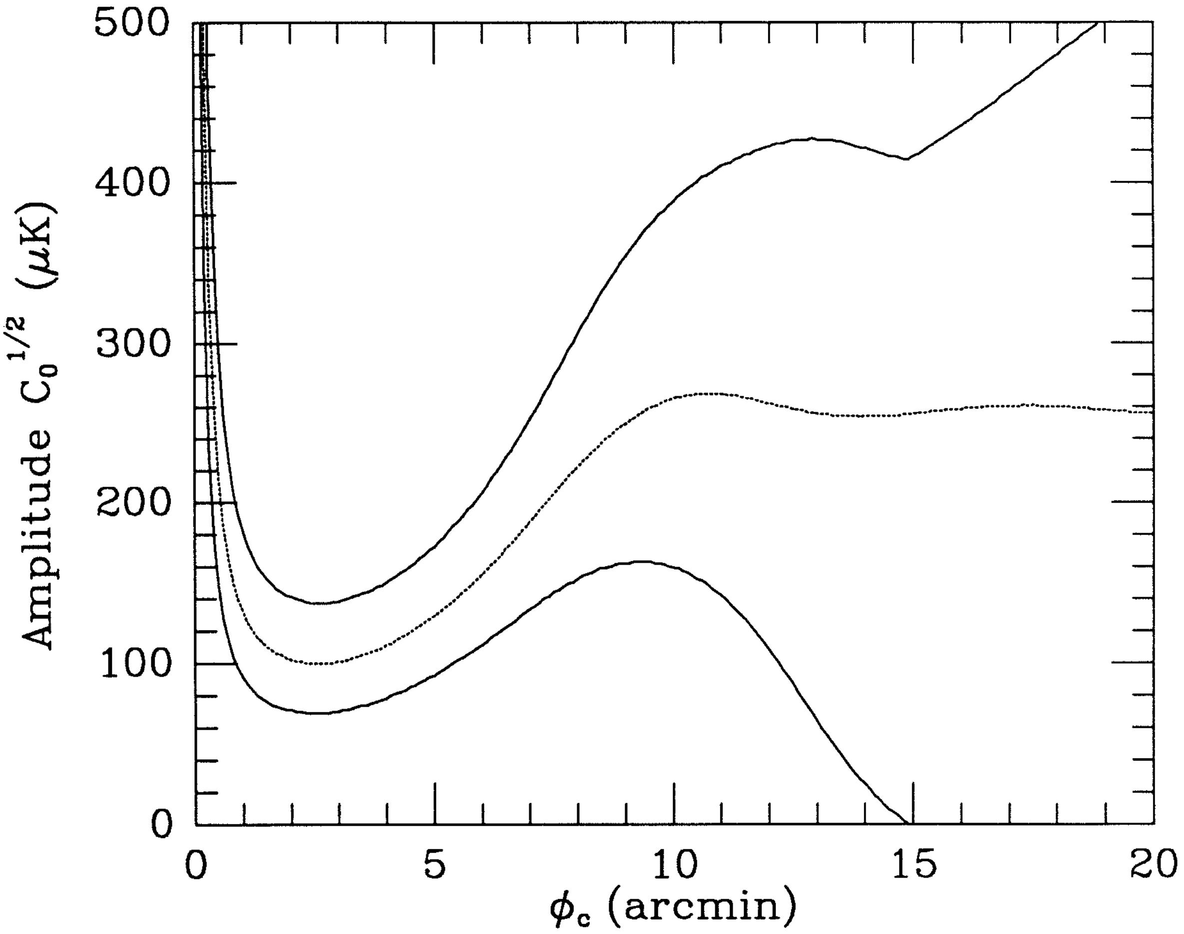

FIGURE 6–3(a). Bayesian 95% HPD limits on the *rms* fluctuation amplitude in the corrected RING data (solid lines) for the Gaussian autocorrelation function model with coherence angle ϕ_c. Also shown is the Maximum Likelihood estimate (dotted curve).

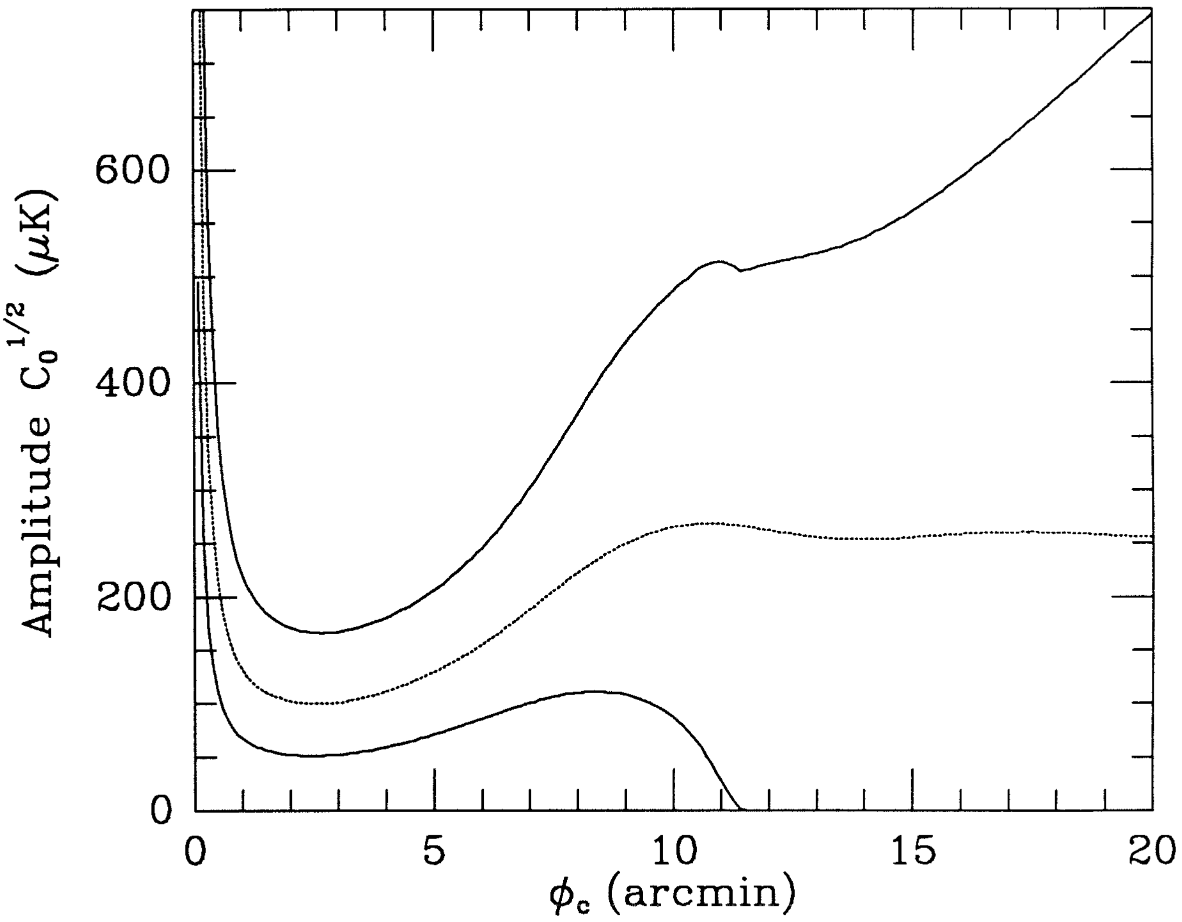

FIGURE 6–3(b). Same as (a) except 99.87% HPD limits (solid curves).

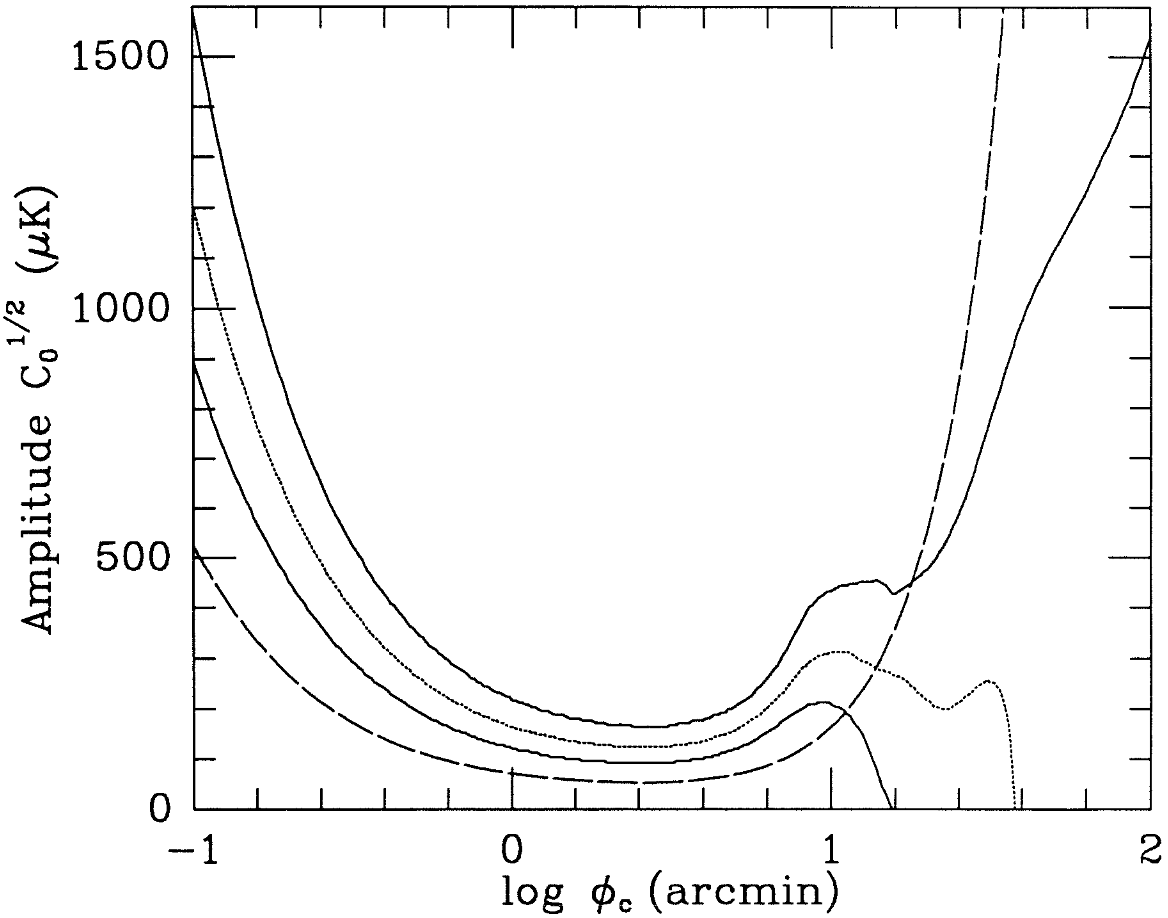

FIGURE 6–4(a). Bayesian 95% HPD limits on the *rms* fluctuation amplitude in the original RING data (solid lines) for the Gaussian autocorrelation function model with coherence angle ϕ_c. Also shown are the Maximum Likelihood estimate (dotted curve) and the corresponding 95% upper limit from the NCP experiment (dashed line).

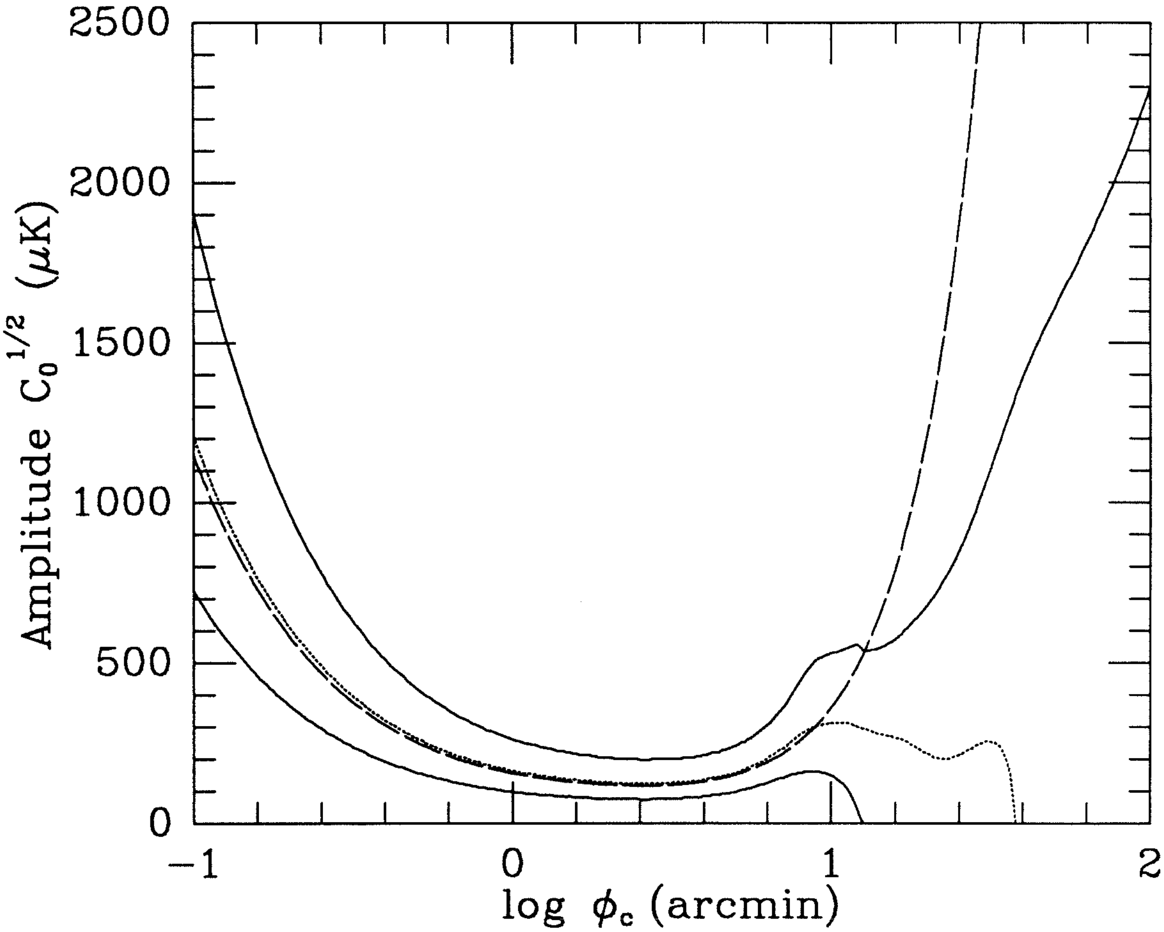

FIGURE 6–4(b). Same as (a) except 99.87% HPD limits (solid and dashed).

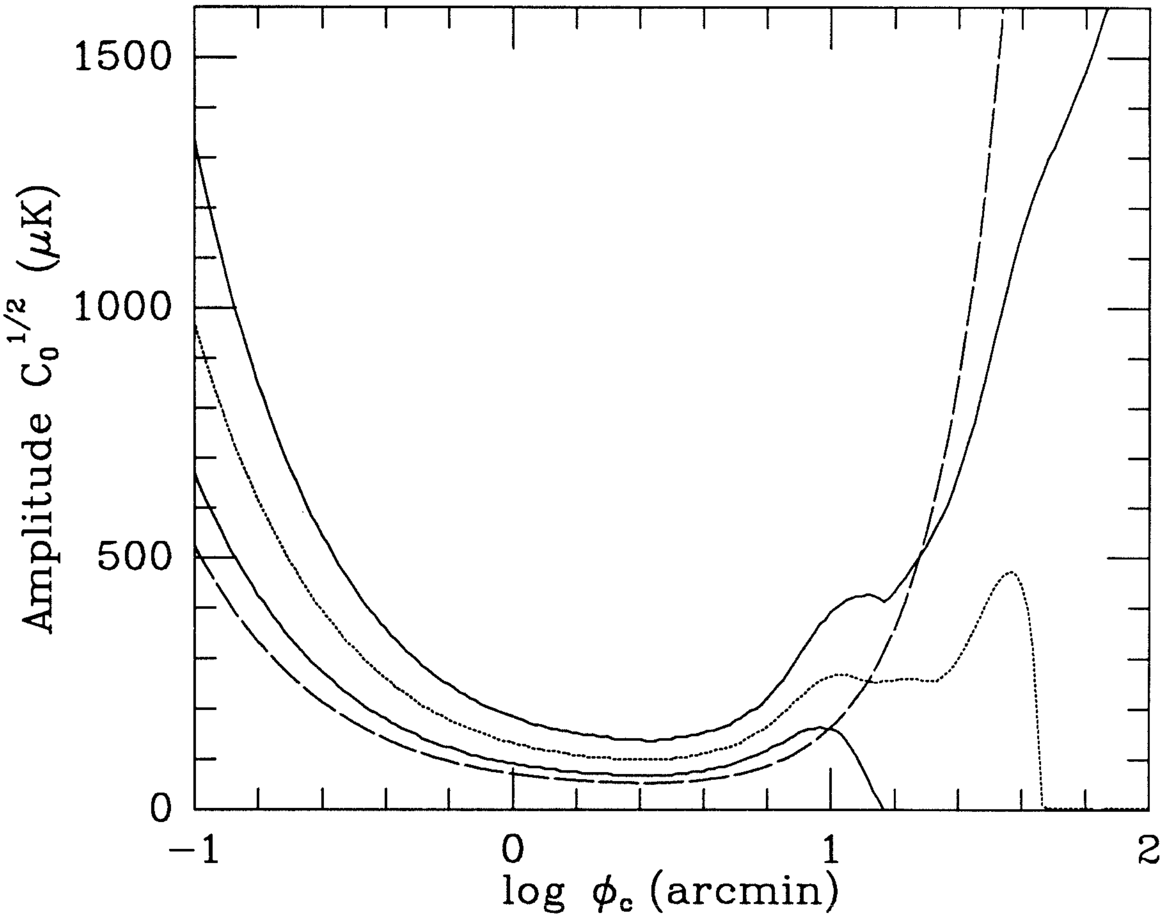

FIGURE 6–5(a). Bayesian 95% HPD limits on the *rms* fluctuation amplitude in the corrected RING data (solid lines) for the Gaussian autocorrelation function model with coherence angle ϕ_c. Also shown are the Maximum Likelihood estimate (dotted curve) and the corresponding 95% upper limit from the NCP experiment (dashed line).

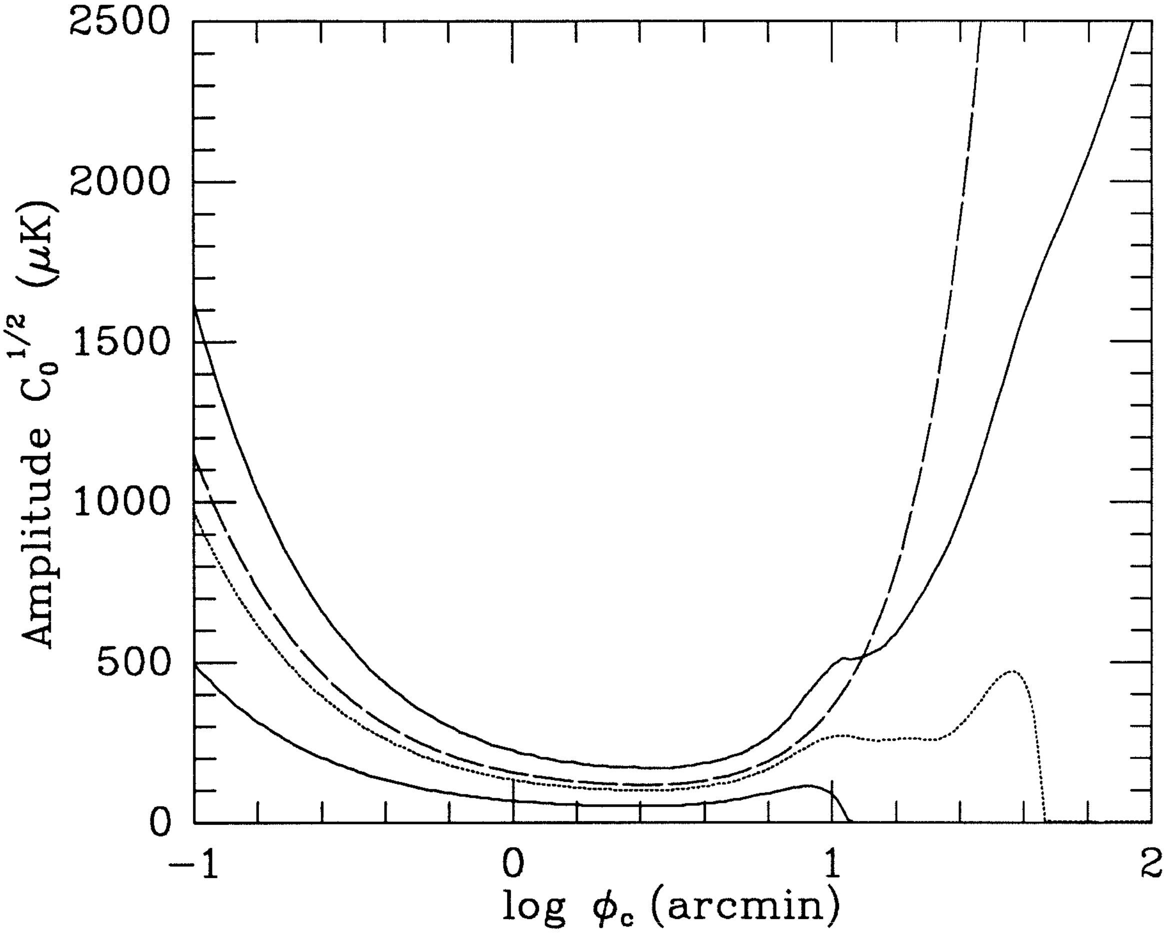

FIGURE 6–5(b). Same as (a) except 99.87% HPD limits (solid and dashed).

CHAPTER 7
Conclusions and Questions

In the preceding chapters, we have presented the observations of the Caltech Owens Valley Radio Observatory survey for microwave background anisotropy on arcminute angular scales at an observing frequency of 20 GHz. Results from the 8-field NCP experiment of Readhead *et al.* 1989 were given in Chapter 3 wherein an upper limit on the *rms* amplitude of Gaussian fluctuations uncorrelated between $1'.8$ FWHM primary beams of

$$\frac{\Delta T}{T} < 1.7 \times 10^{-5}$$

was derived. In Chapter 4, the results of the 96-field RING experiment were presented along with detailed explanations of the calibration and editing procedures and tests of data quality. The presence of a signal in the data in excess of the scatter expected from the instrumental noise was established and matched filtering was used to identify 7 individual fields as candidates for harboring sources of anisotropy, 4 of which were also detected above the 3σ level in a MEM reconstruction. The results of VLA observations of the RING region at 1.4 GHz and selected RING fields at 8.5 GHz were given in Chapter 5. Three of the RING fields indicated as suspect by the matched filtering were shown to contain bright discrete radio sources with signal levels greater than 150 μK while a fourth candidate was found to contain a weaker source of 35 μK. Two RING fields with deflections greater than 350 μK remain unidentified with contaminating sources. A corrected RING dataset, with the best extrapolations of the VLA source fluxes to 20 GHz subtracted, still showed excess variance at the 95% and 99.87% (3σ) level. Because of uncertainties in the extrapolation from 8.5 GHz to 20 GHz, and insufficient sensitivity to flat-spectrum objects, there is likely to remain substantial contamination of the data by confusing signals.

In Chapter 6 a Bayesian statistical analysis of the full and the corrected RING data was performed using uncorrelated and simple coherence angle models for Gaussian fluctuations. Using the VLA source-subtracted data, the 95% limits from the RING and NCP experiments are incompatible for correlation angles below $10'$ and the RING 95% upper limits prove superior for angles above $19'$. The limits from the two experiments are consistent at the 99.87% confidence level and the RING upper limits are lower for models with coherence angles $\phi_c > 12'.6$. The interlinked RING geometry allows increased sensitivity to fluctuations on scales larger than the switching angle $\phi_S = 7'.15$, although the contribution from a large range of angular scales will cause the limits from the approximate Gaussian autocorrelation function model to be inaccurate for models with large correlation angles. The constraints on specific Gaussian fluctuation scenarios were summarized, quantitatively for the NCP limits and qualitatively for the RING results. The desirability of direct comparison with the RING data for models with significant large-angle correlations was indicated. Models predicting non-Gaussian fluctuations were discussed although only one specific prediction for the RING was available. Theories involving cosmic strings, decaying particles and Compton scattering from hot gas in clusters of galaxies were singled out as the most promising targets for RING analysis.

The linked sampling of switched data used in the RING has proved to be a successful approach to optimizing the sensitivity and sky coverage of a many-field experiment. As a compromise between the widely-spaced, nearly independent sampling previously used in small angular scale observations and the drift-scan and other dense sampled techniques used for large-angle anisotropy experiments, the RING interlocking geometry provides increased sensitivity to angular scales outside the switching range, reconstruction and single source detection capability, and noise and bias indication properties while retaining the high point-measurement sensitivity of the small sample experiments. *The fact that no subtraction of bias levels or gradients was required after the final edited and calibrated dataset was produced attests to the robustness of the procedure—the mean of the entire dataset was* $-6\ \mu K$, *less than the expected* 1σ *uncertainty of* $12\ \mu K$ *predicted from the known system noise levels.* The detection, identification and successful subtraction of discrete radio sources lends strong confidence to the final calibration of the data, although the high level of contamination, though not a complete surprise, makes the production of a confusion-free dataset difficult if not impossible. The limits obtained from the corrected RING measurements are competitive with those from the deeper NCP observations on larger angular scales, although it must be stressed once again that *the uncertainty of extrapolation from the lower frequency VLA survey and the lack of information about the spectral properties of discrete sources at high frequency and low flux levels lead us to treat the RING limits as upper limits only.* This may disappoint those eager for the discovery of real anisotropy; however, the large number of mechanisms that could lead to an erroneous lower limit requires us to adopt a conservative approach. Because large experiments such as ours can identify candidate targets for closer study, all hope is not lost for anisotropies, and indeed the RING experiment has yielded two fields for which we have scheduled deeper observations at Owens Valley. If the fluctuations in the microwave background have a non-Gaussian distribution with a large amplitude tail, then it is more efficient to search over a larger area with reduced sensitivity than to probe a few fields deeply. The possibilities for future work using these techniques are exciting and limited only by the availability of reliable receivers and observing time, although the cooperation of the local climate is always a factor.

There is much future work to be done, on both the observational and the theoretical aspects of the subject. Completion of the 8.5 GHz VLA survey of the RING sample to a deeper flux level and full field coverage will begin in 1990. If the spring weather permits, the candidate fields NPR0700 and NPR1015 will be measured with the OVRO 20 GHz system to a sensitivity level of $\sim 30\ \mu\mathrm{K}$ to determine whether these regions contain actual sources or not; this follow-up may extend into the autumn 1990 season. On the analysis side, a careful investigation of the RING field distribution using the $P(D)$ method developed for radio source counts (Scheuer 1957, Condon 1974) will provide limits on the normalization K and index γ of power-law number counts

$$N(T)\,dT = K\,T^{-\gamma} \qquad T > 0$$

for a Poisson point-process of objects with temperature T. It will also be possible to use the full correlation information to place limits on both Gaussian and non-Gaussian models with the combined RING and NCP measurements. Through collaboration with the theorists, we will make direct comparisons with the Gaussian CDM adiabatic and isocurvature models of J.R. Bond and G. Efstathiou, the non-Gaussian cosmic string maps of D. Bennett and A. Stebbins, and the superconducting cosmic string explosion scenarios of C. Thompson. We will also endeavor to investigate the available models of the SZ effect from galaxy clusters and the forthcoming galaxy formation simulations where evolution of the gaseous component is included. In combination with the recent results from the Antarctic experiments on degree scales (Meinhold and Lubin 1990), the RING and NCP observations should place extremely tight constraints upon the free parameters of most models currently under consideration.

It is hoped that over the next few years we can push the sensitivity of the NCP experiment, when expanded to a full 12 fields, at least another factor of two lower to the level where nearly all currently favored theories will be tested. The maps obtained at the VLA should allow us to steer clear of possible confusing discrete sources until the high frequency number counts reach the saturation point; as mentioned in §5–2 estimates by Franceschini *et al.* (1989) place this at around 10^{-5} although removal or avoidance of sources brighter than 0.5 mJy should allow us to get to the 7×10^{-6} level. As the background observations become more sensitive, contemporaneous high resolution measurements at the same frequency will become important to subtract accurately the effect of contaminating objects. The new 5-meter diameter dedicated radio telescope at the Owens Valley Radio Observatory currently equipped with a 30 GHz maser receiver will be coming on-line shortly. This is a Dicke-switched dual horn system like that on the 40-meter telescope, with a primary beam of $7'.5$ FWHM ($\phi_0 = 3'.2$) and switching angle $\phi_S = 24'$, ideal for probing theories with correlation angles slightly larger than the last scattering surface dispersion of $10'$. It is likely that a high resolution companion system, also at 30 GHz, will be installed on the 40-meter telescope probably in 1991. In addition to aiding source subtraction from the 5-meter program measurements, this receiver could be used to survey the RING fields as a complement to this work. Upgrades of the 20 GHz and 30 GHz receivers to wide-bandwidth HEMT systems should occur in late 1990. Finally, design studies are underway for an interferometer array aimed at imaging of the microwave background on scales of $\sim 1^\circ$.

The next decade should prove to be an exciting time in the field of observational cosmology. Already we have witnessed the launch and first results from the COBE satellite, which along with the proposed Soviet counterpart RELIKT-2 (to be launched in 1992) should yield very sensitive maps on the largest angular scales at a variety of frequencies. The spectral measurements by COBE should place tight limits on backgrounds in the millimeter, submillimeter and infrared wavelength bands not available from the ground. The microwave and millimeter anisotropy experiments in the Antarctic armed with the newest and best bolometer and HEMT receivers will be probing fluctuations on degree scales in the next few years while the interferometer arrays such as that being built by the group at Cambridge will be producing images by the mid-90's. Extensive optical surveys of large-scale structure at moderate and high redshifts should be well underway in a few years perhaps providing sufficiently accurate information about the density and velocity fields in the Universe to make such studies a rival of the microwave background in the constraint of theory. It is much more difficult to project the progress of cosmological theory, especially from an observer's point of view. It is likely that larger and more sophisticated numerical simulations will provide quantitative predictions for the observers to puzzle over, while advances in our knowledge of the physics of the early universe may point the way to the solution of the outstanding problems besetting models at present. The failure of current simple models to account for the lack of structure in the cosmic background while producing structure in the Universe today is leading to the development of more complex and less intuitive theories and it is not clear whether this will continue or if a breakthrough in our understanding of the fundamental physics will return things to a 'simplified' state once again. It is also possible that basic flaws in the assumptions upon which our current models are built may be found—perhaps a true radiative transfer calculation through the era of decoupling or galaxy formation models with astrophysics included will change our view of the relation between the amplitude of perturbations and the ability to form galaxies before a redshift $z = 2$ and reconcile the models with the observations. On the other hand, it is possible (but not probable, I'll take bets) that some new 'wonder theory' will arise that will banish anisotropy to the 10^{-7} level or beyond turning those remaining in the anisotropy field into members of that admired but not envied class of professional skeptics who test such things as r^{-2} gravity and general relativity. I myself am optimistic about the opportunities for the discovery of new knowledge and insight into the origins and evolution of our universe and look forward to the advances that future projects such as those mentioned above and others that have not yet been dreamed of will make possible. However, many arduous years behind the controls of temperamental radio telescopes have instilled in me a certain pessimism that often dampens the enthusiasm displayed in the preceding paragraphs and I will conclude with my true predictions for the future of observational and theoretical cosmology :

- In the year 1999, COBE-2 will discover a distortion in the microwave background spectrum assuring theorists of funding until the next satellite launch.
- In the year 2003, RELIKT-3 will disprove existence of background distortion and theorists will claim that they "needed to do all those calculations anyway."
- In the year 2008, the completion of the CfA complete all-sky survey will reveal a structure designated the 'Great Elvis.' Theorists will be baffled but rock-and-roll historians and supermarket tabloids will become interested in cosmology, opening new opportunities for funding.
- In the year 2013, the satellite WILKINSON-1 will discover a distortion in the microwave background spectrum. In the same year, the satellite PEEBLES-1 will be launched and succeed in settling the question once and for all by shooting down WILKINSON-1 and observing a 3 K cold-load for the remainder of its mission.
- At a Vatican conference in the year 2222 observers will report upper limits on the anisotropy of the microwave background of less than 10^{-10} on all angular scales and theorists will finally admit that we do not exist. Philosophers will say "I told you so."

But I could be wrong.

References

Alpher, R.A. and Herman, R.C. (1949), *Phys. Rev.*, **75**, 1089.

Baars, J.W.M., Genzel, R., Pauliny-Toth, I.I.K. and Witzel, A. (1977), *Astron. Astrophys.*, **61**, 99.

Bouchet, F.R., Bennett, D.P. and Stebbins, A. (1988), *Nature*, **335**, 410.

Berger, J.O. (1985), *Statistical Decision Theory and Bayesian Analysis*, (New York: Springer-Verlag).

Berger, J.O. and Wolpert, R.L. (1984), *The Likelihood Principle*, (Hayward: Institute of Mathematical Statistics).

Bernstein, G.M., Fischer, M.L., Richards, P.L., Petersen, J.B. and Timusk, T. (1989), *Ap. J.*, **337**, L4.

Birkinshaw, M. (1987), in *Observational Cosmology, I.A.U. Symposium 124*, ed. A. Hewitt, G. Burbidge and L.Z. Fang (Dordrecht: Kluwer) pp. 83–86.

Birkinshaw, M., Gull, S.F. and Hardebeck H.E. (1984), *Nature*, **309**, 34.

Bond, J.R. (1986), in *NATO Summer School on the Early Universe*, ed. W.G. Unruh and G.W. Semenoff (Dordrecht: Reidel) pp. 283–334.

Bond, J.R. (1988), in *The Epoch of Galaxy Formation*, ed. C.S. Frenk, R.S. Ellis, T. Shanks, A.F. Heavens, J.A. Peacock (Dordrecht: Kluwer) pp. 211–226.

Bond, J.R., Carr, B.J. and Hogan, C.J. (1986), *Ap. J.*, **306**, 428.

Bond, J.R., Carr, B.J. and Hogan, C.J. (1989), preprint.

Bond, J.R. and Efstathiou, G. (1984), *Ap. J. Lett.*, **285**, L45.

Bond, J.R. and Efstathiou, G. (1987), *M.N.R.A.S.*, **226**, 655.

Bond, J.R. and Szalay, A.S. (1983), *Ap. J.*, **274**, 443.

Boughn, S.P., Cheng, E.S. and Wilkinson, D.T. (1981), *Ap. J. Lett.*, **243**, L113.

Boynton, P.E. and Partridge, R.B. (1973), *Ap. J.*, **181**, 243.

Bracewell, R.N. (1986), *The Fourier Transform and Its Applications*, (New York: McGraw-Hill).

Bridle, A.H. (1986), in *Synthesis Imaging, Course Notes from an NRAO Summer School held in Socorro, New Mexico, August 5–9, 1985*, ed. R.A. Perley, F.R. Schwab and A.H. Bridle (NRAO) pp. 253–278.

Bridle, A.H. and Perley, R.A. (1984), *Ann. Rev. Astron. Astrophys.*, **22**, 319.

Cole, S. and Efstathiou, G. (1989), *M.N.R.A.S.*, **239**, 195.

Cole, S. and Kaiser, N. (1989), *M.N.R.A.S.*, **233**, 637.

Coles, P. (1988), *M.N.R.A.S.*, **234**, 509.

Coles, P. and Barrow, J.D. (1987), *M.N.R.A.S.*, **228**, 407.

Condon, J.J. (1974), *Ap. J.*, **188**, 279.

Condon, J.J. (1988), in *Galactic and Extragalactic Radio Astronomy*, ed. G.L. Verschur, and K.I. Kellerman (New York:Springer-Verlag) pp. 641–678.

Condon, J.J., Condon, M.A. and Hazard, C. (1982), *Astron. J.*, **87**, 739.

Conklin, E.K. and Bracewell, R.N. (1967), *Nature*, **216**, 777.

Cornwell, T. (1986), in *Synthesis Imaging, Course Notes from an NRAO Summer School held in Socorro, New Mexico, August 5–9, 1985*, ed. R.A. Perley, F.R. Schwab and A.H. Bridle (NRAO) pp. 109-121.

Cornwell, T. (1986a), in *Synthesis Imaging, Course Notes from an NRAO Summer School held in Socorro, New Mexico, August 5–9, 1985*, ed. R.A. Perley, F.R. Schwab and A.H. Bridle (NRAO) pp. 137–147.

Daly, R. A. (1988), *M.N.R.A.S.*, **232**, 853.

Danese, L., De Zotti, G., and Mandolesi, N. (1983), *Astron. Astrophys.*, **121**, 114.

Davies, R.D., Lasenby, A.N., Watson, R.A., Daintree, E.J., Hopkins, J., Beckman, J., Sanchez-Almeida, J. and Rebolo, R. (1987), *Nature*, **326**, 462.

de Lapparent, V., Geller, M.J. and Huchra, J.P. (1988), *Ap. J.*, **332**, 44.

Dicke, R.H., Peebles, P.J.E., Roll, P.G. and Wilkinson, D.T. (1965), *Ap. J.*, **142**, 414.

Djorgovski, S. and Weir, N. (1990), *Ap. J.*, **351**, 343.

Doroshkevich, A.G. (1984), *Sov. Astron.*, **28**, 253.

Doroshkevich, A.G., Klypin, A.A. and Khlopov, M.U. (1989), *M.N.R.A.S.*, **239**, 923.

Doroshkevich, A.G., Zel'dovich, Y.B. and Sunyaev, R.A. (1978), *Sov. Astron.*, **22**, 523.

Edwards, A.W.F. (1972), *Likelihood*, (Cambridge: Cambridge University Press).

Efstathiou, G. (1988), in *Large Scale Motions in the Universe*, ed. V.C. Rubin and G.V. Coyne (Princeton: Princeton Univ. Press) pp. 299–319.

Efstathiou, G. and Bond, J.R. (1987), *M.N.R.A.S.*, **227**, 33P.

Faber, S.M., Burstein, D. (1988), in *Large Scale Motions in the Universe*, ed. V.C. Rubin and G.V. Coyne (Princeton: Princeton Univ. Press) pp. 115–167, and references therein.

Fixsen, D.J., Cheng, E.S. and Wilkinson, D.J. (1983), *Phys. Rev. Lett.*, **50**, 8, No. 1, 620.

Fomalont, E.B., Kellerman, K.I., Anderson, M.C., Weistrop, D., Wall, J.V., Windhorst, R.A. and Kristian, J.A. (1988), *Astron. J.*, **96**, 1187.

Franceschini, A., Toffolatti, L., Danese, L. and De Zotti, G. (1989), *Ap. J.*, **344**, 35.

Gamow, G. (1946), *Phys. Rev.*, **70**, 572.

Geller, M.J. and Huchra, J.P. (1988), in *Large Scale Motions in the Universe*, ed. V.C. Rubin and G.V. Coyne (Princeton: Princeton Univ. Press) pp. 5–29, and references therein.

Gull, S.F. (1989), in *Maximum Entropy and Bayesian Methods*, ed. J. Skilling (Dordrecht: Kluwer) pp. 53-71.

Gull, S.F. and Skilling, J. (1984), *IEEE Proc.*, **131 (F)**, 646.

Guth, A.H. (1981), *Phys. Rev.*, **D32**, 347.

Halpern, M., Benford, R., Meyer, S., Meuhlner, D. and Weiss, R. (1989), *Ap. J.*, **332**, 596.

Hogan, C.J. (1984), *Ap. J. Lett.*, **284**, L1.

Hogan, C.J. and Bond, J.R. (1988), in *The Post-Recombination Universe*, ed. N. Kaiser and A.N. Lasenby (Dordrecht: Kluwer) pp. 141–150.

Hogan, C.J. and Partridge, R.B. (1989), *Ap. J. Lett.*, **341**, L29.

Holtzman, J.A. (1989), *Ap. J. Suppl.*, **71**, 1.

Ikeuchi, S. (1981), *Pub. Ast. Soc. Japan*, **33**, 211.

Kaiser, N. and Silk, J. (1986), *Nature*, **324**, 529.

Kellerman, K.I. and Owen, F.N. (1988), in *Galactic and Extragalactic Radio Astronomy*, ed. G.L. Verschur, and K.I. Kellerman (New York:Springer-Verlag) pp. 563–602.

Kellerman, K.I. and Wall, J.V. (1987), in *Observational Cosmology, I.A.U. Symposium 124*, ed. A. Hewitt, G.R. Burbidge, and L.Z. Fang (Dordrecht:Kluwer) pp. 545–564.

Kendall, M. and Stuart, A. (1977), *The Advanced Theory of Statistics, Vol. 1, 4th ed.*, (New York: Macmillan).

Kendall, M. and Stuart, A. (1979), *The Advanced Theory of Statistics, Vol. 2, 4th ed.*, (New York: Macmillan).

Klein, M.J. and Gulkis, S. (1978), *Icarus*, **35**, 44.

Klypin, A.A., Sazhin, M.V., Strukov, I.A. and Skulachev, D.P. (1987), *Soviet. Astr. Lett.*, **13**, 104.

Kofman, L.A. and Pogosyan, D.Y. (1988), *Phys. Lett.*, **B 214**, 508.

Kraus, J.D. (1982), *Radio Astronomy*, (Ohio:Cygnus-Quasar).

Lasenby, A.N. and Davies, R.D. (1988), in *Large Scale Motions in the Universe*, ed. V.C. Rubin and G.V. Coyne (Princeton: Princeton Univ. Press) pp. 278–298.

Lawrence, C.R., Readhead, A.C.S., and Myers, S.T. (1988), in *The Post-Recombination Universe*, ed. N. Kaiser and A.Lasenby (Dordrecht: Kluwer) pp. 173–181.

Lehmann, E.L. (1986), *Testing Statistical Hypotheses*, (New York: Wiley-Interscience).

Linde, A.D. (1982), *Phys. Lett.*, **108B**, 389.

Longair, M.S. and Sunyaev, R.A. (1969), *Nature*, **223**, 719.

Lubin, P., Villela, T., Epstein, G. and Smoot, G. (1985), *Ap. J. Lett.*, **298**, L1.

Lynden-Bell, D., Faber, S.M., Burstein, D., Davies, R.L., Dressler, A., Terlevich, R.J. and Wegner, G.W. (1988), *Ap. J.*, **326**, 19.

Martin, H.M. and Partridge, R.B. (1988), *Ap. J.*, **324**, 794.

Mather, J.C., Cheng, E.S., Eplee, R.E., Isaacman, R.B., Meyer, S.S., Shafer, R.A., Weiss, R., Wright, E.L., Bennett, C.L., Boggess, N.W., Dwek, E., Gulkis, S., Hauser, M.G., Janssen, T., Kelsall, T., Lubin, P.M., Moseley, Jr., S.H., Murdock, T.L., Silverberg, R.F., Smoot, G.F. and Wilkinson, D.T. (1990), Preprint.

Matsumoto, T., Hayakawa, S., Matsuo, H., Murakami, H., Sato, S., Lange, A.E. and Richards, P.L. (1988), *Ap. J.*, **329**, 567.

Meinhold, P. and Lubin, P. (1990), in preparation.

Melchiorri, F., Melchiorri, B.O., Ceccarelli, C. and Pietraner, L. (1981), *Ap. J. Lett.*, **250**, L1.

Ostriker, J.P. and Cowie, L.L. (1981), *Ap. J. Lett.*, **243**, L127.

Ostriker, J.P. and Thompson, C. (1987), *Ap. J. Lett.*, **323**, L97.

Ostriker, J.P., Thompson, C.J. and Witten, E. (1987), *Phys. Lett.*, **B180**, 231.

Parijskij, Y.N., Petrov, Z.E. and Cherkov, L.N. (1977), *Sov. Astron. Lett.*, **3**, 263.

Pauliny-Toth, I.I.K., Witzel, A., Preuss, E., Baldwin, J.E. and Hills, R.E. (1978), *Astron. Astrophys. Supp.*, **34**, 253.

Peebles, P.J.E. (1968), *Ap. J.*, **153**, 1.

Peebles, P.J.E. (1972), *Physical Cosmology*, (Princeton: Princeton Univ. Press).

Peebles, P.J.E. (1980), *The Large Scale Structure of the Universe*, (Princeton: Princeton Univ. Press).

Peebles, P.J.E. (1981), *Ap. J.*, **248**, 885.

Peebles, P.J.E. (1982), *Ap. J. Lett.*, **263**, L1.

Peebles, P.J.E. (1983), *Ap. J.*, **274**, 1.

Peebles, P.J.E. (1987), *Ap. J.*, **315**, L73.

Peebles, P.J.E. and Yu, J.T. (1970), *Ap. J.*, **162**, 815.

Penzias, A.A. and Wilson, R.W. (1965), *Ap. J.*, **142**, 414.

Press, W.H., Flannery, B.P., Teukolsky, S.A. and Vetterling, W.T. (1986), *Numerical Recipes*, (Cambridge; Cambridge University Press).

Press, W.H., Ryden, B.S. and Spergel, D.H. (1989), *Ap. J.*, **347**, 604.

Readhead, A.C.S., Lawrence, C.R., Myers, S.T., Sargent, W.L.W., Hardebeck, H.E. and Moffet, A.T. (1989), *Ap. J.*, **346**, 566.

Rees, M.J. (1978), in *Observational Cosmology, SAAS FEE 1978*, ed. A. Maeder, L. Martinet and G. Tammann (Geneva Observatory) pp. 261–321.

Rees, M.J. (1982), in *The Very Early Universe*, ed. G.W. Gibbons, S.W. Hawking and S.T.Siklos (Cambridge: Camb. Univ. Press) pp. 29–89.

Robinson, E.A. (1967), *Statistical Communication and Detection*, (London:Griffin).

Ryu, D., Vishniac, E.T. and Chiang, W. (1989) preprint.

Sachs, R.K. and Wolfe, A.M. (1967), *Ap. J.*, **147**, 73.

Schaefer, R.K., Shafi, Q. and Stecker, F.W. (1989), *Ap. J.*, **347**, 575.

Schaeffer, R. and Silk, J. (1988), *Ap. J.*, **333**, 509.

Scheuer, P.A.G. (1957), *Proc. Camb. Phil. Soc.*, **53**, 764.

Silk, J. (1968), *Nature*, **218**, 453.

Silk, J. (1984), in *Inner Space/ Outer Space*, ed. E.W. Kolb, M.S. Turner, D. Lindley, K. Olive and D. Seckel (Chicago: Univ. Chi. Press) pp. 143–158.

Silk, J. and Wilson, M.L. (1980), *Physica Scripta*, **21**, 708.

Skilling, J. (1989), in *Maximum Entropy and Bayesian Methods*, ed. J. Skilling (Dordrecht: Kluwer).

Sramek, R.A. and Schwab, F.R. (1986), in *Synthesis Imaging, Course Notes from an NRAO Summer School held in Socorro, New Mexico, August 5–9, 1985*, ed. R.A. Perley, F.R. Schwab and A.H. Bridle (NRAO) pp. 67–86.

Sunyaev, R.A. (1978), in *The Large Scale Structure of the Universe, I.A.U 97*, ed. M.S. Longair and J. Einasto (Dordrecht: Reidel) pp. 393-404.

Sunyaev, R.A. and Zel'dovich, Y.B. (1970), *Astrophys. Space Sci.*, **7**, 3.

Sunyaev, R.A. and Zel'dovich, Y.B. (1981), *Astrophys. Space Sci. Rev.*, **1** **(E)**, 1.

Thompson, A.R., Clark, B.G., Wade, C.M. and Napier, P.J. (1980), *Ap. J. Suppl.*, **44**, 151.

Timbie, P.T. and Wilkinson, D.T. (1988), *Rev. Sci. Instrum.*, **59**, 914.

Turok, N. (1989), *Phys. Rev. Lett.*, **63**, 2624.

Ulich,B.L., Davis, J.H., Rhodes, P.J. and Hollis, J.M. (1980), *IEEE Trans. Antennas Propagat.*, **AP-13**, 367.

Uson, J.M. and Wilkinson D.T. (1984a), *Ap. J. Lett.*, **277**, L1.

Uson, J.M. and Wilkinson D.T. (1984b), *Ap. J.*, **283**, 471.

Uson, J.M. and Wilkinson D.T. (1984c), *Nature*, **312**, 427.

Vilenkin, A. (1981), *Phys. Rev. Lett.*, **46**, 1169.

Vilenkin, A. (1986), in *Inner Space/ Outer Space*, ed. E.W. Kolb, M.S. Turner, D. Lindley, K. Olive and D. Seckel (Chicago: Univ. Chi. Press) pp. 269–278.

Vishniac, E.T. (1987), *Ap. J.*, **322**, 597.

Vittorio N. and Silk, J. (1984), *Ap. J. Lett.*, **285**, L39.

Weinberg, S. (1972), *Gravitation and Cosmology,* (New York: Wiley) .

Wise, M.B. (1988), in *NATO Summer School on the Early Universe*, ed. W.G. Unruh and G.W. Semenoff (Dordrecht: Reidel) pp. 215–238.

Yahil, A. and Vidal, N.V. (1977), *Ap. J.*, **214**, 347.

Zel'dovich, Y.B. and Sunyaev, R.A. (1969), *Astrophys. Space Sci.*, **4**, 301.